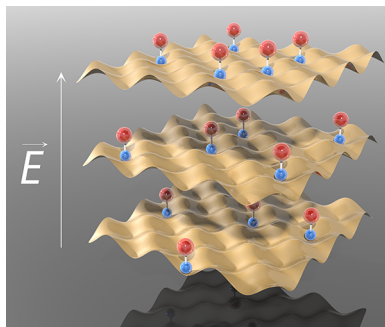


Ultracold Molecules under Control!

Goulven Quéméner*,† and Paul S. Julienne*,‡

†JILA, University of Colorado, Boulder, CO 80309-0440, United States

‡Joint Quantum Institute, NIST and the University of Maryland, Gaithersburg, Maryland 20899-8423, United States



CONTENTS

1. Unconventional Conditions at Ultracold Temperatures	4949	4.8. Direct Imaging of Polar Molecules	4992
1.1. Introduction	4949	4.9. Quantum Stereodynamics of Polar Molecules	4993
1.2. Cooling, Trapping, and Lattices	4951	4.10. Ground-State Molecules in 3D Optical Lattices	4998
1.3. Quantum Threshold Collisions	4952	4.11. Three-Body Collisions of Polar Molecules	5001
1.4. Collision Control with Fano-Feshbach Resonances	4954	5. Perspectives for Ultracold Chemistry	5004
1.5. Obtaining Ultracold Molecules	4957	Author Information	5006
1.5.1. Table of Ultracold Polar Molecules	4959	Corresponding Author	5006
2. Theoretical Framework for Ultracold Molecular Collisions	4959	Notes	5006
2.1. Background	4959	Biographies	5006
2.2. Kinds of Theories	4961	Acknowledgments	5006
2.2.1. Coupled Channels Methods	4961	References	5006
2.2.2. Long-Range Theories	4962		
2.2.3. Models of the Collision Complex	4963		
3. Ultracold Collisions with Alkali Molecules	4964		
3.1. Experiment	4964		
3.1.1. Ultracold Collisions of Rovibrational Molecules	4964		
3.1.2. Tuning Ultracold Molecular Collisions Using Feshbach Molecules and Magnetic Fields	4967		
3.2. Theory	4971		
3.2.1. Ultracold Atom–Molecule Dynamics	4971		
3.2.2. Ultracold Molecule–Molecule Dynamics	4976		
4. Physics and Chemistry with Ultracold, Ultracontrolled Molecules	4976		
4.1. Electric Dipole Moment of Polar Molecules	4977		
4.2. Hyperfine Structure of Polar Molecules	4978		
4.3. Long-Range Interaction of Polar Molecules	4978		
4.4. Chemical Reactivity of Polar Molecules	4980		
4.5. Beyond Rovibronic Control: Hyperfine State Control and Quantum Superposition	4983		
4.6. Ultracold Molecular Chemical Reactions	4984		
4.7. Electric Field Control of Dipolar Collisions and Chemical Reactions	4988		

1. UNCONVENTIONAL CONDITIONS AT ULTRACOLD TEMPERATURES

1.1. Introduction

This review is concerned with the physics and chemistry associated with the interactions, collisions, and reactions of ultracold molecules, that is, molecules having translational temperatures on the order of μK or less. Such molecules can now be produced in their rotational and vibrational ground states in the laboratory by using magnetic and electromagnetic control techniques to assemble them from already ultracold atoms.^{1,2} Theoretical tools are also being developed that are appropriate to this new regime. Chemists have to learn to think differently about the ultracold domain, which is on the order of 9 orders of magnitude removed from room temperature and even 6 orders of magnitude colder than the few K of interstellar space or liquid He. This enormous decrease in accessible temperature and entropy leads to new quantum phenomena and control possibilities, as indicated by Figure 1. In the ultracold regime, even the energy splittings associated with spin hyperfine structure and the normally weak interactions with electromagnetic fields can be very large compared to $k_{\text{B}}T$, where T is temperature and k_{B} is the Boltzmann constant. The de Broglie wavelength associated with the relative motion of two colliding species can be orders of magnitude larger than the range of any chemical interaction, and the intrinsic quantum dynamics of collisions is exquisitely sensitive to very weak long-range interactions subject to experimental control. Chemical reactions at 200 nK have already been observed to occur where all degrees of freedom of the colliding species are controlled and quantized, including vibration, rotation, electron and

Special Issue: 2012 Ultracold Molecules

Received: March 5, 2012

Published: August 24, 2012

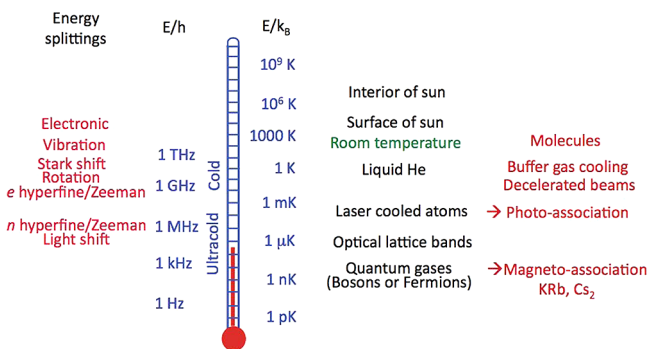


Figure 1. Phenomena associated with various ranges of energy E with E/k_B in units of temperature and E/h in units of frequency. Typical molecular energy splittings are indicated, with e and n referring to electronic and nuclear spin, respectively. We use “cold” to refer to phenomena in the range from 1 mK to a few K and “ultracold” to refer to phenomena below 1 mK, with 10 nK to 10 μ K being typical of the experimentally accessible range. $E/k_B = 1 \mu\text{K}$ is equivalent to $E/h = 20.8 \text{ kHz}$. Cold molecules can be made using a cold buffer gas or by decelerating a molecular beam. The coldest molecules are currently made by associating two already cold atoms.

nuclear spin, orientation, and translation.^{3,4} This review will cover the special aspects of this novel domain, including the essential features of the cooling and trapping of atoms and molecules, the magnetic, electric, and electromagnetic control techniques available for them, the formation of ultracold molecules, the ultracold collisions and reactions of molecules, and then end with some perspectives on the future of this rapidly developing new field. We will concentrate on the collisions and reactions of ultracold alkali molecules, especially polar molecules subject to electric field control.

The motivations, new scientific directions, and applications associated with cold and ultracold molecules have been treated in some detail recently by an article by Carr et al.⁵ in a special 2009 issue of *New Journal of Physics*. Cold molecules are also the topic of the *Faraday Discussion* 142 in 2009 with a special introduction by Hershbach,⁶ a book “*Cold molecules: Theory, Experiments, Applications*” by Krems, Friedrich, and Stwalley,⁷ reviews by Dulieu and Gabbanini,⁸ Schnell and Meijer,⁹ and Bell and Softley,¹⁰ and a themed issue in 2011 of *Physical Chemistry Chemical Physics*.¹¹ We will not reiterate the motivations and opportunities here but only note that there is much promise for applications in fundamental science, precision measurement, quantum simulation of complex systems, quantum information, and computing, in addition to the opportunity to explore novel control aspects for chemical dynamics made possible by the development of ultracold molecular sources. Needless to say, collisions are very important to the ultracold domain for two complementary reasons: they provide tools for precise control of interactions and dynamics, but they also provide destructive inelastic and reactive loss paths that limit the lifetime of the molecular sample or process being studied. We will concentrate in this review on the ultracold domain where T is on the order of μK or less.

Let us start with the familiar description of two interacting species A and B , which could either be atoms or molecules. Each of these species is individually characterized by an internal Hamiltonian H_A or H_B , which includes the effect of any external magnetic, electric, or electromagnetic fields. The Hamiltonian of the combined system is

$$H = H_A + H_B + H_{AB} \quad (1)$$

where H_{AB} describes the relative motion and interaction of A and B , characterized by one or more Born–Oppenheimer electronic potential surfaces, and includes the effect of any external fields. Each individual species has a number of quantized bound states with energies E_n^A or E_m^B , where n and m represent the collective set of quantum numbers needed to define the bound states. These quantum numbers characterize the electronic, vibrational, rotational, and spin degrees of freedom of the molecule, with characteristic splittings indicated in Figure 1. Normally an experiment prepares some distribution of such states, and collisions or reactions occur among the species so prepared. Such collisions are characterized by a set of rate constants or cross sections for elastic, inelastic, or reactive collision events. These rate constants can in principle be determined as a suitable average and sum over all the individual elements $S_{nml,n'm'l'}(E_{\text{tot}})$ of the unitary S -matrix for collisions at total energy $E_{\text{tot}} = E_n^A + E_m^B + \hbar^2 k_{nm}^{-2}/(2\mu)$. The latter term is the kinetic energy for relative collision momentum $\hbar k_{nm}$ of the two species with reduced mass $\mu = m_A m_B / (m_A + m_B)$ for masses m_A and m_B of the individual species. If nm are the initial quantum numbers of A and B , $\hbar^2 k_{nm}^{-2}/(2\mu)$ is the collision energy E_c . The quantum numbers l and l' represent the respective “partial wave” quantum numbers of relative rotational motion of the reactants and products.¹² The quantum numbers of the initial states of A and B are n and m , respectively, and the quantum numbers for the product states n' and m' represent states of A and B in the case of elastic or inelastic collisions and new species in the case of reaction. We define the entrance and exit collision “channels” by the quantum numbers nml or $n'm'l'$.

In conventional chemistry, the number of states encompassed by $k_B T$ is normally large, usually spanning hyperfine and spin structure, molecular rotation, and possibly even several vibrational states (see Figure 1). The de Broglie wavelength $\lambda_{dB} = 2\pi/k_{nm}$ on the order of a few pm is small compared to chemical bond lengths, and many partial waves l , even hundreds, contribute to the collision rate constants. Consequently many $S_{nml,n'm'l'}(E_{\text{tot}})$ values must be calculated, summed, and averaged to calculate a collision rate. The ultracold world is completely the opposite! Each species can be prepared initially in a single internal hyperfine spin state. Unlike in conventional chemistry where the splitting between such states is normally orders of magnitude smaller than $k_B T$, Figure 1 shows that normally negligible hyperfine splitting can be much larger than $k_B T$ for the few μK depth of weak molecular traps. Thus, even an inelastic collision that only changes hyperfine state could release enough energy that the “hot” products would leave the trap. Furthermore, the de Broglie wavelength can be of the order of $\sim 100 \text{ nm}$ ($\sim 2000 a_0$, where a_0 is the Bohr radius), much longer than a chemical bond length ($\lesssim 10 a_0$) and even the range of the long-range potential ($\sim 100 a_0$). Consequently, the longest length scale in the problem is the de Broglie wavelength so that the quantum threshold regime is reached where standard threshold laws apply and only the lowest allowed partial wave contributes to the reaction. Thus, as $T \rightarrow 0$, identical bosonic species (distinguishable or indistinguishable), identical fermionic species (but distinguishable), or any unlike species only have s -wave collisions ($l = 0$), whereas identical and indistinguishable fermionic species only have p -wave collisions ($l = 1$).¹³ It is even possible to put two individual species in a single trapping

cell where the relative translational motion is quantized with energy spacing larger than $k_B T$. Such cells can be achieved by optical lattices, to be described below, and provide tight confinement in one, two, or three dimensions (denoted 1D, 2D, and 3D, respectively), leading to collisions of reduced dimensionality, where the reaction rate can be dramatically modified by changing the molecular orientation.

1.2. Cooling, Trapping, and Lattices

The advent of laser cooling of atoms,¹⁴ recognized by the 1997 Nobel prize in physics to Chu, Phillips, and Cohen-Tannoudji,^{15–17} ushered in a highly productive new era of research with ultracold atomic and molecular species. The availability of laser cooling along with magnetic atom traps fed the development of evaporative cooling methods¹⁸ for bosonic Na and Rb atoms to reach the high phase space density necessary for Bose–Einstein condensation.^{19–21} This phenomenon is a quantum phase transition of a degenerate quantum gas where all atoms in a trapped gas occupy a single quantum state of motion.²² The experimental realization of a condensate was recognized by the 2001 Nobel Prize in Physics to Cornell, Wieman, and Ketterle.^{23,24} While the initial work with ultracold gases was with bosonic species, much progress has subsequently been made with quantum degenerate gases of fermionic atoms,^{25–27} which have quite different properties than bosonic ones.²⁸

Much of the work on ultracold atomic gases has been made possible by the development of optical traps, utilizing the spatially dependent light shift of an atom in a tightly focused region of a laser.²⁹ The laser frequency is usually tuned far from any allowed transitions to keep the light scattering rate low to avoid heating the atoms by recoil kicks. Consequently, trap depths of optical traps are small, typically on the order of a few μK . Trap shapes can vary from spherical to flat “pancake” or elongated “cigar” geometries. Traps are approximately harmonic in each direction with frequencies that range from a few Hz to hundreds of Hz.²⁹ Such traps permit spin states to be trapped that cannot be held by magnetic traps. Thus, any spin component of a state can be trapped, not just the ones that are magnetically trappable because they have increasing energy with increasing magnetic field (Maxwell’s equations only permit a three-dimensional magnetic field minimum but not a maximum). Molecules have similar light shifts to atomic ones and can also be trapped in optical traps.

Quantum degenerate gases are those for which the de Broglie wavelength becomes comparable to or larger than the mean distance between particles. The phase space density, or number of particles per cubic thermal de Broglie wavelength ($\lambda_{\text{dB},T}$)³ = $(h/(2\pi m k_B T)^{1/2})^3$, becomes high, on the order of unity, or equivalently the thermal de Broglie wavelength is comparable to the average spacing between particles $n^{-1/3} \approx \lambda_{\text{dB},T}$ ($n = N/V$ is the density of N particles trapped in the volume V). This happens when the atoms are cold enough, typically in the nK to μK range, that they exhibit condensed matter quantum phenomena in spite of the fact that such gases are very dilute by chemistry standards. Ultracold atom traps typically hold 10^5 – 10^6 atoms at characteristic densities n on the order of 10^{15} cm^{-3} for bosons and 10^{12} cm^{-3} for fermions (Fermi pressure keeps the fermions apart, whereas bosonic clouds at comparable temperature can be much denser²⁷). Although such gases are metastable with lifetimes that can be on the order of many seconds, the lifetime of the denser ultracold bosonic gases is often limited by three-body recombination,

which is suppressed by a factor of 6 in a Bose–Einstein condensate, due to correlations between the particles in the condensate.^{30,31}

Because of the ability to change the geometry and focusing of sets of laser beams used for optical traps, it is possible to realize a variety of optical lattice structures by creating standing wave patterns of light in space.^{32,33} The simplest 1D lattice structure is to superimpose two counterpropagating laser beams, say in the z direction, to make a lattice potential

$$V_L(z) = V_0 \sin^2(k_L z) \quad (2)$$

where $k_L = 2\pi/\lambda_L$ and λ_L is the laser wavelength. The spacing between the spatially periodic lattice cells is $\lambda_L/2$, and the lattice depth is V_0 . This depth $V_0 \gg E_R$ is linear in laser intensity and often expressed in units of photon recoil, $E_R = \hbar^2 k_L^2 / (2m)$, where m is the mass of the atom. The lattice potential is approximately harmonic near its well minimum, with a frequency ν , angular frequency $\omega = 2\pi\nu$, and confinement size for the ground state of $a_h = (\hbar/(m\omega))^{1/2}$. Lattices with λ_L in the optical domain often have depths of tens of E_R units, typically 10–100 kHz but not exceeding $\sim 50E_R$, spacings of a few hundred nm, and harmonic confinement lengths on the order of 50–100 nm.

A single set of counterpropagating laser beams can divide an optically trapped gas into a series of flat “pancake” cells orthogonal to the z direction, each of which can hold hundreds of atoms. If the harmonic confinement a_h in z is much smaller than the de Broglie wavelength λ of the cold atoms, collisions occur in a reduced dimensional “quasi-2D” geometry.³⁴ By using various geometries of counterpropagating laser beams, lattices of sets of elongated “quasi-1D” tubes³⁵ or fully confined 3D cells can be produced, as shown in Figure 2. Bose–Einstein condensates have densities that are commensurate with fillings

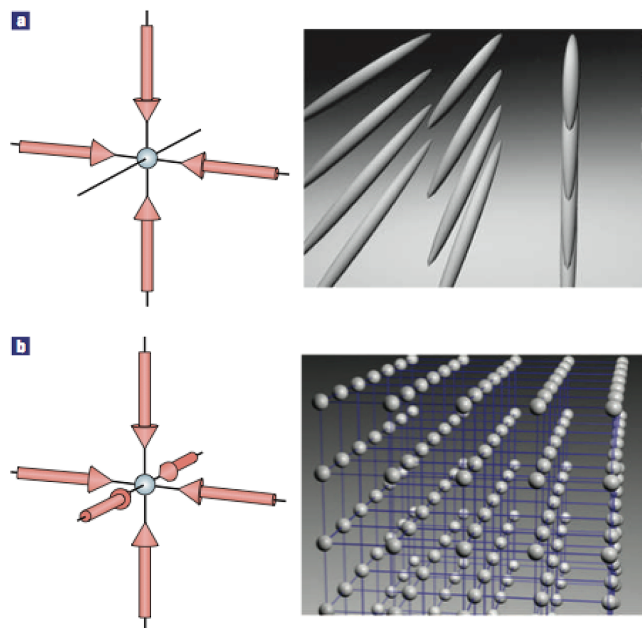


Figure 2. Schematic picture of optical lattices, illustrating (a) a set of elongated tube traps made using four lattice laser beams orthogonal to the tube direction and (b) a set of fully confining 3D cells made using six laser beams propagating in three orthogonal directions. See section 4.9 for figures illustrating flat “pancake” lattices. Reprinted with permission from ref 32. Copyright 2005 Nature Publishing Group.

of one to a few single atoms per lattice site. Figure 3 illustrates the quantum phase transition realized by Greiner et al.,³⁶ who

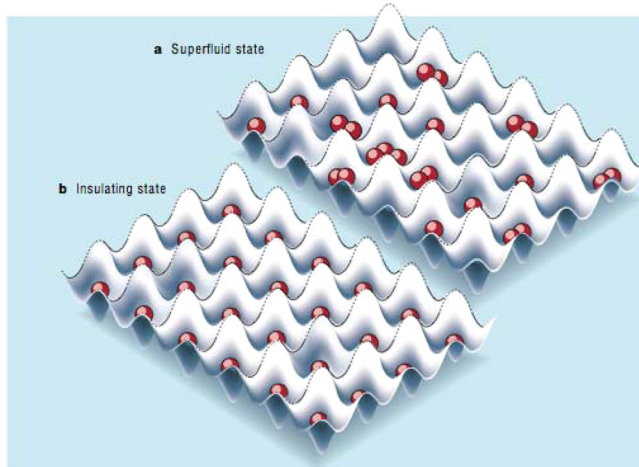


Figure 3. Schematic picture of atoms in an optical lattice illustrating (a) a superfluid state of a Bose–Einstein condensate in a lattice, with a variable occupation of sites and (b) a Mott insulator state with precisely one atom per site. Reprinted with permission from ref 37. Copyright 2002 Nature Publishing Group.

loaded a ⁸⁷Rb condensate into a 3D lattice configuration and increased the lattice depth to decrease the tunneling rate between sites. The quantum phase transition from superfluid to Mott insulator occurs when the tunneling rate becomes sufficiently smaller than the mean-field interaction between atoms in a doubly occupied site, so that atoms localize in the insulator state of panel (b) and do not hop freely between sites in the superfluid state of panel (a).

1.3. Quantum Threshold Collisions

A large part of the work with ultracold atoms and molecules is made possible by the fact that collisions become much simpler in many ways in the quantum threshold region as the collision energy approaches zero. Furthermore, various collision properties can be controlled by the use of laboratory fields. Following the notation in section 1.1, let us assume that the two species A and B are prepared in internal states $|n\rangle$ and $|m\rangle$, respectively. This includes the special case where A and B are the same and the states $|n\rangle$ and $|m\rangle$ are identical. Upon making the usual partial wave expansion of the collisional wave function, the long-range diagonal potential matrix element $V_{nm,nm}(R)$ between the two species at a sufficiently large interspecies separation R will vary as

$$V_{nm,nm}(R) = E_n^A + E_m^B + \frac{C_p(l, nm)}{R^p} + \frac{\hbar^2 l(l+1)}{2\mu R^2} \quad (3)$$

If the coefficient $C_p(l, nm)$ is positive, the overall potential is repulsive and the colliding species are repelled at long range and cannot react. But if the coefficient $C_p(l, nm)$ is negative and $p \geq 3$, the competition between the attractive potential and the repulsive centrifugal potential term will make a long-range centrifugal barrier to reaction, except for the s -wave ($l = 0$). Consequently, barrierless s -wave collisions give the dominant contribution to reaction rates at sufficiently low energy. This is true for any two identical bosons (distinguishable or indistinguishable), two identical (but distinguishable) fermions, or two unlike species. The requirement that the overall wave

function be antisymmetric with respect to exchange of identical particles ensures that identical and indistinguishable fermionic species cannot undergo s -wave collisions, so that the first contributing term in a partial wave expansion in the limit of zero collision energy comes from p -wave collisions ($l = 1$). If $p > 3$, the s - or p -wave contribution is the only one with a non-negligible contribution at sufficiently low collision energy. Other partial waves may contribute at finite energy in the ultracold domain or if $p = 3$ (for example, for a dipole–dipole interaction), even as $k \rightarrow 0$, depending on the magnitude of the $C_p(l, nm)$ term.

It is convenient to define a scale length

$$a_p = \frac{1}{2} (2\mu|C_p|/\hbar^2)^{1/(p-2)} \quad (4)$$

Then when the Schrödinger equation is expressed in dimensionless form with length $r = R/a_p$, the long-range potential term is $2\mu V_{ll}(r)/\hbar^2 = \pm(p-2)^2/r^p + l(l+1)/r^2$. When $R = a_p$, or $r = 1$, the s -wave potential term has a similar magnitude to the kinetic term for a collision kinetic energy of $E_p = \hbar^2/(2\mu a_p^2)$, meaning that the potential is influencing the collision at a distance on the order of a_p for this collision energy. Some authors use other definitions of the potential scale length.³⁸ In the case of a van der Waals potential, we use here a related scale length and energy^{39,40}

$$\bar{a} = 4\pi a_6/\Gamma(1/4)^2 \approx 0.956 a_6 \quad (5)$$

$$\bar{E} = \frac{\hbar^2}{2\mu\bar{a}^2} \approx 1.094 E_6 \quad (6)$$

The Bethe–Wigner threshold laws for low-energy collision cross sections and rate coefficients are well-known.^{41–46} Let us assume for the moment we have prepared each of the species in a specific state and the sample translational temperature T is low enough that the threshold law applies. Elastic scattering then depends only on the single diagonal S-matrix element $S_{nm,nm}(k_{nm})$ with $l = 0$ or 1. This same matrix element determines the total loss probability from the entrance channel due to all inelastic or reactive collisions to be $P^{ls} = 1 - |S_{nm,nm}(k_{nm})|^2$.⁴⁷ Then the threshold rate constants for elastic and loss collisions with relative collision velocity $v_{nm} = \hbar k_{nm}/\mu$ due to a single partial wave $l = 0$ or 1 can be written as⁴⁸

$$K_{nm}^{\text{el}}(k_{nm}) = \frac{\pi\hbar}{\mu} g(2l+1) \frac{|1 - S_{nm,nm}(k_{nm})|^2}{k_{nm}} \quad (7)$$

$$K_{nm}^{\text{ls}}(k_{nm}) = \frac{\pi\hbar}{\mu} g(2l+1) \frac{1 - |S_{nm,nm}(k_{nm})|^2}{k_{nm}} \quad (8)$$

where g is a symmetry factor equal to unity except for identical species ($A = B$) in indistinguishable internal states ($n = m$) when $g = 2$. A rate constant K is related to the corresponding cross section σ by $K_{nm}(k_{nm}) = v_{nm}\sigma_{nm}(k_{nm})$. Comparing to experimental observables requires averaging over the thermal distribution of v_{nm} , and summing over all contributing partial waves. This yields

$$K_{nm}^{\text{el}}(T) = \left\langle \sum_l K_{nm}^{\text{el}}(k_{nm}) \right\rangle_T \quad (9)$$

$$K_{nm}^{\text{ls}}(T) = \left\langle \sum_l K_{nml}^{\text{ls}}(k_{nm}) \right\rangle_T \quad (10)$$

where the brackets $\langle \dots \rangle_T$ imply an average over a Maxwell–Boltzmann distribution at temperature T . Experimental papers often use the symbol β for the loss rate constant instead of K .

If we consider only a single entrance channel nml , we can simplify the notation by dropping the implied indices n and m on S and k . It is useful to write the threshold S -matrix element in terms of a complex phase,

$$S_{l,l}(k) = e^{2i\eta_l(k)} \quad (11)$$

which is related to the complex energy-dependent scattering length $\tilde{a}_l(k)$ with respective real and imaginary parts $-\infty < a_l(k) < \infty$ and $b_l(k) \geq 0$ defined for any l and k by^{43,49–51}

$$\tilde{a}_l(k) = a_l(k) - ib_l(k) = -\frac{\tan \eta_l(k)}{k} = -\frac{i}{k} \frac{1 - S_{l,l}(k)}{1 + S_{l,l}(k)} \quad (12)$$

The negative sign for the imaginary part is included in the equation to ensure a positive value for P^{ls} . Furthermore $P^{\text{ls}} \rightarrow kb_l(k)$ as $k \rightarrow 0$. Consequently, the threshold limits of the rate constants as $k \rightarrow 0$ are

$$K_l^{\text{el}}(k) \rightarrow \frac{4\pi\hbar}{\mu} g(2l+1)kl\tilde{a}_l(k)^2 \rightarrow 0 \quad (13)$$

$$K_l^{\text{ls}}(k) \rightarrow \frac{4\pi\hbar}{\mu} g(2l+1)b_l(k) \rightarrow \text{constant for } l=0 \quad (14)$$

The corresponding cross sections for elastic and loss collisions vary respectively as $|\tilde{a}_l(k)|^2$ and $b_l(k)/k$. At sufficiently low k the s -wave loss cross section continues to increase as $1/k$ with decreasing k and will eventually exceed the elastic cross section, which approaches a constant value as $k \rightarrow 0$.

For potentials between neutral species with $p > 3$, the s -wave scattering length becomes an energy-independent constant $\tilde{a}_{l=0}$ as $k \rightarrow 0$. The p -wave, for which $\tilde{a}_{l=1} = k^2 \tilde{V}_{l=1}$ is linear in collision energy $\hbar^2 k^2 / (2\mu)$, is represented by an energy-independent complex scattering volume $\tilde{V}_{l=1}$. Thus, the thermally averaged threshold rate constants for s - and p -wave inelastic and reactive loss as $k \rightarrow 0$ are

$$K_{l=0}^{\text{ls}}(T) \rightarrow \frac{4\pi\hbar}{\mu} g b_{l=0} \quad (15)$$

$$K_{l=1}^{\text{ls}}(T) \rightarrow 72\pi^2 \frac{k_B T}{\hbar} g \text{Im}(-\tilde{V}_{l=1}) \quad (16)$$

In general, while $\tilde{a}_{l=0}$ and $\tilde{V}_{l=1}$ could be calculated, except in special limiting cases they are very sensitive functions of the system Hamiltonian and potentials and need to be determined experimentally rather than calculated. Experimental data can often be modeled to construct very accurate coupled channels collision models of ultracold ground-state atomic scattering including hyperfine and Zeeman structure.⁴⁰ We will discuss in Section 2.2.2 how simplified models of $\tilde{a}_{l=0}$ and $\tilde{V}_{l=1}$ can be constructed in certain special cases of molecular scattering.

The magnitude of threshold rate constants is constrained by the unitarity property of the S -matrix, which ensures that $0 \leq |1 - S_{l,l}|^2 \leq 4$ and $0 \leq 1 - |S_{l,l}|^2 \leq 1$. Thus, eq 15 shows that the magnitude is set by the product of the constant $4\pi\hbar g/\mu$ times a length. However, the magnitude of the threshold loss rate

coefficient cannot exceed the upper bound set by the unitarity limit for $l = 0$ or 1 :

$$K_{lu}^{\text{ls}} = (2l+1)g \frac{\pi\hbar}{\mu} \langle k^{-1} \rangle_T \quad (17)$$

where $\langle k^{-1} \rangle_T = (2\hbar^2/(\pi\mu k_B T))^{1/2}$ is the thermal expectation value of k^{-1} at temperature T . Thus, eq 15 can only apply for collision energies low enough that $kb_l \leq 4$. In practical units,

$$K_{l=0}^{\text{ls}}/(\text{cm}^3/\text{s}) \approx 4.223 \times 10^{-11} g \frac{b_{l=0}}{m/u} \quad (18)$$

$$K_{l=1}^{\text{ls}}/(\text{cm}^3/\text{s}) \approx 1.121 \times 10^{-22} g (\text{Im}(-\tilde{V}_{l=1})/a_0^3) (k_B T/h) / \text{Hz} \quad (19)$$

where $a_0 = 0.05292 \text{ nm}$ is the Bohr radius of the hydrogen atom and $u = 1.6605 \times 10^{-27} \text{ kg}$ is the universal atomic mass unit. The value of $b_{l=0}$ is often comparable to a length scale associated with the long-range potential, in which case threshold s -wave loss rate constants for strongly allowed processes typically have magnitudes that lie within an order of magnitude of $10^{-10} \text{ cm}^3/\text{s}$. Of course, rate constants for weakly allowed processes can be much smaller. The tuning of threshold resonances can change rate constants by many orders of magnitude.

Figure 4 gives a simple example to demonstrate why the scattering length for the collision of two atoms is so sensitive to

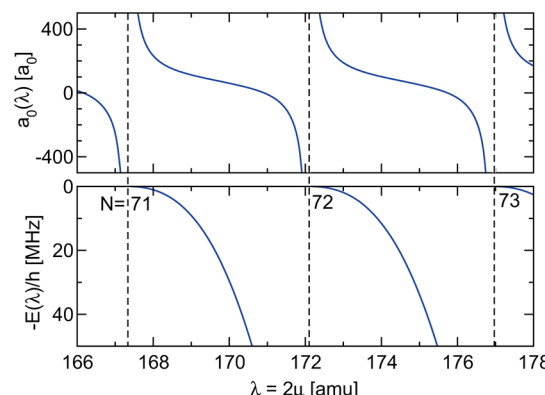


Figure 4. Scattering length and last bound-state energy of Yb_2 molecules of different isotopic combinations, based on an experimental study.⁵² The upper panel shows the calculated scattering length of the single ground-state $^1\Sigma^+$ potential versus $\lambda = 2\mu$ treated as a continuous variable, where μ is the reduced mass of the two Yb atoms. The lower panel shows the corresponding energy of the last bound state. The dashed vertical lines show the pole positions in $a_{l=0}(\lambda)$ where the number of bound states N in the potential change from 71 to 72 to 73.

the details of the short-range potential. One could imagine varying the potential according to some parameter λ that “stretches” it in some way. Section 3.2 illustrates this for molecular collisions. Here we will just vary the reduced mass μ of the atom pair, which in practice can be done in discrete steps by taking different isotopes. The atomic species Yb is very useful here, because it has 7 different stable isotopes with reasonable abundances. The naturally occurring isotopic combinations of two atoms take on 28 discrete values of $\lambda = 2\mu$ between 168 and 176. Kitagawa et al.⁵² accurately measured the binding energies of the last bound states of 6 different homonuclear isotopic combinations using Raman two-color photoassociation spectroscopy of ultracold Yb atoms. By

solving Schrödinger's equation with the specific reduced masses for the 6 species, the single ground-state potential could be adjusted so the calculated binding energies were in excellent agreement with the measured ones.⁵² Figure 4 shows that the scattering length goes through a singularity and thus takes on any value, as λ varies continuously so as to increase the number of bound states supported by the potential. Any potential that does not get the correct absolute number of bound states N supported by the potential cannot claim to predict $a_{l=0}$ accurately for all isotopes.

Gribakin and Flambaum³⁹ showed that the scattering length for a single (barrierless) potential with a van der Waals tail is accurately given by

$$a_{l=0} = \bar{a} \left(1 - \tan \left(\Phi - \frac{\pi}{8} \right) \right) \quad (20)$$

where the phase Φ is given by the standard Jeffreys-Wenzel-Kramers-Brillouin (JWKB) threshold phase integral,^{53,54}

$$\Phi = \int_{R_{in}}^{\infty} \left(\frac{2\mu}{\hbar^2} (-V(R)) \right)^{1/2} dR \quad (21)$$

R_{in} is the inner classical turning point of the potential for $E = 0$ collisions, and $\pi/8$ represents a quantum correction.^{39,55} Recalling Levinson's theorem that the exact quantum phase at threshold is $N\pi$, where N is the total number of s -wave ($J = 0$) bound states supported by the potential, we find that $N = [\Phi/\pi - 5/8] + 1$, where the brackets [...] imply the integer part of the enclosed expression. The scattering length, which controls how the quantum mechanical phase varies with k as k increases from 0, depends on the "leftover" part of the Φ integral after the $N\pi$ part is removed. Consequently, there is no possibility of predicting a reliable scattering length from a theoretical potential unless that potential has both the correct number of bound states of the actual molecule it represents and the correct leftover part of the phase integral. Because the number of bound states is determined by the whole potential, one must have the complete potential with sufficient accuracy over its full range that determines the bound-state spectrum. The same sensitivity exists for more complex systems with several coupled potentials or for molecules instead of atoms. In practice, this sensitivity to the whole potential means that the theoretical treatment of threshold scattering requires semi-empirical parametrizations based on actual experimental data about near-threshold bound states and, if possible, their isotopic sensitivity. Quantitative coupled channels models based on such data have been highly successful in accounting for the rich and detailed Feshbach spectroscopy of alkali-metal atomic collisions and for the isotopic variation of scattering and bound-state properties,^{40,56} as illustrated in the next section of this review.

1.4. Collision Control with Fano-Feshbach Resonances

One of the most powerful tools to emerge in ultracold matter studies is the ability to control the scattering length of ground-state atoms very precisely by using external magnetic fields to tune scattering resonances of the collision complex of the two atoms (that is, a diatomic molecule) near threshold. This is a key feature because the mean-field interaction between ultracold atoms in a quantum degenerate gas using the standard Fermi pseudopotential^{22,28} is proportional to $a_{l=0}(B)$, which is subject to experimental control. Thus, a wide variety of properties of both bosonic gases and fermionic mixtures can be

engineered by tuning such resonances, as extensively reviewed by Köhler et al.⁵⁷ and Chin et al.⁴⁰ These resonances are commonly known as Feshbach resonances in the cold atom literature, but for historical reasons are also sometimes called Fano-Feshbach resonances,⁴⁰ which is the designation we will use in this review. We now summarize the properties of such tunable resonances, because they are a key to the magneto-association process for combining two already ultracold atoms to make an ultracold molecule. We use as an example the KRB molecule, for which the adiabatic potential energy curves correlating with ground-state atoms with hyperfine structure are shown in Figure 5. To get a sense of typical molecular energy

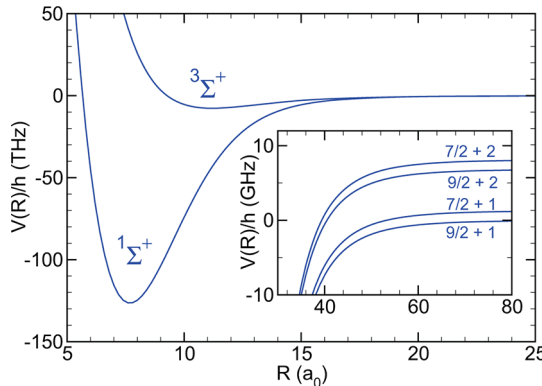


Figure 5. Potential energy curves of the ${}^1\Sigma^+$ and ${}^3\Sigma^+$ states of the KRB molecule that correlate with two separated atoms in their ground 2S state. The inset shows the long-range adiabatic potentials of the fermionic ${}^{40}\text{K}{}^{87}\text{Rb}$ molecule near its dissociation threshold, including the hyperfine structure for magnetic field $B = 0$. The ${}^{40}\text{K}$ fermion has two spin states with total angular momentum $f = 9/2$ and $7/2$ with hyperfine splitting $\Delta E_{hf}/h = 1.29$ GHz, and the ${}^{87}\text{Rb}$ boson has $f = 1$ and 2 states with splitting $\Delta E_{hf}/h = 6.83$ GHz.

scales, the van der Waals length $\bar{a} = 69a_0$ and $\bar{E}/h = 14$ MHz. The dissociation energy, the vibrational splitting between $v = 1$ and $v = 0$, and the rotational splitting between the $v = 0, J = 1$ and $v = 0, J = 0$ levels for the ground ${}^1\Sigma^+$ state with rotational quantum number J are, respectively, 125 THz, 2.23 THz, and 2.23 GHz in E/h frequency units.

A resonance with a pole in the scattering length versus magnetic field B occurs when a bound state $|b\rangle$ of the collision complex with energy $E_b(B)$ crosses threshold at some field.⁵⁸ For simplicity we take the zero of energy to be the B -dependent asymptotic channel energy so that the total energy $E_{tot} = E_c = \hbar^2 k^2 / (2\mu) \rightarrow 0$ at threshold. Such tuning is possible when the bound state that makes the resonance has a different magnetic moment from that of the two free atoms. Let us assume the atoms are prepared in their lowest-energy ground-state Zeeman component, which thus has no two-body decay channels and only experiences elastic scattering. The s -wave scattering length $a_{l=0}$ is real, has a pole at the magnetic field B_0 for which $E_b(B) = 0$, and near threshold varies as

$$a_{l=0}(B) = a_{l=0}^{bg} \left(1 - \frac{\Delta}{B - B_0} \right) \quad (22)$$

where $a_{l=0}^{bg}$ is the background scattering length of the entrance channel in the absence of a resonance and Δ is called the width of the resonance (Δ has units of magnetic field).⁵⁹ A bound state exists just below threshold for positive $a \rightarrow +\infty$, but no bound state exists (except far from threshold) for negative a .

The energy of the bound state of the collision complex that crosses threshold at B_0 is universally related to the scattering length in the limit of large scattering length ($a \gg \bar{a}$ in the case of a van der Waals potential)⁴⁰

$$E_b(B) = -\frac{\hbar^2}{2\mu a(B)^2} \quad (23)$$

Here “universal” means that this relation depends only on the magnitude of the (positive) scattering length. This limiting relationship only applies when the scattering length is larger, possibly much larger, than the scale length a_p of the long-range potential. The relationship between scattering length and threshold bound states is described in detail in refs 40, 56, and 57.

Figure 6 illustrates the properties of Fano-Feshbach resonance tuning using the case of ⁴⁰K and ⁸⁷Rb collisions.

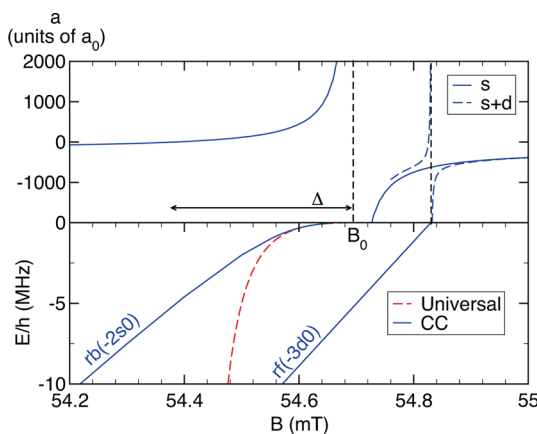


Figure 6. Lower panel shows the calculated (CC) energies of two bound states of the ⁴⁰K⁸⁷Rb molecule. The dashed red line shows the universal energy in eq 23. The upper panel shows the calculated scattering lengths with the vertical dashed lines giving the location of the poles. The solid and dashed curves, respectively, show $a_{l=0}(B)$ calculated with *s*-waves and with *s*- and *d*-waves in the basis. The width Δ of the broader feature is indicated. Reprinted with permission from ref 61. Copyright 2009 Royal Society of Chemistry.

The bound level labeled *rb*(−2s0) in the figure causes a pole in $a_{l=0}(B)$ when it crosses threshold at $B_0 = 54.676(5)$ mT (546.76(5) G).⁶⁰ Away from threshold this state takes on the character of the second *s*-wave bound state below the ⁴⁰K($f = 7/2, m_f = -7/2$) + ⁸⁷Rb($f = 1, m_f = 0$) separated atom limit, where f and m_f , respectively, denote the quantum number for total angular momentum and its projection on the magnetic field axis. Similarly, the level labeled *rf*(−3d0) has the character of the third *d*-wave bound state with $l = 2, m_l = 0$ below the ⁴⁰K($f = 7/2, m_f = -7/2$) + ⁸⁷Rb($f = 2, m_f = 0$) separated atom limit. The much narrower scattering length feature at the higher B -field is a “*d*-wave resonance”⁴⁰ where a bound state of *d*-wave character couples to the entrance channel *s*-wave collision through the small anisotropic magnetic dipole terms in the system Hamiltonian due to the unpaired electron spin on each atom.

The properties of near-threshold bound states as well as scattering states are controlled to a great extent by the power law form R^{-p} of the long-range potential.^{53,54,62–64} This form along with the reduced mass sets the density and spectrum of near-threshold levels corresponding to different l values and permits a classification of different types of Fano-Feshbach

resonance states.⁴⁰ The theory of near-threshold bound states can be developed for various values of p , including the van der Waals ($p = 6$) (refs 38, 40, 51, and 65) and the $p = 3$ (ref 66) and $p = 4$ (refs 67–70) cases, similar to the formulation of LeRoy and Bernstein,⁶² which needs correction near threshold.^{55,63,71–74} A key parameter set by the long-range potential is a characteristic length scale defined in section 1.3. We especially will make use of the characteristic length

$$\bar{a} = [2\pi/\Gamma(1/4)^2](2\mu C_6/\hbar^2)^{1/4} \quad (24)$$

of the van der Waals potential with long-range coefficient C_6 .^{39,40,75} This length, typically a few nm, is much larger than the length of a chemical bond but has a characteristic energy scale $\bar{E} = \hbar^2/(2\mu\bar{a}^2)$ that is much less than 1 K but much more than $k_B T$ in the ultracold regime. The distance \bar{a} separates the range of a threshold collision into an asymptotic region and an interaction region. The long-range centrifugal barrier of the *l*-wave van der Waals potential has a peak energy of $0.0879\bar{E}[l(l+1)]^{3/2}$ at a distance of $R = 2.75\bar{a}/[l(l+1)]^{1/4}$. This gives a *p*-wave barrier of height $0.249\bar{E}$ at $R = 2.32\bar{a}$. As an example, the ground-state ⁴⁰K⁸⁷Rb molecule in its $v = 0, J = 0$ level has $\bar{a} = 6.2$ nm and $\bar{E}/h = 2.04$ MHz for $C_6 = 16\,133 E_h a_0$.⁶ The *p*-wave barrier for the interaction of two such molecules in identical spin states is 24 μK at $R = 14.5$ nm.

The length \bar{a} and energy \bar{E} have played an important role in characterizing threshold atomic interactions. All bound states of any l have outer classical turning points for $R < \bar{a}$, with the possible exception of the last *s*-wave bound state. When $a_{l=0} \gg \bar{a}$, this state takes on the universal energy in eq 23 with wave function $(2/a)^{1/2}\exp(-R/a)$ for $R \gg \bar{a}$. This state is called a “halo state,” because most of the norm is in the long-range region outside of the outer classical turning point. For such a universal bound state, the expectation value of R is $a_{l=0}/2 \gg \bar{a}$. The term “Feshbach molecule” is used for such a state, as well as for other near-threshold states accessible to B -field tuning.⁴⁰

The threshold bound-state and scattering properties of Fano-Feshbach resonance states depend on the parameter $s_{\text{res}} = (a_{l=0}^{\text{bg}}/\bar{a})(\delta\mu_B\Delta/\bar{E})$, where $\delta\mu_B$ is the difference of the magnetic moments of the two separated atoms and the bound molecular state that generates the resonance. The s_{res} parameter expresses the strength of the resonance in a dimensionless form by scaling by the van der Waals parameters \bar{a} and \bar{E} .⁴⁰ We can distinguish two fundamentally different kinds of resonances. One is the “open channel dominated” class, for which $s_{\text{res}} \gg 1$. Such resonances correspond to strong coupling of the closed and open channels and have a universal halo state with dominant open channel character over a significant fraction of their width Δ . The halo bound state has a relatively small admixture of the resonant bound state component of the wave function, which, in any case, vanishes as $B \rightarrow B_0$. The broader resonance in Figure 6 is tending toward this type, with $s_{\text{res}} = 1.96$.⁴⁰ The other class is designated as “closed channel dominated” and is exemplified by the narrow resonance in Figure 6, for which $s_{\text{res}} \ll 1$. In this case, the bound state has nearly pure closed-channel character and only becomes a halo state in a very narrow region of magnetic field tuning $|B - B_0| \ll s_{\text{res}}(a_{l=0}^{\text{bg}}/\bar{a})|\Delta|$ near B_0 .

Halo Feshbach molecules are significant because a halo Feshbach molecule of two fermions in different spin states exhibits a Pauli suppression of their three-body recombination rate.⁷⁷ This suppression permits the tuning of the scattering length in the region near B_0 to make a Bose-Einstein condensate of halo Feshbach molecules that are not destroyed

by collisions with themselves or with the fermionic atoms of which they are comprised. Any vibrational quenching collision would release so much energy that the product molecules would not be trapped. The extraordinary stability of halo molecules comprised of two fermions has been demonstrated with ^6Li ^{78–80} and ^{40}K .⁸¹ The $^6\text{Li}_2$ halo Feshbach molecules so condensed are truly remarkable, having negligible binding energies of only a few hundred kHz and halo sizes greater than $1000a_0$. Yet the molecules are stable against quenching in spite of undergoing hundreds of collisions with similar molecules. Halo molecules composed of two bosons are not expected to show any such stability but to quench rapidly. We generally should expect closed channel dominated narrow resonances of unlike fermions to be more like the bosons and have no special stability against vibrational quenching. Their smaller size $\langle \bar{a} \rangle$ due to lack of halo character gives them more conventional short-range collisional properties.

The study of few-body phenomena like three-body recombination or Efimov physics has been another area of great significance made possible by Fano-Feshbach resonance tuning of cold atom interactions. One of the very first measurements on such tuning effects in a cold atomic gas demonstrated the rapid destruction of a Bose–Einstein condensate through three-body recombination when a resonance is tuned through threshold.⁸² The existence of the two-body resonance leads also to a dramatic increase in the three-body recombination coefficient L_3 . Observing such loss provides a good diagnostic tool for detecting the resonances. Furthermore, other few-body resonances such as those associated with Efimov states can be detected in this way. Thus, it is critical to have a good experimental and theoretical understanding of three-body recombination and other few-body phenomena for both atoms and molecules. We do not have space here to review this material in detail but will summarize some of the essential aspects of three-body recombination and Efimov states as these relate to the molecular three-body phenomena described in section 4.11.

If a is the s -wave scattering length, the three-body recombination coefficient L_3 for three identical bosons of mass m scales as a^4 and can be written^{84–87}

$$L_3 = 3C(a) \frac{\hbar}{m} a^4 \quad (25)$$

where at threshold $C(a)$ can vary between 0 and ~ 68 ; the decay of gas density is given by $\dot{n} = -L_3 n^3$. Sometimes a “recombination length” $\rho_3 = [2mL_3/(\hbar\sqrt{3})]^{1/4}$ is used instead of L_3 .^{83,84} Efimov quantum states^{88,89} in a system of three identical bosons provide a paradigm for universal few-body physics. In 2006 Kraemer et al.⁸³ reported experimental evidence for the existence of the Efimov effect in the three-body recombination of an ultracold gas of Cs atoms tuned by a magnetic field. Figure 7 shows the Cs data. Figure 8 illustrates the basic framework for the Efimov effect. Efimov physics is reflected in a logarithmically periodic behavior $C(e^{\pi/s_0}a) = C(a)$, where the scaling factor $e^{\pi/s_0} \approx 22.7$ for $s_0 \approx 1.00624$, corresponding to the scaling of the infinite series of weakly bound trimer states. Using a magnetic field to tune the scattering length across a singularity, the region near $0 < |1/a| \ll 1/\bar{a}$ can be accessed experimentally in a cold gas ($|a| \gg \bar{a}$ is necessary for universal properties to apply). The three-body recombination rate will be greatly enhanced when a trimer bound state passes threshold, either the three-body threshold for $1/a < 0$ or the atom + dimer threshold for $1/a > 0$. This is

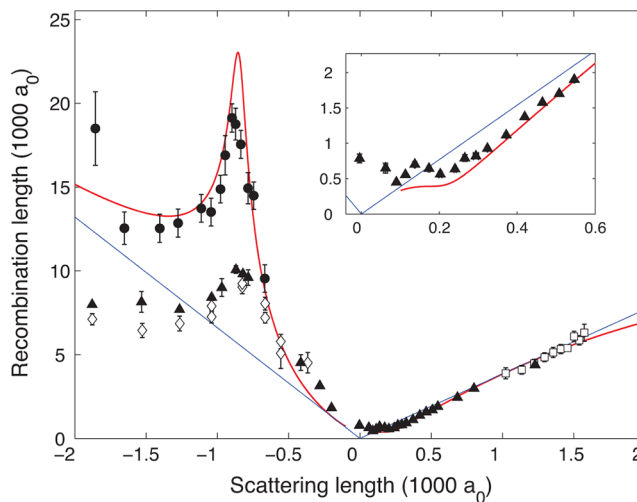


Figure 7. Measured recombination length ρ_3 of three ultracold Cs atoms versus scattering length selected by tuning a Fano-Feshbach resonance with a magnetic field near the resonance location of 0.75 mT. The dots represent data at 10 nK, whereas the filled triangles and open diamonds are at 240 and 250 nK, respectively. The straight lines show the a^4 scaling, and the solid line curve shows a theory fit to the data. The inset shows an expanded view near $a = 0$. Reprinted with permission from ref 83. Copyright 2006 Nature Publishing Group.

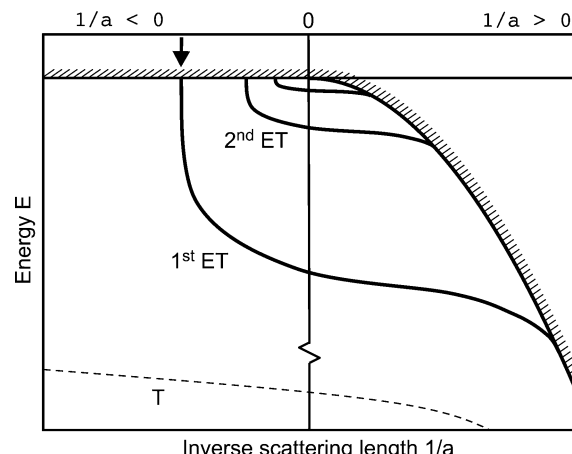


Figure 8. Trimer bound-state energies of three identical bosons. For $1/a > 0$, the hatched line shows the two-body bound state energy below the three-body threshold in the horizontal line; there is no two-body threshold bound state for $1/a < 0$. Trimer bound states can exist below the hatched line. The dashed line labeled T represents a deeply bound trimer state. The solid lines represent the members of an Efimov series of states. There are an infinite number of such states when $1/a \rightarrow 0$. The arrow shows where an Efimov trimer state crosses threshold and dissociates. The three-body recombination rate will show a maximum when the scattering length is tuned to this value. Reprinted with permission from ref 83. Copyright 2006 Nature Publishing Group.

precisely what was observed by Kraemer et al. in 2006, when they detected the first member of the Efimov series in 2006. Chin et al.⁴⁰ review subsequent work on Efimov physics with cold atoms, and Braaten and Hammer⁹⁰ give a much longer review of the universal few-body properties in the limit of large scattering length.

1.5. Obtaining Ultracold Molecules

Molecules normally cannot be laser-cooled, because they do not have the simple two-level structure of atoms needed for scattering many photons without decay to other states different from the two states involved. However, recent work has shown that at least some diatomic molecules with a strongly diagonal Franck–Condon matrix may satisfy the requirements for laser-cooling.⁹¹ Other methods of making cold molecules, such as deceleration of molecular beams^{92,93} or buffer gas cooling,⁵ only produce cold molecules at quite small phase space density. We will not discuss these methods in this review. These are discussed in the review articles of van de Meerakker et al.⁹⁴ and Hutzler et al.⁹⁵ in the present issue. There are currently only two proven ways to get ultracold molecules. Both of these rely on combining two already ultracold atoms into diatomic molecule using either photoassociation as discussed by Koch and Shapiro⁹⁶ in the present issue and Jones et al.⁹⁷ or magneto-association as discussed by Köhler et al.⁵⁷ The former, illustrated in Figure 9, uses light to excite two colliding atoms to

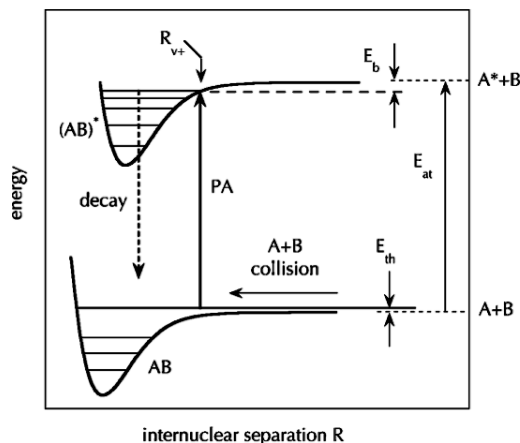


Figure 9. Schematic representation of photoassociation (PA). Two cold ground-state atoms collide with energy E_{th} and are excited by a PA laser of frequency $\hbar\nu$ to an excited-state vibrational level. The process is tuned on-resonance where $\hbar\nu = E_{\text{at}} - E_b - E_{\text{th}}$, where E_b is the binding energy of the excited level relative to the energy E_{at} of the excited atom A^* . The excited level can decay into the ground-state scattering continuum to make two hot atoms or to a vibrational level in the ground electronic state. Reprinted with permission from ref 97. Copyright 2006 American Physical Society.

an excited state, for which some fraction of its spontaneous emission produces bound ground-state molecules.⁹⁸ By using the right kind of tricks, a significant number of vibrational ground-state molecules can be produced, as demonstrated for

$\text{Cs}_2^{99,100}$ and LiCs^{101} molecules. Photoassociation has mainly proved useful for atoms trapped at quite low phase space density in magneto-optical traps, as reviewed by Jones et al.⁹⁷ In contrast, magneto-association has proven to be a very powerful tool for making weakly bound Feshbach molecules at the high phase space densities of quantum degenerate, or near-quantum-degenerate gases, as reviewed by Köhler et al.⁵⁷ and Chin et al.⁴⁰ Magneto-association does not experience the excited-state spontaneous radiative emission losses that accompany photoassociation and can approach unit efficiency for converting atom pairs to Feshbach molecules.¹⁰² Figure 10 illustrates three different ways that have been used in conjunction with a magnetically tunable resonance to associate two ultracold atoms to make a Feshbach molecule: a time-dependent ramp of the field across resonance, an oscillatory field, and three-body recombination. The first of the three is the commonly used method that we call magneto-association. This is the method that has been used for the initial step in the successful production of dense samples of KRb^1 or Cs_2^2 ground-state molecules.

The possibility to make a dense sample of ultracold molecules in their electronic and vibrational ground state by first associating two ultracold atoms was proposed for homonuclear¹⁰³ and heteronuclear polar¹⁰⁴ alkali-metal diatomic molecules. These proposals invoked a multiple sequence of optical Raman steps for which the first step was to make a highly vibrationally excited ground-state molecule by photoassociation of the atom pair, assumed to be held in one of an ensemble of optical lattice cells. Subsequent Raman steps were assumed to convert the population in the excited vibrational level to the ground-state $v = 0$ level. Because the molecules would still be trapped in the lattice cells, turning off the lattice would result in a dense, quantum degenerate gas of ground-state molecules. These ideas were developed in more detail by Bergeman et al.¹⁰⁵ and Stwalley.¹⁰⁶ The former looked in detail at the state structure, spectroscopy, and possible paths for making RbCs molecules, whereas the latter looked at magneto-association using a Fano-Feshbach resonance to access levels of the $a^3\Sigma^+$ state, which could be converted into ground $X^1\Sigma^+$ $v = 0$ molecules following excitation to a mixed excited level having both singlet and triplet character. The feasibility of such conversion was demonstrated by Sage et al.,¹⁰⁷ who demonstrated the transfer of population from the $v = 37$ level to the $v = 0$ level of RbCs . This was done with an atomic sample at quite low phase space density in a magneto-optical trap near $100 \mu\text{K}$. The $v = 37$ level was populated via spontaneous emission from an excited level formed by photoassociation, and several rotational levels of the ground $v = 0$ level were populated in the experiment.

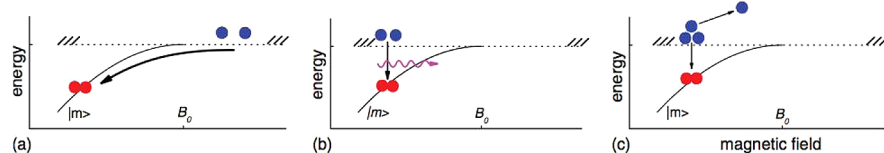


Figure 10. Schematic representation of Feshbach molecule formation. (a) Two ultracold atoms are prepared with B above B_0 , where a Feshbach molecular bound state appears below threshold. A time-dependent sweep of the field to $B < B_0$ produces a Feshbach molecule in the process of magneto-association. (b) The two atoms are prepared at a static magnetic field $B < B_0$, and an oscillatory field is used to associate them. (c) The two atoms are prepared at a static magnetic field $B < B_0$, and three-body recombination converts them to a bound molecule with the binding energy converted into relative kinetic energy of the resulting atom and diatom. Reprinted with permission from ref 40. Copyright 2010 American Physical Society.

A group at the University of Innsbruck was able to demonstrate the magneto-association of two ultracold ^{87}Rb atoms to make weakly bound $^{87}\text{Rb}_2$ Feshbach molecules,¹⁰⁸ and even to move the population to more deeply bound states by a combination of magnetic field and radio frequency field tuning¹⁰⁹ or by optical Raman processes.^{110,111} These experiments were done with ^{87}Rb atom pairs in an optical lattice. They demonstrated both the long lifetime of such molecules, because they are protected from quenching collisions by tight confinement in lattice cells with negligible tunneling between cells, and the coherent and reversible transfer of population between lattice atom pairs and Feshbach molecules. The latter is possible because, with lattice confinement, the translational degrees of freedom of the atoms are quantized, and the association process occurs at constant entropy.

The experimental group at JILA was able to demonstrate the production of an ultracold sample of $\sim 40\,000$ $^{40}\text{K}^{87}\text{Rb}$ fermionic molecules in their electronic, vibrational, and rotational ground state, $v = 0, J = 0$ of the $X^1\Sigma^+$ state at a near-quantum degenerate density of 10^{12} cm^{-3} .¹ Figure 11

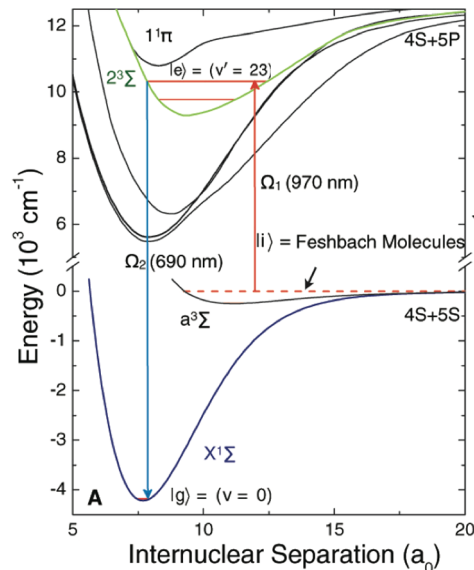


Figure 11. Scheme used to make $v = 0, J = 0$ $^{40}\text{K}^{87}\text{Rb}$ molecules by magneto-association of ^{40}K and ^{87}Rb atoms in an optical trap.¹ A weakly bound Feshbach molecule with predominant $a^3\Sigma^+$ character is switched in a few μs to the $v = 0, J = 0$ ground state using coherent stimulated Raman adiabatic passage through the intermediate $v' = 23$ level of the upper $2^3\Sigma^+$ state. The molecules were measured to have the same temperature as the initial atomic sample in the range of 200–800 nK. Reprinted with permission from ref 1. Copyright 2008 AAAS.

shows the steps used to achieve this. The first step was magneto-association of a pair of atoms in an ultracold mixture of the two atomic species using the broader resonance marked with B_0 in Figure 6. This association process to make a Feshbach molecule at 54.594 mT with a binding energy $E_b/h = 230$ kHz was $\sim 20\%$ efficient at their high phase space density, but not quantum degenerate trapped gas (a lattice was not used in this case). At this B field, the Feshbach molecule is in a mixed state between being a halo molecule with entrance channel spin character and a shorter-ranged resonant state of different spin character. The halo characteristics protect it from quenching collisions,¹¹² whereas the short-range characteristics improve the Franck–Condon matrix element between the

Feshbach level and the excited state. Stimulated Raman adiabatic passage (STIRAP) with only two colors using pulsed frequency and phase-stabilized lasers moved the population of the Feshbach molecule to the $v = 0, J = 0, X^1\Sigma^+$ molecular state. The experiment demonstrated that STIRAP is a coherent, reversible process that is $\sim 90\%$ efficient in the one-way conversion of population, returning 80% of the initial Feshbach molecule when reversed.

Figure 12 shows the effect of a magnetic field in lifting the 36-fold nuclear spin degeneracy of the $J = 0$ rotational ground

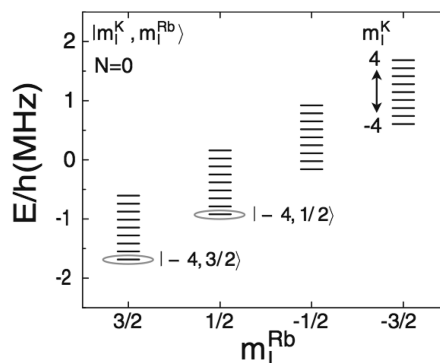


Figure 12. Nuclear spin structure of the $v = 0, J = 0 X^1\Sigma^+$ level of the $^{40}\text{K}^{87}\text{Rb}$ molecule at 54.594 mT.³ The independent atomic spins are uncoupled to one another or the molecular axis and are split according to their small nuclear magnetic moments. The ^{40}K atom has nuclear spin $I = 4$ with 9 projections $-4 \leq m_I \leq +4$, whereas the ^{87}Rb atom has $I = 3/2$ and 4 projections $\pm 3/2, \pm 1/2$. The states $|m_I^{\text{K}}, m_I^{\text{Rb}}\rangle = |-4, 1/2\rangle$ and $| -4, 3/2\rangle$ were prepared experimentally. The thermal energy $k_{\text{B}}T/h = 0.021$ MHz at 1 μK is small compared to the splitting.

state of this $^1\Sigma^+$ molecular state. At $B = 54.59$ mT the 9-fold degeneracy of the ^{40}K atoms with nuclear spin quantum number $I = 4$ and the 4-fold degeneracy of the ^{87}Rb atom with $I = 3/2$ are lifted by the field, which causes splittings much larger than the very small $k_{\text{B}}T/h = 4$ kHz thermal energy.³ The experiment starts with a Feshbach molecule in a single $M_{\text{tot}} = -7/2$ spin projection state, and the STIRAP pulse prepares the target ground state molecules in a single $M_{\text{tot}} = -7/2$ spin component of this 36-fold manifold. Two-color microwave processes can be used to populate other spin components or to prepare a mixture of spin states.^{113,114} Consequently, all internal degrees of freedom, including electronic, vibrational, rotational, and electron and nuclear spin, can be coherently controlled in single quantum states in experiments like this. The manipulation of such states is discussed in detail in section 4.5.

The experimental group at Innsbruck has succeeded in preparing a sample of ground state $v = 0, J = 0$ Cs_2 molecules in a similar manner, except that a four-color Raman process was needed.² The Cs experiment was done in an optical lattice and prepared the molecules in a single spin component of the 64-fold spin-degenerate ground state. The optical lattice offers the advantage that collisions of the molecules are prevented, until they can be released to interact by turning off the lattice lasers. Although ground-state Cs_2 molecules do not have any reactive or vibrational–rotational quenching channels, the lower STIRAP efficiency in the experiment resulted in a spread of other vibrational levels being populated. These other levels quench rapidly when the lattice is removed, resulting in loss of molecules. This is discussed in section 4.10. It should be

possible to improve the efficiency of the Raman conversion in the future. Also, the Innsbruck group is making progress toward working with ultracold samples of ^{87}Rb and Cs ,^{115–117} so that it may be possible to realize the formation of ultracold ground-state RbCs polar molecules in the near future. Such molecules can be expected to have very different collisional properties, since two $v = 0, J = 0$ molecules have no reactive channels, unlike KRb molecules. Furthermore, their dipole moment is double that of KRb .

1.5.1. Table of Ultracold Polar Molecules. We summarize in Table 1 a list and associated references for

Table 1. List of Ultracold Polar Molecules of Current Experimental Interest^a

polar molecule	city/country of the group	T	comments
$^{40}\text{K}^{87}\text{Rb}$	Boulder, CO, U.S.A.	$\sim 250 \text{ nK}$	GS, QR ^{1,114,119}
$^{40}\text{K}^{87}\text{Rb}$	Boulder, CO, U.S.A.	$\sim 300 \text{ nK}$	not GS but coherent population transfer, QR ¹¹⁸
$^{41}\text{K}^{87}\text{Rb}$	Tokyo, Japan	$\sim 130 \mu\text{K}$	GS, not QR ¹²⁰
Sr^{19}F	New Haven, CT, U.S.A.	$\sim 300 \mu\text{K}$	GS, not QR ^{91,121}
$^{85}\text{Rb}^{133}\text{Cs}$	New Haven, CT, U.S.A.	$\sim 100 \mu\text{K}$	GS but not ground rotational state, not QR ¹⁰⁷
$^7\text{Li}^{133}\text{Cs}$	Heidelberg, Germany	$\sim 260 \mu\text{K}$	GS, but not coherent population transfer, not QR ¹⁰¹
$^{85}\text{Rb}^{133}\text{Cs}$	New Haven, CT, U.S.A.		not GS ¹²²
$^{39}\text{K}^{85}\text{Rb}$	São Paulo, Brazil	$\sim 150 \mu\text{K}$	not GS ¹²³
$^{23}\text{Na}^{133}\text{Cs}$	Rochester, NY, U.S.A.	$\sim 260 \pm 130 \mu\text{K}$	not GS ^{124–126}
$^{39}\text{K}^{85}\text{Rb}$	Storrs, CT, U.S.A.		not GS ¹²⁷
$^{174}/^{176}\text{Yb}^{87}\text{Rb}$	Düsseldorf, Germany		not GS ¹²⁸
$^{85}\text{Rb}^{133}\text{Cs}$	Pisa, Italy		not GS ¹²⁹
$^6\text{Li}^{40}\text{K}$	Paris, France		not GS ¹³⁰
$^{85}\text{Rb}^{133}\text{Cs}$	Taiyuan, China		not GS ¹³¹
$^{87}\text{Rb}^{—133}\text{Cs}$	Innsbruck, Austria		AAM ^{115–117}
$^{87}\text{Rb}^{—133}\text{Cs}$	Durham, U.K.		AAM ^{132,133}
$^{23}\text{Na}^{—40}\text{K}$	Cambridge, MA, U.S.A.		AAM ¹³⁴
$^6\text{Li}^{—85}\text{Rb}$	Vancouver, Canada		AAM ¹³⁵
$^6\text{Li}^{—173/174}\text{Yb}$	Kyoto, Japan		AAM ¹³⁶
$^6\text{Li}^{—174}\text{Yb}$	Seattle, WA, USA		AAM ^{137,138}
$^{87}\text{Rb}^{—176}\text{Yb}$	Düsseldorf, Germany		AAM ¹³⁹
$^6\text{Li}^{—23}\text{Na}$	Cambridge, MA, U.S.A.		AAM ¹⁴⁰

^aThe domain of temperature is indicated as well as the experimental groups involved. Comments and related references are also provided on the status of the molecules. The symbol “GS” means here that all the molecules are formed coherently in the ground electronic, vibrational, rotational, and spin state. The symbol “QR” indicates the quantum regime where only one partial wave contributes to the molecule–molecule dynamics: *s*-wave for indistinguishable bosonic molecules or distinguishable molecules or *p*-wave for indistinguishable fermionic molecules. The symbol “AAM” means the experiments are working with atom–atom mixtures with the goal of achieving GS molecules.

different polar molecules in the ultracold regime ($T < 1 \text{ mK}$) that have either been made or, if not yet made, are being studied by different experimental groups. A number of polar molecules have been produced in the cold regime ($T \geq 1 \text{ mK}$), as discussed in the review article of van de Meerakeer et al.⁹⁴ in the present volume or in Table 1 of ref 9.

2. THEORETICAL FRAMEWORK FOR ULTRACOLD MOLECULAR COLLISIONS

2.1. Background

We will examine here what makes ultracold molecular collisions so different from ordinary molecular collisions or even ultracold atomic collisions. There exist well-developed theoretical methods for treating either of these latter cases, whereas the ultracold molecular domain poses some serious challenges to standard theoretical methodology. The heart of the difficulty is already clear from Figure 1, namely, the enormous separation in energy scale between the initial species prepared and trapped in a single quantum state and the energy scale of chemical interactions during a collision. The exquisite sensitivity of the scattering length or volume (i.e., a specific field-tunable quantum phase) to the subtle details of the interaction Hamiltonian makes it nearly impossible in general to calculate threshold collision rates with confidence. This is because the necessary potential energy surface(s) (PES) and interactions can never be specified to sufficient accuracy and detail to be fully predictive, especially if threshold resonances are involved. The resonance positions would need to be calculated to within ~ 1 part in 10^{10} of the potential well depth of the collision complex (100 peV out of 1 eV). The problem is made more complex by the necessity to include spin-dependent couplings, which often play an essential role in the ultracold dynamics.

There is hope, however, in bringing some theoretical order and computational tools to this seemingly impossible situation. In particular, it is desirable to develop tools for characterizing the near-threshold region, where the long-range potential plays a critical role. There are many situations where an underlying simplicity emerges, such as the quantum limit of Langevin-type models for very reactive systems. In this limiting model, resonances are suppressed, and the details of the short-range PESs are not important if one only desires the overall reaction rate. In general, one can seek to build in analytically or numerically the properties of long-range interactions and the density of threshold resonance states. This approach has been very successful for ultracold atomic collisions, where a combination of computational models and experimental data can provide highly quantitative and detailed theory of threshold scattering and bound states.⁴⁰ Also, as described in section 1.3 for atoms (see Figure 4), one can introduce some scaling parameter λ that tests the sensitivity of collision rate constants to variations in the PES and determines what features are robust and what features are not robust with respect to varying the PES. Such ideas will be presented in detail in section 3.2. Here we only outline the basic framework of the issues.

Normally one would calculate collision rates for simple molecules or atoms by setting up some coupled channels (CC) basis set with a Hamiltonian that describes the separated species and their interactions and then get the needed S-matrix elements for state-to-state collisions by solving the Schrödinger equation using computer codes appropriate to either the nonreactive or reactive scattering of the system. Figure 13 schematically represents a set of diagonal potentials for such a

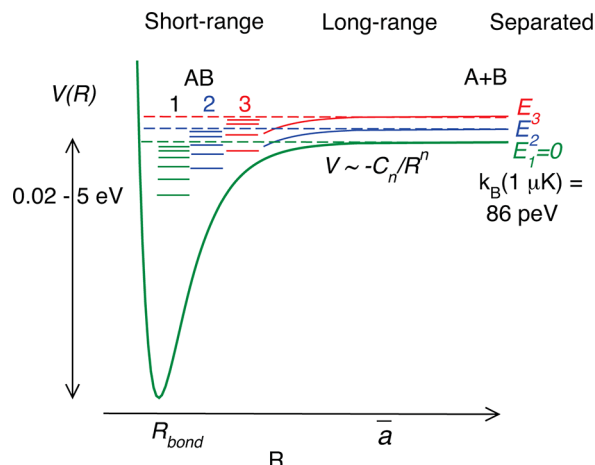


Figure 13. Schematic picture (not to scale) of a set of interaction potentials versus some separation coordinate R of two molecular species A and B showing a set of energy levels of the separated species, a long-range interaction, and a set of short-range states of the collision complex with near-threshold bound states; additional product channels may be present but are not indicated. Long-range potentials could be attractive or repulsive and have centrifugal barriers if the channel is not an s -wave. Reprinted with permission from ref 61. Copyright 2009 Royal Society of Chemistry.

problem and the distinctively different regions of separation R that are relevant to ultracold collisions. The separated molecule levels E_1, E_2, \dots could be associated with spin, rotational, or vibrational structure of the molecules. Figure 1 indicates the typical energy scales for each kind of structure; R_{bond} and \bar{a} , respectively, indicate the characteristic distances associated with the chemical bonding and with the long-range potential. The power law of the long-range potential sets the density of near-threshold bound states associated with that potential. These long-range bound states have an extent comparable to the scale length \bar{a} of the long-range potential.¹⁴¹ In addition, there may be other near-threshold bound states of the collision complex associated with the other degrees of freedom in a molecule. These can have an extent much less than \bar{a} , more on the order of R_{bond} . The near-threshold bound states, which will be much more dense for a molecule than for an atom, may tune with some external field to make a set of Fano-Feshbach resonances for threshold collisions.

It is important to emphasize that the key new feature of ultracold molecules is the precise control one has over all degrees of freedom in preparing the initial species and the additional ability to control the long-range interactions in the case of polar molecules. All the advantage of working with such sources lies in these kinds of control. There is very little control that one can get over the strong short-range interactions, with the possible exception of being able to tune resonances of the collision complex. Resonances thus act as a “bridge” between the long-range and short-range regions, connecting the ultracold with the conventional. One great advantage of having molecules rather than atoms is that in principle much more control is possible with the molecules, because of the extra internal degrees of freedom and the anisotropy and multipole moments of the molecules, especially dipolar species. One could envision using various kinds of electromagnetic control of the collision complex by coupling different resonances. In fact, the coherent production of ground-state molecules using Raman coupling of a Feshbach molecule to the ground state

is an excellent example of tuning the properties of a “collision complex” of two atoms to switch to a target molecular state. Clearly, other frequencies could be used to select other vibrational levels.¹¹⁸ Similarly, if two nonreactive or weakly reactive ultracold molecules have accessible resonances of their collision complex, then in principle the full range of bound or quasi-bound states of a molecular collision complex is subject to probing or control. Thus, having a theory for understanding the near-threshold resonances of molecular collision complexes will be a key to exploiting such resonances.

There are two other distance scales that are important in the ultracold regime in addition to the long-range potential scale a_p defined in section 1.3. These are the de Broglie wavelength $\lambda_{\text{dB}} = 2\pi/k$, or alternatively the length $1/k$, and the confinement length $a_h = (\hbar/(m\omega))^{1/2}$ for a lattice trap. Recall that a polar molecule in field-free space, where it is in an eigenstate of rotation, has no space-frame dipole moment, even though it has a dipole moment in its own body coordinate frame (see section 4.1). In the case of a simple $^1\Sigma$ diatomic molecule in its rotational ground state with rotational constant B_0 and body-frame dipole d_0 , a weak electric field F causes a space-frame dipole moment $d(F)$ of the molecule that varies as $Fd_0^2/(3B_0)$ in the limit $Fd_0 \ll B_0$ and approaches d_0 when $Fd_0 \gg B_0$. Thus, the long-range dipolar potential and its scale length $a_3(F) = \mu d(F)^2/\hbar^2$ can be controlled by varying the electric field. Although we typically have $a_6 \ll a_h < 1/k$, the range $a_3(d)$ can readily be tuned with laboratory fields on the order of a few kV/cm to be much larger than a_h or even $1/k$ for typical sub- μK collision energies, as long as d_0 is on the order of 1 D or so (1 Debye (D) = 3.336×10^{-30} C m).

A useful group of molecules that are of great interest for ultracold molecule studies are the diatomic species made of two alkali-metal atoms, because these are all in principle capable of being made by similar techniques to those used for the KRb molecule. Julienne et al.⁷⁵ give the various scale lengths for the ground state of 10 different heteronuclear polar mixed alkali-metal species. The dipole moments range from the smallest value ~ 0.5 D for LiNa to the largest ~ 5 D for LiCs.¹⁴² The order of magnitude for some of these lengths are 0.3 nm for R_{bond} ($\sim 6 a_0$), 10 nm for $a_6 \approx \bar{a}$ ($\sim 200 a_0$), 50–100 nm for a_h (~ 1000 – $2000 a_0$) for typical harmonic trapping frequencies on the order of 30 kHz, ~ 100 nm ($\sim 2000 a_0$) for $1/k$ at $E/k_B = 100$ nK, and ~ 1000 nm ($\sim 20000 a_0$) for $a_3(F)$ in the high field limit. Clearly, $a_3(F)$ can be tuned to zero by turning off the field and can be varied to select some desired strength. From the perspective of Figure 13, both the form and strength of the long-range potential can be varied by field control, and if the interaction occurs with an optical lattice turned on, the separated species experience trapping forces that limit the extent of their asymptotic motion and cause additional quantization that restricts the geometry of the collision.

The fact that the confinement length a_h can be much smaller than the de Broglie wavelength means that the collision can be profoundly modified by controlling the confinement, that is, the dimensionality N of the collision can be controlled, where $N = 1, 2$, or 3 . We have been describing a normal 3D collision of a plane wave represented by a partial wave expansion. When the confinement in $(3 - N)$ orthogonal directions is much smaller than the de Broglie wavelength, then the collisions have their translational degree of freedom quantized in $(3 - N)$ dimensions and are only free to roam in N dimensions. In the case of a 1D optical lattice in the z direction, which makes a set of traps that are analogous to a stack of pancakes, the

motion is tightly confined in the z direction but free in the orthogonal x and y directions. Such a collision goes asymptotically to a cylindrical wave, not a plane wave, and is known as a quasi-2D collision.^{34,143–145} On the other hand, if there is tight confinement in the x and y directions, as in the upper panel of Figure 2, the collision is only free in the orthogonal z direction, going asymptotically to “tube” or “cigar” geometry, and is known as a quasi-1D collision.^{35,143} One can even envision quasi-0D systems, as in the lower panel of Figure 2, where confinement is in all three directions, all translational motion is quantized, and only bound states of the molecular pairs exist.

Collisions in reduced dimension can be treated by a formalism very similar to that used in eqs 7 and 8. The fully 3D short-range part of the collision is coupled to the asymptotic waves of the reactants in reduced dimension.¹⁴³ The threshold contributions to the elastic and inelastic rate constants for collisions with relative momentum $\hbar\kappa$ in dimension N are^{75,146}

$$K_j^{\text{el}}(\kappa) = \frac{\pi\hbar}{\mu} F_N \frac{|1 - S_{jj}(\kappa)|^2}{\kappa^{N-2}} \quad (26)$$

$$K_j^{\text{ls}}(\kappa) = \frac{\pi\hbar}{\mu} F_N \frac{1 - |S_{jj}(\kappa)|^2}{\kappa^{N-2}} \quad (27)$$

where S_{jj} is the diagonal S -matrix element indexed by the channel states in reduced dimension and the factor $F_N = 1/\pi, 2/\pi, 2$ for molecules colliding in identical spin states in $N = 1, 2, 3$ dimensions, respectively. The indices of the lowest partial wave are $j = 0$ for bosons and $j = 1$ for fermions. In 3D, $j = 1$ has 3 components of its projection m that have to be summed over. In quasi-2D with an external field aligned along the confined direction z , j refers to the projection m of relative rotational angular momentum along z , with two components $+1$ and -1 that have to be summed over for $j = 1$; in quasi-1D, it refers to the symmetric ($j = 0$) or antisymmetric ($j = 1$) state propagating along z . In the case of unlike species, the threshold rate constant is $(K_{j=0} + K_{j=1})/2$ in any dimension. The contribution from the lowest index is dominant for ultracold loss collisions in an electric field, and any additional partial waves can be summed over in other cases to get the total rate constants K^{ls} or K^{el} . The loss rate for a gas with N -dimensional density n is $\dot{n} = -K^{\text{ls}} n^2$, where n has units of $\text{cm}^{-1}, \text{cm}^{-2}$, and cm^{-3} for $N = 1, 2, 3$, respectively.

A very attractive feature of molecular collisions in lattices is the ability to control all aspects of the degrees of freedom available to the reactant molecules, including spatial orientation, the long-range potential between the colliding species, and the dimensionality of the collision. Fast collisions between ultracold bosonic Feshbach molecules can be strongly suppressed by many-body correlations when they are placed in tightly confining tubes of quasi-1D geometry,^{147,148} as discussed in section 3.1.2. There are proposals to use tunable dipolar interactions between polar molecules to control their long-range interactions and turn off fast reaction rates in quasi-2D geometry,^{146,149–154} as discussed in section 4.9. This suppression by controlling the potential has been demonstrated experimentally for reactive collisions of KRb dipoles oriented by an electric field orthogonal to the “pancake” planes of a 1D lattice, deep enough to prevent tunneling between planes.¹⁵⁵ This control effect as well as others will be explained in detail in section 4.9.

2.2. Kinds of Theories

We now turn our attention to a brief survey of the kinds of theoretical approaches that are possible for ultracold molecular collisions, namely, what kind of theories have been or need to be implemented in this novel regime. Figure 14 summarizes the

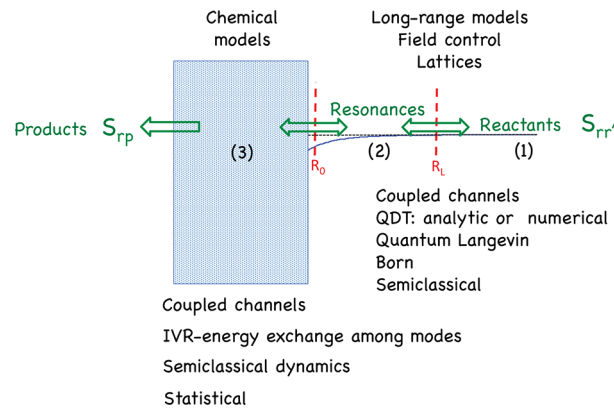


Figure 14. Schematic figure of a PES along some reaction coordinate R summarizing concepts associated with three distinct aspects of ultracold molecular collisions: (1) the preparation or detection of the reactant channels r or r' at large separation $R \gg R_L$; (2) the influence of the weak long-range potential between some characteristic distances $R_0 \lesssim R \lesssim R_L$; (3) the generally complicated and unknown dynamics of the strongly interacting collision complex for $R < R_0$ that leads to reaction products p . Collisions can result in elastic (S_{rr}), inelastic ($S_{rr'}$), or reactive (S_{rp}) processes.

key issues and concepts of the theoretical approach. The arrows indicate the incoming and outgoing scattering flux moving between the three distinct regions of the collision. The shaded box indicates the region of conventional chemical dynamics calculations. The figure indicates the theoretical techniques appropriate to the different regions. Resonance states associated with the long-range region can act as a bridge between the asymptotic ($R \gg R_L$) and chemical ($R < R_0$) regions, requiring theoretical tools that can connect the different regions.

Recall that the goal of a theoretical approach is to obtain the state-to-state S -matrix elements that characterize the transition amplitudes between the initially prepared states and the detected product states. Recall that in section 1.3 we discussed that if loss from the initially prepared channel r is all we are interested in, we only need to know the diagonal S_{rr} for that channel. However, in some cases, one may want to know the transition amplitudes $S_{rr'}$ or S_{rp} respectively associated with inelastic collisions returning the reactants to some other reactant channel r' or to reactive collisions producing some product channel p . In the early stages of experiments with ultracold molecules where reactant loss is easy to measure and product detection is difficult, we can concentrate on the single S_{rr} matrix elements. However, as this field develops experimentally and the question of the branching ratios to various product channels becomes relevant, it will be necessary to understand the full S -matrix for the problem. We will now examine the various kinds of theories that can be brought to bear on these questions.

2.2.1. Coupled Channels Methods. The most powerful computational tools we can apply to the problem of calculating the general S -matrix for ultracold collisions are various numerical methods for solving the Schrödinger equation for the full Hamiltonian of the system. This is certainly possible

and in some cases even routine with coupled channels methods, given the PES for the system, as we describe in section 3.2. However, such conventional approaches are clearly made much more difficult by the exquisite sensitivity to the details of the Hamiltonian, including spin degrees of freedom with a large multiplication in number of channels, that we discussed in section 2.1. The *s*-wave scattering length and the precise location of threshold collision resonances are essentially impossible to calculate accurately from first principles using ab initio or semiempirical sources of a PES. If this is not possible for atoms,⁴⁰ it will not be possible for molecules.

An approach that has been very successful with atoms⁴⁰ is to find a suitable approximate representation of the short-range part of the potential and carry out coupled channels calculations calibrated to reproduce measurements of threshold scattering resonances. Such generalized semiempirical models need to build in a sufficiently accurate account of short-range interactions, i.e., exchange forces or spin-dependent interactions, to permit accurate modeling of a narrow energy region near the threshold energy; the best models are based on an as accurate as possible representation of the actual Born–Oppenheimer adiabatic potential energy curve(s) for the diatomic system. One example of this is the KRb molecules, for which the potentials are so well-known¹⁵⁶ that all bound states of the molecule, including the threshold domain, can be calculated to spectroscopic accuracy.⁶¹ In general, it may be sufficient that only a few near-threshold bound states be represented accurately by the potential, which then serves as a pseudopotential for the real one.

It is not clear whether predictive coupled channels calculations with the full Hamiltonian will be feasible for threshold molecular collisions with all degrees of freedom, since such collisions are vastly more complex than atomic ones. However, there have been a number of attempts to carry out coupled channels calculations of cold and ultracold molecular collision processes. These are surveyed in section 3.2. It is fair to say that such calculations give important insights into such collisions and can help us to understand which aspects of the calculations are robust with respect to uncertainty in the PES and which are not. This in itself is quite valuable in predicting or interpreting experimental aspects of such collisions.

2.2.2. Long-Range Theories. In many respects, if we only need to understand S_{rr} or $S_{rr'}$ for the reactant channels, it is possible to produce quite simple parametrized models based on the properties of the long-range potential, which controls threshold quantum reflection by the potential and the density of threshold resonance states. Thus, in some cases, referring to Figure 14, single-channel or few-channel models can be set up for the low-energy dynamics in the long-range and asymptotic regions $R > R_0$, with a simple parametrization of the role of the high-energy, short-range chemical region $R < R_0$. The goal of such theories is to get the “transmission function” $1 - |S_{rr}|^2$ in eq 8, which represents the fraction of the initial unit scattering flux that is removed from the single entrance channel r and produces loss products $r' \neq r$ or p .

The simplest such models are Langevin models, which assume unit loss probability from the reactant channel for any trajectories captured by the long-range potential ($R > R_0$) that reach the short-range chemical domain ($R < R_0$). The classical Langevin model can be generalized to include the threshold effects where scattering is controlled by the quantum reflection and tunneling dynamics associated with the long-range potential. This dynamics can be subject to control by external

field manipulation or lattice confinement of the molecules. Such models give no information about product distributions but can determine the energy-dependent “transmission function” $1 - |S_{rr}|^2$ as affected by external fields and lattice confinement. Such Langevin models give “universal” rate constants determined solely by the long-range potential and independent of any detailed considerations of short-range chemical dynamics. These models will be discussed in detail in section 4.6. The simplest is the analytic quantum threshold (QT) model of Quéméner and Bohn,¹⁵⁷ where a simple threshold approximation is introduced into the usual Langevin treatment so it satisfies the known threshold law. In some cases of power law potentials, the near-threshold quantum transmission function can be found analytically.^{51,70,158,159} Arbitrary potentials can be treated by a single-channel numerical model with a short-range complex potential to represent unit loss.^{4,76,160,161}

As an example, the universal threshold Langevin rate constants from eqs 13 and 14 for a van der Waals potential with $p = 6$ are given by the analytic result⁵¹ that $\tilde{a}_{l=0} = \bar{a}(1 - i)$ and $V_{l=1} = \bar{a}^2 \tilde{a}_{l=1}(-1 - i)$, where $\tilde{a}_{l=1} = \bar{a}\Gamma(1/4)^6/(144\pi^2\Gamma(3/4)^2) \approx 1.06428\bar{a}$. Thus the *s*- and *p*-wave loss rate constants are respectively determined by a length \bar{a} and volume \bar{a}^3 determined by the long-range potential. In the case of the ground-state mixed alkali-metal diatomic molecules, representative values for \bar{a} are ~ 6 nm ($120a_0$) for the KRb molecule and ~ 30 nm ($600a_0$) for the LiCs molecule,^{75,162} which has the largest dipole moment of any of the alkali-metal polar diatomics. The universal *s*-wave $K_{l=0}^{ls}$ coefficient has a typical magnitudes within a few factors of 10^{-10} cm³/s for all 10 of these species, and the *p*-wave $K_{l=1}^{ls}$ values for $T < 1 \mu\text{K}$ are for most cases much smaller than for the corresponding *s*-wave. These universal *s*- and *p*-wave loss rate constants remain below the unitarity upper bound for collision energies below $1 \mu\text{K}$.⁷⁵

Another class of theories are based on the generalized form of quantum defect theory (QDT),^{163–166} which is highly developed for cold atomic interactions.^{38,61,65,167–174} It can be fruitfully applied to collisions of ultracold molecules,^{51,158,161,175} including reduced dimensional collisions in lattices,¹⁴⁶ or to ion–molecule collisions.^{70,159} Generalized QDT is not unique but can spawn a variety of treatments based on different approximations. The essence of any QDT model is to write the exact solutions to the Schrödinger equation in terms of the solutions to a reference problem one can solve, either analytically or numerically, such as the long-range region $R \gtrsim R_0$ in Figure 14. The theory then seeks connections between the wave function as it varies as a function of R across different regions of coupling R_0 or R_L or as it varies as a function of E across collision thresholds. The latter allows relations to be developed between scattering and bound states. QDT can analytically continue solutions from the ultracold domain into the cold domain with a much larger energy scale.^{70,158,159,172} The theory quite naturally brings closed-channel resonances into its scope and is especially valuable near thresholds where much of the variation of the wave function with R and E can be captured with the solutions for the long-range potential and a few energy-insensitive quantum defect parameters. In addition to allowing analytic approaches, the general QDT can be implemented for cold molecular collisions by purely numerical means with numerical reference functions for arbitrary potentials.¹⁷⁵ It is therefore complementary to more conventional coupled channels approaches.

Using an analysis of incoming and outgoing components of the wave function in the different regions in Figure 14 gives much insight about the collisions as well as some practical tools. Gao³⁸ gives a QDT account of the flux passing between the regions around R_0 and R_L in the figure, giving a picture of how resonances cause multiple reflections that decay after multiple passes. Semiclassical interpretations of the wave function and flux are natural to QDT treatments. Idziaszek and Julienne⁵¹ develop a two-parameter QDT of a general molecular collision based on two quantum defect parameters designated y and s , with y related to the probability of reaction in the short-range region and s related to the phase of the standing wave in the $R \gtrsim R_0$ region due to interference between the incoming and outgoing waves in that region. The Langevin model in the previous paragraph can be derived as a limiting case of a QDT analysis, where $y = 1$ parametrizes the unit probability of reaction in the chemical region without back-reflection of flux so that the rate constant is independent of s .⁵¹ The QDT models are also readily implemented as a function of energy, and Gao gives the universal energy-dependent Langevin loss rate constants for both van der Waals molecular collisions¹⁵⁸ and ion–molecule collisions.¹⁵⁹ The analytic QDT theory can also be implemented for reduced dimensional collisions in an optical lattice for the case of a long-range van der Waals potential.¹⁴⁶

An important property of the special limiting case of the Langevin model is that such collisions do not have resonances. The short-range chemical region serves as totally absorbing “black hole” to incoming flux, and there is nothing to “resonate” back into the long-range region. Any scattering flux that passes from $R \gtrsim R_0$ in Figure 14 to $R \lesssim R_0$ is irreversibly lost from the entrance channel, so there is only incoming flux and no back-reflected outgoing flux in the long-range region $R_0 \lesssim R \lesssim R_L$. However, there will be back-reflected flux in the region $R \gtrsim R_L$, due to quantum scattering from the long-range potential.

When the long-range interaction does not correspond to a single power law varying as R^{-p} , simple analytic QDT theories are not possible. However, numerical implementation in the long-range region with QDT short-range boundary conditions becomes feasible. This is especially useful in the Langevin limit, where there is incoming flux only in the region $R_0 \lesssim R \lesssim R_L$. Micheli et al.¹⁴⁶ used such boundary conditions in a purely numerical coupled channels calculation in the region $R \gg R_0$ to get reactive loss rate constants for two ground-state KRb molecules colliding in the quasi-2D collision geometry of an optical lattice. Similar calculations were done by Quéméner and co-workers,^{153,154} where an absorbing complex potential at short-range achieved the same result. Such calculations can be done in any dimension. The numerical calculations with mixed van der Waals and dipolar interactions in the presence of an electric field are described in section 4.7. When the magnitude of the dipole is large enough so the length a_3 associated with the long-range dipolar potential becomes the largest length scale in the problem, then the scattering is characterized by universal dipolar scattering discussed in sections 4.7 and 4.9.

2.2.3. Models of the Collision Complex. Given the challenge of implementing coupled channels calculations with accurate potentials over the full range of motion and given the limitations of purely long-range models to discard many details of short-range chemical dynamics, there is a clear need to develop approximate models to build in the “chemical” structure of the collision complex and represents the behavior in the $R < R_0$ region of Figure 14. This is certainly necessary if

we ever want to get S_{rp} in Figure 14 and predict the distribution of reaction products for species like KRb or more complex molecules, but it is also necessary for less reactive or nonreactive species if we would like to gain all the control over ultracold collisions that is possible by tuning the states of the collision complex. These states can serve as a launchpad for manipulating the complex and switching population to another molecular state with a different energy or configuration. The fundamental theoretical problem lies in the sensitivity to the detailed spectrum of the collision complex, that is, it is necessary to calculate the exact positions and character of a dense set of tunable bound or quasi-bound resonance states of the collision complex on a very fine energy scale. Consequently, what we need are adequate models for predicting and interpreting experiments, even if quantitative ab initio calculations of the dynamics are not going to be possible.

Little work has started on understanding the chemical dynamics of the collision complex formed in an ultracold molecular collision. There are several potentially helpful approaches grounded in earlier chemical insights and knowledge to getting a better understanding of the role and dynamics of the collision complex. The problem is related to long-standing concepts and techniques in chemistry, such as molecular association and unimolecular decomposition, or internal vibrational relaxation (IVR). An ultracold collision is similar to IVR, where a highly excited internal mode of a molecule is excited by a laser, for example, and subsequent relaxation occurs among the various modes coupled to the mode that was excited. Such IVR processes were studied in the frequency domain by high-resolution spectroscopy or in the time domain using a pump–probe sequence. Molecular association or unimolecular dissociation are textbook cases with rate constants given in terms of statistical theories that require counting the states of the reactants and collision complex and evaluating partition functions. The new ultracold domain differs from earlier work in the extraordinarily narrow energy range of the collision complex that can be accessed and the very low entropy of the reactants.

As an example from the old literature, Mies^{176,177} gave a scattering theory of molecular association and unimolecular decomposition that is remarkably similar to the kind of theory that is used to treat ultracold collisions with decaying resonances, such as photoassociation. He assumed that a molecular association process took place through a dense set of overlapping resonances of a collision complex that decayed by a spontaneous process (taken in his case to be due to a collision with a third body) represented by a complex eigenvalue with the imaginary part giving the decay rate of the level. Mies’ S-matrix treatment of the molecular association rate constant is analogous to eq 4, although he dealt with a conventional high-temperature case with many overlapping resonances encompassed within $k_B T$.

The general challenge is to formulate theories for threshold molecular collisions that are adequate to understand and interpret the kinds of experimental work that will be possible with these systems. While general S-matrix theories may give formal tools for treating the problem, there are many practical difficulties. Will it prove possible in the long run to couple long-range theories describing the approach and separation of the reactants with short-range models based on more conventional chemical dynamics methods, such as coupled channels dynamics, semiclassical trajectories, IVR coupling among the internal modes of the problem, and statistical methods based

on approximations to the density of near-threshold states of the collision complex? These more chemical methods await future development. We now turn our attention to surveying the preliminary work that has been done in a number of these areas in section 3, and specifically the very recent work on the fully controlled quantum collisions of KRb molecules in section 4.

3. ULTRACOLD COLLISIONS WITH ALKALI MOLECULES

In this section, we now review some of the pioneering experimental and theoretical work on ultracold collisions with molecules. We focus here on molecular systems made of atoms ($A = H, Li, Na, K, Rb$, and Cs).

The first part, section 3.1, covers experimental progress made from 2000 on measuring and controlling ultracold molecular collisions, involving ultracold molecules in given excited rovibrational state or in a near-threshold Feshbach molecule. The second part, section 3.2, covers the theoretical work on ultracold atom–molecule $A + A_2$ and molecule–molecule $A_2 + A_2$ collisions, using a full quantum mechanical treatment and including full potential energy surfaces. The present section provides the link between the early work on ultracold molecules and the more recent work with ultracontrolled molecules, the subject of section 4.

3.1. Experiment

3.1.1. Ultracold Collisions of Rovibrational Molecules.

$Rb + Rb_2$. As early as 2000, Wynar et al.¹⁷⁸ formed molecules of $^{87}Rb_2$ from a Bose-Einstein condensate (BEC) of Rb atoms. Stimulated Raman transitions (see the scheme in Figure 15)

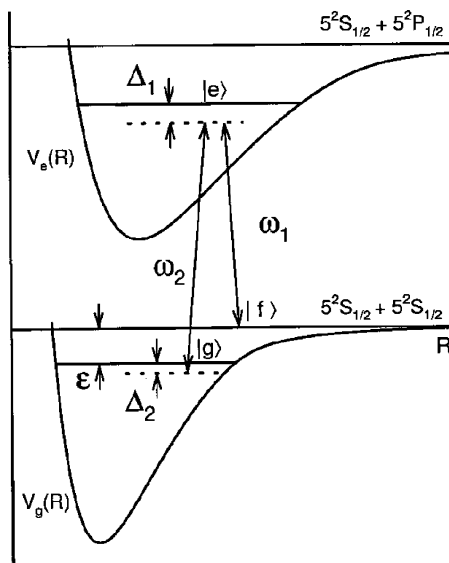


Figure 15. Stimulated Raman coupling between free and bound states of ^{87}Rb atoms in a Bose-Einstein condensate. Reprinted with permission from ref 178. Copyright 2000 AAAS.

were used to coherently transfer free atoms of Rb ($|f\rangle$) with a kinetic energy of ~ 100 nK to bound-state molecules of Rb_2 ($|g\rangle$) in the second-to-last vibrational state below threshold. By measuring the stimulated Raman transition rates as a function of the two-laser detuning $\omega_2 - \omega_1$ for different densities, they were able to observe a loss of the atoms when the Raman resonance condition is satisfied, $\omega_2 - \omega_1 = \epsilon$, where ϵ is the difference in energy between the free atom pairs and the bound

molecules (see Figure 16). The transition line widths were remarkably narrow, ~ 1.5 kHz, and were neither due to Doppler

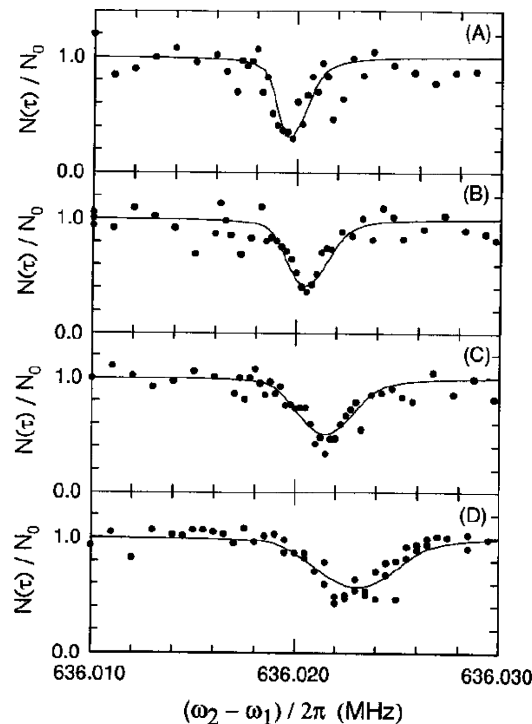


Figure 16. Stimulated Raman free-bound transition line shapes in a Bose-Einstein condensate for four different peak condensate densities: (A) $n_0 = 0.77 \times 10^{14} \text{ cm}^{-3}$; (B) $n_0 = 1.22 \times 10^{14} \text{ cm}^{-3}$; (C) $n_0 = 1.75 \times 10^{14} \text{ cm}^{-3}$; and (D) $n_0 = 2.60 \times 10^{14} \text{ cm}^{-3}$. Each spectrum shows the fraction of atoms remaining in the condensate. The resonant decrease in atom number arises from the formation of molecules by stimulated Raman free-bound transitions, followed by their subsequent loss from the trap. Reprinted with permission from ref 178. Copyright 2000 AAAS.

nor to kinetic energy spread broadening of the atoms in the BEC. The width and the center frequency of the Raman resonance condition increased with increasing condensate densities, as shown in Figure 16, suggesting atom–condensate and molecule–condensate mean-field interactions attributed to atom–molecule collisions. By writing a rate equation for the loss of atoms, the authors fitted the experimental results to estimate the real and imaginary components of the complex s -wave scattering length in eq 12 for molecule–atom (ma) collisions. They found $a_{\text{ma}} = -180 \pm 150 a_0$ and $b_{\text{ma}} < 110 a_0$. The atom–molecule inelastic collision rate were found to be $K_{\text{inel}} < 8 \times 10^{-11} \text{ cm}^3/\text{s}$ at ultracold temperature.

$Cs_2 + Cs/Cs_2$. In 2006, Staanum et al.¹⁷⁹ and Zahzam et al.¹⁸⁰ formed $^{133}Cs_2$ molecules from ultracold atoms, using a photoassociation technique. $Cs(6s)$ atoms are excited by photoassociation into a rovibrational state of the 0_g^- Cs_2 potential. A significant population of the photoassociated molecules decays to a rovibrational state of the lower electronic state $^3\Sigma_u^+$.¹⁸¹ In these experiments, the two different groups studied the collisions of such molecules in a dipole trap with and without remaining Cs atoms. The temperature was $T = 60 \pm 20 \mu\text{K}$ and $T = 40 \pm 10 \mu\text{K}$ for the first and second experiment, respectively. The densities were comparable, $\sim 3 \times 10^9 \text{ cm}^{-3}$ and $\sim 10^{10} \text{ cm}^{-3}$, respectively. Different schemes of photoassociation led to different vibrational populations of the

electronic triplet state of Cs_2 . A first scheme led to population in low vibrational states $v = 7\text{--}9$ (first experiment) and $v = 4\text{--}6$ (second experiment), and a second scheme led to population in high vibrational states $v = 32\text{--}47$ (for both experiments). By measuring the loss of molecules per unit of time, the experimentalists determined the rate coefficients of the atomic and molecular collisions. To measure the number of molecules lost, the Cs_2 molecules were photoionized into Cs_2^+ ions, which in turn are measured with a high resolution time-of-flight mass spectrometer.^{107,182} Staanum et al.¹⁷⁹ found atom–molecule rate coefficients at $T = 60 \mu\text{K}$ of $\beta(v = 32\text{--}47) = (0.96 \pm 0.02_{\text{stat}} \pm 0.3_{\text{syst}}) \times 10^{-10} \text{ cm}^3/\text{s}$ and $\beta(v = 4\text{--}6) = (0.98 \pm 0.07_{\text{stat}} \pm 0.3_{\text{syst}}) \times 10^{-10} \text{ cm}^3/\text{s}$, for molecules in high and low vibrational states, respectively. The atom–molecule rate coefficients β were proportional to the atomic density as shown in Figure 17 and were found to be independent of the

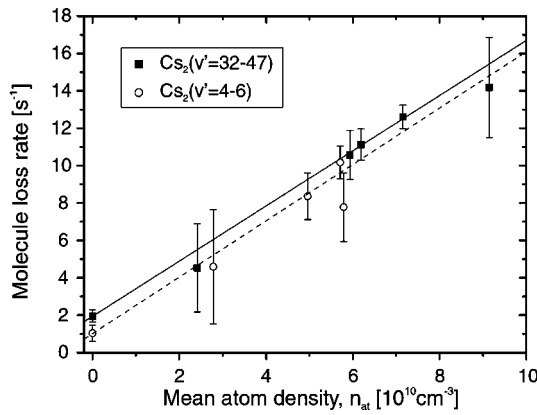


Figure 17. Molecule loss rate $8\beta n_{\text{at}}/(27)^{1/2} + \Gamma_{\text{mol}}$ versus n_{at} for collisions between $\text{Cs}(F = 3)$ and $\text{Cs}_2(v' = 32\text{--}47)$ (solid squares) and $\text{Cs}_2(v' = 4\text{--}6)$ (circles). The straight lines represent fits discussed in the text (solid, $v' = 32\text{--}47$; dashed, $v' = 4\text{--}6$). Reprinted with permission from ref 179. Copyright 2006 American Physical Society.

initial vibrational states of the molecules. Zahzam et al.¹⁸⁰ found an atom–molecule rate coefficient at $T = 40 \mu\text{K}$ of $\beta = 2.6^{+4}_{-1.3} \times 10^{-11} \text{ cm}^3/\text{s}$ and also independent of the initial vibrational state of the molecules. Investigating the lifetime of a pure molecular sample of Cs_2 as shown in Figure 18, they also found a molecule–molecule rate coefficient of $\beta = 1.0(5) \times 10^{-11} \text{ cm}^3/\text{s}$.

RbCs + Rb/Cs. In 2008, Hudson et al.¹⁶⁰ investigated the collisional properties of heteronuclear alkali polar molecules of $^{85}\text{Rb}^{133}\text{Cs}$ with ^{85}Rb and ^{133}Cs atoms. The molecules were formed in high vibrational states of the electronic triplet state $^3\Sigma^+$, around $v \approx v_0 = 37$, and detected via photoionization. The lifetimes of the RbCs molecules are shown in Figure 19 for different collisional conditions: RbCs molecules only (black points), RbCs with Cs (red points), RbCs with Rb (blue points), and Cs atoms only (green points). As seen in Figure 19, the presence of atoms dramatically decreases the lifetimes of the molecules, indicating strong inelastic loss collisions due to vibrational relaxation. As presented in Figure 20, the authors found a RbCs + Rb rate coefficient of $\sim 3 \times 10^{-10} \text{ cm}^3/\text{s}$ for the initial vibrational states $v_0 - 1$, v_0 , $v_0 + 2$, and $v_0 + 6$ at $T = 250 \mu\text{K}$. For RbCs + Cs, for $v_0 - 1$, v_0 , and $v_0 + 2$ the rate is $\sim 2\text{--}3 \times 10^{-10} \text{ cm}^3/\text{s}$ and for $v_0 + 6$ it is $\sim 7 \times 10^{-10} \text{ cm}^3/\text{s}$. The rates exhibit no significant dependence on the initial vibrational quantum number, confirming what has been seen for $\text{Cs} +$

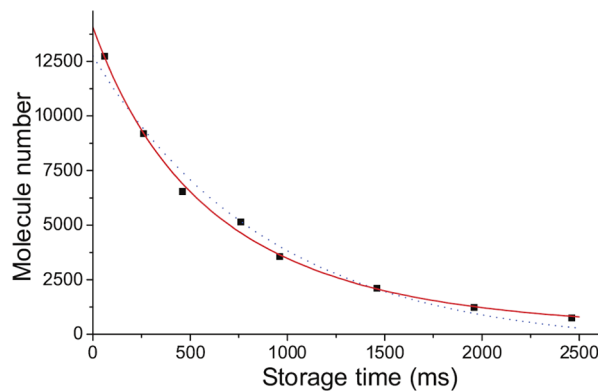


Figure 18. Trap lifetime of a pure molecular sample. The evolution of the number of molecules, formed via PA of the $0_g^-(6s + 6p_{3/2})(v = 6, J = 2)$, is plotted (solid squares) and fitted with a function accounting for two-body collisions (solid line). A fit with an exponential decay function is also represented (dotted line). The fit yields a lifetime of 900 ms and a two-body rate coefficient of $1.0(5) \times 10^{-11} \text{ cm}^3 \text{ s}^{-1}$. Reprinted with permission from ref 180. Copyright 2006 American Physical Society.

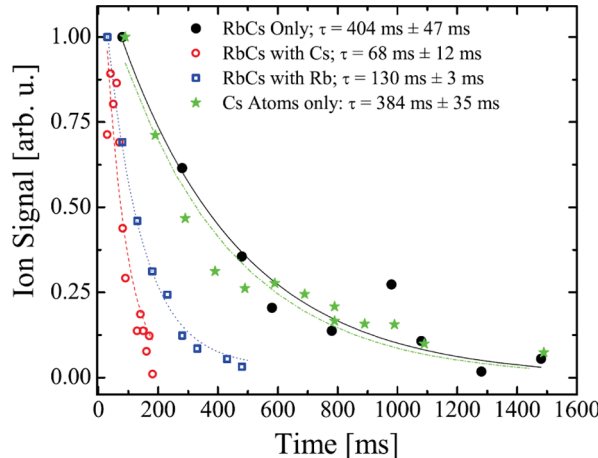


Figure 19. Typical molecular lifetime data. Here, the number of molecules in the $a^3\Sigma^+(v = v_0)$ state with binding energy $E_B = -5.0 \pm 0.6 \text{ cm}^{-1}$ is observed as a function of time. The presence of inelastic collisions between the atoms and molecules is evidenced by the dramatic reduction of the molecular lifetime when atoms are present. With no atoms present, molecule lifetimes are consistent with the background gas-limited lifetime seen for isolated atomic clouds in the trap. Reprinted with permission from ref 160. Copyright 2008 American Physical Society.

Cs_2 .^{179,180} Hudson et al.¹⁶⁰ confronted the value of the observed rate coefficients of $\text{Cs} + \text{RbCs}$ and $\text{Rb} + \text{RbCs}$ collisions with a quantum scattering calculation, assuming a full loss when the atoms encounter the molecules at short-range, either due to inelastic collisions and reactions. They calculated and employed accurate long-range van der Waals atom–molecule C_6 coefficients for the different initial vibrational states and summed over the contributing partial waves. Figure 20 shows their theoretical result as dashed boxes, indicating good agreement within the large experimental error bars.

Classical Capture Model. The temperatures involved in these experiments require several partial waves for the scattering dynamics so that a classical capture Langevin model^{183–186} given by

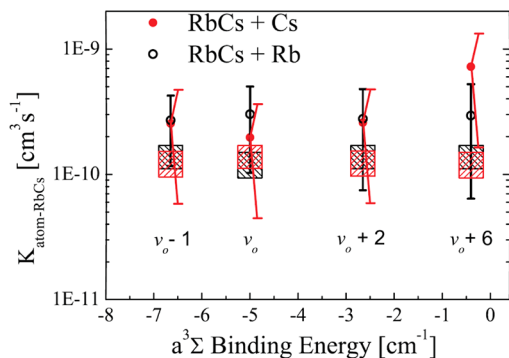


Figure 20. Molecular trap-loss scattering rate constant K versus binding energy E_B , for molecules in specific vibrational levels of the $a^3\Sigma^+$ state. Vibrational state labels appear below each data point. The black (red) cross-hatched box is the prediction of the quantum scattering model for collisions with Cs (Rb). The width of the boxes reflects the uncertainty in the collision temperature. Reprinted with permission from ref 160. Copyright 2008 American Physical Society.

$$k_{\text{Lang}} = \pi \left(\frac{8k_B T}{\pi \mu} \right)^{1/2} \left(\frac{2C_6}{k_B T} \right)^{1/3} \Gamma(2/3) \quad (28)$$

might be appropriate to simply describe the molecular collisions.¹⁸⁷ The Langevin model assumes a full loss probability when the two colliding species meet at a sufficiently short distance. The results of the model along with the results of the different experiments described above are summarized in Figure 21. The Langevin model prediction is in good agreement with the experimental results discussed previously, consistent with a high atom/molecule loss probability at short distances.

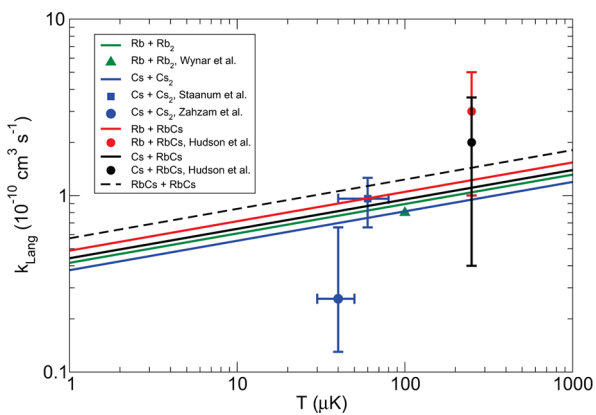


Figure 21. Rate coefficients as functions of the temperature predicted by the Langevin model^{183–186} in eq 28 compared with experimental data. The curves correspond to the Langevin results, and the symbols denote the experimental results of ref 178 for Rb + Rb₂, refs 179 and 180 for Cs + Cs₂, and ref 160 for RbCs + Rb/Cs.

LiCs + Cs/LiCs. Similar studies have been undertaken by Deiglmayr et al.^{188–190} in 2011 for LiCs molecules in the electronic ground state, the most dipolar heteronuclear alkali molecule. The authors reported inelastic rate coefficients of LiCs + Cs collisions for temperatures around 50 μK of $K_{\text{in},\nu'=28} = (2.8 \pm 0.4 \pm 0.5) \times 10^{-10} \text{ cm}^3 \text{ s}^{-1}$ and $K_{\text{in},\nu'=26} = (2.3 \pm 0.3 \pm 0.5) \times 10^{-10} \text{ cm}^3 \text{ s}^{-1}$ for two different schemes of photo-association.^{188,189} One is via the excited $B^1\Pi$, $\nu' = 28$, $J' = 1$ state and the second is via the excited $B^1\Pi$, $\nu' = 26$, $J' = 1$. After

spontaneous decay, the molecules can be in a different vibrational state of the ground electronic state $X^1\Sigma^+$ (see ref 191) and also the $a^3\Sigma^+$ state. The measured rate coefficients are therefore effective rates for molecules in high-lying levels of the ground electronic state $X^1\Sigma^+$, most likely with a contribution from the first excited electronic state $a^3\Sigma^+$. The rate is again about the same order of magnitude as for the experimental studies previously described showing fast relaxation to lower quantum states of the molecules. Deiglmayr et al.¹⁹⁰ also investigated the rovibrational population redistribution of an optically trapped gas of LiCs molecules. The authors started with molecules of LiCs photoassociated in the excited $B^1\Pi$, $\nu' = 26$, $J' = 1$ level and observed the distribution of molecules in different vibrational levels ν'' of the ground electronic state $X^1\Sigma^+$ following spontaneous decay of the excited state. Figure 22 shows a theoretical simulation of the population distribution

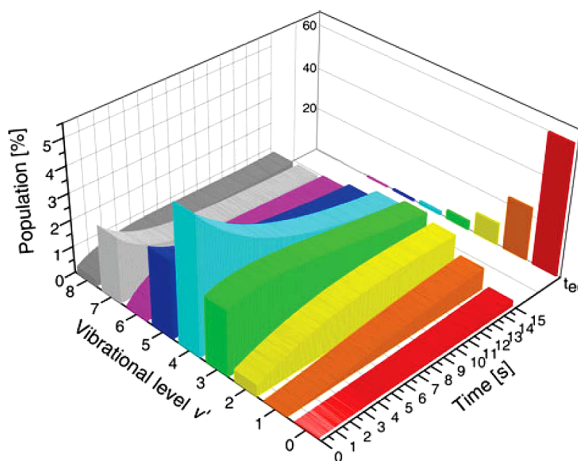


Figure 22. Solution of eq 29 for the population in the lowest nine vibrational levels of the $X^1\Sigma^+$ after spontaneous decay from $B^1\Pi$, $\nu' = 26$, $J' = 1$. The population is given as a percentage of the initial total ground-state population. Reprinted with permission from ref 190. Copyright 2011 Institute of Physics and the Deutsche Physikalische Gesellschaft.

for the first nine vibrational levels as a function of time. This simulation is based on a rate equation for the population $N_i(t)$ of the rovibrational state i

$$\begin{aligned} \dot{N}_i(t) = & \sum_{j>i} A_{ji} N_j(t) - \sum_{j< i} A_{ij} N_i(t) + \sum_{j\neq i} \tilde{B}_{ji} N_j(t) \\ & - \sum_{j\neq i} \tilde{B}_{ij} N_i(t) - \Gamma N_i(t) \end{aligned} \quad (29)$$

In this equation, A_{ij} is the Einstein coefficient corresponding to the spontaneous decay from state ψ_i to state ψ_j . \tilde{B}_{ij} , \tilde{B}_{ji} are the Einstein coefficients corresponding to the stimulated absorption and emission, respectively, due to the coupling of black-body radiation from the surrounding environment (walls of the vacuum chamber), multiplied by the spectral density of the radiation at the temperature of the environment. The Einstein A_{ij} coefficients were computed from all the transition dipole moments $\mu_{ij} = \langle \psi_i | \mu(r) | \psi_j \rangle$ from a rovibrational state i to a rovibrational state j calculated from all the rovibrational wave functions, as done in ref 142, for example, as well as all the transition energies $\tilde{\nu}_{ij}$ and the Hönl-London factor.¹⁹⁰ Γ is a one-body decay corresponding to losses from the trap. Figure 22 shows the importance of radiative decay and black-body

radiation for the dynamics of LiCs molecules on the time scale relevant to this experiment. The authors attributed this to the large electric dipole moment of ground-state LiCs molecules and the associated strong variation of the dipole moment function with the internuclear distance.

A comparison with the experimental results is shown in Figure 23 for the final vibrational state $\nu'' = 3$. The dotted line

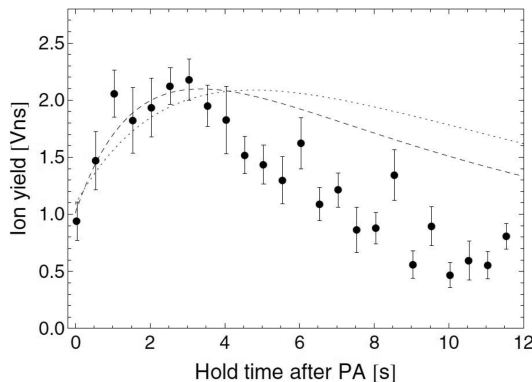


Figure 23. Ion yield from LiCs $\nu'' = 3$ molecules ionized at $16\ 886.3\text{ cm}^{-1}$ and low intensity ($\sim 2\text{ J/cm}^2$) after a varying hold time. Every point is an average of 15 measurements, given uncertainties are the standard deviation of the mean value. The dotted (dashed) line shows the simulated signal for the adjusted first (second) order model as discussed in the text. Reprinted with permission from ref 190. Copyright 2011 Institute of Physics and the Deutsche Physikalische Gesellschaft.

shows the result of the simulation for the rate equation provided in eq 29. The dashed line is the result of the same simulation where the one-body decay $-\Gamma N_i(t)$ is replaced by a two-body decay term $-2\beta_{\text{LiCs-LiCs}} \bar{n}_{0,\text{LiCs}} [\sum_j N_j(t)/N_{0,\text{tot}}] N_i(t)$, corresponding to loss from molecule–molecule LiCs collisions. The two theoretical curves are in good qualitative agreement with the experimental results and lead to the values of $1/\Gamma = 21(1)\text{ s}$ if the one-body decay is the loss mechanism, or $\beta_{\text{LiCs-LiCs}} = 2 \times 10^{-10}\text{ cm}^3\text{ s}^{-1}$ if the two-body decay is the loss mechanism. The molecule–molecule loss rate coefficient is consistent with the high values found in other experiments described above. However, the authors could not affirm if the molecular loss came from one-body or two-body decay, because the two processes have similar effects as seen in Figure 23.

3.1.2. Tuning Ultracold Molecular Collisions Using Feshbach Molecules and Magnetic Fields. A first way of control consisted of using Feshbach molecules (molecules in the halo regime; see discussion in section 1.4) and applying a magnetic field to change their scattering length in collisions. Some examples of molecular experiments with magnetic field control are presented in the next articles. A more complete review on studies of Feshbach molecules is provided by Chin et al.⁴⁰

$\text{Na}_2 + \text{Na}/\text{Na}_2$. In 2004, Mukaiyama et al.¹⁹² observed the effect of atom–Feshbach molecule and Feshbach molecule–molecule inelastic collisions of $^{23}\text{Na} + ^{23}\text{Na}_2$ and $^{23}\text{Na}_2 + ^{23}\text{Na}_2$. Bosonic Na₂ Feshbach molecules, at a temperature of $\sim 200\text{ nK}$, were formed through magneto-association of an ultracold pair of colliding atoms using a Feshbach resonance at an appropriate magnetic field. The colliding pair of free atoms are in resonance with a near-threshold molecular vibrational state. This study investigated how, during the time of the magnetic ramp, inelastic collisions (as rovibrational relaxation) between the

remaining atoms and the molecules formed can affect their lifetime. To study the effect of collisions between molecules only, the atomic sample was irradiated by resonant light to remove the unpaired atoms. Because the molecules were transparent to this radiation, only molecules remained after the atomic blast, and the effect of molecular collisions only can be explored. Figure 24 shows the molecular loss as a function of

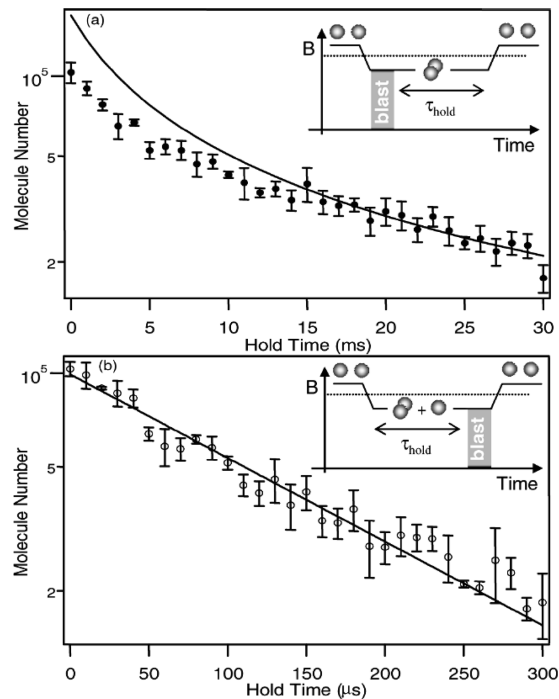


Figure 24. Decay of ultracold Na₂ Feshbach molecules trapped alone (a) or together with atoms (b). The solid lines in (a) and (b) are fits to data, which assume vibrational relaxation in the collision of molecules (a) or collisions between molecules and atoms (b). The insets illustrate the experimental sequences. Reprinted with permission from ref 192. Copyright 2004 American Physical Society.

time for molecule–molecule collisions only (top panel) and for atom–molecule collisions (bottom panel). The extracted rate coefficients were found to be $K_{\text{mm}} < 5.1 \times 10^{-11}\text{ cm}^3/\text{s}$ and $K_{\text{am}} < 5.5 \times 10^{-11}\text{ cm}^3/\text{s}$, respectively. This is similar to Rb + Rb₂ collisions in ref 178, indicating huge losses from inelastic collisions. The authors also showed that the inelastic losses determine the conversion efficiency from atoms to molecules. With the blast radiation (no more atom–molecule collisions but still molecule–molecule collisions), the number of molecules formed is larger than if the blast is not performed (the atoms remain). This was quite independent of the ramping time. This was attributed to a compensation effect between two contributions. On one hand, longer ramp times smoothly and slowly turn the atoms into molecules so that atom-to-molecule conversion efficiency is better. On the other hand, the atoms and molecules spend more time together at the Fano-Feshbach resonance, allowing them more time to collide and be lost from the trap and decreasing the atom-to-molecule conversion efficiency. Collisions are so destructive that the atom-to-molecule conversion is $\sim 4\%$ for bosonic atoms,^{193,194} far from the values of 50–85% reached in other work with fermionic atoms,^{195–200} which are discussed in the next paragraph.

$\text{Li}_2 + \text{Li}/\text{Li}_2$, $K_2 + K/K_2$. Collisions between atoms and Feshbach molecules made of bosonic atoms are very

destructive, leading to the poor atom-to-Feshbach molecule conversion efficiency, described just previously. However, if the molecules are made of two unlike fermions F and F' , the conversion of atoms to Feshbach molecule was much higher. This was due to the suppression of inelastic atom–molecule and molecule–molecule collisions at large positive scattering length or, in other words, when the bosonic molecules FF' are of the Feshbach type. This was explained by Petrov et al.^{77,201} The authors showed that the inelastic relaxation rate to deeper molecular state behaves as $\alpha_{\text{rel}} \propto a^{-3.33}$ in $F/F' + FF'$ collisions and behaves as $\alpha_{\text{rel}} \propto a^{-2.55}$ in $FF' + FF'$ collisions. The inelastic collisions are then suppressed when the atom–atom F – F' scattering length a increases. The authors also showed that the dimer–dimer scattering length behaves as $a_{\text{dd}} = 0.6a$, increasing with the atom–atom scattering length a . This “Pauli blocking” mechanism due to Pauli exclusion principle, also seen in three-body recombination of fermions,^{202–204} explained the remarkable stability of ultracold bosonic FF' Feshbach molecules. It is worthwhile to note that the fermionic “effective repulsion” of the atoms constituting the halo bosons enables these molecules to survive destructive collisions better than the usual deeply bound molecules, despite the fact the halo molecules have a large spatial extent on the order of $\sim 1000a_0$, much bigger than the usual spatial extent of molecules on the order of 10 – $100a_0$. This particular property further led to the creation of molecular Bose–Einstein condensates. This was done starting with a spin mixture of fermionic ^6Li atoms and ^{40}K atoms and was converted respectively into Bose–Einstein condensates of $^6\text{Li}_2$ ^{78–80} and $^{40}\text{K}_2$ ⁸¹ molecules after evaporative cooling. One example is shown in Figure 25.

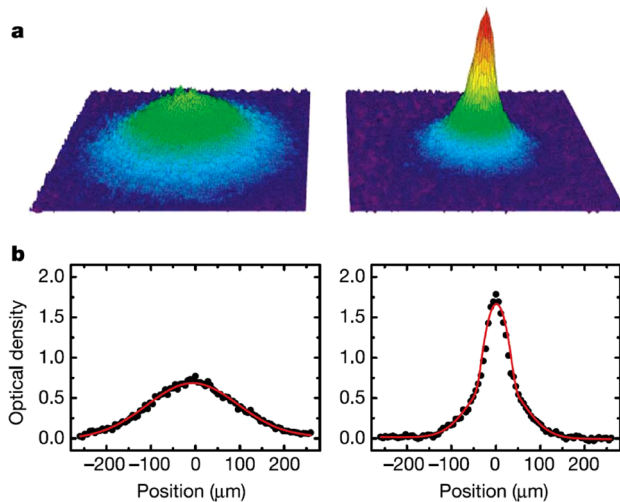


Figure 25. Time-of-flight images of the $^{40}\text{K}_2$ molecular cloud, taken with a probe beam along the axial direction after 20 ms of free expansion. Data are shown for temperatures above and below the critical temperature for Bose–Einstein condensation. Reprinted with permission from ref 81. Copyright 2006 Nature Publishing Group.

$\text{Cs}_2 + \text{Cs}/\text{Cs}_2$. Another study performed by Chin et al.²⁰⁵ in 2005 dealt with molecular collisions of bosonic Feshbach molecules of $\text{Cs}_2 + \text{Cs}_2$ tuned on- and off-resonance by a magnetic field for a temperature of 250 nK. Two off-resonance Feshbach molecular states were probed by ramping a magnetic field across a Fano-Feshbach resonance. The first state $|\alpha\rangle$ of Feshbach Cs_2 molecule is created at a magnetic field of 15.4 G,²⁰⁶ and the second state $|\beta\rangle$ is created at a magnetic field of

12.1 G. These are the off-resonance Feshbach molecules. The number of $|\alpha\rangle$ or $|\beta\rangle$ molecules as a function of time appears as open circles and closed circles, respectively, in Figure 26. The

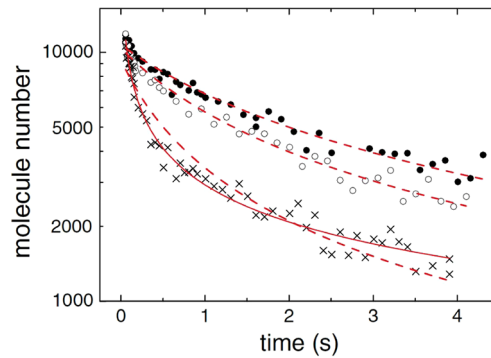


Figure 26. Time evolution of the molecule number in the CO_2 -laser trap for molecules in state $|\alpha\rangle$ at 15.4 G (open circles), in state $|\beta\rangle$ at 12.1 G (off-resonance, solid circles), and at 12.7 G (on-resonance, crosses). Fits based on two-body loss (dashed lines) work well for 15.4 and 12.1 G. A fit based on three-body loss (solid line) works better for 12.7 G. Reprinted with permission from ref 205. Copyright 2005 American Physical Society.

corresponding two-body $\text{Cs}_2 + \text{Cs}_2$ loss rate coefficients were fit to the data (dashed lines) and found to be $5 \times 10^{-11} \text{ cm}^3 \text{ s}^{-1}$ and $3 \times 10^{-11} \text{ cm}^3 \text{ s}^{-1}$, respectively. At a magnetic field of 12.7 G, the molecules are on-resonance, strongly coupling the states $|\alpha\rangle$ and $|\beta\rangle$. The number of molecules versus time is shown as crosses in Figure 26. The lifetime of the molecules is significantly reduced compared to the two former conditions. If a fit (dashed line) is based on two-body loss, the loss rate coefficient is found to be $2 \times 10^{-10} \text{ cm}^3 \text{ s}^{-1}$, an order of magnitude larger than the two previous conditions, suggesting a scattering resonance of two free Cs_2 molecules magnetically tuned on-resonance with a Cs_4 molecular bound state. However, a fit based on three-body loss (solid line) is also in agreement with the experimental data, and the authors cannot rule out the possibility that three-body processes may also play a role on-resonance.

In 2010 Knoop et al.²⁰⁷ were also able to magnetically control the dynamics of Feshbach Cs_2 molecules with Cs atoms, especially the energetic nature of the process. The atom-exchange process in concern was $A_2 + B \rightarrow A + AB$, where A and B are Cs atoms but in different hyperfine states. The temperature was 50 nK. The energy threshold of the channel $A + AB$ can open for a certain value of the magnetic field as shown in Figure 27b. As the magnetic field is increased, the process can be tuned from endoergic to exoergic when crossing this critical value of the magnetic field. The energy difference ΔE is shown in Figure 27c for different initial hyperfine state $m_f = 2, 3, 4$ of the atom A , where $\Delta E > 0$ corresponds to an endoergic process while $\Delta E < 0$ corresponds to an exoergic process. The loss rate coefficient β that leads to the loss of an A_2 molecule is shown in Figure 28 as a function of the magnetic field. This includes the atom-exchange process $A_2 + B(m_F) \rightarrow A + AB$ and the relaxation to a more deeply bound state $A_2 + B(m_F) \rightarrow A_2(\text{deep}) + B$. For the initial $m_f = 2, 3$ states, the experimental data show that the process is tuned from endoergic to resonant to exoergic when the magnetic field is increased. A pronounced threshold behavior is observed at the magnetic field for which the energy threshold becomes resonant ($\Delta E = 0$) in Figure 27b and 27c. Once energetically

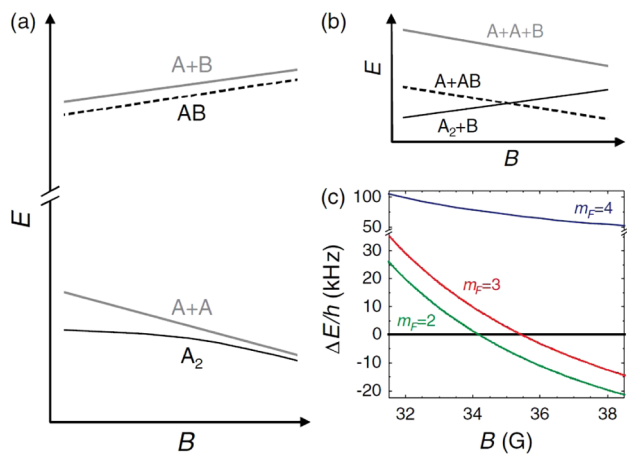


Figure 27. (a) Zeeman diagram of the most weakly bound dimer states A_2 and AB below the $A + A$ and $A + B$ dissociation thresholds, respectively; here A and B are two hyperfine sublevels of Cs. (b) Schematic representation of a crossing between the $A_2 + B$ and $A + AB$ channels. (c) The energy difference ΔE between the $A_2 + B(m_F)$ and $A + AB(m_F)$ channels, with $m_F = 2, 3$, or 4 , showing channel crossings around 35 G for $m_F = 2$ and 3 . Reprinted with permission from ref 207. Copyright 2010 American Physical Society.

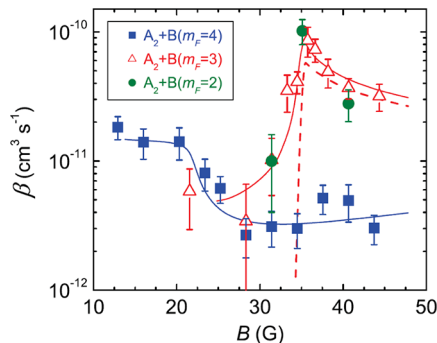


Figure 28. Rate coefficient β for inelastic atom–molecule collisions for the $B + A_2$ mixtures at a temperature of 50(10) nK as a function of the magnetic field B , comparing the experimental results (symbols) with the model calculations (lines). The solid curves represent the total A_2 loss rate including relaxation to more deeply bound states, whereas the dashed curve shows the contribution of the exchange process. The error bars contain the uncertainties of the trap frequencies and temperature measurements, required to convert the measured particle numbers into densities. Reprinted with permission from ref 207. Copyright 2010 American Physical Society.

allowed, the atom-exchange contribution is 80% of the total inelastic contribution. This was explained by the fact that the exchange process takes place in a regime where the relevant two-body scattering lengths are very large and the dimers A_2 and AB are in the halo regime⁹⁰ (see discussion in section 1.4). The authors actually saw that most of the lost A_2 molecules are accompanied by the appearance of the A atoms (still energetically trapped because of the small energy release), providing a clear evidence that the atom-exchange process dominates. Also, the authors argued the fact that the pronounced peaks in the rate are the same for the $m_F = 2$ and 3 initial state is a consequence of the universal halo regime because the dynamics does not depend on the details of the short-range physics. Finally, for the initial $m_F = 4$ state, where the process is always endoergic for the magnetic fields spanned in the experiment, the experimental results were in good

agreement with a theoretical calculation. For this case, a strong coupling was found between the $A_2 + B$ and the $A + AB$ channels, manifesting itself in a repulsive barrier in both channels, leading to the observed suppression of $A_2 + B$ collisions.

$Rb_2 + Rb/Rb_2$. Another confirmation of high loss molecular collisions at ultralow energy was observed by Syassen et al.²⁰⁸ They investigated the collisions of bosonic $^{87}Rb_2$ Feshbach molecules formed by magneto-association from an atomic Bose–Einstein condensate of Rb atoms¹⁹⁴ and found a Feshbach molecule–molecule loss rate coefficient of $K_{mm} = 3 \times 10^{-10} \text{ cm}^3 \text{ s}^{-1}$ and an atom–Feshbach molecule loss rate coefficient of $K_{am} = 2 \times 10^{-10} \text{ cm}^3 \text{ s}^{-1}$.

In a subsequent experiment, Syassen et al.¹⁴⁷ pursued their investigation of Feshbach molecule collisions in reduced dimensions. They investigated the dynamics of the $^{87}Rb_2$ Feshbach molecules in two-dimensional optical lattices where the molecules collide in one-dimensional tubes, as in Figure 2a. The authors showed that inelastic interactions can be used to reach a strongly correlated regime. The optical lattice potential is given by $-V_\perp \cos^2 kx - V_\perp \cos^2 ky - V_\parallel \cos^2 kz$, where $k = 2\pi/\lambda$ is the wavevector associated with wavelength λ of the light used to create the optical lattice. The depths V_\perp, V_\parallel can be changed by varying the intensity of the light. $V_\parallel = 0$ corresponds to a series of one-dimensional (1D) tubes along the z direction, $V_\perp = 0$ corresponds to a series of two-dimensional (2D) pancakes in the x and y directions, while $V_\perp = V_\parallel$ corresponds to a three-dimensional (3D) lattice in the x, y, z directions.

The authors started first to investigate the dynamics of the Feshbach molecules in the 1D tubes $V_\parallel = 0$. They measured the number of molecules lost as a function of time and fit the data to the rate equation

$$\frac{dn}{dt} = -Kn^2g^{(2)} \quad (30)$$

where $n = n(t)$ is the 1D density (in units of cm^{-1}) of molecules as a function of time, K is the 1D loss rate coefficient that can be related to a corresponding rate coefficient K_{3D} in free 3D space, and $g^{(2)} = \langle n^2 \rangle / \langle n \rangle^2$ is the pair correlation function that gives the reduction factor of the loss rate compared with an uncorrelated state where $g^{(2)} = 1$. For the conditions of their experiment, an analytic expression of $g^{(2)}$ can be obtained,^{148,209,210} leading to the rate equation

$$\frac{dn}{dt} = -\chi n^4 \quad (31)$$

where χ is related to the 1D rate coefficient K . The 1D interaction strength for a standard delta function representation of the scattering potential is proportional to a dimensionless parameter γ . The pair correlation function and γ are related by $g^{(2)} = 4\pi^2/(3|\gamma|^2)$ in the limit $|\gamma| \ll 1$. By fitting their experimental results to equation 31, the authors extracted a value of $K_{3D} = (2.2 \pm 0.2) \times 10^{-10} \text{ cm}^3/\text{s}$ and a value of $g^{(2)} = 0.11 \pm 0.01$. This confirms that the loss rate is strongly reduced because the system is correlated with $g^{(2)} < 1$. If the system were not correlated so that $g^{(2)} = 1$, the corresponding rate equation would not fit their observed experimental data. Also the power law dependence would be $dN/dt \propto N^2$ for the usual free-space two-body collisions. In their experiment, Syassen et al. observed a $dN/dt \propto N^p$ dependence with $p = 4.3 \pm 0.6$, in agreement with the correlated regime $dN/dt \propto N^4$, as expected from eq 31.

The authors added an optical lattice in a third dimension and increased the lattice depth V_{\parallel} while keeping $V_{\parallel} \ll V_{\perp}$. This is illustrated in Figure 29. The figure shows the number of

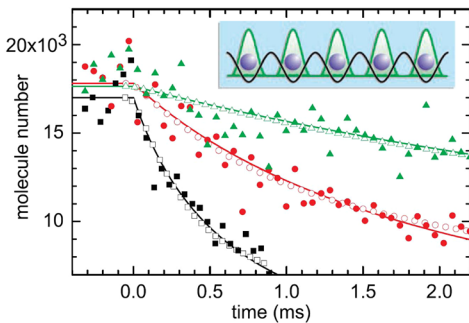


Figure 29. Loss for $V_{\parallel} \neq 0$. Solid lines show fits of eq 32 to the experimental data (solid symbols). Open symbols show results of numerical calculations. Black squares, red circles, and green triangles correspond to V_{\parallel}/E_r values of 1.8, 3.9, and 6.0, respectively. Reprinted with permission from ref 147. Copyright 2008 AAAS.

molecules lost as a function of time for $V_{\parallel} = 1.8E_r$ (black squares), $3.9E_r$ (red circles), and $6.0E_r$ (green triangles), where $E_r = \hbar k^2/2m$ is the molecular recoil energy and m is the mass of one molecule. Note that the case of collisions in pure 1D tubes discussed previously when $V_{\parallel} = 0$ resembles the curve for small $V_{\parallel} = 1.8E_r$ (see Figure 1 of ref 147). Integrating the equation in eq 30 over space leads to

$$\frac{dN}{dt} = -\frac{\kappa}{N(0)}N^2(t) \quad (32)$$

where the actual loss rate is $\kappa = Kn(0)g^{(2)}$. The loss number of molecules as a function of time for different V_{\parallel} observed in their experiment is shown in Figure 29 as filled symbols. Fitting to the eq 32 (solid lines in Figure 29), they extracted the value κ . This is shown in Figure 30A for different V_{\parallel} as filled circles.

Using a Bose–Hubbard model²¹¹ to describe the motion of molecules hopping from site to site with a tunneling amplitude J , on-site molecule–molecule interaction $\text{Re}(U)$, and on-site molecule–molecule loss $\Gamma = -2\text{Im}(U)/\hbar$ and considering strong loss collisions so that $J/(\hbar\Gamma) \ll 1$, the authors showed that the actual rate κ is given by

$$\kappa = \frac{32J^2}{\hbar^2\Gamma} \left\{ 1 + \left[\frac{\text{Re}(a)}{\text{Im}(a)} \right]^2 \right\}^{-1} \quad (33)$$

where a is the complex scattering length as defined in eq 12 and related to the elastic and loss rate coefficient by eqs 13 and eq 14. The open circles come from an extensive numerical calculation that involves solution of the master equation for the time-evolution of the density matrix of the many-body system and agrees with the experimental data and the equation 33. The equation 33 shows that the stronger the loss rate Γ , the weaker the actual rate coefficient. The fast on-site loss tends to suppress tunneling, preserving the initial state. The authors interpreted this result as a manifestation of the quantum Zeno effect:²¹² fast dissipation freezes the system in its initial state. Without this effect, the naive loss rate would consist of the tunneling rate from one site to another followed by an immediate on-site loss so the rate would be $\sim 2J/\hbar$. This is plotted as a green dashed line in Figure 30A, overestimating the observed data. Finally, Figure 30B shows that the correspond-

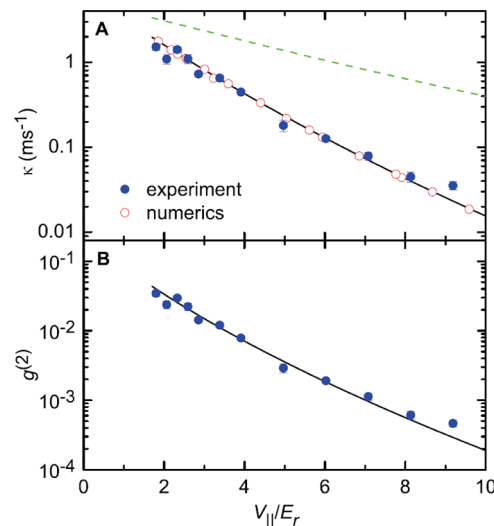


Figure 30. Loss at different lattice depths V_{\parallel} . (A) Fits as in Figure 29 yield the experimental results (filled circles) for κ . A fit of eq 33 to the data yields the solid line. The best-fit value is $K_{3D} = 1.7 \times 10^{-10} \text{ cm}^3/\text{s}$. The experimental data and the analytical model agree well with results of numerical calculations (open circles). For comparison, the dashed line shows the naive estimate $\kappa_{\text{naive}} = 2J/\hbar$, which is nowhere close to the data. Error bars indicate one statistical standard error. (B) Pair correlation function $g^{(2)} = \kappa/\Gamma$ calculated from the data in (A). Reprinted with permission from ref 147. Copyright 2008 AAAS.

ing pair correlation function $g^{(2)}$ decreases with V_{\parallel} , increasing the correlation of the system as V_{\parallel} is turned up.

This remarkable experiment demonstrated an effect that does not occur in normal 3D collisions. A reduced dimension ensemble of ultracold molecules with rapid loss collisions leads to strongly correlated many-body physics that greatly modifies and reduces the loss rate.

KRb + K/Rb. In 2008, Zirbel et al.¹¹² created Feshbach fermionic molecules of ${}^{40}\text{K}{}^{87}\text{Rb}$ from a Bose–Fermi atomic mixture. These molecules are composed of a boson B (${}^{87}\text{Rb}$) and a fermion F (${}^{40}\text{K}$). In their experiment, the authors can control the scattering length of the heteronuclear Feshbach molecules, referred to as BF , by tuning the magnetic field. They can also control the identity and the statistics of the surrounding colliding atoms, that is, whether these atoms are the same as one of the atoms B or F in the BF Feshbach molecule or whether these atoms, denoted X , are different from either atom in the BF Feshbach molecule. The authors explored the possibility of tuning the atom–molecule dynamics offered by this experiment. They showed that the inelastic loss due to an atom–molecule collision near the Fano-Feshbach resonance is dramatically affected by the quantum statistics of the colliding particles and the value of the scattering length. Note that, in the study, the authors ignored molecule–molecule $BF + BF$ collisions because indistinguishable fermionic particles should collide in a p -wave and the rate should be suppressed compared to the rate of s -wave atom–molecule collisions. The results of these experiments are presented in Figures 31 and 32. Figure 31 corresponds to the loss rate coefficient β of $BF + B$ collisions whereas Figure 32 corresponds to the loss rate coefficient of $BF + F$ collisions, plotted as a function of the BF Feshbach molecule scattering length a . In the figures, the dashed line corresponds to a power law fit to the loss rate coefficient of $BF + X$ collisions, found to be $\beta_{\text{fit}} \propto a^p$ with $p = -0.97 \pm 0.16$, in

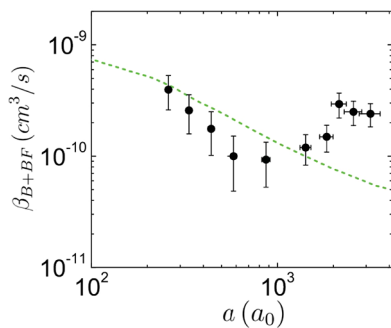


Figure 31. BF molecule loss coefficient for collisions with indistinguishable bosons B versus heteronuclear scattering length. For large a , β increases with increasing a . In this regime, the molecular loss is enhanced compared to loss due to BF molecule collisions with distinguishable X atoms (dashed curve). For small a , β increases with decreasing scattering length. Reprinted with permission from ref 112. Copyright 2008 American Physical Society.

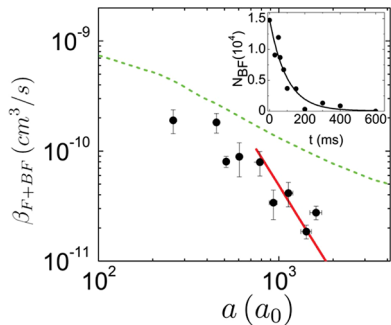


Figure 32. BF molecule loss coefficient β for collisions with indistinguishable fermions F . For large a , the loss rates scale as $a^{-1.6 \pm 0.2}$. The power law dependence is consistent with numerical calculations for this scattering length regime (solid curve). In addition, the molecular loss is suppressed compared to inelastic decay of BF molecules due to collisions with distinguishable X atoms (dashed curve). Inset: Molecule decay at $a \approx 1300a_0$. The $1/e$ -lifetime of the molecular cloud is $\tau = 100 \pm 20$ ms. Reprinted with permission from ref 112. Copyright 2008 American Physical Society.

agreement with the theoretical prediction of D’Incao and Esry²¹³ of $p = -1$.

In their study, Zirbel et al. found an enhancement of β that increases with increasing a , for collision of BF molecules with B atoms (Figure 31). This is consistent with the expectation that Bose statistics should enhance the molecule decay rates due to the attractive character of the effective atom–molecule interaction.^{214,215} In contrast, for collision of BF molecules with F atoms (Figure 32), they found a suppression of β as a increases, in agreement with theoretical expectations.^{214,215} At finite a , the experimental rate was fitted and found to follow $\beta \propto a^{-1.6 \pm 0.2}$. The trend qualitatively agrees with a numerical calculation (red solid line).

Zirbel et al. also observed two different trends depending upon the statistics of the colliding atom. For $BF + B$ collisions, β is found to be larger than if the atom were a distinguishable atom X (see the difference between the experimental points and the dashed curve), whereas for $BF + F$ collisions, the observed rate is suppressed compared with the case with a distinguishable colliding X atom. However, the authors argued that the generality of this observed behavior can also depend on the short-range physics and can be different for other system.

Finally, the authors measured the role of three-body recombination of atoms in the mixture, near a heteronuclear Feshbach resonance. They observed an increased three-body recombination rate K_3 as $|a|$ increased, with the expected $|a|^4$ behavior^{214,215} of eq 25.

3.2. Theory

We focus in this section on the theoretical studies of atom–molecule and molecule–molecule dynamics performed at low and ultralow collision energies, involving the atoms of the first column of the periodic table (hydrogen and alkali atoms), because much experimental work in the ultracold regime has focused on these atoms and molecules. The theoretical studies presented here were performed using full quantum scattering calculations, involving the full potential energy surface of the H_3 , Li_3 , Na_3 , and K_3 triatomic systems for the $H + H_2$, $Li + Li_2$, $Na + Na_2$, and $K + K_2$ atom–molecule collisions, and the full potential energy surface of the H_4 tetramer system for the molecule–molecule collision $H_2 + H_2$. Much theoretical work on ultracold collisions involving these and other species has appeared in the literature. Although we will not be able to cover all of this work, we want to give strong credit to these other studies by providing here the references and the authors of previous reviews articles and book chapters that have broadly covered these topics. Krems²¹⁶ covered theoretical work on the external control of ultracold molecular dynamics with electric and magnetic fields. Hutson and Soldán^{217,218} wrote two reviews on theoretical studies of barrierless atom–molecule collisions involving alkali atoms at ultralow energies. Chemical reactions at cold and ultracold temperatures were reviewed by Weck and Balakrishnan²¹⁹ with an emphasis on the importance of the long-range interaction of the atom–molecule approach. Bodo and Gianturco²²⁰ focused on collisional quenching of rovibrational states of simple neutral and ionic diatomic species, both polar and homonuclear, interacting with a helium buffer gas at ultralow energy. Hu and Schatz²²¹ presented the different theoretical methods employed to describe the reactive scattering of atoms and molecules, using time-independent and time-dependent approaches. Krems²²² also wrote another review covering the topic of cold controlled chemistry. Several chapters in the book “Cold Molecules: Theory, Experiment, Applications”, edited by Krems, Friedrich, and Stwalley, have also brought a lot of insight on theoretical molecular collision studies performed in the scientific literature. We want to cite the chapters of Hutson,²²³ Bohn,²²⁴ Quéméner, Balakrishnan, and Dalgarno,¹⁸⁷ and Tscherbul and Krems.²²⁵

3.2.1. Ultracold Atom–Molecule Dynamics. $H + H_2$. In 1997, Balakrishnan et al.^{49,226} studied the vibrational relaxation dynamics of ultracold $H + H_2(X^1\Sigma_g^+, \nu, j = 0)$ collisions with $\nu = 1–14$, using the H_3 potential energy surface of Boothroyd et al.,²²⁷ as well as a quantum scattering dynamics formalism using the code MOLSCAT written by Hutson and Green.²²⁸ The total relaxation rate coefficients⁴⁹ for vanishing collision energy $E_c \rightarrow 0$ for different initial vibrational ν numbers are reported in Figure 41 later in this review and compared with the results of other alkali–dialkali collisions. It is seen that, as the vibration quantum number increases, the inelastic rate coefficients increase. The threshold rate coefficient of $10^{-17} \text{ cm}^3 \text{ s}^{-1}$ for $\nu = 1$ quenching is rather low, whereas the coefficient for $\nu = 12$ increases 7 orders of magnitude to $10^{-10} \text{ cm}^3 \text{ s}^{-1}$. This shows that the inelastic rates of ultracold $H + H_2$ collisions depends on the initial vibrational state probed and, despite being ultracold, can lead to high relaxation rates to deeper molecular

bound state. A similar study was also performed later in 2006 by Bodo et al.²²⁹ The dependence of the inelastic rate on the initial vibrational quantum number is discussed in detail later for the Li + Li₂ and Na + Na₂ system.

Na + Na₂. In 2002 Soldán et al.²³⁰ performed a theoretical study of the Na + Na₂($a^3\Sigma_u^+$, $\nu = 1, j = 0$) collision, involving spin-stretched Na atoms. They computed the elastic and inelastic cross section as a function of collision energy for the s-wave scattering. This was performed using the HYP3D code written by Launay and Le Dourneuf,²³¹ based on a full time-independent numerical quantum scattering calculation using democratic hyperspherical coordinates, including the possibility of atom-exchange processes to account for the indistinguishability of the atoms as they encounter one another. This study included a full potential energy surface for the Na₃ trimer system, calculated by Higgins et al.²³³ for the quartet state 4A . The potential energy surface is composed by an additive two-body term V_2 , which is the sum of three diatomic potential energy curves, and by a nonadditive three-body term V_3 ,^{234,235} which represents the electronic correlations between the three atoms. The authors showed the importance of the nonadditive three-body term in trimer spin-stretched alkali potential energy surfaces. This was also confirmed by Colavecchia et al.²³⁶ for the Li₃ potential energy surface and more generally by Soldán et al.²³² for Li₃, Na₃, K₃, Rb₃, and Cs₃ at specific trimer geometries. Figure 33 from ref 232 shows that, for the D_{3h} geometry where the three atoms form an equilateral triangle of side r , the potential energy differs when the full potential energy is used (a) and when only the two-body additive terms are considered (b). At the equilibrium geometry r_{eq} , the contributions of the nonadditive term V_3 to the full potential vary from 120% for Li₃ down to 50% for Cs₃. Similar conclusions were found in calculations for trimers of alkaline-earth atoms by Kaplan et al.,²³⁷ where the contributions of V_3 vary from 100% for Be₃ to 60% for Ca₃. Nonadditive contributions to the potential energy for alkali and alkaline-earth trimers strongly contrast with systems of rare-gas trimer, for which nonadditive terms are responsible for only 0.5–2.5%.^{238,239} The elastic (solid line) and inelastic (dashed line) cross sections are shown in Figure 34 using the additive potential energy surface (top panel) and the full potential energy surface (bottom panel). The authors found that the omission of the three-body term can lead to large differences, up to an order of magnitude, in the atom–molecule total cross sections and can lead to dramatic change in the final state-to-state distributions. This is a manifestation of the sensitivity of threshold cross sections to details of the potential, as described in section 1.3. The rate coefficients approach the threshold law forms from eqs 14 and 13 for collision energies below $\sim 100 \mu\text{K}$ and the inelastic ones dominate the elastic ones as energy decreases.

In 2004, using the same code in a subsequent study, Quéméner et al.²⁴⁰ performed a more systematic study on the sensitivity of the cross sections on the nonadditive three-body term λV_3 of Na₃, where λ is a scaling parameter. The ultracold total inelastic cross sections (full symbols) for Na + Na₂($\nu = 1, 2, 3, j = 0$) as a function of the scaling parameter λ are shown in Figure 35, for a fixed collision energy of 1 nK. The open symbols represent the final vibrational ν_f resolved cross sections. The authors found that, by changing the three-body term by $\pm 2\%$ ($\lambda = 0.98$ –1.02), the cross sections can vary by an order of magnitude for Na + Na₂($\nu = 1, j = 0$). For Na + Na₂($\nu = 2, j = 0$), the total cross sections vary by about a factor of 2,

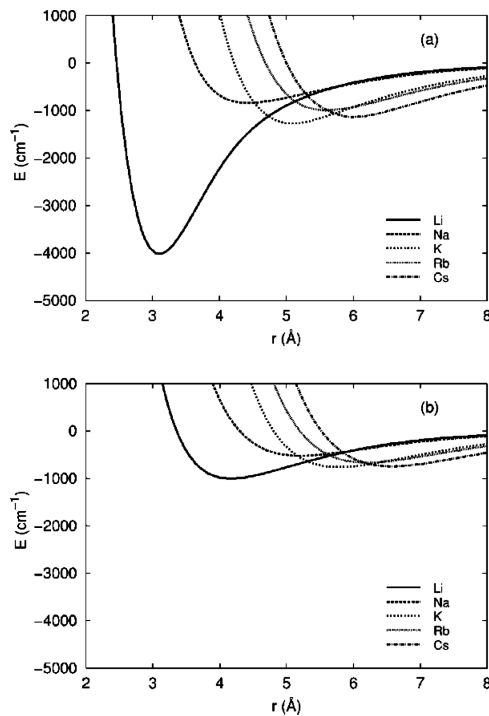


Figure 33. RCCSD(T) interaction energies of spin-polarized alkali-metal trimers at D_{3h} geometries (a) full potentials including nonadditive contributions and (b) additive potentials. Reprinted with permission from ref 232. Copyright 2003 American Physical Society.

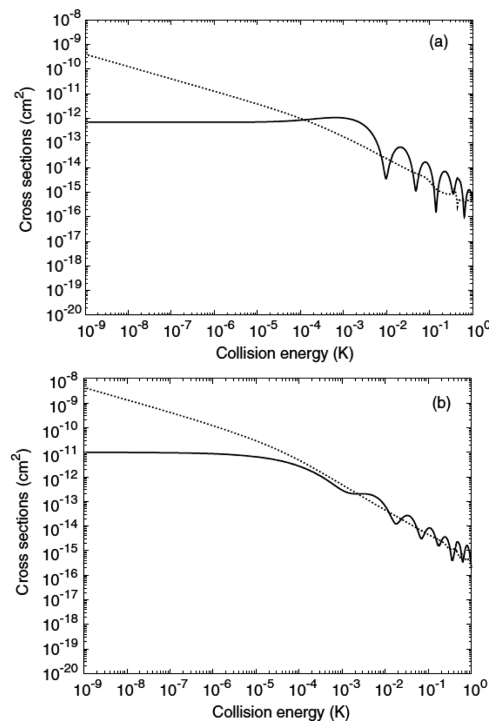


Figure 34. Cross sections from quantum reactive scattering calculations for Na + Na₂($\nu = 1, j = 0$) (s-wave scattering). The elastic and quenching cross sections, shown respectively as solid and dotted lines, follow the Bethe–Wigner forms at low collision energy: (a) additive potential and (b) nonadditive potential. Reprinted with permission from ref 230. Copyright 2002 American Physical Society.

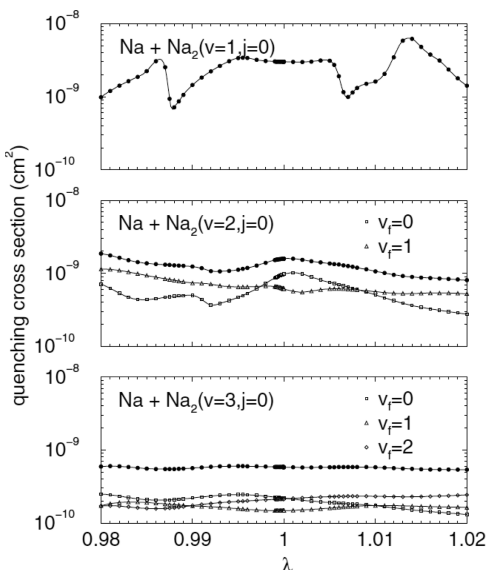


Figure 35. Quenching cross sections (full circle) for $\text{Na} + \text{Na}_2$ collisions for three initial rovibrational states ($v = 1, j = 0$), ($v = 2, j = 0$), and ($v = 3, j = 0$) of Na_2 as a function of the scaling parameter λ at a collision energy of 1 nK. For initial vibrational states $v = 2$ and $v = 3$, quenching cross sections for a final vibrational state $v_f = 0$ (square), $v_f = 1$ (triangle), and $v_f = 2$ (cross) are also shown. Reprinted with permission from ref 240. Copyright 2004 Institute of Physics and the Deutsche Physikalische Gesellschaft.

but the variations of the vibrationally resolved cross sections are more pronounced (varying by a factor of 3–4). For $\text{Na} + \text{Na}_2(v = 3, j = 0)$, there is no more dependence of the total cross sections, and at most a factor of 2 for the vibrationally resolved cross sections. However, the final rotational j_f resolved cross sections shown in Figure 36 can still vary a lot, at most by an order of magnitude. The total inelastic cross sections are sensitive to the three-body term for the vibrational states $v = 1$ but become less and less sensitive for $v = 2$ and $v = 3$. This is because of the need to sum over more final states with increasing v . The state-to-state cross sections in Figure 36 are much more sensitive to the variation of the scale parameter λ than are the total cross sections summed over several final states. This sensitivity is associated with the presence of Fano-Feshbach resonances that vary as λ is changed and tunes the bound and quasi-bound state spectrum of the collision complex. Particular resonant paths influence different transitions differently. The resonance “width” versus λ is relatively

broad, due to the high probability of resonance decay associated with strong coupling within the collision complex. Trends in the inelastic cross sections with v were further explained by an analysis of Hutson.⁵⁰ Collision of Na atoms with higher vibrational states of Na_2 molecules was also investigated in ref 241. Inelastic rate coefficients of $\text{Na} + \text{Na}_2$ for different initial vibrational states are summarized in Figure 41 later in the text.

The collisions of $\text{Na} + \text{Na}_2$ were only considered for spin-stretched atoms so that only the quartet surface ${}^4\text{A}'$ can be used. For the most general case, change in electronic and nuclear spin can occur in molecular collisions as they do in atomic ones. For this purpose, the two doublet surfaces ${}^2\text{A}'$ also have to be used. In 2006 Simoni and Launay²⁴² investigated in detail such collisional processes. To keep the calculations tractable, they neglected atomic-exchange processes and employed a rigid rotor approximation. However, they considered the hyperfine interaction between electron and nuclear spins. This interaction couples the different electronic surfaces ${}^1\text{A}'$, ${}^2\text{A}'$, and ${}^4\text{A}'$ together. Using a hyperfine coupled-channel basis set at long range, a spin-coupled channel basis set at short range, and the frame transformation between spin representations, they computed the rate coefficients of rotational-changing, spin-changing, and hyperfine-changing processes at ultralow energies. They considered Na atoms in their highest total spin state $f = 2$ and Na_2 molecules in their electronic spin $S = 1$ (triplet state) with vanishing nuclear spin $I = 0$. The authors found that in general triplet-state molecules in the presence of atoms will rapidly decay into the singlet state so that evaporative-cooling techniques will be useless for additional cooling of the molecular samples. Simoni et al.²⁴³ also investigated the presence of Fano-Feshbach resonances in ultracold $\text{Na} + \text{Na}_2(v = 0, j = 0)$ collisions, and its consequence for interpreting future atom–molecule collision experiments.

$K + K_2$. In 2005 Quéméner et al.²⁴⁴ computed the potential energy surface of the quartet state of K_3 and used it to study the dynamics of the $\text{K} + \text{K}_2(a^3\Sigma_u^+, \nu = 0, j)$ system. The method was the same employed for the $\text{Na} + \text{Na}_2$ collision in refs 230 and 240 but extended to more partial waves to explore the effect of higher collision energies. Figure 37 shows the elastic (top panel) and quenching (bottom panel) cross sections of ${}^{39}\text{K} + {}^{39}\text{K}_2$ as a function of collision energy for the different partial waves, and the dashed lines shows the total cross sections. At ultralow energy (~ 1 nK), the elastic scattering is ~ 3 orders of magnitude smaller than the inelastic scattering, consistent with previous findings for $\text{Na} + \text{Na}_2$ collisions.^{230,240} These conclusions hold for the dynamics of the other isotopes ${}^{40}\text{K}$ and ${}^{41}\text{K}$. The inelastic rate coefficients of ${}^{39}\text{K} + {}^{39}\text{K}_2$ for $v = 1, j$

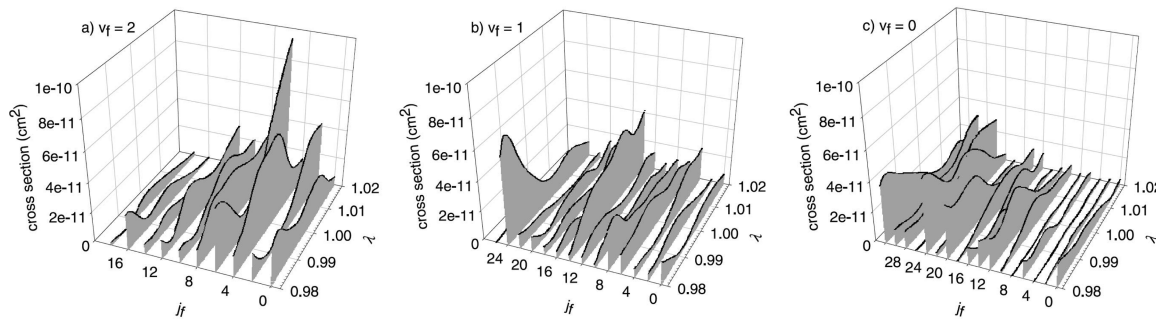


Figure 36. Three-dimensional plots for rotational distributions for the vibrational relaxation $\text{Na} + \text{Na}_2(v = 3, j = 0) \rightarrow \text{Na} + \text{Na}_2(v_f, j_f)$ or $\text{Na}_2(v_f, j_f) + \text{Na}$ with $v_f = 2$ (panel a), $v_f = 1$ (panel b), and $v_f = 0$ (panel c) as a function of λ at a collision energy of 1 nK. Reprinted with permission from ref 240. Copyright 2004 Institute of Physics and the Deutsche Physikalische Gesellschaft.

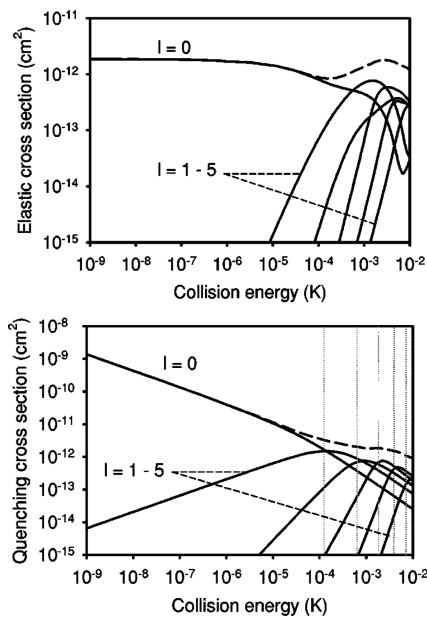


Figure 37. Elastic (upper panel) and quenching (bottom panel) cross sections versus collision energy in Kelvin for $^{39}\text{K} + ^{39}\text{K}_2$ ($v = 1, j = 0$). The contributions from individual partial waves are shown as solid lines, and their sum is shown as a dashed line. The figure shows how it is necessary to take more partial waves into account as collision energy increases. Reprinted with permission from ref 244. Copyright 2005 American Physical Society.

$= 0$ are reported in Figure 41 later in the text. The final rotational distribution probability of $\text{K} + \text{K}_2(v = 1, j = 0) \rightarrow \text{K} + \text{K}_2(v = 0, j' = 0-26)$ is shown in Figure 38 as a function of the

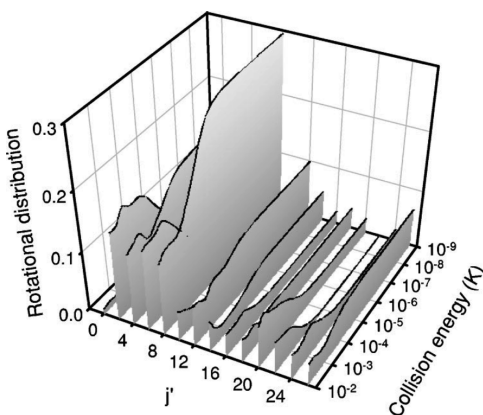


Figure 38. Rotational distributions as a function of the collision energy. The label j' is the final rotational quantum number of $^{39}\text{K}_2$ ($v = 1, j'$). Collision energy is in Kelvin. Reprinted with permission from ref 244. Copyright 2006 American Physical Society.

final rotational state j' in the ground vibrational state $v = 0$ and as a function of the collision energy. As the collision energy vanishes, all the inelastic state-to-state transition probabilities for $v = 1, j = 0 \rightarrow v = 0, j'$ are independent of the collision energy, thus obeying the Bethe–Wigner law for ultracold s -wave collisions. The rotational distribution differs from ultralow to higher energies. At ultralow energy (10^{-6} K or below), $j' = 8$ is, for example, the most favorable relaxation state, whereas for higher energies (10^{-2} K), $j' = 2, 4, 6$, and 8 are the most favorable states. This distribution is governed by the strength of the couplings between the different molecular transitions at

different collision energies and represents a strong signature of the anisotropy of the triatomic potential energy surface of K_3 . As a consequence, if future experiments can provide these inelastic state-to-state transitions, one can obtain a lot of information on the molecular potential energy surface itself, and especially on its anisotropy.

Lysebo and Veseth²⁴⁵ also performed in 2008 a study of $\text{K} + \text{K}_2$ and $\text{Na} + \text{Na}_2$ collisions in the ground electronic and vibrational state. They invoked the rigid rotor approximation so that the exchange processes of the identical atoms are not treated. They also found that inelastic processes are much faster than elastic scattering, as described previously.

Although the K_3 system is the heaviest one treated with a full quantum scattering calculation, there exist other potential energy surfaces of systems with higher mass, such as the Rb_3 system²⁴⁶ and the Cs_3 system.²⁴⁷ Calculations on the dynamics for $\text{Rb} + \text{Rb}_2$ and $\text{Cs} + \text{Cs}_3$ remain to be carried out.

$\text{Li} + \text{Li}_2$. In 2005 and 2007, Cvitaš et al. performed three studies on the $\text{Li} + \text{Li}_2(a^3\Sigma_u^+, v, j)$ system^{248–250} involving collisions of Li atoms with both homonuclear and heteronuclear Li_2 molecules. They computed a potential energy surface for Li_3 from an all-electron coupled-cluster electronic structure calculation. The conclusions were mainly similar to the previous studies discussed above. The authors also compared the rate coefficient as a function of the collision energy for initial vibrational state of $v = 1$ and $v = 2$ for bosonic and fermionic $\text{Li} + \text{Li}_2$ collisions with the Langevin classical capture model.^{183,184} The classical capture formula in eq 28 depends on the mass and van der Waals coefficient of the system but is independent of initial quantum state of the atom. Accordingly, Figure 39 shows the result that the numerical

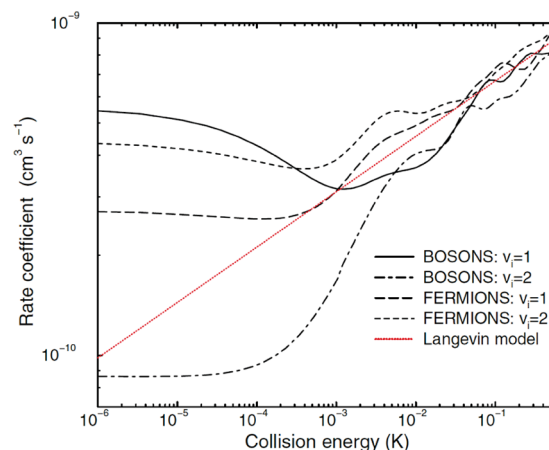


Figure 39. Total inelastic rate coefficients for collisions of Li with Li_2 ($v = 1$ and 2 , with $n = 0$ for bosons and $n = 1$ for fermions). Reprinted with permission from ref 248. Copyright 2005 American Physical Society.

calculations for the different initial vibrational states converge toward the classical model for collision energies above $\sim\text{mK}$, changing from the rate coefficients in the regime $\ll\text{mK}$ where the Bethe–Wigner laws^{41,42} are obeyed.

In 2007 Quéméner et al.²⁵¹ studied the initial vibrational dependence of the elastic and inelastic rate coefficients of $^7\text{Li} + ^7\text{Li}_2(a^3\Sigma_u^+, v, j = 0)$ and $^6\text{Li} + ^6\text{Li}_2(a^3\Sigma_u^+, v, j = 1)$ for all the vibrational states of the triplet electronic state, from $v = 0$ to $v = 10$ for the bosonic ^7Li species and from $v = 0$ to $v = 9$ for the

fermionic ${}^6\text{Li}$ species. The authors used the potential energy surface of Colavecchia et al.²³⁶ for the lowest quartet state of Li_3 . The molecular basis set used in the quantum calculation has to be increased to converge the numerical results. This is illustrated in Figure 40 for the ${}^7\text{Li}_3$ molecular system, where the

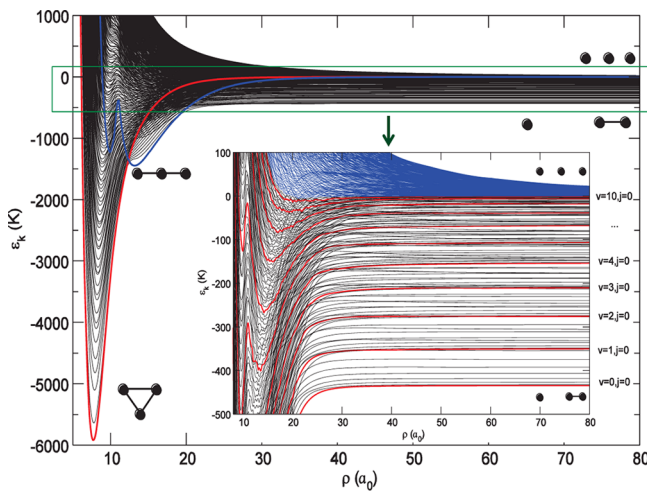


Figure 40. Adiabatic energies as a function of the hyperspherical radius ρ for the lowest quartet state of the ${}^7\text{Li}_3$ potential energy surface.

adiabatic energies are plotted as a function of the hyperspherical radius. The figure shows a global picture of these curves, along with the minimum potential energy curve for equilateral (in red) and colinear (in blue) geometries. The inset in Figure 40 provides a view on the molecular states involved. The red curves are the ${}^7\text{Li} + {}^7\text{Li}_2(v = 0-10, j = 0)$ energy thresholds, and the blue curves represent the double continuum states, configurations for three separated ${}^7\text{Li} + {}^7\text{Li} + {}^7\text{Li}$ atoms. For $\text{Li} + \text{Li}_2$, ~ 1200 of such curves are needed to converge the rate coefficients of the high-lying vibrational state $\text{Li}_2(v = 10, j = 0)$. This shows how hard and difficult numerical calculations can become in order to treat high vibrational states of the molecules to compare with observed experimental data.^{178–180} The inelastic rate coefficients of ${}^7\text{Li} + {}^7\text{Li}_2(v = 0-10, j = 0)$ are plotted in Figure 41 for the different initial vibrational states and are discussed in the following.

Comparison for Different Alkali Systems. Figure 41 compiles the different inelastic rate coefficients of the previous studies of ultracold alkali–dialkali collisions, as a function of their initial vibrational quantum number. The figure reports the inelastic rate coefficients of $A + A_2(v, j = 0)$ for $A = \text{H}, {}^7\text{Li}, {}^{23}\text{Na}$, and ${}^{39}\text{K}$. The inelastic rates increase with the vibrational number, except for a decrease for the last quantum number. This can be explained by an argument made by Stwalley.²⁵² The small overlap between the highest excited vibrational wave function of the diatomic, which has the biggest spatial extent, and the lower vibrational ones, which have a smaller spatial extent, can lead to small inelastic couplings, hence lowering the vibrational relaxation rate. This decrease of the inelastic rate for the highest vibrational state is seen for the $\text{H} + \text{H}_2$, $\text{Li} + \text{Li}_2$, and $\text{Na} + \text{Na}_2$ systems in Figure 41. Note that the decrease occurs for both the bosonic system ${}^7\text{Li} + {}^7\text{Li}_2$ and the fermionic one ${}^6\text{Li} + {}^6\text{Li}_2$ in ref 251, so that it is not related to quantum statistics. This is in contrast with the Pauli blocking mechanism that only occurs for fermionic atoms in halo states when the

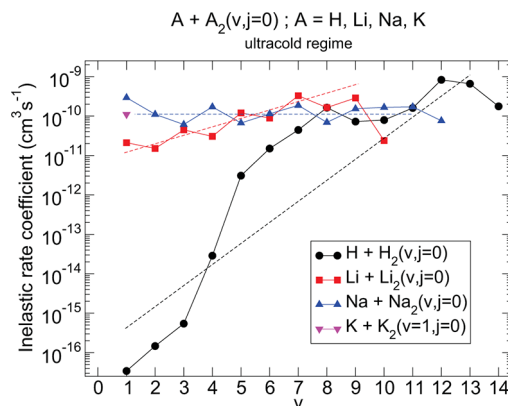


Figure 41. Compilation of inelastic rate coefficients for different initial vibrational states, for a collision energy of 10^{-9} K: $\text{H} + \text{H}_2(X^1\Sigma_g^+, v = 1-14, j = 0)$ (black line with circles), taken from ref 49, also studied in ref 229. ${}^7\text{Li} + {}^7\text{Li}_2(a^3\Sigma_u^+, v = 1-10, j = 0)$ (red line with squares), taken from ref 251. ${}^{23}\text{Na} + {}^{23}\text{Na}_2(a^3\Sigma_u^+, v = 1-12, j = 0)$ (blue line with upward triangle), unpublished results, taken from ref 241. ${}^{39}\text{K} + {}^{39}\text{K}_2(a^3\Sigma_u^+, v = 1, j = 0)$ (pink downward triangle), taken from ref 244. The solid lines are only to guide the eye between points for different v for a given species.

scattering length of the molecule is large and positive, in which case the inelastic rates are suppressed.^{77,201}

Quéméner et al.²⁵¹ showed that the three-body nonadditive potential can be omitted to determine the total inelastic relaxation rate coefficients for molecules in high vibrational states, as already described in refs 230, 240, and 250, because the three-body term vanishes at large atomic separations. This is especially the case when molecules are in high vibrational states with spatially large extent. It cannot be neglected for low v as described in ref 240.

It is interesting to compare the trend of the plots for the different molecular systems. It appears that the lighter system $\text{H} + \text{H}_2$ has a strong dependence with the initial vibrational state, the heavier system $\text{Na} + \text{Na}_2$ has much less dependence, and the system $\text{Li} + \text{Li}_2$ stands somewhat in between. This can be explained by some qualitative arguments.²⁵¹ First, if all systems had a small density of states and molecular couplings, the inelastic rates will be proportional to the number of molecular states to relax into. Because for high quantum numbers v there are more channels to relax into than for small quantum numbers v , we can conclude that the inelastic rate should globally increase for increasing v . This is the case for $\text{H} + \text{H}_2$ because H_3 has a low density of molecular states because it is a light system with a very deep minimum potential energy ($\sim -40\,000\text{ cm}^{-1}$, ref 253). However, molecular densities and couplings can play a role as well and affect our preceding qualitative conclusion. Li_3 is already heavier than H_3 with a less deep minimum potential energy ($\sim -4022\text{ cm}^{-1}$; see Figure 33). The density of molecular state increases, increasing the strength of the molecular couplings. Our previous conclusion must be affected by this. We still see an overall increase of the rate with v , confirming that the rate is proportional to the number of relaxation channels, but now with a weaker slope for $\text{Li} + \text{Li}_2$, showing the effect of the molecular couplings. As one goes down in the first column of the periodic table $A = \text{Na}, \text{K}, \text{Rb}$, and Cs , the A_3 system gets heavier, and combined with the fact that the minimum potential energy gets shallower (at least compared to the H_3 and Li_3 system; see Figure 33), the density

of A_3 states increases, increasing the molecular couplings. The couplings can be strong enough so that, even for low vibrational state, the inelastic rates will already be big and independent of the number of relaxing channels. This seems to be the case for $\text{Na} + \text{Na}_2$, for which no more vibrational dependence is seen on average. Similar plots, with no ν dependence, might be expected for the heavier systems $\text{K} + \text{K}_2$, $\text{Rb} + \text{Rb}_2$, and $\text{Cs} + \text{Cs}_2$. This is also consistent with experimental measurements of inelastic rate of $\text{Cs} + \text{Cs}_2$, for which no vibrational dependence was found.^{179,180} This was also explained by Bodo et al.²²⁹ for the $\text{H} + \text{H}_2$ system, by artificially increasing the mass of the H atoms. If they increased the mass from 10 to 100, the strong vibrational dependence of $\text{H} + \text{H}_2$ vanishes and looks like the dependence of the $\text{Na} + \text{Na}_2$ system in Figure 41.

Finally, the overall magnitudes of the loss rate coefficients in Figure 41 tend, with the exception of H, to be within an order of magnitude of $\sim 10^{-10}$ cm³/s. This corresponds to the imaginary part of the scattering length in eq 12 having an order of magnitude ranging from that of a typical length of a chemical bond to the scale length of the van der Waals potential. The latter characterizes the quantum limit of the Langevin capture rate, as discussed in section 2.2.2. Consequently, with the exception of $\text{H} + \text{H}_2$ in low ν levels, these threshold rate processes seem to be due to strong coupling in the short-range part of the collision, with a relatively high probability of quenching, and are limited by the threshold capture ability of the long-range potential. The variation among different species and ν levels shows that the dynamics is still influenced to a significant extent by the details of short-range aspects of the dynamics and could be affected by broad resonance features in some of the exit channels, as discussed in relation to Figure 36. The small quenching rates for $\text{H} + \text{H}_2$ at low ν are likely due to the quite weak forces associated with the weak binding of H with H_2 , with binding energy much less than the H_2 vibrational quantum.

3.2.2. Ultracold Molecule–Molecule Dynamics. In 2008 Quéméner et al.^{254,255} and Balakrishnan et al.²⁵⁶ studied vibrational and rotational relaxation in collisions of molecules of *para*- H_2 at ultralow energy. They identified an efficient mechanism of rovibrational energy transfer, which involves the best simultaneous conservation of internal energy and total rotational angular momentum. The inelastic cross sections are shown in Figure 42 for different initial vibrational and rotational quantum numbers. For collisions of $\text{H}_2(\nu_1 = \nu, j_1 = 0)$ with $\text{H}_2(\nu_2 = \nu', j_2 = 0)$ at temperatures of 1 μK , a high inelastic cross section is found, as shown by the black line, and the final distribution is largely dominated by the state $\text{H}_2(\nu_1 = \nu, j_1 = 2) + \text{H}(\nu_2 = \nu', j_2 = 0)$, where the first molecule has been rotationally excited and the second has been rotationally de-excited. This is the quasi-resonant rovibrational energy transfer. The final state satisfies the best conservation of internal energy and total rotational angular momentum $\Delta j_{12} = j_{12}^f - j_{12}^i = 0$ between two combined molecular states, where j_{12} is the total rotational angular momentum composed by the rotational angular momenta j_1 and j_2 of molecules 1 and 2, with j_{12}^i and j_{12}^f being its initial and final values before and after the collision, respectively. For collisions of $\text{H}_2(\nu_1 = \nu, j_1 = 0)$ with $\text{H}_2(\nu_2 = \nu', j_2 = 0)$, the cross sections are 3–6 orders of magnitude smaller depending on the initial vibrational states. There is no preferred final distribution because internal energy and total rotational angular momentum cannot have the best conservation simultaneously. The collisions of $\text{H}_2(\nu_1 = \nu, j_1 = 2)$ with $\text{H}_2(\nu_2 = \nu', j_2 = 0)$ are somewhat intermediate, 1 order of

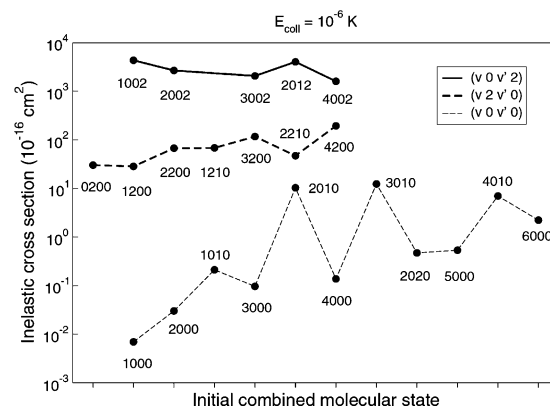


Figure 42. Inelastic cross sections as functions of the initial combined molecular state (CMS) for a collision energy of 10^{-6} K. Solid line ($v_1 = v, j_1 = 0, v_2 = v', j_2 = 2$); dashed bold line ($v_1 = v, j_1 = 2, v_2 = v', j_2 = 0$); dashed line ($v_1 = v, j_1 = 0, v_2 = v', j_2 = 0$). The cross section values are labeled by the corresponding initial CMSs, and the vibrational energy increases along the horizontal axis. Reprinted with permission from ref 254. Copyright 2008 American Physical Society.

magnitude smaller than the resonant process. This is explained by a good (but not the best) conservation of internal energy and rotational angular momentum. Similar work was also carried out by Fonseca dos Santos et al.²⁵⁷ in the study of *ortho*- $\text{H}_2 +$ *para*- H_2 molecular collisions.

4. PHYSICS AND CHEMISTRY WITH ULTRACOLD, ULTRACONTROLLED MOLECULES

Before 2010, there was still a gap between experimental measurements and theoretical calculations of molecular collisions, even if the orders of magnitude of the experimental and theoretical rate coefficients were correct. On one hand, experimentalists were dealing with heavy alkali molecules (Rb_2 , Cs_2 , and RbCs) in rather high vibrational states and with temperatures much larger than 1 μK . If the molecules were in low vibrational states, the exact quantum number was not specified. On the other hand, theoreticians performed full quantum dynamics calculations, using full potential energy surfaces, in specified and rather low vibrational states. Description of collisions of molecules in high vibrational states were restricted to the lighter systems Li_3 and Na_3 and required large basis sets, including states of the double continuum. Similar numerical calculations for heavier alkali systems, the ones used in the experiments, were not tractable.

A strong connection between experiment and theory was established in 2010, when experimental rate coefficients of ultracold ground-state KRb molecules in specified quantum states were measured and compared with theoretical predictions. This was made possible by the creation in 2008 of a dense sample of ground-state polar molecules in the ground electronic, vibrational, and rotational state,¹ as described in section 1.5. This achievement stimulated a large amount of theoretical and experimental work, which we will cover in the present section. Subsections 4.1 and 4.2 discuss the electric dipole moment and the hyperfine structure of the polar molecules. Subsection 4.3 discusses the long-range interaction of two polar molecules. Their chemical reactivity is discussed in the following subsection 4.4. Subsection 4.5 describes how polar molecules can be made in a specific hyperfine state using microwave transitions and how a superposition of two rotational states in well-defined hyperfine states can be studied.

Table 2. Computed Permanent Dipole Moments $|D|$ of the $X^1\Sigma^+$ State (in Debye) at Equilibrium Distances R_e^X , at the Minimum Distance R_d^X (in Atomic Units), and for the $\nu = 0$ Level of the X State^a

		this work					expt.			theoretical		
		$D(R_e^X)$	R_e^X	$D(R_d^X)$	R_d^X	$D(\nu = 0)$	D	R_e	ref	$D(R_e)$	R_e	ref
LiNa	A	0.561	5.43	0.630	6.85	0.566	0.45()		61	1.24	5.64	55
	B	0.554	5.42	0.633	6.89	0.556	0.47(3)	5.33	58	0.485	5.429	56
							0.463(10)	5.31	60	0.485	5.42	77
							0.45		64	0.487	5.47	45
LiK	A	3.558	6.21	3.807	7.50	3.565	3.510(5)		62	3.437	6.292	45
	B	3.533	6.21	3.792	7.49	3.555	3.45(2)	6.18	60	3.50	6.25	51
							3.87		64			
LiRb	A	4.168	6.52	4.442	7.78	4.165	4.05		64	4.13	6.52	51
	B	4.142	6.48	4.414	7.78	4.131						
LiCs	A	5.520	6.81	6.023	8.33	5.529	6.30		64	5.48	6.89	51
	B	5.512	6.82	5.998	8.31	5.524						
	C	5.462	6.81	5.970	8.33	5.478						
NaK	A	2.760	6.50	2.854	7.42	2.759	2.73(9)		63	3.6	6.9	53
	B	2.763	6.49	2.862	7.47	2.762	2.690(14)	6.55	60	2.735	6.36	45
							3.42		54	2.95	6.614	54
NaRb	A	3.304	6.84	3.413	7.75	3.306	3.10(3)	6.73	60	3.33	6.85	51
	B	3.301	6.84	3.413	7.76	3.301	3.51		64			
NaCs	A	4.613	7.20	4.821	8.26	4.607	4.75(20)	6.91	60	4.60	7.23	51
	B	4.661	7.20	4.864	8.26	4.660	4.75		78			
	C	4.580	7.20	4.793	8.29	4.579	5.86		64			
KRb	A	0.615	7.64	0.620	8.20	0.615	0.20		64	0.64	7.65	51
	B	0.589	7.64	0.605	8.49	0.589				0.71	7.7	57
KCs	A	1.906	8.01	1.957	8.87	1.906	2.58		64	1.92	8.05	51
	B	1.921	8.02	1.967	8.85	1.921						
	C	1.835	8.02	1.891	8.93	1.837						
RbCs	A	1.238	8.28	1.278	9.19	1.237	2.39		64	1.26	8.71	51
	B	1.278	8.30	1.309	9.12	1.280						
	C	1.205	8.30	1.240	9.19	1.204						

^aThe results are compared to available experimental and theoretical values. Reprinted with permission from ref 142. Copyright 2005 American Institute of Physics.

The ultracold molecular chemistry of indistinguishable and distinguishable fermions is the topic of subsection 4.6. Quantum statistics governs the chemistry at ultracold temperatures depending on whether the molecules are all in the same internal quantum state (*only p*-wave collisions) or not (*s*- and *p*-wave collisions). Subsection 4.7 describes the chemistry of the polar molecules in an electric field. The chemical rate coefficients show a strong dependence on the electric dipole–dipole interaction. The spatial anisotropy of the interaction is also probed in a rethermalization experiment with the polar molecular cloud. Subsection 4.8 deals with direct imaging of polar molecules inside the cloud. Subsection 4.9 shows the molecular quantum stereodynamics that occurs when the polar molecules are loaded into a one-dimensional optical lattice in the presence of electric field. A further step toward control of all degrees of freedom is taken when molecules are created in three-dimensional optical lattices, as explained in subsection 4.10. Finally, the last subsection 4.11 describes studies of three-body collisions of polar molecules.

4.1. Electric Dipole Moment of Polar Molecules

The electric dipole moment of a polar molecule is one of its most important properties. In 2005 Aymar and Dulieu¹⁴²

performed a systematic study of the electronic properties of the 10 heteronuclear alkali dimers, namely, LiNa, LiK, LiRb, LiCs, NaK, NaRb, NaCs, KRb, KCs, and RbCs, including the potential energy curves of the ground and excited states, as well as the permanent and transition dipole moments. The authors used a standard quantum chemistry approach based on pseudopotentials for atomic core representation, three different Gaussian basis sets (called A, B, and C by the authors), and effective terms for core polarization effects. They determined the molecular electric dipole moments of the different mixed alkali polar molecules in the singlet $X^1\Sigma^+$ and triplet $a^3\Sigma^+$ electronic states, as functions of the interatomic distances and vibrational level. We refer to the references of this paper for former studies of calculation and measurement of electric dipole moments of bialkali molecules. The electric dipole moment of molecules in the electronic singlet state is summarized in Table 2 from Aymar and Dulieu,¹⁴² which shows the permanent dipole moments at the equilibrium distance R_e at the minimum distance R_d , and for the $\nu = 0$ ground-state vibrational level, for the different Gaussian basis sets (A, B, and C) used in the quantum calculations. The smallest electric dipole moment was found for the LiNa molecule (~ 0.55 D), and the biggest one was found for the

LiCs molecule (~ 5.5 D). The results are also compared with pre-existing theoretical and experimental data. Similar studies were also performed later by Deiglmayr et al.²⁵⁸ and González-Férez et al.²⁵⁹

The electric dipole moment of a molecule is permanent only in the frame of the molecule, because eigenstates of molecular rotation have a vanishing laboratory-frame dipole moment. However, applying an external electric field results in an electric dipole moment in the laboratory frame by mixing rotational eigenstates of different spatial parity.²²⁴ At sufficiently large electric fields, the laboratory-frame dipole moment approaches its maximum value given by the permanent dipole moment. However, for weaker fields, the induced dipole moment can take any value between 0 and the full dipole moment. The ability of a molecule to respond to an electric field and acquire an electric dipole moment in the laboratory frame is called its polarizability. This is an important property, because in experiments the strength of an applied electric field is often limited to ~ 10 kV/cm, where the polar molecule may not realize its full dipole moment. Therefore, to get a sense of the polarizability of the molecules, a useful plot is the electric dipole moment of the alkali polar molecules as a function of the applied external electric field. This is presented in Figure 43

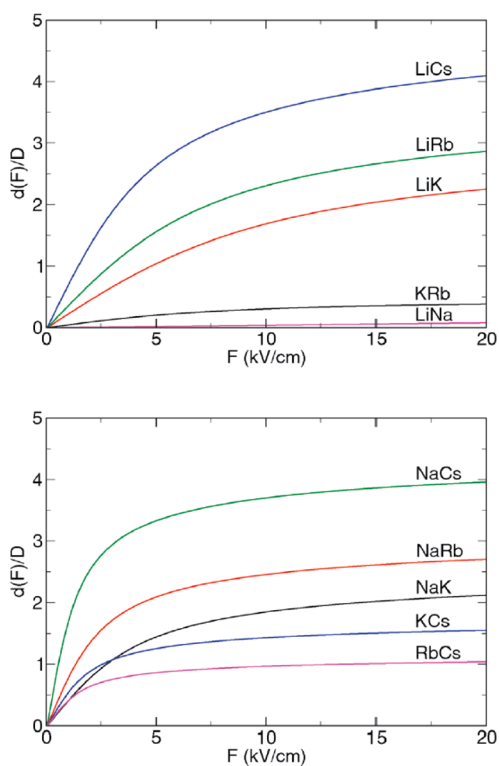


Figure 43. Dipole moment $d(F)/D$ versus F for the five reactive mixed alkali-metal species (upper panel) and for the five nonreactive mixed alkali-metal species (lower panel), where $D = 0.3934$ au = 3.336×10^{-30} C m. Reprinted with permission from ref 75. Copyright 2011 Royal Society of Chemistry.

taken from Julienne et al.⁷⁵ One can see that different molecules have different polarizabilities. To give an example, polar molecules like NaCs, NaRb, KCs, and RbCs have a rather strong polarizability since; at a typical experimental electric field of 5 kV/cm, they are almost fully polarized, reaching an induced dipole moment close to their permanent value. The remaining molecules have a weaker polarizability because at 5

kV/cm they are only partially polarized. From an experimental point of view, molecules with a strong polarizability obviously have an advantage, because strong dipolar effects will be “turned on” quickly.

4.2. Hyperfine Structure of Polar Molecules

Other important properties of the polar molecules were computed by Aldegunde et al.²⁶⁰ and Ran et al.²⁶¹ This is important when external magnetic and electric fields are present. The full Hamiltonian can be separated into different parts. Apart from the electronic, vibrational, rotational, and electronic spin structure, molecules can have an internal hyperfine structure Hamiltonian H_{hf} , and under external magnetic and electric fields, the molecules can have an additional Zeeman H_z and Stark H_s interaction Hamiltonian. The hyperfine Hamiltonian for a molecule AB can be described by

$$H_{hf} = \vec{V}_A \cdot \vec{Q}_A + \vec{V}_B \cdot \vec{Q}_B + c_1 \vec{N} \cdot \vec{I}_A + c_2 \vec{N} \cdot \vec{I}_B + c_3 \vec{I}_A \cdot \vec{T} \cdot \vec{I}_B + c_4 \vec{I}_A \cdot \vec{I}_B \quad (34)$$

$\vec{V}_A \cdot \vec{Q}_A$ ($\vec{V}_B \cdot \vec{Q}_B$) represents the interaction of the nuclear quadrupole moment \vec{Q}_A (\vec{Q}_B) of nucleus A (B) of the molecule with the electric field gradient \vec{V}_A (\vec{Q}_B) at nucleus A (B) created by the surrounding charges. The associated coupling constant is denoted $(eqQ)_A$ ($(eqQ)_B$).²³⁴ The interaction between the nuclear magnetic moment of nucleus \vec{I}_A (\vec{I}_B) and the magnetic field created by the rotation \vec{N} of the molecule is $c_1 \vec{N} \cdot \vec{I}_A$ ($c_2 \vec{N} \cdot \vec{I}_B$) with the spin-rotation coupling constant c_1 (c_2).²³⁴ The terms $c_3 \vec{I}_A \cdot \vec{T} \cdot \vec{I}_B$ and $c_4 \vec{I}_A \cdot \vec{I}_B$ represents the tensor and scalar interactions between the nuclear dipole moments \vec{I}_A and \vec{I}_B , with spin–spin coupling constants c_3 and c_4 , respectively.²³⁴ The Zeeman Hamiltonian is given by

$$H_Z = -g_r \mu_n \vec{N} \cdot \vec{B} - g_l \mu_n (1 - \sigma_A) \vec{I}_A \cdot \vec{B} - g_2 \mu_n (1 - \sigma_B) \vec{I}_B \cdot \vec{B} \quad (35)$$

The term $-g_r \mu_n \vec{N} \cdot \vec{B}$ comes from the interaction between the magnetic field \vec{B} and the magnetic moment $g_r \mu_n \vec{N}$ produced by the molecular rotation. The term $-g_l \mu_n (1 - \sigma_A) \vec{I}_A \cdot \vec{B}$ ($-g_2 \mu_n (1 - \sigma_B) \vec{I}_B \cdot \vec{B}$) is the interaction between the magnetic field \vec{B} and the nuclear magnetic moment $g_l \mu_n \vec{I}_A$ ($g_2 \mu_n \vec{I}_B$) produced by the nuclear spin of the atom A (B), including an isotropic shielding term $(1 - \sigma_A)$ ($1 - \sigma_B$).²³⁴ Finally, the Stark Hamiltonian is given by

$$H_S = -\vec{\mu} \cdot \vec{E} \quad (36)$$

which represents the interaction between the electric dipole moment $\vec{\mu}$ of the polar molecule AB with the electric field \vec{E} . Using a density-functional theory with different density functionals adapted to the evaluation of each specific interaction, the authors computed the coupling constants for the KRb and RbCs polar molecules²⁶⁰ and for the LiCs molecule.²⁶¹ The constants for KRb are reported in Table 3. Understanding the internal structure of the molecules is important for spectroscopy and manipulation of polar molecules with microwave fields,^{113,114,261} as discussed later in subsection 4.5. Aldegunde and Hutson performed a similar calculation for homonuclear molecules of Li_2 , Na_2 , K_2 , Rb_2 , and Cs_2 .²⁶²

4.3. Long-Range Interaction of Polar Molecules

At typical ultracold temperatures and in the absence of an electric field, the ground-state molecules are only sensitive to

Table 3. Nuclear Properties and Coupling Constants for the Different Isotopic Species of the KRb Molecule^a

	³⁹ K ⁸⁵ Rb	³⁹ K ⁸⁷ Rb	⁴⁰ K ⁸⁵ Rb	⁴⁰ K ⁸⁷ Rb	⁴¹ K ⁸⁵ Rb	⁴¹ K ⁸⁷ Rb
I_K	3/2	3/2	4	4	3/2	3/2
I_{Rb}	5/2	3/2	5/2	3/2	5/2	3/2
g_K	0.261	0.261	-0.324	-0.324	0.143	0.143
g_{Rb}	0.541	1.834	0.541	1.834	0.541	1.834
B_v (GHz)	1.142	1.134	1.123	1.114	1.104	1.096
$(eQq)_K$ (MHz)	-0.245	-0.245	0.306	0.306	-0.298	-0.298
$(eQq)_{Rb}$ (MHz)	-3.142	-1.520	-3.142	-1.520	-3.142	-1.520
σ_K (ppm)	1321	1321	1321	1321	1321	1321
σ_{Rb} (ppm)	3469	3469	3469	3469	3469	3469
c_K (Hz)	19.9	19.8	-24.2	-24.1	10.5	10.4
c_{Rb} (Hz)	127.0	427.5	124.8	420.1	122.8	413.1
c_3 (Hz)	11.5	38.9	-14.2	-48.2	6.3	21.3
c_4 (Hz)	482.5	1635.7	-599.0	-2030.4	264.3	896.2
g_r	0.0144	0.0142	0.0141	0.0140	0.0139	0.0138
μ (D)	0.76	0.76	0.76	0.76	0.76	0.76

^aReprinted with permission from ref 260. Copyright 2008 American Physical Society.

the most long-range molecule–molecule interaction, the van der Waals interaction $-|C_6|/r^6$. Although molecules have quadrupole moments, we note here that the anisotropic quadrupole–quadrupole interaction has no diagonal contribution for an *s*-wave collision nor for an interaction involving a rotationless ($j = 0$) molecular state. In the general case, the C_6/R^5 quadrupole–quadrupole interaction would need to be taken into account, where it may be significant at shorter range than the van der Waals length. The calculation of the C_6 coefficient comes basically from a second-order perturbation theory calculation and can be qualitatively understood by the second-order perturbation formula of the dispersion energy.^{234,235} The dispersion energy between two particles *A* and *B*, in given states *n* and *m*, and energies E_n^A and E_m^B , is

$$E_{\text{disp}} = \sum_{n', m' \neq n, m} \frac{\langle \psi_n^A \psi_m^B | V_{\text{dd}} | \psi_{n'}^A \psi_{m'}^B \rangle \langle \psi_{n'}^A \psi_{m'}^B | V_{\text{dd}} | \psi_n^A \psi_m^B \rangle}{(E_n^A + E_m^B) - (E_{n'}^A + E_{m'}^B)} \propto -\frac{C_6}{r^6} \quad (37)$$

where V_{dd} is the dipole–dipole interaction between the two molecules separated by a distance *r* and is proportional to $1/r^3$. Note that if both molecules are in the ground state $m = n = 0$, the dispersion energy will always be negative, making the van der Waals interaction attractive. Also, since the V_{dd} behaves as r^{-3} , the van der Waals interaction behaves as r^{-6} . In other words, to determine the dispersion energy between two molecules in given states *m*, *n* (for example, the ground state $n = m = 0$), one has to compute all the dipole transition elements $\langle \psi_n^A \psi_m^B | V_{\text{dd}} | \psi_{n'}^A \psi_{m'}^B \rangle$ for all the combined eigenstate wave functions $\psi_n^A \psi_m^B$ of molecules *A*, *B*, including the rotational, vibrational, and electronic wave functions. It is useful to separate the C_6 coefficient into two main contributions: a contribution from dipole transitions elements between molecular quantum states of the same electronic potential, for example, the ground singlet electronic state $X^1\Sigma^+$ for alkali polar molecules, and a contribution from dipole transition elements between molecular quantum states of different electronic states potential, say, for example, the triplet electronic state $a^3\Sigma^+$ or other excited states (Π , Δ).

Kotochigova⁷⁶ calculated the isotropic C_6 coefficient of the KRb–KRb and RbCs–RbCs pairs and distinguished the contribution from the electronic ground state and from the excited ones. The isotropic C_6 coefficient as a function of the vibrational state ν of the $J = 0$ (black curve) and the $J = 1$ (red curve) is represented in Figure 44. The left panel corresponds to RbCs–RbCs, and the right panel corresponds to KRb–KRb. The blue curves represent the contribution of the C_6 coefficient for the $J = 0$ state within the electronic ground state $X^1\Sigma^+$. There is a striking difference between both systems for $J = 0$ and small ν . The C_6 coefficient is an order of magnitude bigger for RbCs–RbCs than for KRb–KRb. This is due mainly to the electronic ground-state contribution and can be approximated to $C_6 \approx d^4/(6B_v)$.²⁶³ As the permanent dipole moment *d* of RbCs is bigger than that of KRb and the rotational constant B_v is smaller, then the C_6 coefficient is bigger for RbCs than for KRb. This contribution is even bigger than its electronic excited-states contribution (see the difference between the blue and black curves on the left panel of Figure 44). This does not apply for $J = 1$ anymore, because the contribution of the $J = 2$ state will be negative and the one for $J = 0$ would be positive, approximately canceling each other in eq 37. Thus C_6 is mainly dominated by the electronic excited-states contribution. The ground-state contribution decreases for larger ν because the

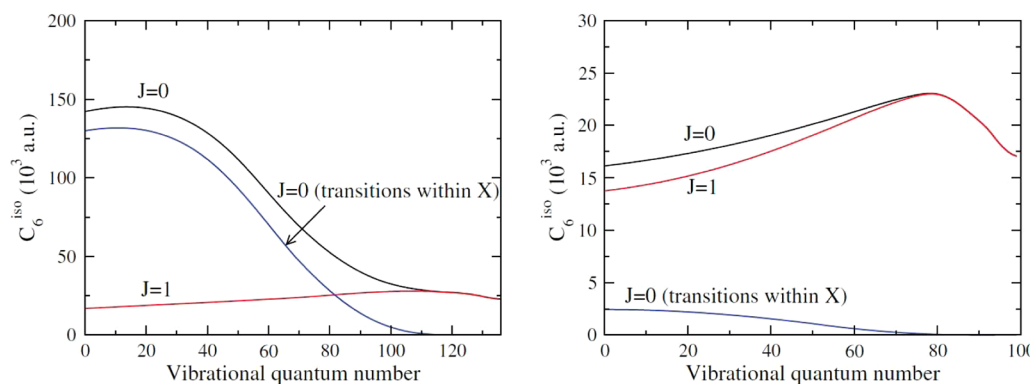


Figure 44. Isotropic molecule–molecule van der Waals coefficients in atomic units for the $J = 0$ and 1 rotational levels of the $X^1\Sigma^+$ ground state of RbCs (left panel) and KRb (right panel) as a function of vibrational quantum number. The curves labeled “ $J = 0$ (transitions within X)” correspond to an isotropic van der Waals coefficient where only the contributions from transitions to rovibrational levels of the $X^1\Sigma^+$ potential are included. Reprinted with permission from ref 76. Copyright 2010 Institute of Physics and the Deutsche Physikalische Gesellschaft.

permanent dipole moment decreases with ν so that the electronic excited-states contribution dominates. Kotochigova also computed the anisotropic C_6 coefficients.

Table 4 shows that these coefficients are smaller than the isotropic ones. The C_6 coefficients for atom–molecule pairs of K–KRb, Rb–KRb, Rb–RbCs, and Cs–RbCs are also reported in Table 4.

Table 4. van der Waals Coefficients in Atomic Units for the Interaction between Two Molecules in the $\nu = 0, J = 0$ and 1 Rovibrational Levels of the $X^1\Sigma^+$ Potential As Well As between Such a Molecule and an Atom^a

system	C_6^{iso}		$C_{6,20}^{\text{aniso}}$		$C_{6,22}^{\text{aniso}}$	
	$J = 0$	$J = 1$	$(J,M) = (1, 0)$	$(J,M) = (1, \pm 1)$	$(J,M) = (1, 0)$	$(J,M) = (1, \pm 1)$
KRb + KRb	16 133	13 749	2 569	-1 285	-43	-11
RbCs + RbCs	142 129	16 865	1 443	-2 886	-630	-157
KRb + Rb	7 696	7 686	1 428	-714		
KRb + K	6 905	6 896	1 278	-639		
RbCs + Rb	7 326	7 274	798	-399		
RbCs + Cs	8 479	8 416	929	-465		

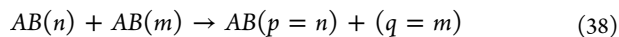
^aThe uncertainty in the coefficients is 5%. Reprinted with permission from ref 76. Copyright 2010 Institute of Physics and the Deutsche Physikalische Gesellschaft.

Zemke et al.²⁶⁴ also computed the C_6 coefficients of the polar diatom pair NaK–NaK and found a value of $C_6 = 6\,493$ au. This value is obtained from the contribution of the two dominant allowed excited electronic states $A^1\Sigma^+$ and $B^1\Pi$.

Quéméner et al.¹⁶² calculated the C_6 coefficients for other pairs of alkali molecules such as LiNa–LiNa, LiK–LiK, LiRb–LiRb, and LiCs–LiCs. Table 5 summarizes the values for ground-state $J = 0$ molecules. Similar conclusions hold for these polar molecules. As LiNa has a small permanent dipole moment, the C_6 contribution comes mainly from the electronic excited states. For LiK, LiRb, and LiCs, the dipoles are larger and the main part comes from the electronic ground state, especially from the transition to the first level $J = 1$ as explained above for RbCs. When an electric field is present, Julianne et al.⁷⁵ evaluated the field-dependent terms in eq 37 to obtain the field-dependence of the C_6 coefficient. The coefficient for RbCs decreases strongly with increasing field strength, due to the changed matrix elements and larger energy denominators using the field-mixed states. Interestingly, they found only a small effect on the universal Langevin threshold rate constants for highly reactive molecules, because the long-range potential becomes dominated by the first-order dipolar interaction, not the van der Waals potential, as field increases.

4.4. Chemical Reactivity of Polar Molecules

In a chemical point of view, different types of outcomes can generally happen during a collision of two molecules AB in initial states n and m , respectively (using similar notation from section 1.1):



for an elastic collision,

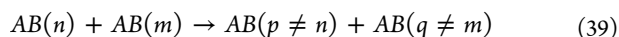
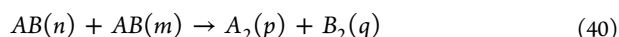


Table 5. van der Waals C_6 Coefficients in Atomic Units for the Interaction between the Two Molecules in the $\nu = 0, J = 0$ Rovibrational Levels of the $X^1\Sigma^+$ Potential and Other Molecular Characteristics Used to Calculate C_6 ; $\alpha_{\text{exc}}(0)$ is the Isotropic Static Polarizability Due to Transitions to Electronically Excited Potentials; B and d_p Are the Rotational Constant and Electric Permanent Dipole Moment, Respectively^a

$\alpha_{\text{exc}}(0)$ (a.u.)	$B/\hbar c$ (cm ⁻¹)	d_p (D)	$C_6^{(\text{exe})}$ (a.u.)	$C_6^{(\text{inf})}$ (a.u.)	$C_6^{(\text{gr})}$ (a.u.)	C_6 (a.u.)
LiNa + LiNa						
237.8	0.377	0.557 ^b	3 673	23	222	3 917
		0.531 ^c	3 673	21	186	3 880
LiK + LiK						
324.9	0.258	3.556 ^b	6 269	1 271	542 000	550 000
		3.513 ^c	6 269	1 241	517 000	524 000
LiRb + LiRb						
346.2	0.220	4.130 ^b	6 323	1 829	1 160 000	1 170 000
		4.046 ^c	6 323	1 754	1 070 000	1 070 000
LiCs + LiCs						
389.7	0.188	5.478 ^b	7 712	3 620	4 200 000	4 210 000
		5.355 ^c	7 712	3 460	3 830 000	3 840 000

^aThese three properties are evaluated at the equilibrium separation R_e . The value of B is from ref 258. The next three columns are the excited-state, interference, and ground-state contributions to the total C_6 , shown in the last column. Reprinted with permission from ref 162. Copyright 2011 American Physical Society. ^bAymar and Dulieu.¹⁴² ^cQuéméner et al.¹⁶²

for an inelastic collision, and



for a reactive collision. Elastic and inelastic collisions are the collisions for which the products have the same chemical identity from the reactants. For an elastic collision, the internal states of the products are the same as the ones of the reactants, while for inelastic collisions, the internal states of the products are different than the ones of the reactants. Reactive collisions are the collisions for which the products are chemically different than the reactants.

The chemical reactivity $AB + AB \rightarrow A_2 + B_2$ is an important characteristic of polar molecules. Chemical reactivity can be an advantage to study molecular ultracold chemistry but can be a drawback for the formation of stable, long-lived gases of polar molecules. To conserve the total energy of the ultracold initial reactants with an ultralow initial kinetic energy, an exothermic chemical reaction will result in a large release of final kinetic energy of the products, overcoming any weak trapping potential that confines the molecules. For similar reasons, inelastic collisions are also a drawback for long-lived polar molecule gases, again resulting in loss of molecules. In contrast, if molecules are in their absolute internal ground state and are not chemically reactive, only elastic collisions are allowed, and the final kinetic energy should remain the same as the initial kinetic energy. If the molecules are ultracold, the initial and final kinetic energies are therefore smaller than the confining trap depth, and the molecules do not have enough energy to escape. The molecules are not lost. Thus, chemical reactivity of polar molecules has been the topic of much work.

In 2008 Tscherbul et al.²⁶⁵ explored the chemical reactivity of RbCs molecules. They showed using electronic-structure calculations that chemical reaction $RbCs + RbCs \rightarrow Rb + Cs$ for ground states RbCs is not allowed at ultralow energy. They

also found that, despite the potential being sensitive to the level of approximation employed in the calculation, this reaction (and the inverse one) is barrierless. The minimum path is presented in Figure 45, where $\Delta R \rightarrow -\infty$ corresponds to the

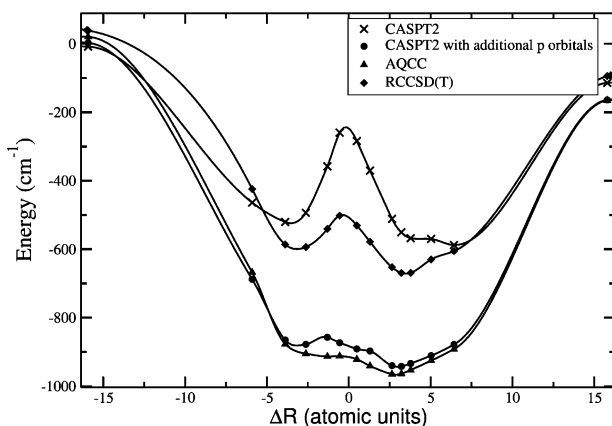


Figure 45. Potential energy of the RbCs–RbCs reaction complex from an optimized geometry calculation. $\Delta R = (R_{\text{Rb–Rb}} + R_{\text{Cs–Cs}})/2 - (R_{\text{Rb–Cs}} + R'_{\text{Rb–Cs}})/2$, where $R_{\text{A–B}}$ is the separation between the atoms A and B. Reprinted with permission from ref 265. Copyright 2008 American Physical Society.

energy of two separated Rb_2 and Cs_2 molecules and $\Delta R \rightarrow +\infty$ corresponds to the energy of two separated RbCs molecules. They also found that the atom–molecule chemical reaction $\text{Rb} + \text{RbCs} \rightarrow \text{Rb}_2 + \text{Cs}$ is allowed at ultracold energies for ground states RbCs, but not the reverse one, and that this reaction is also barrierless.

In 2010 Źuchowski and Hutson,²⁶⁶ Byrd et al.,²⁶⁷ and Meyer and Bohn²⁶⁸ investigated the chemical reactivity of different polar molecules of experimental interest, performing ab initio electronic-structure calculations on the lowest doublet state potential energy surfaces of A_2B systems, with $A, B = \text{Li}, \text{Na}, \text{K}, \text{Rb}$, and Cs . Their results are summarized in the following paragraph. Table 6, taken from ref 266, gives the energy

Table 6. Energy Changes ΔE_2 for the Reactions $2AB \rightarrow A_2 + B_2$ (in cm^{-1})^a

	Na	K	Rb	Cs
Li	-328(2)	-533.9(3)	-618(200)	-415.38(2)
Na		74.3(3)	45.5(5)	236.75(20)
K			-8.7(9)	37.81(13)
Rb				29.1(1.5)

^aThe quantities in parentheses are uncertainties in the final digit(s). Reprinted with permission from ref 266. Copyright 2010 American Physical Society.

changes ΔE_2 for the reactions $AB + AB \rightarrow A_2 + B_2$. On the basis of molecular dissociation energies available in the literature, it was found that the dissociation energy of $AB + AB$ is bigger than the dissociation energy of $A_2 + B_2$ for the molecules $AB = \text{KRB}$, LiNa , LiK , LiRb , and LiCs (hereafter referred to as category I) because ΔE_2 is negative (exoergic). On the other hand, the dissociation energy of $AB + AB$ is lower than the one for $A_2 + B_2$ for the molecules $AB = \text{NaK}$, NaRb , NaCs , KCs , and RbCs (hereafter referred to as category II) because ΔE_2 is positive (endoergic). Chemical reaction is always energetically allowed for molecules in category I but only allowed for

molecules in category II if they are in an excited state (such as rotational, vibrational, or electronic) with sufficient energy to be exoergic. Table 7, taken from ref 266, presents the energy

Table 7. Energy Changes ΔE_3 for the Reactions $2AB \rightarrow A_2B + B$, Obtained by Combining the Trimer Results with Dimer Dissociation Energies Obtained with the Same Method^a

	ΔE_3 (cm^{-1})				
	Li	Na	K	Rb	Cs
Li	3759	4145	3979	3910	3660
Na	2539	3843	3281	3287	2962
K	1639	2611	2460	2444	2264
Rb	1393	2421	2266	2295	2101
Cs	965	1974	1943	1981	1958

^aThe columns correspond to different A atoms while the lines correspond to different B atoms. Reprinted with permission from ref 266. Copyright 2010 American Physical Society.

changes ΔE_3 for the reactions $AB + AB \rightarrow A_2B + B$. The dissociation energies computed for the different possible trimers are positive and indicate that the dissociation energy $AB + AB$ is always lower than the one for $A_2B + B$. Therefore these ultracold ground-state polar molecules will not produce trimers in a chemical reaction. Figure 46 shows the minimum

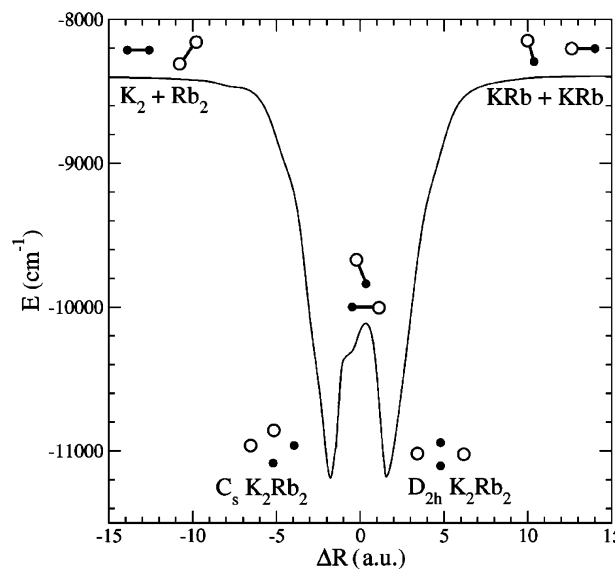


Figure 46. Minimum energy path connecting the KRb + KRb and $\text{K}_2 + \text{Rb}_2$ dissociation limits. Included are schematic geometric points of interest, where open and solid circles represent rubidium and potassium atoms, respectively. Reprinted with permission from ref 267. Copyright 2010 American Physical Society.

energy path from ref 267 as a function of a reaction coordinate $\Delta R = (R_{\text{K–K}} + R_{\text{Rb–Rb}})/2 - (R_{\text{K–Rb}} + R'_{\text{K–Rb}})/2$. It shows how the two dissociation limits are connected with the two minima for the K_2Rb_2 collision complex. The dissociation limit $\text{K}_2 + \text{Rb}_2$ connects with the K_2Rb_2 minimum with C_s geometry whereas the KRb + KRb limit connects with the K_2Rb_2 minimum with D_{2h} geometry. Both dissociation limits are barrierless. The authors found a transition state of 1167.3 cm^{-1} above the D_{2h} geometry in the tetramer region. Figure 47, taken from ref 267, summarizes the different energetics involved in the K_2Rb_2 system. Starting with two KRb molecules, the

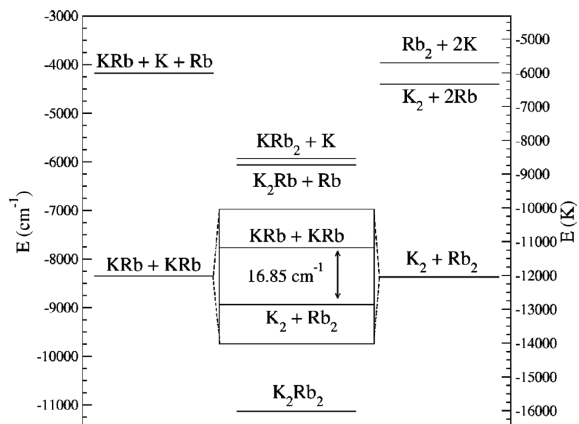


Figure 47. Schematic energy-level diagram for fragment and structure energies involving KRB with KRB and separated atoms. Inset shows the small difference between the KRb + KRb and K₂ + Rb₂ asymptotes. Reprinted with permission from ref 267. Copyright 2010 American Physical Society.

homonuclear diatom + homonuclear diatom and the tetramer configurations are exoergic, while the other configurations, atom + trimer and dimer + atom + atom, are endoergic. Finally, Figure 48, taken from ref 268, shows a typical contour plot of the two potential energy surfaces ²A₁ and ²B₂ of the trimer K₂Rb.

The lowest quartet state of A₂B (A, B = Li, Na, K, Rb, and Cs) has also been investigated by Soldán.^{269,270} This electronic state is the one for a spin-polarized alkali atom A and a triplet ³Σ⁺ molecule AB. This is also important to investigate because polar molecules in the electronic triplet state have also been formed in their ground rovibrational state.¹ Soldán found that the configurations atom + dimer → trimer and dimer + dimer → trimer + atom are always exoergic, even for ground-state molecules, and that the entrance channel of the atom + dimer → trimer configuration is always barrierless.

Meyer and Bohn²⁷¹ have also investigated the chemical path of two SrF molecules. Shuman et al.⁹¹ have cooled the absolute ground state of these molecules down to cold temperatures of $T \approx 300 \mu\text{K}$, using direct cooling methods with lasers. Such molecules with an open-shell ²Σ electronic state are also of experimental interest because they have both an electric dipole moment, ~1.4 D for SrF, and a magnetic dipole moment. Consequently, they can be manipulated with both electric and magnetic fields. This property is also shared by other polar molecules, such as OH and others,^{9,272} RbSr,^{273,274} YbRb,¹³⁹ or LiYb.^{136–138,275–278} In their study, Meyer and Bohn²⁷¹ explored the chemical reactivity of ground-state SrF molecules. They found that the reactions SrF + SrF → Sr₂ + F₂ and SrF + SrF → Sr₂F + F are not allowed at ultracold energies. Only the chemical reaction SrF + SrF → SrF₂ + Sr is allowed. When so, only the singlet state of the trimer SrF₂ is possible. This is illustrated in Figure 49 where the energy threshold of the SrF₂ trimer + Sr atom is below the one of two SrF dimers. The minimum energy path is also depicted in this figure and indicates that the chemical reaction is barrierless. The authors also showed that the chemical reaction proceeds with one SrF molecule “handing off” a fluorine atom to the other molecule, reminiscent of an abstraction reaction.

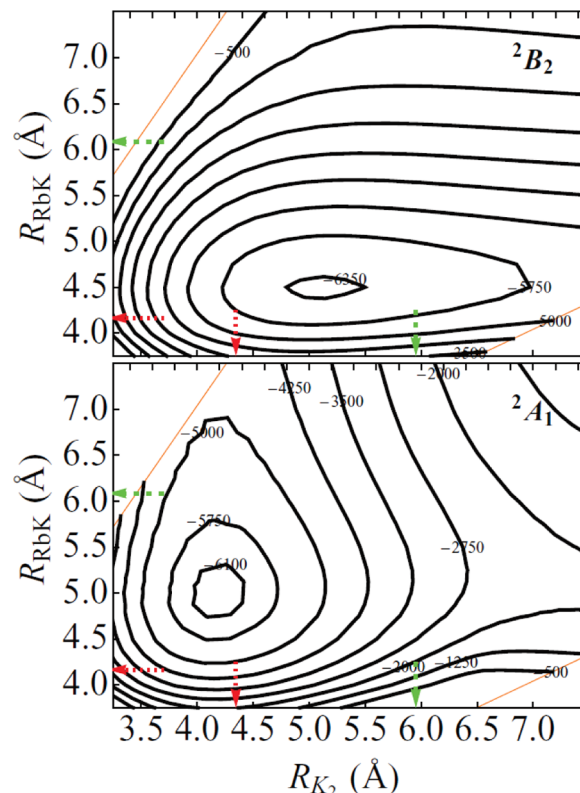


Figure 48. Contour plots for the doublet ground state PESs of K₂Rb versus interatomic spacings in an isosceles triangle geometry. The top panel shows the ²B₂ surface while the bottom panel shows the ²A₁ surface. Contours are labeled in increments of 750 cm⁻¹ from -5750 to -500 with an additional contour near the minimum of each surface. The small-dashed red arrows on the vertical (horizontal) axes near 4 Å represent the singlet bond lengths of RbK (K₂). The medium-dashed green arrows on the vertical (horizontal) axes near 6 Å represent the triplet bond lengths of RbK (K₂). Reprinted with permission from ref 268. Copyright 2010 American Physical Society.

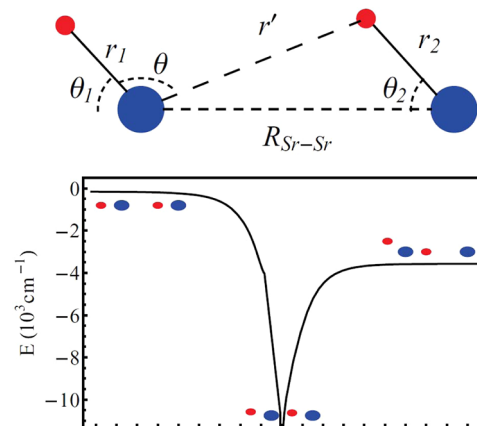


Figure 49. Top portion of the figure describes the geometry of two SrF molecules; r_1 , r_2 , θ_1 , and θ_2 are optimized so as to produce the minimal energy for a fixed $R_{\text{Sr}-\text{Sr}}$. The left-hand side of the lower panel describes the approach of two dipole objects. The horizontal axis represents $\Delta = r_2 - r'$ in Å. On the right-hand side, the approach is more van der Waals-like where the polar SrF₂ polarizes the Sr atom. The approach to the transition state near $\Delta = 0$ Å is very nearly linear up to the point of F capture. Then θ_1 and θ_2 rotate to form a complex that contains a slightly distorted SrF₂ configuration. Reprinted with permission from ref 271. Copyright 2011 American Physical Society.

4.5. Beyond Rovibronic Control: Hyperfine State Control and Quantum Superposition

In 2008, molecules were formed in their ground rovibronic state,¹ but nothing was known about their hyperfine quantum state. The formation of ground rovibronic KRb molecules was done in the presence of a magnetic field, because of the magneto-association via a Fano-Feshbach resonance at a magnetic field B of 546 G. For such a field, the Zeeman interaction of the nuclear spins of the K and Rb atoms with the magnetic field can be of the order of hundreds of kHz, or alternatively on the order of μK ; see Figure 12. This splitting is large compared to the molecular gas temperature of hundreds of nK. In the ground rotational state $N = 0$ of the KRb molecules, the spin eigenstates split into 36 hyperfine states. Therefore, the KRb molecules can be formed in any of these hyperfine states during their creation, and not necessarily in their ground hyperfine state. However, it is crucial that all the molecules are formed in the same internal state to achieve a degenerate quantum gas.

In 2010, Ospelkaus et al.¹¹⁴ demonstrated a scheme to control any hyperfine state of ground rovibronic molecules, using two-photon microwave transitions. In the presence of a magnetic field, the molecular Hamiltonian²⁷⁹ has a hyperfine term (eq 34), a Zeeman term (eq 35), and a Stark term (eq 36). If only the Zeeman term were taken into account (no hyperfine term), m_N, m_K, m_{Rb} would be good quantum numbers and the eigenstates will be classified according to these numbers as sketched in Figure 50a. Microwave transitions will only

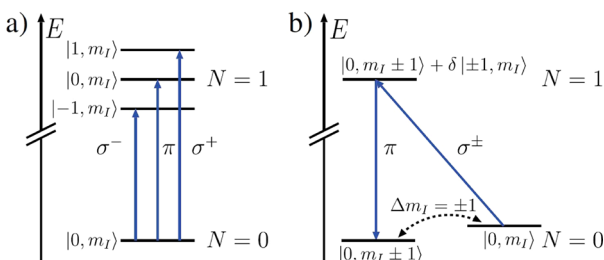


Figure 50. (a) Electric-dipole transitions between the rotational ground state $N = 0$ and the first rotationally excited state $N = 1$. To first order, electric-dipole transitions will keep the hyperfine state unchanged $\Delta m_I = 0$. (b) The interaction between the nuclear electric-quadrupole moment of $^{40}\text{K}/^{87}\text{Rb}$ and the electric-field gradient of the electronic cloud mixes quantum states with different nuclear spin quantum number $\Delta m_I^{\text{K/Rb}}$ in $N = 1$. This allows the implementation of a two-photon scheme to transfer molecules between different hyperfine states within the rovibrational ground state ($\Delta m_I^{\text{K/Rb}} = \pm 1$). Reprinted with permission from ref 114. Copyright 2010 American Physical Society.

populate states with same values of m_K and m_{Rb} with values $\Delta m_N = 0, \pm 1$ depending on the π, σ^\pm polarization of the microwave field. However, the hyperfine term cannot be neglected. For example, it turns out that, for KRb molecules, the electric quadrupole interaction is strong enough²⁶⁰ to create some admixture δ , between states of different projection of rotational m_N and nuclear m_K, m_{Rb} quantum numbers, within a rotational manifold ($N = 1$, for example), as illustrated in Figure 50b. Then a microwave transition σ^\pm can be driven from a state $|0, m_I\rangle$ in $N = 0$ to an admixed state $|0, m_I \pm 1\rangle + \delta |1, m_I\rangle$ in $N = 1$ because both states share a component with same value of m_I . Here m_I can represent either m_K or m_{Rb} and the ket is abbreviated to $|m_N, m_K \text{ or } m_{\text{Rb}}\rangle$ for a given N and a spectator

m_{Rb} or K . Finally, a π microwave transition can drive the state $|0, m_I \pm 1\rangle + \delta |1, m_I\rangle$ in $N = 1$ to a $|0, m_I \pm 1\rangle$ in $N = 0$ because of the state with same $m_I \pm 1$ number. With this procedure, Ospelkaus et al. measured the Rabi oscillations between different hyperfine states, as presented in Figure 51. The Rabi

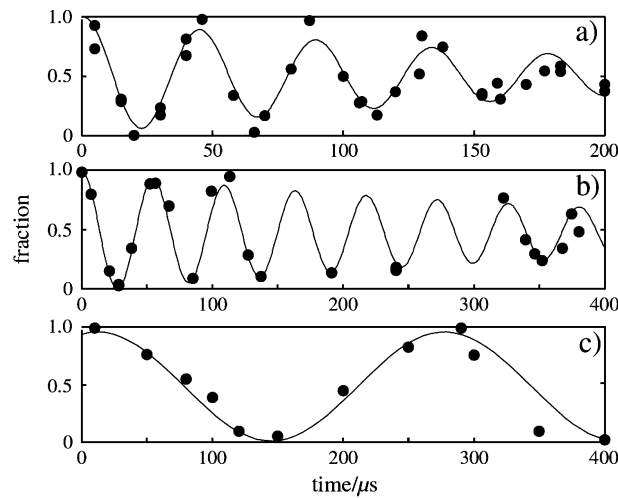


Figure 51. Rabi oscillations on a (a) hyperfine preserving microwave transition $|0, 0, -4, 1/2\rangle \rightarrow |1, 1, -4, 1/2\rangle$; (b) Rb hyperfine changing transition $|0, 0, -4, 1/2\rangle \rightarrow |1, 0, -4, 3/2\rangle + \delta |1, 1, -4, 1/2\rangle$; (c) K hyperfine changing transition $|0, 0, -4, 1/2\rangle \rightarrow |1, 0, -3, 1/2\rangle + \delta |1, 1, -4, 1/2\rangle$. Note the different time axis in panel (a). The microwave power was reduced by a factor of 4 for the data in (a), resulting in an effective decrease of the Rabi frequency by a factor of 2. Reprinted with permission from ref 114. Copyright 2010 American Physical Society.

oscillations are respectively from the state $|0, 0, -4, 1/2\rangle$ to $|1, 1, -4, 1/2\rangle$ in panel (a) (spin-preserving transition), from the state $|0, 0, -4, 1/2\rangle$ to $|1, 0, -4, 3/2\rangle + \delta |1, 1, -4, 1/2\rangle$ in panel (b) (Rb hyperfine changing transition), and from the state $|0, 0, -4, 1/2\rangle$ to $|1, 0, -3, 1/2\rangle + \delta |1, 1, -4, 1/2\rangle$ in panel (c) (K hyperfine changing transition). Here the kets are now abbreviated as $|N, m_N, m_K, m_{\text{Rb}}\rangle$. The Rabi oscillations frequency decreases from a to c and is consistent with the decreasing strength of the transitions.¹¹⁴ Using this scheme and another microwave transition from $N = 1$ to $N = 0$ as sketched in Figure 50b, the authors demonstrated the preparation in the lowest hyperfine state $|1, 0, -4, 3/2\rangle$ at a magnetic field of $B = 546$ G. Finally, they measured with this scheme the rotational transition frequencies $N = 0 \rightarrow N = 1$ for different hyperfine states $|i\rangle, |j\rangle$. Three molecular parameters, the rotational constant B_e and the electric-quadrupole moments eqQ_K, eqQ_{Rb} , were fitted to compare with the theoretical calculation of the spectrum. The best reduced χ^2 -squared fit was found for $B_e = 1.113950(5)$ GHz, $eqQ_K = 0.45(6)$ MHz, and $eqQ_{\text{Rb}} = -1.41(4)$ MHz. The results were consistent with the magnitudes of $B_e = 1.1139$ GHz found in ref 1 for the rotational constant and $eqQ_K = 0.306$ MHz and $eqQ_{\text{Rb}} = -1.520$ MHz found in ref 260 for the electric quadrupole constant. Concerning the rotational constant, Aikawa et al.,¹²⁰ in a study appearing in 2010, formed polar molecules of bosonic $^{41}\text{K}^{87}\text{Rb}$ in their ground rovibronic state. They determined its rotational constant to be $B_e = 1.0954(1)$ GHz. This value was in very good agreement with the fermion-to-boson mass-rescaled rotational constant $B_e = 1.095362(5)$ GHz determined from the value measured by Ospelkaus et al.¹¹⁴

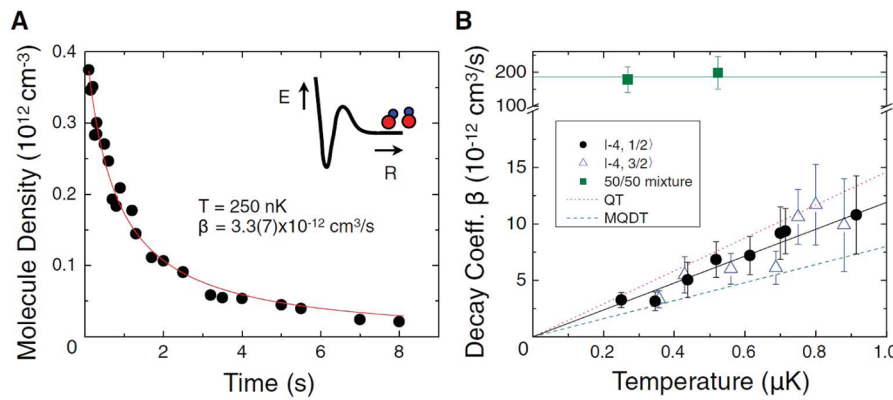


Figure 52. Inelastic collisions between spin-polarized (indistinguishable) or different spin-state (distinguishable) fermionic molecules in the rovibronic ground state of $^{40}\text{K}^{87}\text{Rb}$. (A) Sample data showing the time dependence of the molecule number density. (B) Loss rate coefficient versus temperature. The dotted and dashed lines are theoretical predictions from the QT model and MQDT, respectively. Reprinted with permission from ref 3. Copyright 2010 AAAS.

The control of the rotational/hyperfine states and the ability of quantum superposition realized in the study of Ospelkaus et al.¹¹⁴ is of crucial importance for future perspectives in ultracontrolled many-body molecular physics, as discussed in the review article of Baranov et al.²⁸⁰ in this issue and the references therein.

As particular recent examples where the internal hyperfine structure is relevant for alkali polar molecules of experimental interest, Wall and Carr²⁸¹ and Gorshkov et al.^{282,283} discussed the possibility to use polar molecules in lattices to simulate many-body systems. In their paper, Wall and Carr²⁸¹ investigated the role of the hyperfine structure of polar molecules into a one-dimensional lattice, and subject to interaction with dc electric, ac microwave, and static magnetic fields. By tuning the angle between the electric and magnetic fields and the strength of the magnetic and ac fields, the authors showed that it is possible to change the number and time scale of internal states contributing to the many-body dynamics. Gorshkov et al.^{282,283} showed that two dressed rotational states of polar molecules in an optical lattice can provide a highly tunable generalization of the t-J model, referred to as the “t-J–V-W” model. The authors showed that the tunability and the long-range dipole–dipole interaction between the polar molecules can lead to enhanced superfluidity. The model proposed by Gorshkov et al. is expected to exhibit exotic physics and provide insights into strongly correlated phenomena in condensed-matter systems.

Another example is given by Pellegrini et al.^{284,285} The precise control of the quantum states of polar molecules constitutes the basis of quantum computation.^{286–290} Taking $^{85}\text{Rb}^{133}\text{Cs}$, $^{40}\text{K}^{87}\text{Rb}$, and $^{41}\text{K}^{87}\text{Rb}$ as examples, Pellegrini et al.²⁸⁴ proposed implementations of universal quantum gates using the hyperfine levels of these ultracold heteronuclear polar molecules in their ground electronic state and ground vibrational and rotational state. The authors discussed the possibilities of driving high-fidelity logic gates by microwave pulses between the hyperfine states of the ground states heteronuclear dimers. A similar study was pursued for implementations taking place in the lowest two rotational levels of the ground electronic and vibrational state of the polar molecules.²⁸⁵ The works of Pellegrini and co-workers can be generalized with schemes involving more rotational levels, more than one vibrational level, and with other polar molecules.

4.6. Ultracold Molecular Chemical Reactions

In 2010 Ospelkaus et al.³ showed that the precise control of the internal state of a molecule determines the collisional properties. The $^{40}\text{K}^{87}\text{Rb}$ molecules are fermionic species so that if the molecules are in the same internal quantum state, they are indistinguishable and should collide only in a *p*-wave at ultracold temperature. This is what Ospelkaus et al. observed in their experiment. If the molecules are all in a same hyperfine state, the loss rate coefficient, due to the chemical reaction $\text{KRb} + \text{KRb} \rightarrow \text{K}_2 + \text{Rb}_2$, behaves linearly with the ultracold temperature, in agreement with the Bethe–Wigner threshold laws in eq 16 for a *p*-wave collision, with a rate coefficient per unit *T* of $1.2 \pm 0.3 \times 10^{-5} \text{ cm}^3 \text{ s}^{-1} \text{ K}^{-1}$. Now if the molecules are in different hyperfine states, the molecules are distinguishable and should collide in a *s*-wave. Again, this is what the authors observed. They found a loss rate coefficient of 1–2 orders of magnitude larger than the *p*-wave collision, with a rate coefficient of $1.9 \pm 0.4 \times 10^{-10} \text{ cm}^3 \text{ s}^{-1}$ that was independent of temperature, in accordance with the Bethe–Wigner law for an *s*-wave collision in eq 15. The left panel of Figure 52 shows the molecular density as a function of time for indistinguishable molecules, and the right panel shows the rate coefficient as a function of temperature, for indistinguishable fermions (circles and triangles) and distinguishable fermions (squares).

The experimental results were explained using a quantum threshold (QT) model¹⁵⁷ and a quantum defect theory (QDT) formalism⁵¹ (described later). Both theoretical descriptions assume full chemical loss when the two molecules meet at close distance (universal loss). On the basis of a classical capture model with the use of Bethe–Wigner threshold laws, the QT model provides an upper limit of the *p*-wave rate of $1.5 \pm 0.1 \times 10^{-5} \text{ cm}^3 \text{ s}^{-1} \text{ K}^{-1}$. The QDT formalism provides a *p*-wave rate of $0.8 \pm 0.1 \times 10^{-5} \text{ cm}^3 \text{ s}^{-1} \text{ K}^{-1}$. For the *s*-wave rate, the QDT formalism provides a rate of $0.8 \pm 0.1 \times 10^{-10} \text{ cm}^3 \text{ s}^{-1}$. The smaller theoretical rate is attributed to the fact that the system deviates from the universal loss regime at short distance, so that the probability is <1. Finally, Ospelkaus et al. studied the atom–molecule collisions for both atoms and molecules in their absolute ground state. The chemical reaction $\text{K} + \text{KRb} \rightarrow \text{K}_2 + \text{Rb}$ is energetically allowed while the reaction $\text{Rb} + \text{KRb} \rightarrow \text{Rb}_2 + \text{K}$ is forbidden for the temperature of the experiment. The authors performed two separate experiments, one with K atoms and KRb molecules and the other with Rb atoms and KRb molecules. The results are presented in Figure 53. The left

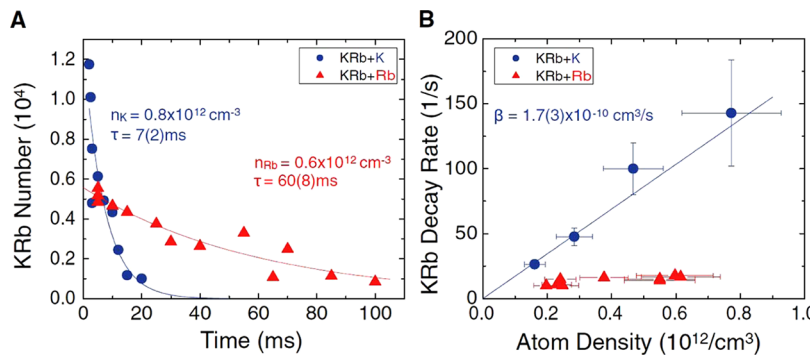


Figure 53. Collisions of atoms and molecules in their lowest-energy internal states. (A) Sample decay curves for the molecular number when subject to collisions with K atoms (circles) and with Rb atoms (triangles). (B) Dependence of molecule loss rate on atomic gas density. Reprinted with permission from ref 3. Copyright 2010 AAAS.

panel presents the number of KRB molecules as a function of time with K atoms (in circles) and Rb atoms (in triangles). The lifetime of the molecules is shorter with the presence of K atoms than with the Rb atoms. The right panel shows the rate coefficient as a function of atom density. A clear linear dependence is found for the K + KRB collisions, yielding a rate of $1.7 \pm 0.3 \times 10^{-10} \text{ cm}^3 \text{ s}^{-1}$. The QDT formalism predicts a rate of $1.1 \pm 10^{-10} \text{ cm}^3 \text{ s}^{-1}$, suggesting again a deviation from the universal regime. For Rb + KRB, the density dependence of the loss rate is less obvious. With a linear fit, the authors found a rate coefficient of $0.13 \pm 0.04 \times 10^{-10} \text{ cm}^3 \text{ s}^{-1}$, an order of magnitude smaller than that for K + KRB. This is consistent with the absence of a chemical reaction for Rb + KRB. The residual rate coefficient can be attributed to collisions of KRB with undetected molecules in high vibrational states or three-body collisions KRB + Rb + Rb. If either the molecules or the atoms are in an excited hyperfine state, the rate coefficient is observed at $10^{-10} \text{ cm}^3 \text{ s}^{-1}$, consistent with two-body losses from inelastic hyperfine changing transitions. Then a tiny change in the quantum state of the atoms or molecules leads to dramatic effects on loss.

A simple and intuitive model was proposed by Quéméner and Bohn.¹⁵⁷ Mixing a classical capture Langevin model¹⁸⁴ with the quantum threshold laws,^{41,42} one arrives at a simple and intuitive formula. If we consider only the incoming channel, the effective potential for a $-C_p/R^p$ interaction seen by the colliding particles is

$$V_{\text{eff}}(R) = \frac{\hbar^2 l(l+1)}{2\mu R^2} - \frac{C_p}{R^p} \quad (41)$$

This is sketched in Figure 54. For p -wave collisions, as in the KRB experiments,^{3,4} a characteristic energy is given by the height of the p -wave centrifugal barrier $E^* = V_b = p^{-(p/(p-2))}(p-2)\mu^{-(p/(p-2))}C_p^{-(2/(p-2))}[\hbar^2 L(L+1)]^{(p/(p-2))}/2$. The height $E^* = (8\hbar^6/(54\mu^3 C_6))^{1/2}$ for an attractive van der Waals interaction $p = 6$ and $E^* = (25\hbar^6/(108\mu^3)) \times (d^2/(4\pi e_0))^{-2}$ for an attractive dipole–dipole interaction $p = 3$. This model was further exploited for s -wave collisions,¹⁶² for which the characteristic energy is given by $E^* = (\hbar^3/(8\mu^3 C_6)^{1/2})^{1/2}$ for an attractive van der Waals interaction and by $E^* = (15\hbar^6/(16\mu^3)) \times (d^2/(4\pi e_0))^{-2}$ for an attractive dipole–dipole interaction. At short range it is assumed that the couplings between the incoming reactant channel and all the other product channels are so strong that the short-range probability P_{sr} to undertake an inelastic or reactive collision is 1. Now, the question is what is the probability to go from the long-range region to the short-

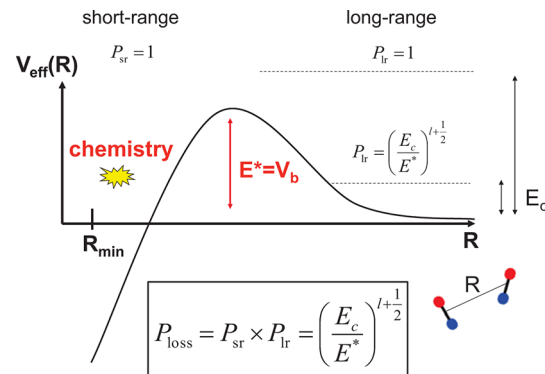


Figure 54. Sketch of the incident barrier for a molecular collision at long-range.

range region? At long range, the authors used two criteria. The first one is a classical capture model criterion, or Langevin model.¹⁸⁴ When the collision kinetic energy E_c is higher than the characteristic energy $E_c \geq E^* = V_b$, it is assumed that the long-range probability to go to the short-range region is $P_{\text{lr}} = 1$. The second criterion is the Bethe–Wigner quantum threshold laws.^{41,42} When $E_c \rightarrow 0$, the long-range probability should behave as $P_{\text{lr}} \propto E_c^{l+1/2}$ for a partial wave l . Combining both equations, the long-range probability to go to the short-range region is $P_{\text{lr}} = (E_c/E^*)^{l+1/2}$. The total loss probability P_{loss} is the product of the short-range probability P_{sr} with the long-range probability P_{lr} . As P_{sr} is chosen to be 1 (universal full-loss condition), one has

$$P_{\text{loss}} = \left(\frac{E_c}{E^*} \right)^{l+1/2} \quad (42)$$

This yields a general quantum threshold expression for one partial wave l , m_l for the loss cross section as a function of the collision energy

$$\sigma_l^{\text{ls}} = \frac{\hbar^2 \pi}{2\mu(E^*)^{l+1/2}} E_c^{l-1/2} g \quad (43)$$

and for the loss rate coefficient as a function of temperature²⁹¹

$$\beta_l^{\text{ls}} = \frac{\hbar^2 \pi}{\sqrt{2\mu^3(E^*)^{l+1/2}}} \langle E_c^l \rangle g \quad (44)$$

The factor $g = 2$ for indistinguishable particles and $g = 1$ for distinguishable ones. The temperature dependence appears in

the quantity $\langle E_c^l \rangle$, which is a Maxwell–Boltzmann average of E_c^l at the temperature T . Then, for p -wave collision, the loss rate coefficient is given by¹⁵⁷

$$\beta_{l=1}^{\text{ls}} = \frac{\pi}{8} \left\{ p_1 \times \left(\frac{3^{17} \mu^3 C_6^3}{\hbar^{10}} \right)^{1/4} + p_2 \times \left(\frac{2^{9/2} 3^{11/2} \mu^3}{S^3 \hbar^7} \right) \right. \\ \left. \frac{d^6}{(4\pi\epsilon_0)^3} \right\} k_B T \times g \quad (45)$$

for indistinguishable fermionic dipoles ($g = 2$) and for s -wave collisions the loss rate coefficients are given by¹⁶²

$$\beta_{l=0}^{\text{ls}} = \pi \left\{ p_3 \times \left(\frac{2\hbar^2 C_6}{\mu^3} \right)^{1/4} + p_4 \times \frac{\sqrt{16/30}}{\hbar} \frac{d^2}{4\pi\epsilon_0} \right\} \times g \quad (46)$$

for indistinguishable bosonic dipoles ($g = 2$). If $P_{\text{loss}}(E_c = E^*) = 1$ (classical Langevin criterion), then $p_1 = p_2 = p_3 = p_4 = 1$ in these expressions. Using this classical argument, the formula will overestimate the quantum rate coefficient. In quantum mechanics, the condition $P_{\text{loss}}(E_c = E^*) = 1$ is not true, because there is a quantum transmission probability as well as a quantum reflection probability at the top of the barrier, and the sum of them is one. Then, the quantum transmission probability should be < 1 . To account for this, the numerical factors in front of each expression were found by comparing the analytic expressions with a close-coupling numerical quantum calculation. The authors found $p_1 = 0.53$, $p_2 = 0.54$, $p_3 = 1.92$, and $p_4 = 3.74$.¹⁶² The formula (including $g = 2$ for the collision of indistinguishable KRb fermions and $p_1 = 1$),

$$\beta = \frac{\pi}{4} \left(\frac{3^{17} \mu^3 C_6^3}{\hbar^{10}} \right)^{1/4} k_B T \quad (47)$$

was used in the work of Ospelkaus et al.,³ appearing as a dotted line in Figure 52b. The advantage of this simple model provides an intuitive formula for the loss rate coefficients, for any $-C_p/r^p$ attractive potential ($p \geq 3$), including both van der Waals ($p = 6$) and attractive dipole–dipole interaction ($p = 3$).

Ospelkaus et al.³ also compared their data to the predictions of the generalized quantum defect theory treatment of Idziaszek and Julienne.⁵¹ As discussed in section 2.2.2, the latter authors introduced two QDT parameters y and s to characterize a collision with a single entrance channel. These parameters are used in representing the incoming and outgoing parts of the quantum mechanical wave function for intermolecular separations outside the short-range chemical region (R_0 in Figure 14) and inside the characteristic distance of the long-range potential (R_L in Figure 14). The short-range reaction probability is related to $0 \leq y \leq 1$ as $P_{\text{sr}} = 4y/(1+y)^2$, and the phase of the wave function is related to $s = a_{l=0}/\bar{a}$, where $a_{l=0}$ parametrizes the scattering length of the uncoupled entrance channel. In the limit of small enough collision energy that $|k\bar{a}| \ll 1$, the model gives the following analytic expressions for the s - and p -wave complex scattering length \tilde{a}_l in the case of the van der Waals attractive potential:

$$\tilde{a}_{l=0}(k) = a + \bar{a}y \frac{1 + (1-s)^2}{i + y(1-s)} \quad (48)$$

$$\tilde{a}_{l=1}(k) = -2\bar{a}_1(k\bar{a})^2 \frac{y + i(s-1)}{ys + i(s-2)} \quad (49)$$

where \bar{a} was defined in eq 4 and $\bar{a}_1 = \bar{a}\Gamma(1/4)^6/(144\pi^2\Gamma(3/4)^2) \approx 1.064\bar{a}$. The QDT model gives a remarkably simple result for \tilde{a}_l for the special case of the Langevin limit with unity short-range reaction probability, $P_{\text{sr}} = y = 1$. In this limit, eq 48 and eq 49 become independent of s and y and consequently independent of any details of the short-range dynamics, and depend only on \bar{a} . The quantities b_l and $\text{Im}(-\tilde{V}_{l=1})$ in eqs 15 and 16 become \bar{a} and $\bar{a}_1\bar{a}^3$, respectively. The universal Langevin rate coefficients for threshold collisions are

$$K_{l=0}^{\text{el}} = 4g \frac{\hbar}{\mu} k\bar{a}^2 \text{ and } K_{l=0}^{\text{ls}} = 2g \frac{\hbar}{\mu} \bar{a} \quad (50)$$

and

$$K_{l=1}^{\text{el}} = 4\sigma g \frac{\hbar}{\mu} k\bar{a}_1^2 (k\bar{a})^4 \text{ and } K_{l=1}^{\text{ls}} = 2\sigma g \frac{\hbar}{\mu} \bar{a}_1 (k\bar{a})^2 \quad (51)$$

Here $\sigma = 3$ to sum over the three $m_l = 0, \pm 1$ components of the $l = 1$ partial wave. The thermally averaged version of the last formula (see eq 16) was used in the work of Ospelkaus et al.,³ appearing as a dashed line in Figure 52b.

Gao³⁸ also developed a general quantum defect treatment of near-threshold molecular collisions, as discussed in section 2.2.2 in relation to Figure 14. The theory is applicable to different inverse power law potentials and gives the quantum threshold implementation of the Langevin model, converging to the limit of the standard classical capture models as collision energy increases. Gao has given the universal Langevin expressions for the $p = 6$ ¹⁵⁸ and $p = 4$ ¹⁵⁹ potentials using scaled units of length $\beta_G = 2a_p$ (see eq 4 for our definition of a_p), energy $s_E = \hbar^2/(2\mu\beta_G^2)$, and rate constant $s_K = \pi\hbar\beta_G/\mu$. Figure 55 illustrates the scaled rate constant versus scaled temperature for an attractive van der Waals potential. For this $p = 6$ case, the scaled loss rate coefficient $\mathcal{K} = K/s_K$ for collisions of indistinguishable bosons as a function of the scaled temperature $T_s = T/(s_E/k_B)$ is the following, using Gao's notation:

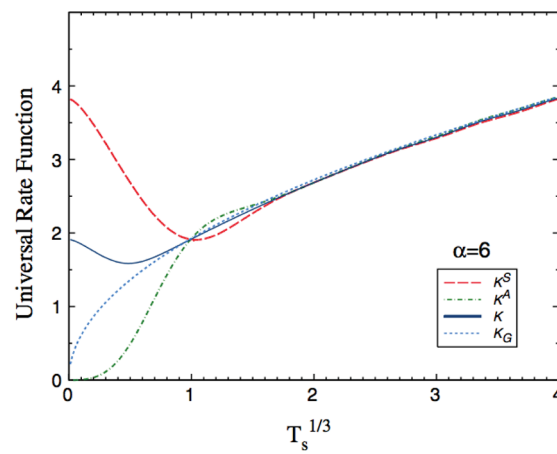


Figure 55. Universal scaled quantum mechanical rate constant $\mathcal{K}(T_s)/s_K$ versus scaled temperature T_s for a van der Waals potential, shown for indistinguishable bosons (\mathcal{K}^S), indistinguishable fermions (\mathcal{K}^A), distinguishable particles (\mathcal{K}), and the classical capture (Langevin) limit (\mathcal{K}_G). Reprinted with permission from ref 158. Copyright 2010 American Physical Society.

$$\mathcal{K}^S(T_s) = 8\bar{a}_{sl=0} \left[1 - \frac{4\bar{a}_{sl=0}}{\sqrt{\pi}} T_s^{1/2} + 3\bar{a}_{sl=0}^2 T_s + O(T_s^{3/2}) \right] \quad (52)$$

where $\bar{a}_{sl=0} = 2\pi/[\Gamma(1/4)]^2 \approx 0.4779888$ is the scaled scattering length for $l = 0$. For indistinguishable fermions,

$$\mathcal{K}^A(T_s) = 36\bar{a}_{sl=1} T_s \left[1 - \frac{16\bar{a}_{sl=1}}{\sqrt{\pi}} T_s^{3/2} + O(T_s^2) \right] \quad (53)$$

where $\bar{a}_{sl=1} = [\Gamma(1/4)]^2/(36\pi) \approx 0.1162277$ is the scaled scattering length for $l = 1$. For distinguishable particles,

$$\begin{aligned} \mathcal{K}(T_s) = 4\bar{a}_{sl=0} - \frac{(4\bar{a}_{sl=0})^2}{\sqrt{\pi}} T_s^{1/2} + (12\bar{a}_{sl=0}^3 + 18\bar{a}_{sl=1}) T_s \\ + O(T_s^{3/2}) \end{aligned} \quad (54)$$

The scaled rate constant in the high-temperature limit, $T_s \gg 1$,

$$\mathcal{K}^S(T_s) \approx \mathcal{K}^A(T_s) \approx \mathcal{K}(T_s) \approx \mathcal{K}_G(T_s) \approx \frac{2^{4/3}\Gamma(2/3)}{\sqrt{\pi}} T_s^{1/6} \quad (55)$$

is in agreement with eq 28, also known as the Gorin model.^{292,293}

Gao also found the analytic rate constants for a $-C_4/r^4$ interaction potential.¹⁵⁹ For distinguishable particles at low temperatures, $T_s \ll 1$, the scaled inelastic/reaction rate coefficient as a function of the scaled temperature is given by

$$\begin{aligned} \mathcal{K}(T_s) = 4\bar{a}_{sl=0} - \frac{(16\bar{a}_{sl=0})^2}{\sqrt{\pi}} T_s^{1/2} + 18[\bar{a}_{sl=0}^3 + \bar{a}_{sl=0}] T_s \\ + O(T_s^2) \end{aligned} \quad (56)$$

with $\bar{a}_{sl=0} = 1$ and $\bar{a}_{sl=0} = 1/225$. At high temperatures, $T_s \gg 1$,

$$\mathcal{K}(T_s) \approx 2 \quad (57)$$

in agreement with the classical Langevin model.^{184,293}

Kotochigova also performed quantum dynamics studies of KRb + KRb \rightarrow K₂ + Rb₂ reactive collisions.⁷⁶ To model the way particles are affected by the short-range physics, Kotochigova used a short-range scattering matrix $S = \zeta e^{2i\delta}$ depending on two parameters ζ and δ . The first parameter $0 \leq \zeta \leq 1$ describes the ratio of the reflected flux over the transmitted flux of particles at short range. The limit $\zeta = 0$ corresponds to a case of full transmission and no reflection (imitating a situation of full loss probability at short range, leading to the universal rates), and $\zeta = 1$ corresponds to the opposite case of full reflection and no transmission. The second parameter $0 \leq \delta \leq \pi$ corresponds to the scattering phase shift created by the (unknown) short-range potential. Kotochigova calculated the rate coefficient for a given collision energy of 350 nK, as a function of these two parameters ζ and δ , for both cases of distinguishable and indistinguishable molecules. The distinguishable case is presented in Figure 56. She also performed a similar calculation for the reaction RbCs($v = 1, N = 0$) + RbCs($v = 1, N = 0$) \rightarrow Rb₂ + Cs₂ at a collision energy of 250 μ K, which is allowed for these initial states of the RbCs molecules. This is presented in Figure 57. For $\zeta = 0$, the rate coefficients converge to the universal limit described above^{51,158,162} and are independent of δ , as also found by Idziaszek and Julienne.⁵¹ No matter the short-range potential, the rate coefficient will always be the same if full loss is assumed when the particles meet at short range. As $\zeta \rightarrow 1$, the rates

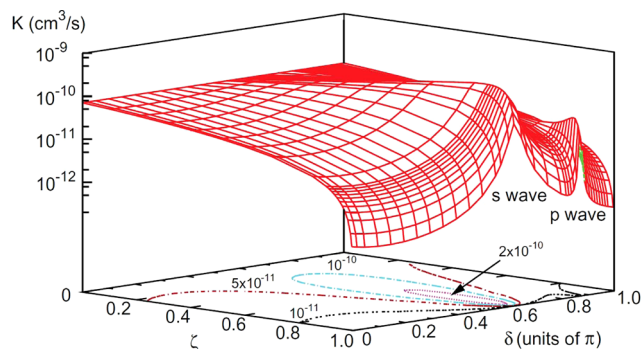


Figure 56. Total inelastic loss rate coefficient for a nuclear spin unpolarized sample of $v = 0, J = 0$ $^{40}\text{K}^{87}\text{Rb}$ molecules in the $X^1\Sigma^+$ potential as a function of the short-range parameters ζ and δ at a collision energy of $E/k_B = 350$ nK. The loss rate of the unpolarized case contains non-negligible contributions from *s*- and *p*-wave contributions. Reprinted with permission from ref 76. Copyright 2010 Institute of Physics and the Deutsche Physikalische Gesellschaft.

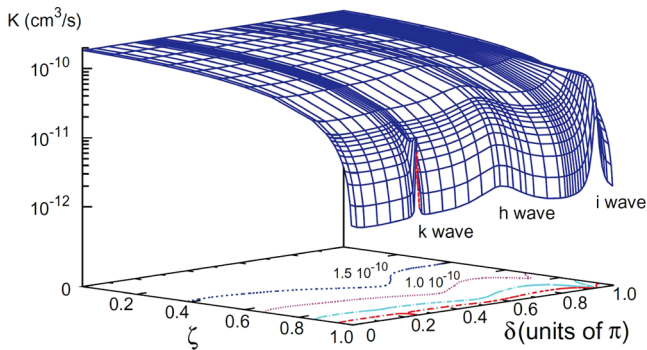


Figure 57. Total inelastic loss rate coefficient for an unpolarized sample of $v = 1, J = 0$ $^{87}\text{RbCs}$ molecules in the $X^1\Sigma^+$ potential as a function of the short-range parameters ζ and δ at a collision energy of $E/k_B = 250 \mu\text{K}$. At this collision energy, many partial waves contribute. Reprinted with permission from ref 76. Copyright 2010 Institute of Physics and the Deutsche Physikalische Gesellschaft.

depend more and more on the scattering phase shift at short range. Shape resonances can be seen in the rates (*s*- and *p*-wave for KRb + KRb, *k*-, *h*-, *i*-wave resonances for RbCs + RbCs). Since $\zeta \neq 0$, there is an allowed reflected flux, and if the collision energy matches the position of a particle-particle quasi-bound state due to the centrifugal barrier of the partial wave l (or a virtual bound state for *s*-wave), a resonant feature appears in the cross section and rate coefficients. This is a useful procedure to parametrize the short-range physics. However, it does not take into account possible Fano-Feshbach resonances coming from other particle-particle channels.

Mayle et al.²⁹⁴ have recently investigated the role of these other particle-particle channels that can presumably hold a large number of particle-particle bound states. The authors included a statistical procedure to account for Fano-Feshbach resonances that can appear in the cross section and rate coefficients.

The models of Idziaszek and Julienne,⁵¹ Kotochigova,⁷⁶ and Gao³⁸ all incorporate the effect on collision rates due to the back-reflection of scattering flux into the entrance channel and all show in different ways that the back-reflected flux modifies the quantum scattering from the long-range potential. Multiple reflections result when entrance channel shape resonances occur, or if Fano-Feshbach resonances are present. The analytic

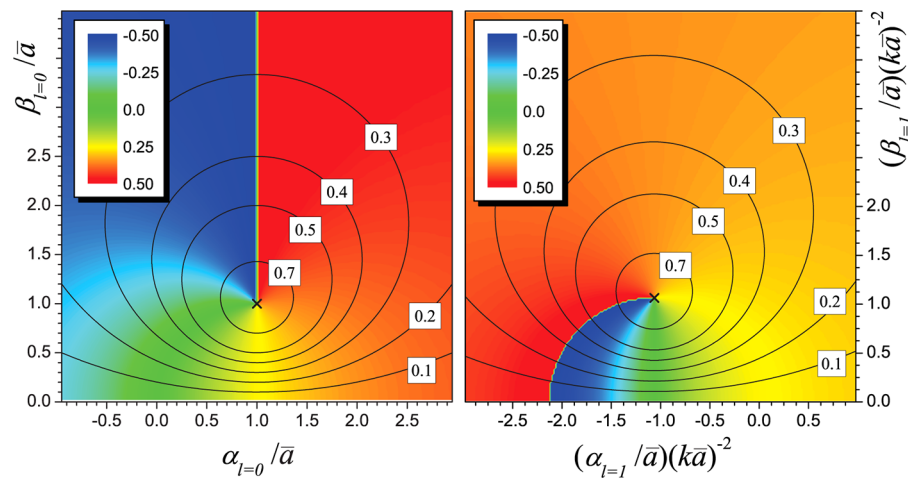


Figure 58. Plot of the imaginary part of \tilde{a}_l versus the real part of \tilde{a}_l , valid in the threshold limit, $k\tilde{a}|^2 \ll 4$, for a van der Waals potential for different values of the two QDT parameters y (constant along the solid circular lines) and s (color coded according to $\arctan(s)/\pi$, where red means large and positive and blue means large and negative). The respective left and right panels are for the s -wave $\tilde{a}_{l=0}/\bar{a}$ and for the p -wave $\tilde{a}_{l=1}/[\bar{a}(k\bar{a})^2]$). The “ \times ” symbol in the center corresponds to the universal Langevin limit. Reprinted with permission from ref 51. Copyright 2010 American Physical Society.

expressions of Idziaszek and Julienne in eq 48 and eq 49 give some insight into the general relationship between the real and imaginary parts of \tilde{a}_l . This is illustrated by Figure 58. The loss rate coefficient, proportional to $\text{Im}(\tilde{a}_l)$, has a magnitude that moves away from the universal Langevin point depending of the values of y and s . As y decreases from unity, resulting in more back-reflection, the range of departure becomes larger, depending on s . The red–blue boundary for s -waves corresponds to a scattering length with a magnitude very large compared to the van der Waals length \bar{a} , that is, there is a threshold bound state present. The red–blue boundary for p -waves corresponds to the case where there is a p -wave shape resonance exactly at threshold. Real-world molecules that depart from the unit capture limit ($y = 1$) can have very rich threshold behavior, which is not yet well-understood. The departure of measured rate constants from the Langevin limit then might have useful information about the nature of the dynamics that leads to the departure. Such possibilities have yet to be explored.

4.7. Electric Field Control of Dipolar Collisions and Chemical Reactions

Ni et al.⁴ applied an electric field to a gas of ultracold fermionic KRb molecules to investigate the role of dipolar collisions. KRb molecules are polar molecules, and by applying an electric field, they can obtain a field-dependent dipole moment d in the laboratory frame. By increasing the electric field up to 5 kV/cm, a value of d for KRb up to ~ 0.2 D (Debye) could be achieved. The upper panel of Figure 59 shows the number of KRb molecules at a temperature of 300 nK as a function of time for a small induced dipole ($d = 0.08$ D, triangles) and for a stronger one ($d = 0.19$ D, circles). The electric field has a strong effect on the collisions. The lifetime of the molecules decreases with the electric field. This is due to a greatly increased loss rate coefficient when the induced dipole is increased (see bottom panel of Figure 59).

The Schrödinger equation for the collisional motion can be written using an effective potential including a repulsive centrifugal term $\hbar^2 l(l+1)/(2\mu R^2)$ with $l = 1$, $m_l = 0, \pm 1$, an attractive van der Waals interaction $-C_6/R^6$ with $C_6 = +16\,133$ au,⁷⁶ and a dipole–dipole interaction $-C_3/r^3$, with $C_3 > 0$ (attractive interaction) if $m_l = 0$ (head-to-tail collisions, dipoles aligned with the electric field) and $C_3 < 0$ (repulsive interaction) if $m_l = \pm 1$ (side-by-side collisions, dipoles aligned with the electric field). In the van der Waals regime (no electric field applied), the effective potential forms a barrier of height V_b coming from the attractive van der Waals interaction and the repulsive centrifugal term. This is shown schematically in Figure 60 (top panel). In the electric field regime where the van

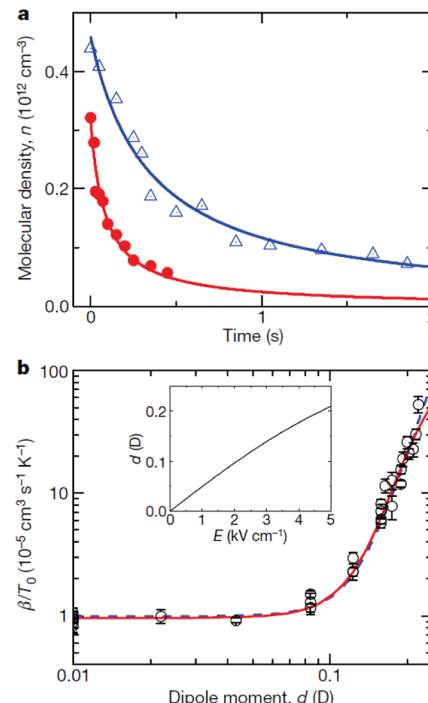


Figure 59. Two-body inelastic loss for fermionic polar molecules. (a) The inelastic loss rate coefficient, β , is extracted from a fit (solid lines) for induced dipole moments of $d = 0.08$ D (open triangles) and $d = 0.19$ D (filled circles), at $T = 300$ nK. (b) Data points show β/T plotted as a function of d . The dashed line shows a fit to a simple model based on the quantum threshold model. The solid line shows the result of a more complete quantum scattering calculation. Inset, the calculated dependence of d on the applied electric field, E . Reprinted with permission from ref 4. Copyright 2010 Nature Publishing Group.

aligned with the electric field) and $C_3 < 0$ (repulsive interaction) if $m_l = \pm 1$ (side-by-side collisions, dipoles aligned with the electric field). In the van der Waals regime (no electric field applied), the effective potential forms a barrier of height V_b coming from the attractive van der Waals interaction and the repulsive centrifugal term. This is shown schematically in Figure 60 (top panel). In the electric field regime where the van

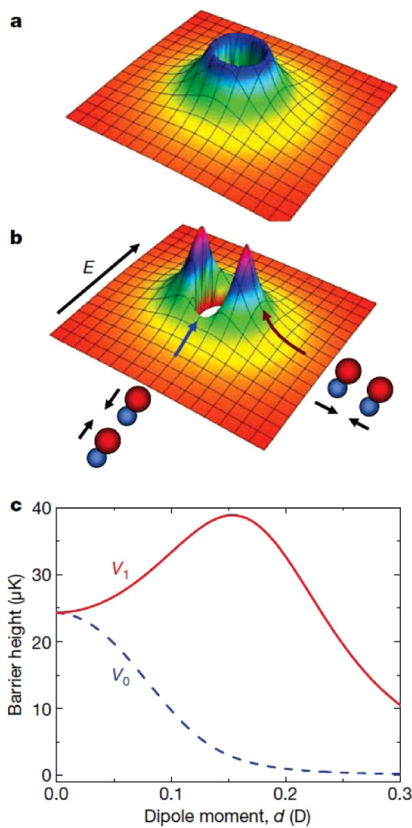


Figure 60. *p*-wave centrifugal barrier for dipolar collisions between fermionic polar molecules. (a) The effective intermolecular potential for fermionic molecules at zero electric field. At intermediate intermolecular separation, two colliding molecules are repelled by a large centrifugal barrier for *p*-wave collisions. (b) For a relatively small applied electric field, the spatially anisotropic dipolar interactions reduce the barrier for head-to-tail collisions and increase the barrier for side-by-side collisions. (c) Height of the *p*-wave barrier as a function of dipole moment. Reprinted with permission from ref 4. Copyright 2010 Nature Publishing Group.

der Waals interaction can be neglected, the effective potential is made from the repulsive centrifugal barrier and the attractive dipole–dipole interaction for the $m_l = 0$ head-to-tail collisions (middle panel) so that increasing the electric field and the induced dipole moment will decrease the barrier V_b (bottom panel, dashed curve). For the $m_l = \pm 1$ side-by-side collisions, the repulsive dipole–dipole interaction (middle panel) will increase the barrier (lower panel) for the lowest dipole moments. The power law dependence of the experimental data points in Figure 59b is found to be $d^{6.1 \pm 0.8}$, in very good agreement with the formula in eq 45 from the QT model. This equation was used to fit the experimental results and is shown as a dashed line in Figure 58b. Finally a time-independent numerical calculation was performed, taking into account the van der Waals and dipole–dipole interactions at long range, assuming a full loss probability (universal regime) when the molecules meet at short distances. The calculation was used to provide an experimental value of the van der Waals coefficient of $C_6 = 21\,000 \pm 7\,000 \text{ au}$, which is consistent with the predicted value of 16 133 au.⁷⁶

Ni et al.⁴ also found that the loss of molecules due to reactive collisions heats the gas. They attributed this effect to the fact that these types of collisions preferentially remove molecules from the center of the trap where the density is the highest and the energy of the particles is the lowest. As a result, because the lost molecules have on average lower energy than the other molecules in the trap, the temperature increases with time. They explained the experimental heating rate by considering a theoretical model in which the energy lost from the gas due to collisions in different directions and electric fields is taken into account. The authors also probed the spatial anisotropy of dipolar collisions as illustrated by the data shown in Figure 61. They looked at the expansion energies of the molecular cloud (or equivalently temperatures), in the vertical (along the electric field, blue open squares) and horizontal directions (perpendicular to the electric field, red filled circles), after heating initially one specific direction (vertical in panels a, b, and c and horizontal in panels d, e, and f). They observed a

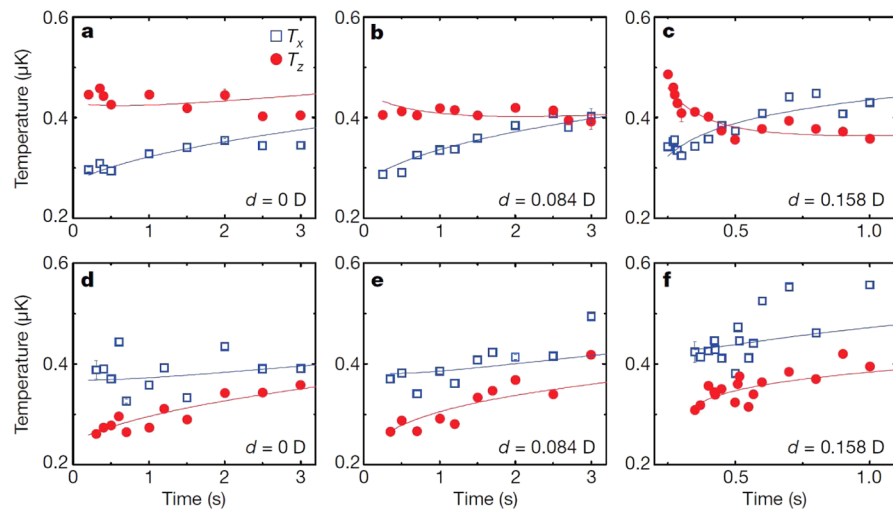


Figure 61. Apparent cross-dimensional rethermalization in the polar molecule gas. Shown as a function of dipole moment, d , for $T_z > T_x$ (a–c) and $T_z < T_x$ (d–f). The experimental data reveal a striking difference between heating the gas in the vertical direction (a–c) and heating it in the horizontal directions (d–f) and thus provide evidence for the strong anisotropic characteristic of dipolar interactions (see text). The electric field is applied along the z direction. Error bars show 1 s.d. uncertainties for a few example points. Reprinted with permission from ref 4. Copyright 2010 Nature Publishing Group.

strong signature of the anisotropic dipolar interactions. Different behavior is seen whether the cloud is heated in the vertical or horizontal directions. For the heating in the vertical direction, they observed an “apparent” rethermalization, where the T_z temperature decreases with time while the T_x direction increases. They used the term “apparent” because they had two reasons to believe that this is not a real thermalization. First, the curves cross each other at the largest dipole (panel c). Second, when heating the horizontal direction, the vertical and horizontal temperatures do not cross each other. In fact, they used their model for the heating rate and predicted that the head-to-tail collisions lead to heating in the horizontal direction but lead to cooling in the vertical direction. The side-by-side collisions lead to heating in the vertical direction and leave unchanged the temperature in the horizontal direction. The trends found are in good agreement with the experimental results in Figure 61 and explain the apparent rethermalization. By including the effect of elastic collisions in the model and fitting their experimental data, the authors estimated an elastic cross section of the order of $\sigma_{\text{el}} \approx 7 \times 10^{-8} \text{ cm}^2 \text{ s}^{-1} \text{ D}^{-4}$.

The elastic cross section is seen to increase as the fourth power of the induced dipole moment. This is in agreement with previous theoretical predictions of elastic collision of dipolar molecules proposed by Bohn et al.²⁹⁵ The scattering phase shift for a partial wave l and a long-range potential in $1/R^p$ is⁴⁶

$$\tan \delta_l \approx Ak^{2l+1} + Bk^{p-2} \quad (58)$$

where the first term provides the contribution of the short-range potential to the phase shift and the second term is only due to the long-range scattering outside the centrifugal barrier. In the case of a long-range van der Waals potential $p = 6$, the phase shift is $\tan \delta_{l=0} \approx Ak + Bk^4$ for s -wave collisions and $\tan \delta_{l=1} \approx Ak^3 + Bk^4$ for p -wave collisions. In both cases, the phase shift due to the short-range potential is the dominant one when $k \rightarrow 0$. However, for a dipole–dipole interaction with $p = 3$, the phase shift is $\tan \delta_{l=0} \approx Ak + Bk$ for s -wave collisions and $\tan \delta_{l=1} \approx Ak^3 + Bk$ for p -wave collisions.²⁹⁶ In this case, the phase shift is dominated by the long-range potential as $k \rightarrow 0$, even for higher partial waves l . Therefore, a Born approximation is applicable for threshold energies of scattering dipoles. Since $\tan \delta_l \approx k$, it also implies that the cross sections should behave as a constant $\sigma \approx (\sin \delta)/k^2 \approx \text{constant}$ as $k \rightarrow 0$. Using the Born approximation, Bohn et al. found that, at ultralow threshold energies, the elastic cross sections for even partial waves behave as

$$\sigma_{\text{thres}}^e = \sigma_{\text{Born}}^e + 4\pi a^2 = 1.117 \frac{\mu^2 d_1^2 d_2^2}{\hbar^4} + 4\pi a^2 \quad (59)$$

where $4\pi a^2$ is the cross section coming from the short-range scattering length $a = A$ (the phase shift is $\tan \delta_{l=0} \approx Ak + Bk$, so the first term (short-range contribution) has the same power law dependence in k as the second term (long-range contribution)). For odd partial waves

$$\sigma_{\text{thres}}^o = \sigma_{\text{Born}}^o = 3.351 \frac{\mu^2 d_1^2 d_2^2}{\hbar^4} \quad (60)$$

where μ is the reduced mass and d is the dipole moment. If the molecules are identical and indistinguishable, $d_1 = d_2 = d$ and one has to multiply the above expression by 2. Using the semiclassical Eikonal approximation, the authors also found that, at higher energies, the elastic cross sections should behave as

$$\sigma_{\text{Ei}} = \frac{8\pi}{3} \frac{d_1 d_2}{\hbar} \sqrt{\frac{\mu}{2E_c}} \quad (61)$$

where E_c is the collision energy. There is no distinction between even and odd partial waves, but to a good approximation they are half the cross section in eq 61. Eq 60 and eq 61 have been used to plot the elastic cross sections in Figure 62 for two fermionic $^{40}\text{K}^{87}\text{Rb}$ molecules in the same

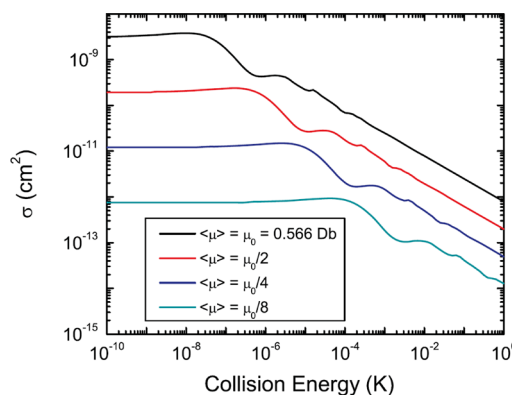


Figure 62. Elastic cross section for scattering of pairs of fermionic $^{40}\text{K}^{87}\text{Rb}$ molecules in identical internal states, averaged over incident directions. This calculation is based on the “universal” calculation that includes only dipole–dipole interactions. The top curve is the cross section for fully polarized molecules with dipole moment $\langle \mu \rangle = 0.566 \text{ D}$. The dipole is halved for each successively lower curve. Reprinted with permission from ref 295. Copyright 2009 Institute of Physics and the Deutsche Physikalische Gesellschaft.

quantum state, for different values of the induced dipole moment $d = d_0 = 0.566 \text{ D}$, $d = d_0/2$, $d = d_0/4$, and $d = d_0/8$. In the threshold limit, the cross section behaves as d^4 , whereas in the semiclassical Eikonal limit, they behave with a weaker power law dependence as d^2 .

The quantum calculation used to compute the reaction rate coefficients as a function of the dipole moment in the work of Ni et al.⁴ assumed a unit short-range probability for the molecules to undergo a chemical reaction. This is a particular case of the universal collisions discussed in section 2.2.2 where the reaction rate coefficient does not depend of the short-range physics between the two particles.^{51,76,157} This is valid when the molecules are highly reactive. However, it is likely that many molecular systems deviate from this universal case. Figure 58 showed such a deviation for the case of a van der Waals potential. This was further developed by Idziaszek et al.¹⁶¹ using a numerical close-coupling formalism to include the effect of the electric field and the dipole–dipole interaction. Using the s -wave and p -wave complex scattering length parametrization in ref 51, the authors calculated the $\text{KRb} + \text{KRb} \rightarrow \text{K}_2 + \text{Rb}_2$ inelastic/reactive (quenching) rate coefficient as a function of the induced dipole moment d for different values of the y and s QDT parameters in eq 48 and eq 49. The parameters provide short-range boundary conditions for the numerical calculation, where the limits $y = 1$ and $y = 0$ correspond to unit probability of respective loss and reflection from the region of short-range dynamics.

Figure 63 illustrates the loss coefficients for various case of y , s pairs with indistinguishable fermions on the left and indistinguishable bosons on the right. The two solid black lines correspond to the universal full-loss case $y = 1$ and are

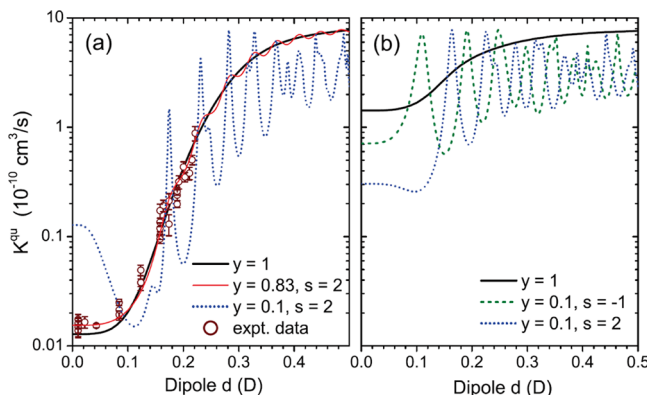


Figure 63. Dependence of chemical reaction rates $K_l^q u$ on dipole moment d for identical (a) fermionic (odd l) or (b) bosonic (even l) KRb molecules. In the case of unit reaction probability, $y = 1$, this variation takes a universal form independent of details of the short-range physics. For $y < 1$, nonuniversal resonances appear that reveal more details of the short-range interaction. The data from ref 4 (circles) are well fit by near-universal scattering, $y = 0.83$. Reprinted with permission from ref 161. Copyright 2010 American Physical Society.

independent of the value of s . The loss rate coefficient increases with the dipole moment d following the predicted behavior scaling at ultralow energies as d^6 for indistinguishable fermions¹⁵⁷ and as d^2 for indistinguishable bosons.¹⁶² Because of the stronger d -dependence for the fermions, the fermionic loss rate coefficients increase to become as large as the bosonic ones as d increases. No resonances are seen for the $y = 1$ universal case as the dipole–dipole interaction is turned on by increasing the electric field. This is in contrast to the cases with other values of $y < 1$. The left panel of Figure 63 shows small wiggles for the $y = 0.83$ case for fermions (bold solid red curve). As the short-range loss probability P_{sr} is further decreased, for example when $y = 0.1$, bigger resonant features appear corresponding to shape resonances of quasi-bound states (blue dotted line). The condition $y = 0.83$ and $s = 2$ corresponds to the best fit to the experimental points of Ni et al.⁴ (see circles in Figure 63) if one fixes the C_6 coefficient to its computed value of $\sim 16\,130$ au.⁷⁶ Note that this implies a near-universal chemical reaction rate. As $y \rightarrow 1$ and unit short-range absorption is approached, any molecule–molecule resonant state rapidly decays in the short-range region and does not have the time to survive a single period of the resonance. Thus, no resonance structure appears in the rate coefficient. When $y \rightarrow 0$, the condition of full reflection from the short range is approached, and any molecule–molecule resonant state survives so that its effect can be seen in the rate coefficient. Similar conclusions hold for the bosonic case in the right panel. This panel also shows the effect of s . For a fixed $y = 0.1$, a change in the entrance channel phase s , for example, from $s = -1$ to $s = 2$, shifts the position of the resonances.

Although the condition of full absorption $y = 1$ sets the value of the universal loss rate coefficient, this condition does not set the maximum value of a chemical reaction rate, as we saw for van der Waals collisions in Figure 58. This is because more amplitude of the wave function can be drawn into the short-range region when threshold resonances are present. The left panel of Figure 63 shows that for the nearly full reflection condition $y = 0.1$ (blue dotted line), the loss rate of the fermionic system for $d = 0$ can be an order of magnitude larger than for the full absorption condition $y = 1$ (solid black line).

The full-loss condition does not necessarily mean the highest chemical reactivity because a nearly full reflection condition can dramatically enhance it! The right panel of Figure 63 shows the opposite result for the same situation, $y = 0.1$ and $s = 2$ (blue dotted line), because the loss rate for $d = 0$ is an order of magnitude smaller than for the full absorption condition $y = 1$ (solid black line). The difference between the fermion and the boson case is explained by the fact that the condition $s = 2$ implies the existence of a threshold p -wave shape resonance in the entrance channel, but no shape resonance exists for any even partial wave when $s = 2$. This is a consequence of the quantum defect theory of Gao for a van der Waals potential.^{40,297} The $y = 0.1, s = 2$ example in Figure 63 also shows that, at zero electric field and induced dipole moment, the reaction rate of a pure p -wave collision between indistinguishable fermions can be comparable to the one of a pure s -wave collision between indistinguishable bosons (in this case only a factor of 3 different). Consequently, just because two particles collide with a centrifugal barrier (say a p -wave) does not mean that the probability of collision cannot be comparable with that of a similar system colliding without a centrifugal barrier (s -wave). In conclusion, the absence or presence of these electric-field-tunable threshold resonances can provide information on whether a chemical system is lossy ($y \rightarrow 1$) or not ($y \rightarrow 0$). The details depend on the mass and density of states of the particle–particle system, on the short- and long-range molecular potential, and on whether the system is barrierless or not (see the discussion in ref 187).

Work on dipolar collisions has been extended to other bialkali molecules of experimental interest. Julienne et al.⁷⁵ and Quéméner et al.¹⁶² have studied the dynamics of alkali molecules of category I (KRb, LiNa, LiK, LiRb, and LiCs) and of category II (NaK, NaRb, NaCs, KCs, and RbCs), assuming full-loss probability when they meet due to inelastic or reactive collisions. Figures 64 and 65 show the loss rate coefficient divided by the temperature for indistinguishable fermionic molecules (Figure 64), and the rate coefficient for indistinguishable bosonic molecules (Figure 65), as a function

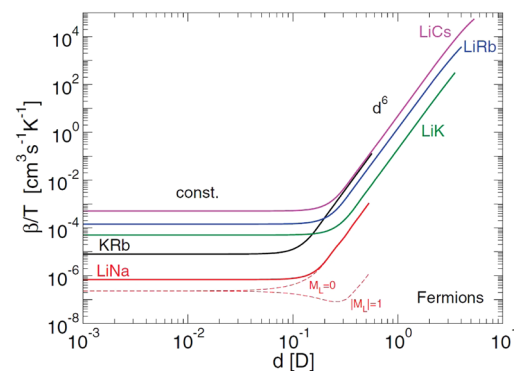


Figure 64. (Solid lines) Loss rate coefficient $\beta_{l=1}$ divided by T in free three-dimensional (3D) space, for the reaction $AB + AB \rightarrow A_2 + B_2$ for different reactive fermionic polar molecules ($AB = \text{LiNa, KRb, LiK, LiRb, and LiCs}$), as a function of the electric dipole moment. The fermions are assumed to be in the same indistinguishable quantum state. In the van der Waals regime, the rate coefficient is constant, whereas in the electric-field regime, the rate coefficient behaves as d^6 . (Dashed lines) $\beta_{l=1, m_l=0}$ and $\beta_{l=1, |m_l|=1}$ components of $l = 1$, shown here for $AB = \text{LiNa}$. Reprinted with permission from ref 162. Copyright 2011 American Physical Society.

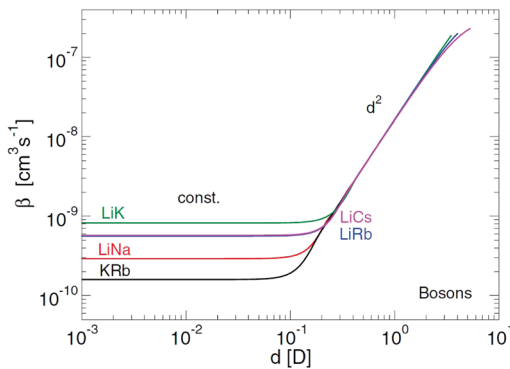


Figure 65. As in Figure 64 for reactive bosonic polar molecules. The rate coefficient $\beta_{l=0}$ is plotted as a function of the electric dipole moment for $T \rightarrow 0$ (Wigner regime). The bosons are considered in the same indistinguishable quantum state. In the van der Waals regime, the rate is constant, whereas in the electric-field regime, the rate coefficient behaves as d^2 . Reprinted with permission from ref 162. Copyright 2011 American Physical Society.

of the induced dipole moment d for the different allowed chemical reactions. The different curves represent the reactions $\text{LiNa} + \text{LiNa} \rightarrow \text{Li}_2 + \text{Na}_2$ (red curve), $\text{LiK} + \text{LiK} \rightarrow \text{Li}_2 + \text{K}_2$ (green curve), $\text{LiRb} + \text{LiRb} \rightarrow \text{Li}_2 + \text{Rb}_2$ (blue curve), $\text{LiCs} + \text{LiCs} \rightarrow \text{Li}_2 + \text{Cs}_2$ (pink curve), and $\text{KRB} + \text{KRB} \rightarrow \text{K}_2 + \text{Rb}_2$ (black curve). Using the C_6 coefficients in Table 5, Quéméner et al.¹⁶² found that the loss rate coefficient behaves as a constant plus a term in d^6 (as in eq 45) for the fermionic species, whereas it behaves as a constant plus a term in d^2 for the bosonic species (as in eq 46). Figure 64 shows that fermionic LiNa is the least reactive species while fermionic LiCs is the most reactive one in both the van der Waals (when $d \rightarrow 0$) and electric field (when $d \rightarrow d_{\text{full}}$) regimes. In the case of bosonic molecules, Figure 65 shows that KRB is the least reactive species while fermionic LiK is the most reactive one in the van der Waals regime. In the electric-field regime, all bosonic polar molecules share the same universal rate coefficient, independent of their chemical identity, suggesting that all polar molecules that are subject to strong inelastic and reactive processes should be lost with the same rate for a given d . These trends are well-explained by the expressions given in eq 45 and eq 46. For the fermionic molecules, the ordering of the rate coefficients for the different molecular systems shown in Figure 64 obtained by numerical calculations scales indeed as $(C_6 \mu^3)^{1/4}$ in the van der Waals regime and as μ^3 for a given d in the electric-field regime, as suggested by the expressions. Similarly for the bosonic molecules, the ordering of the curves obtained numerically scales indeed as $(C_6 / \mu^3)^{1/4}$ in the van der Waals regime and is indeed independent of the properties of the polar molecules in the electric-field regime for a given d , as suggested again by the expressions.

4.8. Direct Imaging of Polar Molecules

Wang et al.²⁹⁸ demonstrated a scheme for direct-absorption imaging of ultracold polar molecules of fermionic $^{40}\text{K}^{87}\text{Rb}$. This technique was proposed to give an alternative to the Feshbach imaging performed in the previous studies of KRB molecules,^{1,3,4,114} where the ground rovibronic molecules were “STIRAP-ed” back onto their Feshbach form at a given magnetic field, and the expansions of the atomic clouds were measured rather than directly imaging ground-state molecules. As illustrated in Figure 66a, the authors used an open bound-bound molecular transition between a ground state g (the

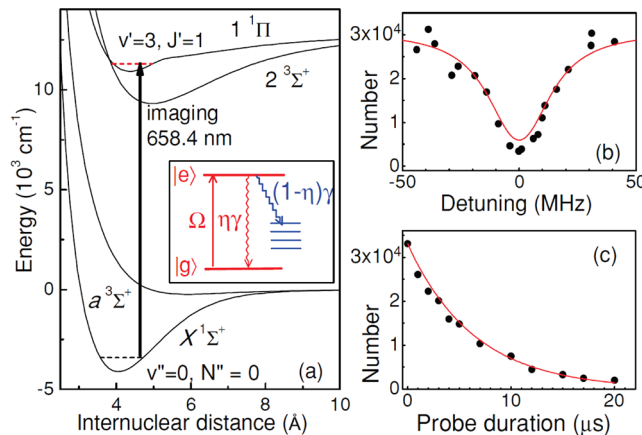


Figure 66. (a) Ab initio electronic potentials for KRB, showing the direct absorption detection scheme for $X^1\Sigma^+$ molecules in the $v'' = 0$, $N'' = 0$ level. The probe light drives a transition to the $v' = 3$ level of the $1^1\Pi$ state. Inset: Schematic of the open two-level model described in the text. (b) An example population-depletion line shape for this transition taken with a $10 \mu\text{s}$ probe pulse duration. (c) Decay of the ground-state population as a function of the probe pulse duration. The probe intensity is $\sim 0.7 \text{ mW/cm}^2$. Solid curves are fits based on the open two-level model. Reprinted with permission from ref 298. Copyright 2010 American Physical Society.

ground rovibronic states of KRB $v = 0$, $N = 0$, $X^1\Sigma^+$) to an excited state e (KRB molecules in $v = 3$, $J = 1$, $1^1\Pi$). Open means that, during the optical transitions, the excited molecules can decay into many dark states (other states than the g and e ones), and $(1 - \eta)\gamma$ corresponds to the decay rate of the excited state into the dark states while $\eta\gamma$ corresponds to the decay rate of the excited state to the ground state. The angular frequency of the transition between the ground and the excited state is $\omega_{ge} = 2\pi c/\lambda$ with $\lambda = 658.4 \text{ nm}$, $\Delta = (\omega - \omega_{ge})$ is the detuning of the probe laser from the transition frequency, and Ω is the probe Rabi frequency. The line shape as a function of the detuning Δ for a probe laser duration of $10 \mu\text{s}$ is shown in Figure 66b. The decay curve as a function of the duration of the probe laser at resonance $\Delta = 0$ is shown in Figure 66c. The probe intensity was taken at 0.7 mW/cm^2 . As can be seen, absorption of ground-state molecules is stronger at resonance and increases with the duration of the open optical transition. Using a set of Bloch equations describing the evolution of the ground ρ_{gg} and excited ρ_{ee} fractional population, and of the coherence $\tilde{\rho}_{eg} = \tilde{\rho}_{ge}^*$, the line shapes and the decay curves for different intensities can be fitted with γ and Ω as free parameters (red lines in Figure 66b and 66c). The open optical transition is then well-characterized and can be used directly to detect the number of ground-state molecules of KRB via absorption imaging.

Using this technique with time-of-flight expansion, the authors can determine the spatial and momentum distributions of the molecular sample. The spatial distribution is illustrated in the absorption image in Figure 67a, for a sample of 39 000 polar molecules in their ground rovibronic state after a time-of-flight of 2 ms. Figure 68a presents the root-mean-squared cloud width as a function of the time-of-flight (TOF) expansion in the radial (blue filled circles) and transverse direction (red open triangles). This measurement provides the radial and transverse temperatures T_x , T_z of the molecular sample. It was found that the mean cloud temperature was $T \approx 220(13) \text{ nK}$, which corresponds to 1.4 times the Fermi temperature T_F of the

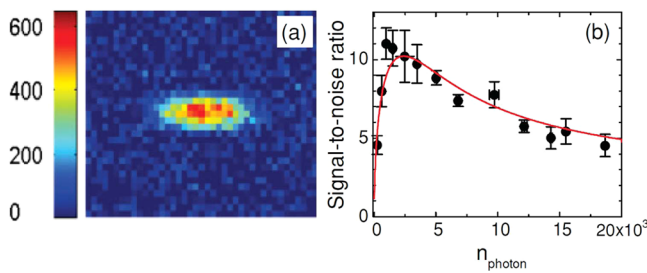


Figure 67. (a) Absorption image ($228 \times 171 \mu\text{m}$) of 39 000 ground-state molecules after a 2 ms TOF. The false color indicates charge-coupled device (CCD) counts, taken for the best signal-to-noise ratio (SNR), with $\sim 75\%$ of the molecules detected. (b) Peak SNR as a function of N_{photon} . Filled circles, experimentally measured peak SNR; solid curve, fit to the model described in the text. The SNR here corresponds to a measured $N_{\text{molecule}} = 950$ per pixel at the cloud center. Reprinted with permission from ref 298. Copyright 2010 American Physical Society.

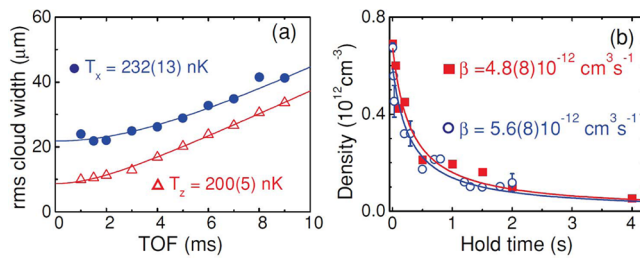


Figure 68. (a) Measurement of the molecular gas temperature by TOF expansion followed by direct absorption imaging. The trap frequencies along the x and z directions are 32 and 195 Hz, respectively. Filled circles and open triangles are the rms cloud widths in the x and z directions, respectively. Solid curves are fits to a ballistic expansion. (b) Measurement of the molecular two-body loss rate β , for an initial temperature of 320 nK, using the direct-imaging (open circles) and Feshbach-imaging (filled squares) methods. Solid curves are fits to a two-body loss model. The extracted values of β agree within the experimental uncertainty. Reprinted with permission from ref 298. Copyright 2010 American Physical Society.

gas.²⁹⁹ Finally, measurements of inelastic collisions (due to chemical reaction $\text{KRb} + \text{KRb} \rightarrow \text{K}_2 + \text{Rb}_2$ and hyperfine-state changing collisions) were also undertaken. Figure 68b shows the ground-state molecular density as a function of time for an initial temperature $T = 320$ nK. The blue open circles corresponds to direct imaging of ground-state molecules while the red filled squares correspond to Feshbach imaging. The main difference between the two techniques comes from the fact that the Feshbach imaging technique is only sensitive to a single hyperfine state, the initial one. Then this technique measures the number of remaining molecules in this initial hyperfine state, providing information on the number of molecules lost by chemical reaction and inelastic hyperfine collision. In contrast, the direct technique provides a simultaneous detection of all hyperfine states in the ground state $N = 0$, because of the larger line width of the probe laser transition compared to the ~ 3 MHz span of the entire hyperfine manifold of states at this magnetic field. In other words, the direct technique will measure (by absorption) all of the molecules, including those that have experienced hyperfine changing collisions, and only provide information on the number of molecules lost by chemical reactions. Those experiencing hyperfine changing collisions will be detected as

not lost, because all the hyperfine states are detected. The two curves in Figure 68b are similar within the experimental uncertainty and provide two similar loss rate coefficients of $\beta_{\text{direct}} = 5.6(8) \times 10^{-12} \text{ cm}^3 \text{ s}^{-1}$ and $\beta_{\text{Feshbach}} = 4.8(8) \times 10^{-12} \text{ cm}^3 \text{ s}^{-1}$. This agreement is consistent with there being no appreciable rate for hyperfine-state-changing collisions. However, in the large magnetic field considered in this experiment, it is also possible that spin-changing collisions to lower energetically states lead to an increase in the kinetic energy of the molecules, so that the hyperfine changed molecules are lost from the trap before the direct imaging.

The direct-imaging technique is advantageous compared to the Feshbach technique. It can be used with arbitrary magnetic and electric external fields. This would be needed, for example, to probe the molecule–molecule scattering resonances for different magnetic and electric fields.³⁰⁰

4.9. Quantum Stereodynamics of Polar Molecules

The paper of Ni et al.⁴ investigated the strong effect of an electric field on a bimolecular chemical reaction. A high loss of molecules was observed, scaling as d^6 . This was attributed to the head-to-tail collisions $m_l = 0$ components of the p -wave collisions $l = 1$ and not to the side-by-side collisions $m_l = \pm 1$. Therefore, to reduce the chemical losses, one can suppress the $m_l = 0$ component and let only the $m_l = \pm 1$ component collide. In free space, one can control the quantum number l associated with the relative angular momentum of the particle collision, by putting all the molecules in the same internal quantum state ($l = 1$ for fermions, $l = 0$ for bosons). However, it is not possible to control the quantum number associated with its projection on the quantization axis \hat{e}_z . For this purpose, Büchler et al.¹⁴⁹ and Micheli et al.¹⁵⁰ proposed in 2007 to load polar molecules into the “pancake” cells of a 1D optical lattice with the direction of confinement \hat{e}_z parallel to an electric field; see section 1.2 for a description of optical lattices. With sufficiently strong confinement, this results in the reduced dimensional quasi-2D collisions in the plane of the pancake, as discussed in section 2.1. As shown in Figure 69, when the electric field is applied, the electric dipole moment is induced along the electric field, and the dipolar molecules collide side-by-side inside the lattice, selecting the $m_l = \pm 1$ partial wave. When the confinement is

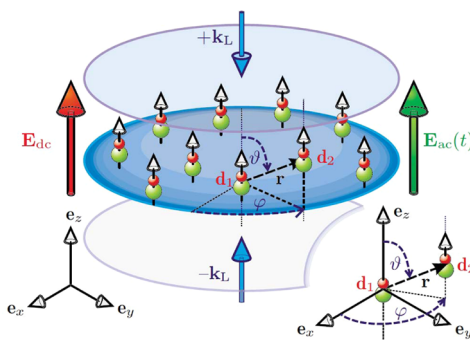


Figure 69. System setup: Polar molecules are trapped in the (x, y) plane by an optical lattice made of two counterpropagating laser beams with wave vectors $\pm k_L = \pm k_L \hat{e}_z$ (arrows on the top and bottom). The dipoles \mathbf{d}_j are aligned in the z direction by a dc electric field $E_{dc} \equiv E_{dc}\hat{e}_z$ (arrow on the left). An ac (microwave) field E_{ac} is indicated (arrow on the right). Inset: Definition of polar (ϑ) and azimuthal (φ) angles for the relative orientation of the intermolecular collision axis r with respect to a space-fixed frame with axes e_x , e_y , e_z . Reprinted with permission from ref 150. Copyright 2007 American Physical Society.

strong enough, Figure 70 shows that a potential energy barrier arises between the two molecules that increases in strength with

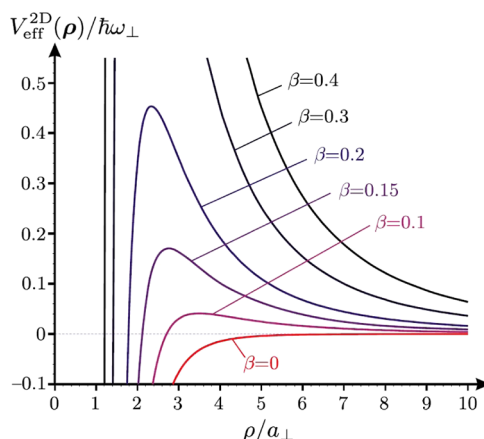


Figure 70. Ground-state effective 2D Born-Oppenheimer potentials $V_{\text{eff}}^{2D}(\rho)$ as a function of the molecular separation ρ in the $z = 0$ plane for various strengths of the dc electric field $\beta = 0, 0.1, 0.15, 0.2, 0.3$, and 0.4 . The quantity a_{\perp} is the harmonic oscillator length in the z direction. The molecular parameters are chosen as $(d^4 m^3 B / \hbar^6)^{1/2} = 1.26 \times 10^6$, and the frequency of the harmonic potential in the z direction is $\omega_{\perp} = 15B/10^6\hbar$. This corresponds to the case of SrO with a mass $m = 104$ amu, a rotational constant $B \approx \hbar \times 10$ GHz, and a permanent dipole moment $d \approx 8.9$ D in a tight confining potential with $\omega_{\perp} = 2\pi \times 150$ kHz, where $a_{\perp} \approx 25$ nm. Reprinted with permission from ref 150. Copyright 2007 American Physical Society.

increasing electric field. This can be used to suppress the chemical reaction of polar molecules, as discussed in several theoretical papers.

In 2009 Ticknor determined the elastic cross section when two particles are confined in a pure 2D environment.³⁰¹ He used the Born approximation in the threshold region of ultralow energies and a semiclassical Eikonal approach when the collision energy is increased and found that scattering between dipoles is governed by universal properties in pure 2D. In the Born approximation regime, Ticknor found that, for $m > 0$, the elastic cross section behaves as

$$\sigma_m^{\text{BA}} = \frac{4}{k} \frac{(Dk)^2}{(m^2 - 1/4)^2} \propto d^4 \quad (62)$$

where $D = \mu d^2/\hbar^2$ is the dipole length.³⁰² The partial wave l is no longer a good quantum number in pure 2D, but m , the projection of the orbital angular momentum onto the z -axis, is still a good quantum number. In the semiclassical regime, when more partial waves contribute, the elastic cross section is

$$\sigma^{\text{SC}} = \frac{4}{k} \sqrt{\pi D k} \propto d \quad (63)$$

In a subsequent study, Ticknor included the effect of the 1D confinement using an harmonic oscillator.¹⁵² He studied the scattering properties of the dipoles in the confinement as a function of $\bar{D} = D/l$, the ratio of the dipole length $D = \mu d^2/\hbar^2$ over the confinement length $l = (\hbar/(\mu\omega))^{1/2}$, where ω is the angular frequency of the harmonic oscillator. He found that there is no adiabatic barrier for the incoming motion when $\bar{D} < 0.34$. He also estimated a JWKB probability for the incident particles to tunnel the adiabatic barrier

$$\ln(P_T) = a(\bar{D})^{2/5} + b(\bar{D})^{-1/10} \quad (64)$$

The parameters a, b , which depend on the energy ratio E/E_D (E is the scattering energy and $E_D = \hbar^2/(2\mu D^2)$ is the dipole energy), are fitted from the numerical data. At large \bar{D} and E/E_D values, Ticknor showed that the tunneling probability can be expressed by

$$P_T = 139.3(E/E_D)^2 e^{-5.86(\bar{D})^{2/5}} \quad (65)$$

and is in good agreement with the numerical data. The exponential dependence was also found by Büchler et al.¹⁴⁹ The results of Ticknor are summarized in Figure 71. The solid red

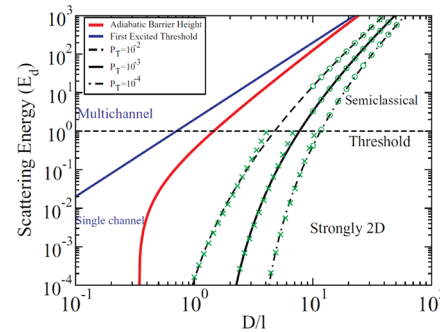


Figure 71. Character of the quasi-2D scattering as a function of E/E_D versus $\bar{D} = D/l$. The excited threshold (solid blue) and the height of the adiabatic barrier (solid red) are shown. The JWKB tunneling probability contours for $P_T = 10^{-2}$ (dashed black), 10^{-3} (solid black), and 10^{-4} (dash-dot black) are plotted. The green x's in each plot are the fitted P_T from eq 62, and the green circles are the fit for the semiclassical energy regime from eq 63. Reprinted with permission from ref 152. Copyright 2010 American Physical Society.

line is the height of the adiabatic barrier, the solid blue line is the first excited threshold, and the black lines are the JWKB tunneling probability P_T , for $P_T = 0.01$ (dashed black), $P_T = 0.001$ (solid black), and $P_T = 0.0001$ (dash-dot black), respectively. One can clearly see that the height of the barrier, expressed in units of the dipole energy E_D , vanishes for $\bar{D} = 0.34$. If the energy E/E_D is below the red curve, it means that there is a barrier for the incoming motion, and the probability of tunneling such a barrier is given by the black curves, with decreasing probability when \bar{D} is increased, that is, when the induced dipole d is increased and/or the confinement l is decreased. In addition, to stay in the quantum regime, $E/E_D < 1$ and has to be below the horizontal dashed line.

In 2010 and 2011, Quéméner and Bohn^{153,154} showed, using quantitative molecular parameters from the previous experiments on KRB polar molecules, how a chemical reaction can be suppressed in an optical lattice by applying an electric field. The idea is the same as the one expressed by Büchler et al.¹⁴⁹ and Micheli et al.,¹⁵⁰ as mentioned above. The authors considered the dynamics of two particles in a 1D optical lattice and an electric field, both applied along the \hat{e}_z direction, using a time-independent quantum formalism. In this study, the optical lattice was supposed to be deep enough to assume that it can be represented with a series of independent harmonic oscillators of frequency ν and angular frequency $\omega = 2\pi\nu$. When the particles 1 and 2 are well-separated, they are confined in a definite eigenstate of the harmonic oscillator, say $|n_1\rangle$ and $|n_2\rangle$, with energies $\epsilon_{n_1} = \hbar\omega(n_1 + 1/2)$ and $\epsilon_{n_2} = \hbar\omega(n_2 + 1/2)$.

In this kind of confining environment, the symmetrization principle provides additional selection rules. Consider the total

wave function of the colliding system (in a cylindrical coordinates representation ρ, z, φ)

$$\begin{aligned} |\Psi\rangle &\propto \{|\alpha_1\rangle|\alpha_2\rangle + \eta|\alpha_2\rangle|\alpha_1\rangle\} \times \{|n_1\rangle|n_2\rangle + \gamma|n_2\rangle|n_1\rangle\} \\ &\times \frac{1}{\sqrt{\rho}} G(\rho) e^{im_l\varphi} \end{aligned} \quad (66)$$

where the first, second, and third terms in the right-hand side of the equation are, respectively, the symmetrized internal wave function (with internal states $\alpha_i, i = 1, 2$), the symmetrized external confining wave function (with external states $n_i, i = 1, 2$), and the collision wave function. $\eta, \gamma, (-1)^{m_l}$ are, respectively, the eigenvalues of the particle permutation operator \hat{P} of each of the three terms in the equation and can take ± 1 values. The symmetrization principle has also to satisfy $\hat{P}|\Psi\rangle = \varepsilon_p|\Psi\rangle$ with $\varepsilon_p = +1$ for identical bosons and $\varepsilon_p = -1$ for identical fermions, so we obtain the selection rule

$$\eta\gamma(-1)^{m_l} = \varepsilon_p \quad (67)$$

For two identical particles (same mass, same isotope), in the same internal states $\alpha_1 = \alpha_2$ (for example, in the absolute rovibronic ground state) and the same external confining state $n_1 = n_2$ (for example, the ground confining state), one has only to consider the eigenvalues $\eta = +1$ and $\gamma = +1$, and the selection rule in eq 67 implies that m_l is restricted to odd values for fermionic particles and restricted to even values for bosonic particles. If the particles are not in the same external state, one has to consider both eigenvalues $\gamma = +1$ and, therefore, all odd and even values of m_l . Note that if the particles are not in the same internal state, one has to consider both eigenvalues $\eta = \pm 1$ and all odd and even values of l .

Two kinds of suppression of the reaction rate were shown:¹⁵⁴ a statistical suppression and a dipole–dipole potential energy suppression. The statistical suppression only works for indistinguishable fermionic particles, at moderate confinement and electric fields, and does not work for indistinguishable bosons or distinguishable particles. Figure 72 shows the height of the barrier for the incoming motion of two fermionic (top panel) and bosonic (bottom panel) indistinguishable KRb molecules in their absolute internal and external ground states, as a function of the dipole moment d induced by the electric field and as a function of the confinement strength ν of the harmonic cells made by the one-dimensional optical lattice. This picture is the equivalent of the barrier in Figure 60. On one hand, for small dipole and confinement strengths, the two particles start at a large distance apart in the confining optical lattice, in a well-defined harmonic oscillator state (in the ground external state $n_1 = n_2 = 0$ in Figure 72), with well-defined harmonic oscillator energy. The particles are confined in the \hat{e}_z direction. As the two particles approach each other, the harmonic oscillator potential becomes weaker while the molecular interaction becomes stronger: the molecules are less confined in the \hat{e}_z direction, the interaction changes in character from cylindrical symmetry to spherical symmetry, and the molecules collide as if in free space. This situation is often called “quasi-2D”. As a consequence, indistinguishable fermions collide in a p -wave with a centrifugal barrier, while indistinguishable bosons collide in a s -wave with no centrifugal barrier, as can be seen in Figure 72. For ground-state fermions, only $m_l = \pm 1$ is allowed, and the centrifugal barrier increases with d , making the statistical suppression only work for fermions (for ground-state bosons, only $m_l = 0$ is allowed and there is no barrier). There is clearly an effect of the quantum

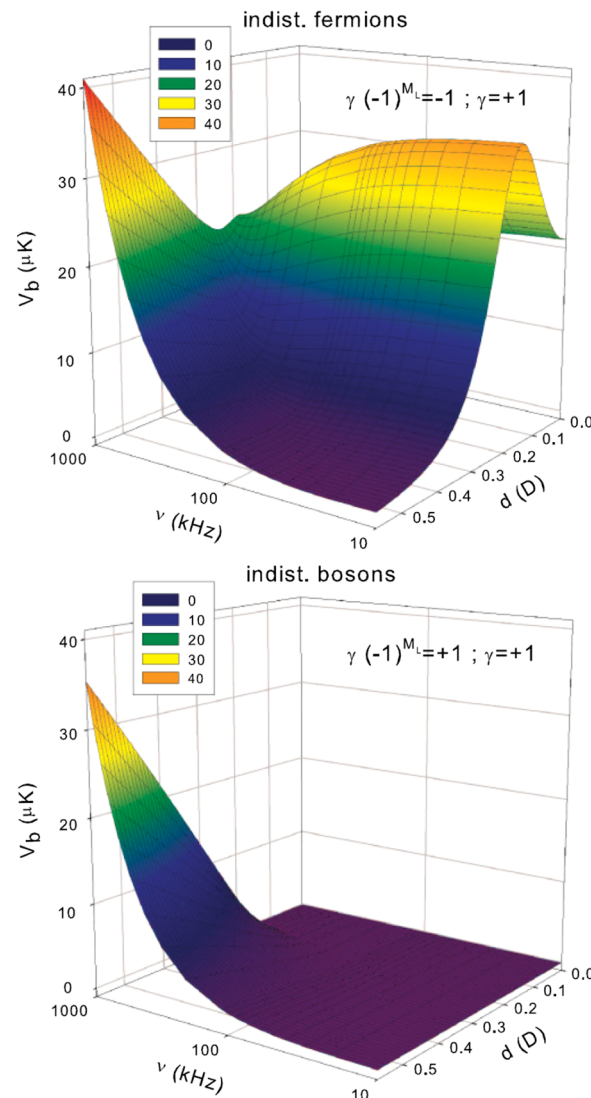


Figure 72. Height of the adiabatic barrier V_b versus d and ν for indistinguishable fermions (top panel) and for indistinguishable bosons (bottom panel) in the lowest confining state. Reprinted with permission from ref 154. Copyright 2011 American Physical Society.

statistics of the system. On the other hand, the dipole–dipole potential energy suppression is a “mechanical” suppression. At large dipole and confinement strengths, the molecules start strongly confined in the \hat{e}_z direction at long distance. As the molecules approach each other, the confinement remains strong and the particles are still confined in \hat{e}_z while they overcome the molecular interaction. This is the situation of pure 2D. Now when the electric field is turned on, there is an induced dipole along \hat{e}_z , and when the molecules approach each other they collide side-by-side, for which the dipole–dipole interaction is repulsive. As a result, the height of the barrier increases more and more as the confinement and dipole strengths are increased, as seen in Figure 72. Because the repulsive dipole interaction is independent of whether the particles are indistinguishable bosons/fermions or not, this is not a statistical effect and will work for any particles with a dipole moment. The corresponding collisional rate coefficients for two fermionic (top panel) and bosonic (bottom panel) indistinguishable KRb molecules are presented in Figure 73. The red curve represents the elastic process while the colored

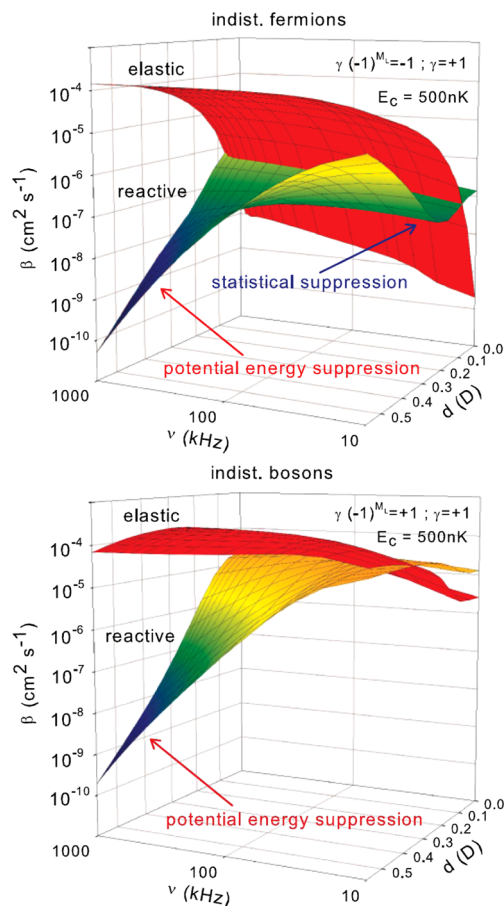


Figure 73. Elastic and reaction rate coefficients versus d and ν for indistinguishable fermions (top panel) and for indistinguishable bosons (bottom panel) at $E_c/k_B = 500$ nK. The elastic curve is plotted in red. Reprinted with permission from ref 154. Copyright 2011 American Physical Society.

curve represents the reactive process. The higher the incident barrier, the lower are the reactive processes. In this potential suppression regime, the reaction rate vanishes and elastic collisions are strong. This regime offers a favorable environment to protect the molecules from bad collisions and losses and to provide strong elastic rates for fast thermalization when evaporative cooling techniques are used. This regime contrasts with the statistical regime, where the suppression occurs only for fermions, not for bosons.

Micheli et al.¹⁴⁶ provided the analytical expressions to describe the universal elastic and reactive scattering of molecules in one- and two-dimensional confinement interacting through a van der Waals potential, using a quantum defect theory.¹⁶¹ For the dipole–dipole regime, they use a time-independent close-coupling formalism. They also arrived to the same conclusions that chemical reactivity of indistinguishable fermions can be suppressed for moderate induced dipole and trapping strength, whereas bosons or unlike fermions require higher dipole and trapping strengths.

Quéméner et al. also considered the reactive collision rates either when the indistinguishable particles start in the same external state (intraband collisions) or when they start in different external states (interband collisions) at ultralow collision energy, in the presence of an electric field. They also investigated the inelastic collision rates when two indistinguishable particles are promoted to a different band (by excitation to

a higher band or by relaxation to a lower band), when the collision energy and the induced dipole are increased.

In 2011 de Miranda et al.¹⁵⁵ explored the quantum stereodynamics effect of an ultracold bimolecular reaction. Ultracold polar molecules of fermionic $^{40}\text{K}^{87}\text{Rb}$ were produced inside a stack of 1D optical lattices with confinement frequency $\nu = 23$ kHz. The lattices were deep enough to consider no interlayer tunneling. They produced $\sim 34\,000$ ground-state molecules in an average of 23 layered pancakes with 2200 molecules in the center layer and a peak density of 3.4×10^7 molecules/cm². They performed a series of three different measures, as sketched in Figure 74c. The first experiment

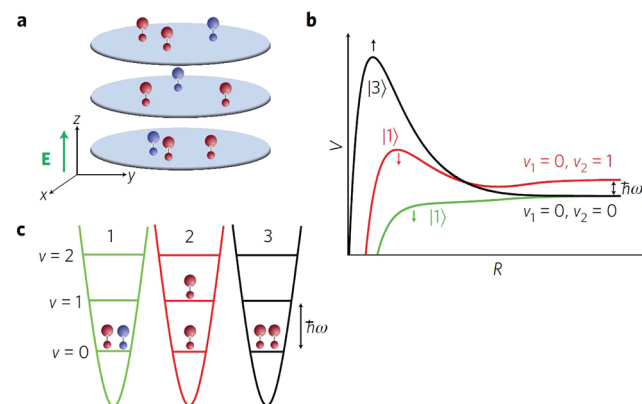


Figure 74. Quantized stereodynamics of ultracold chemical reactions in quasi-two dimensions. (a) A quasi-2D geometry for collisions is realized for polar molecules confined in a 1D optical lattice. An external electric field is applied along the tight confinement axis. (b) Schematic showing the three lowest adiabatic potentials for collisions as a function of the intermolecular separation, R . (c) Schematic showing each individual case for the three lowest collision channels. Reprinted with permission from ref 155. Copyright 2011 Nature Publishing Group.

consisted of loading a 50/50 mixture of polar molecules in different rotational states using microwave transitions.¹¹⁴ They measured the loss of molecules as a function of time and extracted an initial rate coefficient β_1 for this process. The second and third experiments consisted of loading KRB molecules in the same internal state, respectively, with and without a thermal Maxwell–Boltzmann distribution. The thermal distribution had a temperature of $T = 800$ nK. The nonthermal distribution was made by parametric heating in the \hat{e}_z direction, by modulating the lattice intensity at twice the confinement frequency ν to excite the molecules from band $\nu = 0$ to band $\nu = 2$. With these two experiments, they were able to measure the rate coefficient of interband β_2 and intraband collisions β_3 for indistinguishable molecules as sketched in Figure 74c. To extract these rate coefficients, they needed the population number of the molecules in the bands. They measured it with an adiabatic band-mapping technique.^{303,304} The optical lattice is smoothly ramped down, and the molecules in different bands are then adiabatically mapped onto the Brillouin zones. The relative populations n_ν/n_{tot} are extracted from the momentum distribution of the molecules. This is shown in Figure 75a for a thermal distribution at $T = 800$ nK and in Figure 75b for a nonthermal distribution from parametric heating. The authors found, respectively, a population distribution of $n_0/n_{\text{tot}} = 0.76$, $n_1/n_{\text{tot}} = 0.23$, $n_2/n_{\text{tot}} = 0.01$, in agreement with a Maxwell–Boltzmann

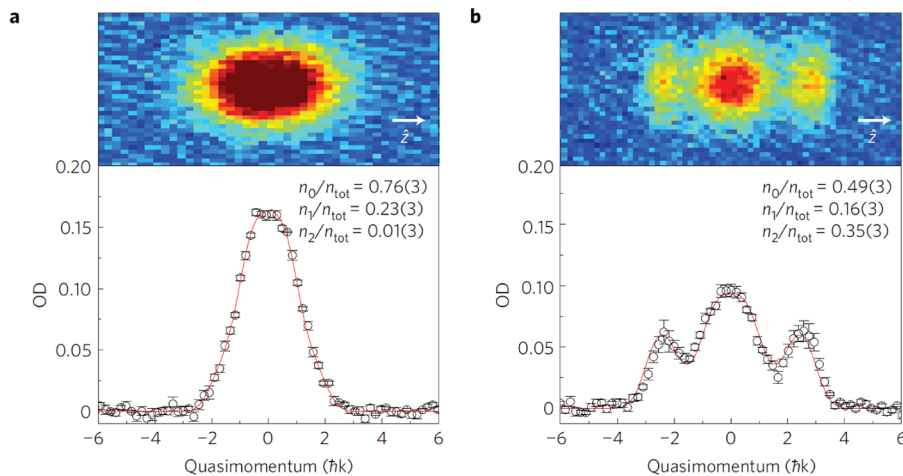


Figure 75. Relative population of molecules in the lattice vibrational levels. (a, b) The results for the initial distribution of molecules (a) and for a nonthermal distribution created by parametric heating in \hat{z} (b). Reprinted with permission from ref 155. Copyright 2011 Nature Publishing Group.

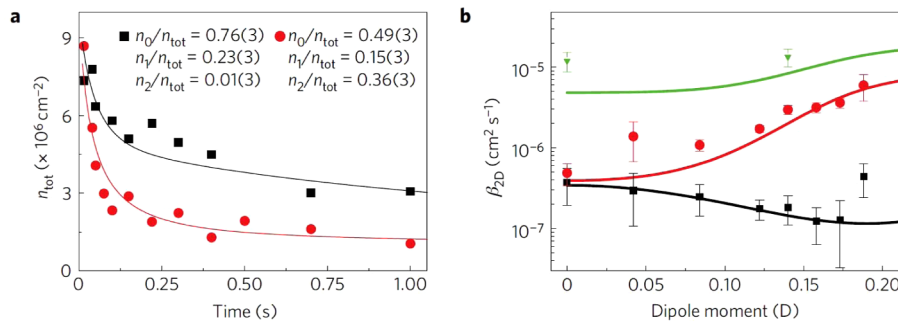


Figure 76. Measurements of 2D loss rates and comparison with theory. (a) A fit (solid lines) to the measured loss curves, with (red circles) and without (black squares) 0.3 ms of parametric heating in \hat{z} , is used to extract the loss-rate constants β_{13} and β_{12} . (b) The extracted loss-rate constants for collisions of molecules in the same lattice vibrational level (black squares) and from different lattice vibrational levels (red circles) plotted for several dipole moments. Measured loss-rate constants for molecules prepared in different internal states are shown as green triangles. The solid lines represent the results of a quantum scattering calculation. (See Figure 74b and 74c.) Reprinted with permission from ref 155. Copyright 2011 Nature Publishing Group.

distribution, and $n_0/n_{\text{tot}} = 0.49$, $n_1/n_{\text{tot}} = 0.16$, $n_2/n_{\text{tot}} = 0.35$ using the parametric heating. For these two experiments, they measured the molecular loss as a function of time, as shown in Figure 76a. Using three different equations that describe the evolution of the population of the three vibrational levels $\nu = 0$, 1, and 2 in time, they extracted the interband β_2 and intraband β_3 rate coefficients. They repeated the measurements with different dipole moments d for different electric fields. The three chemical rate coefficients β_1 , β_2 , and β_3 as a function of d are reproduced in Figure 76b, for distinguishable molecules (green triangle points) and for indistinguishable molecules, for the interband collisions (red circle points) and for the intraband collisions (black square points). The theoretical predictions using the formalism developed by Quéméner and Bohn^{153,154} are also shown, respectively, in green, red, and black curves, showing very good agreement with the experiment. The qualitative trend can be explained using the symmetrization rules developed in refs 153 and 154. The coefficient β_1 corresponds to a case of collisions of distinguishable molecules. This leads to *s*-wave collisions, so there is no centrifugal barrier in the effective potential curve for the incoming motion of the KRb molecules, as sketched in Figure 74b for the green curve. This curve gets more and more attractive when the electric field is increased, as indicated by the arrow pointing down. It is then easier and easier for the

molecules to come together and chemically react, so the reaction rate coefficient should increase with the electric field and the induced dipole moment, as seen in Figure 76b. The coefficients β_2 and β_3 correspond to a case of collisions of indistinguishable fermionic molecules. They collide in a *p*-wave, and there is a centrifugal barrier for the incoming motion. Therefore, the rates β_2 and β_3 are smaller than those for *s*-wave collisions of distinguishable molecules. The coefficient β_2 corresponds to interband collisions, where the molecules are not in the same confining state. Therefore, as mentioned previously with the symmetrization rules, both components $|m_l| = 0$ and 1 have to be included in the dynamics. The effective potential curve for the dominant term $m_l = 0$ is plotted in Figure 74b in red, and the barrier decreases with increasing electric fields, as indicated by the arrow. Therefore, the corresponding rate coefficient increases with d . Finally, β_3 corresponds to intraband collisions, where the molecules are in the same confining state. For fermionic molecules, this corresponds to the selection of $|m_l| = 1$. The effective potential curve for this term is plotted in Figure 74b in black, and the barrier increases with the electric field. As a consequence, the chemical reaction rate decreases with d . This leads to a chemical reaction suppression of ~ 60 , at the highest electric field reached in the experiment, compared when the molecules are not loaded into an optical lattice. Calculations performed by

Quéméner and Bohn¹⁵³ showed that the elastic rate coefficient, at the highest electric field reached in the experiment and at the same confinement lattice, should also be of about a factor 60 higher than their suppressed chemical losses. This is a favorable situation for trying to perform evaporative cooling of the molecules.

D’Incao and Greene³⁰⁵ investigated the collisional aspects of fermionic and bosonic molecules in quasi-2D geometry with an emphasis on scattering resonances of the elastic and inelastic/reactive processes. Except when dipole–dipole scattering resonances occur, they found a very good agreement between a JWKB phase shift formula and a numerical calculation for strong confinement, large dipole strength, and small collision energies. This universality is due to the fact that the phase shift is mainly due to the long-range $1/R^3$ interaction and does not depend on the short-range physics.²⁹⁵ The elastic scattering resonances that appear when the induced dipole is varied are extremely narrow. In addition, contributions from a number of m_l values have to be summed, washing out the narrow resonances because they are out of phase. Therefore, the interaction between dipoles in a dipolar gas may be difficult to tune for many-body physics applications. The authors also computed the scattering amplitude in the quasi-2D geometry as a function of the scattering angle and induced dipole moment and found that the forward and backward directions are the main directions of dipolar scattering. However, as the dipole is increased, other specific directions of scattering appear but are less pronounced than the backward and forward directions. Finally they proposed an energy-dependent analytical form of the pseudopotentials for dipolar scattering, which can be helpful for future studies of a strongly interacting gas of polar molecules from a many-body point of view.

Dipolar collisions in the quasi-2D geometry from 1D optical lattice cells have also been investigated for different alkali polar molecules by Julienne et al.⁷⁵ and Quéméner et al.¹⁶² Figure 77 shows the loss rate coefficient from numerical calculations⁷⁵ as a function of the induced dipole moment d , assuming a full-loss probability when the molecules meet, for inelastic and/or reactive collisions of fermionic KRb + KRb (red curves),

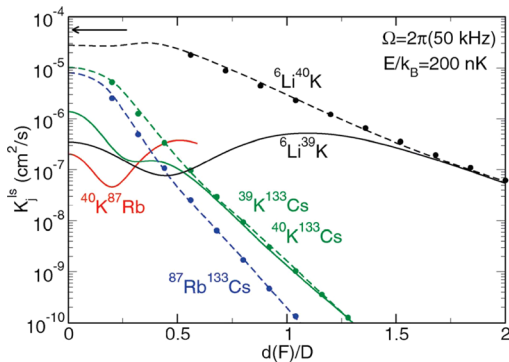


Figure 77. Universal loss rate constant K_{ls}^0 for quasi-2D collisions at $E/k_B = 200$ nK in an $\omega = 2\pi(50$ kHz) 1D lattice cell for bosonic (dashed lines) ${}^6\text{Li}{}^{40}\text{K}$, ${}^{39}\text{K}{}^{133}\text{Cs}$, and ${}^{87}\text{Rb}{}^{133}\text{Cs}$ and K_{ls}^0 for fermionic (solid lines) ${}^6\text{Li}{}^{39}\text{K}$, ${}^{40}\text{K}{}^{87}\text{Rb}$, and ${}^{40}\text{K}{}^{133}\text{Cs}$. In the case of the nonreactive species KCs and RbCs, these rate constants are given because they may apply to vibrational quenching for low vibrational levels with $v \geq 1$. The black arrow shows the quasi-2D unitarity limit $2\hbar/\mu$ for bosonic ${}^6\text{Li}{}^{40}\text{K}$. Reprinted with permission from ref 75. Copyright 2011 Royal Society of Chemistry.

fermionic (solid black curve) and bosonic (dashed black curve) ${}^6\text{Li}{}^{40}\text{K}$, and for inelastic collisions of bosonic ${}^{40}\text{K}{}^{133}\text{Cs}$ + ${}^{40}\text{K}{}^{133}\text{Cs}$ (dashed blue curve), and fermionic (solid green curve) and bosonic (dashed green curve) ${}^6\text{Li}{}^{39}\text{K}$ + ${}^6\text{Li}{}^{39}\text{K}$. The harmonic confinement frequency was set to 50 kHz, and the collision energy was set to 200 nK. The electric field and dipole are assumed to be aligned along the z direction of tight confinement. As for normal 3D collisions, the fermionic species have smaller rate coefficients at zero dipole than the corresponding bosonic species. The rate coefficients for the bosonic and fermionic forms of a given species converge to the same values at sufficiently strong dipole strength. The figure shows that effective suppression of the loss rate can occur for certain species such as RbCs and KCs for moderate conditions of electric field, confinement, and temperature. For example, at $d \approx 1$ D the rate coefficients lie in the range between 10^{-10} and 10^{-9} $\text{cm}^2 \text{s}^{-1}$. For similar conditions, losses of other species like KRb or LiK are not suppressed. Even at $d = 2$ D for LiK, the loss rate coefficient is still as high as 10^{-7} $\text{cm}^2 \text{s}^{-1}$. Note that, for a 2D density of 10^7 molecules/ cm^2 , a collisional decay lifetime of 1 s corresponds to a rate coefficient of 10^{-7} cm^2/s . Smaller rate coefficients result in lifetimes longer than 1 s for this density.

The ground state of vibration, rotation, and spin for the RbCs molecule has no reactive or inelastic quenching channels and, thus, will not be subject to two-body loss collisions. Consequently, two such molecules will only experience elastic collisions, which might have tunable scattering resonances similar to the ones illustrated in section 4.7 by Figure 63 in the limit of small loss $y \ll 1$ and studied by D’Incao and Greene.³⁰⁵ Hanna et al.³⁰⁶ investigated such resonances that appear in quasi-2D elastic collisions using a simple toy model of two RbCs molecules in their vibrational–rotational ground state interacting through a single potential that supports only a few bound states. They also numerically calculated the eigenstates of the two molecules in a tightly confining 3D harmonic trapping cell with a “pancake” aspect ratio. The lattice cell had tight confinement in the z -direction, along which the electric field orienting the direction of the RbCs dipoles was pointing, and very weak confinement in the x , y directions. The limit of vanishing x , y confinement corresponds to quasi-2D collision geometry. Figure 78 compares the quasi-2D elastic scattering rate coefficient with the pattern of eigenvalues for the 3D pancake trap geometry with the same z confinement as the quasi-2D case. Figure 78 illustrates how a series of resonances appear when the electric field tunable bound states of the pancake cell cross the collision threshold. The resonance widths are quite narrow versus dipole strength, as expected from the work of D’Incao and Greene.³⁰⁵ Hanna et al.³⁰⁶ show that the resonance coupling is much stronger if the confinement is strong in all three dimensions. The toy model is limited in that it omits coupling to higher rotational states of the dipoles and to their internal nuclear spin structure. It will be important to assess the role of such couplings, especially that of nuclear spin, in modifying this relatively simple resonance picture.

4.10. Ground-State Molecules in 3D Optical Lattices

In 2010 Danzl et al.² formed ultracold Cs₂ molecules in their ground rovibronic state in a three-dimensional optical lattice. The experimental procedure is summarized in Figure 79. A Bose–Einstein condensate of Cs atoms is loaded into a 3D optical lattice. Then this superfluid regime is driven into the Mott-insulator regime by increasing the lattice depth. The

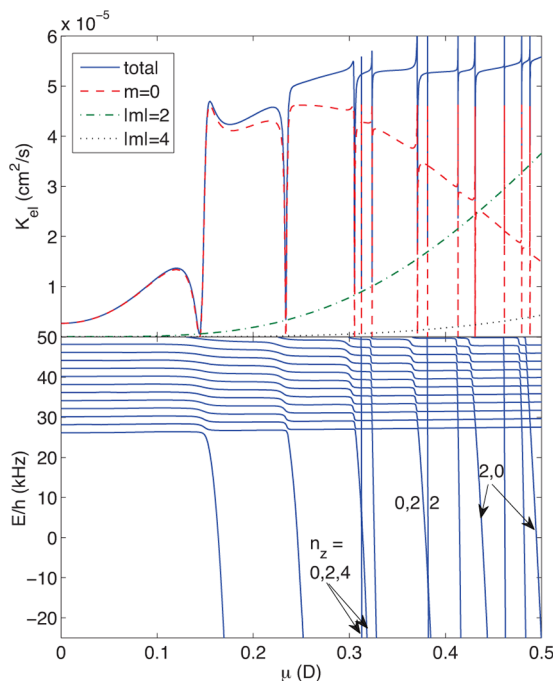


Figure 78. Upper panel shows the elastic collision rate coefficient versus electric field-induced dipole strength μ in D for quasi-2D scattering with a model potential of identical bosonic RbCs collisions at $E/k_B = 200$ nK and for a z confinement frequency of 50 kHz. The lower panel shows the calculated eigenstates for the same RbCs potential when weak harmonic confinement with a frequency of 1 kHz is added in the x and y directions. Several bound states cross threshold as dipole strength increases, corresponding to narrow resonances in the quasi-2D scattering. Reprinted with permission from ref 306. Copyright 2012 American Physical Society.

authors optimized the experimental conditions to obtain the highest number of lattice sites with two atoms per site in the central region of the lattice. They finally obtained up to 45% of the atoms in a double occupied site. The two atoms per site are then magneto-associated to form Feshbach molecules with 94% efficiency and are further magnetically ramped in the high vibrational state $|1\rangle = |\nu = 155\rangle$ (see Figure 80b). This is the starting condition for the experimentalists to form molecules in the ground states. Although the molecules are still in a high vibrational level, they are in the ground motional state of the lattice and are well-protected from collisional losses. Afterward, a stimulated Raman adiabatic passage technique is used with four laser transitions L_1 , L_2 , L_3 , and L_4 , as sketched in Figure 80a, for the transition between the different states $|1\rangle \rightarrow |2\rangle \rightarrow |3\rangle \rightarrow |4\rangle \rightarrow |5\rangle$ to coherently transfer the molecules into the lowest rovibronic level ($\nu = 0$, $N = 0$, $X^1\Sigma_g^+$) of Cs₂ molecules. This experimental configuration ensures the population of a particular hyperfine sublevel with total spin $I = 6$ and projection onto the magnetic field axis $M_I = +6$, indicated as a bold red line in Figure 80c. This state becomes the absolute ground state for magnetic fields larger than ~ 13 mT (130 G).

To ensure an efficient transfer from the Feshbach molecule to the ground-state molecule in a site of the optical lattice, there should be a good matching of their motional wave functions. If there is a bad matching, this leads to unwanted excitation in higher lattice bands and to loss of state control during the transfer. As a result, Danzl et al. operated at the magic wavelength,^{307,308} the wavelength of the optical lattice for which both initial Feshbach and final ground-state molecules

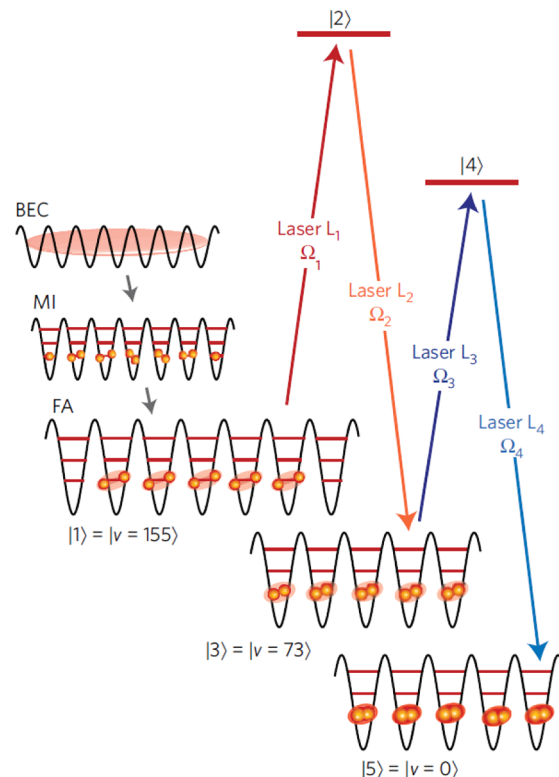


Figure 79. Molecular quantum-gas preparation procedure. A BEC of Cs atoms is loaded into an optical lattice. By increasing the lattice depth, a Mott-insulator state (MI) with preferentially two atoms per site is created. Feshbach association (FA) subsequently converts atom pairs into weakly bound molecules in state $|1\rangle$. These are then transferred in the presence of the lattice to a specific hyperfine level $|I = 6, M_I = 6\rangle$ of the rovibronic ground state $|5\rangle = X^1\Sigma^+|\nu = 0, J = 0\rangle$ by a stimulated four-photon process (STIRAP) involving lasers L_i with Rabi frequencies Ω_i , $i = 1, 2, 3$, and 4, and three intermediate levels $|2\rangle$, $|3\rangle$, and $|4\rangle$. Reprinted with permission from ref 2. Copyright 2010 Nature Publishing Group.

have an equal polarizability and consequently an equal light shift in an optical lattice cell, so that they have the same motional wave function.

Danzl et al. investigated the band structure of the ground-state molecules. They extracted in Figure 81 the band energies as a function of different lattice depths by phase and amplitude modulation of one lattice beam generating the lattice. The inset (iii) shows a typical plot of the amplitude (top) and phase (bottom) modulation experiment, for the normalized ground-state molecule number as a function of the modulation frequency. The resonant shape is a signature of the excitation to higher excited bands. Inset (i) presents a typical molecular momentum distribution when the molecules are transferred, in-resonance in inset (iii) to higher lattice bands by amplitude modulation. The momentum distribution barely changes when off-resonance in inset (iii), so that almost no ground-state molecules are excited to higher bands as seen in inset (ii). By using the band structure calculations to fit all modulation spectra curves, as the ones in inset (iii), using the dynamic polarizability as a free parameter, Danzl et al. extracted a polarizability of $P_{\nu=0} = 2.1(1) \times P_a$ for the ground-state molecules and a polarizability of $P_F = 2.0(1) \times P_a$ for the Feshbach molecules, where P_a is the atomic polarizability. This confirmed that the two types of molecules saw the same

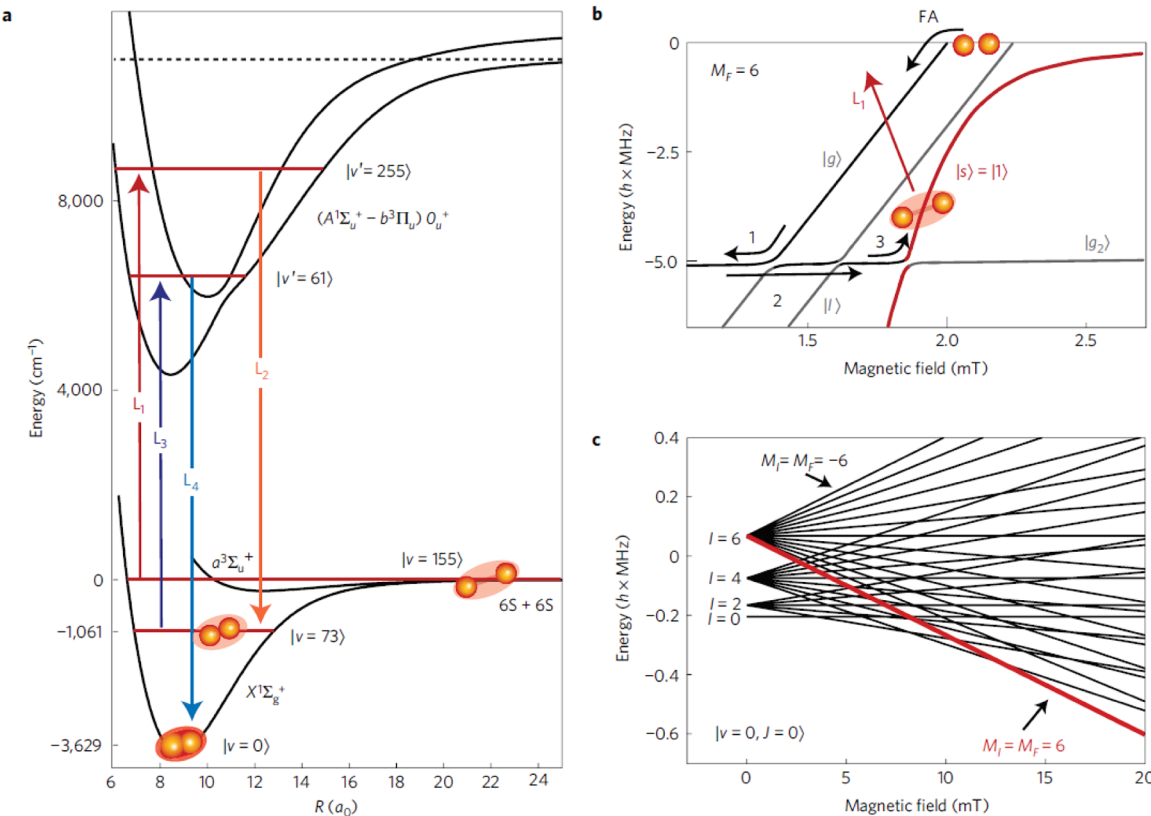


Figure 80. Molecular potentials and level schemes for ground-state transfer. (a) The four-photon transfer from the weakly bound Feshbach level $|l1\rangle = |v \approx 155\rangle$ (the $6S + 6S$ asymptote) to the rovibrational ground state $|l\rangle = |v = 0, J = 0\rangle$ of the singlet $X^1\Sigma_g^+$. (b) Zeeman diagram for weakly bound molecules near the $6S + 6S$ asymptote. (c) Calculated Zeeman diagram for the hyperfine manifold of the rovibronic ground state $|l\rangle = |v = 0, J = 0\rangle$. There are no avoided crossings between different hyperfine sublevels. Reprinted with permission from ref 2. Copyright 2010 Nature Publishing Group.

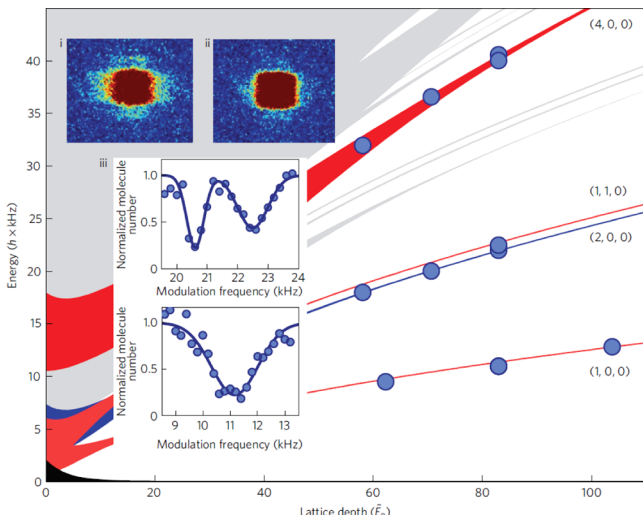


Figure 81. Lattice band structure for $|v = 0\rangle$ molecules. Band energies as a function of lattice depth in units of the molecular recoil energy E_R as measured by phase and amplitude modulation of the lattice. Inset (i) shows the molecular momentum distribution after transfer to higher lattice bands by resonant lattice amplitude modulation. For comparison, inset (ii) shows that hardly any population is transferred to higher bands for off-resonant modulation. Inset (iii) shows typical excitation spectra for amplitude (top) and phase (bottom) modulation at $83 E_R$. Reprinted with permission from ref 2. Copyright 2010 by the Nature Publishing Group.

potential in the lattice, and that they worked indeed at the magic wavelength.

Finally, Danzl et al. measured the lifetime of the ground-state Cs_2 molecules. Using a single-body exponential decay fit, they extracted a $1/e$ lifetime of $\tau = 8.1(6)$ s. The experiment performed by Danzl et al. is a major step toward a future achievement of a molecular Bose–Einstein condensate of ground-state molecules, if favorable elastic collisions between Cs_2 molecules lead to efficient evaporative cooling of the molecular sample. This experiment also offers a perfect environment for studying accurate inelastic state-to-state hyperfine changing collisions when the magnetic field is below 130 G, or pure elastic collisions when the magnetic field is above 130 G. Such collisions could be studied, for example, by turning off the lattice or lowering its depth so that the molecules could start to collide.

In 2011 Chotia et al.³⁰⁹ realized a three-dimensional optical lattice with long-lived $^{40}\text{K}^{87}\text{Rb}$ polar molecules in their ground state. They first loaded an optical dipole trap with ultracold K and Rb atoms, created a one-dimensional optical lattice in the z direction, then converted the x, y optical dipole trap to a 3D array of optical lattice cells (see Figure 2), and adjusted the intensities of the three optical lattice beams to their final values. Inside the 3D lattice, they performed the STIRAP procedure to create ground-state molecules. During this procedure, residual K and Rb atoms are removed using resonant light pulses. The detection of ground-state molecules is done by reversing the STIRAP procedure to go back to Feshbach molecules, and the K atoms are imaged using a probe laser. Figure 82 shows the

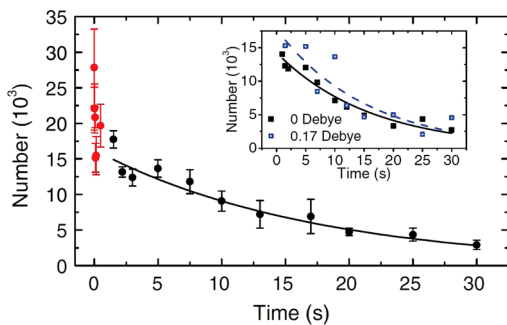


Figure 82. Loss of ground-state KRb molecules as a function of time in a 3D lattice with depths of $56E_R$, $56E_R$, and $70E_R$ in x , y , and z , respectively. Neglecting the very short time points (red solid circles), the number of molecules for times larger than 1 s (black solid circles) are fit to a single exponential decay, yielding a $1/e$ lifetime of 16.3 ± 1.5 s. Inset: Lifetime in an isotropic lattice with a depth of $50E_R$ with (blue open squares, 0.17 D) and without (black squares, 0 D) an applied electric field. The lifetimes at 0.17 D (15 ± 4 s) and 0 D agree within uncertainty. Reprinted with permission from ref 309. Copyright 2012 American Physical Society.

number of molecules as a function of time for optical lattice depths of $56E_R$, $56E_R$, and $70E_R$ in the x , y , and z directions, respectively, and for no electric field applied ($d = 0$ D). The inset of the figure shows a similar curve in the presence of an electric field (open blue squares) corresponding to a dipole moment of $d = 0.17$ D. The initial fast decay is interpreted as due to collisions of ground-state molecules with molecules formed in higher excited states. The slow decay is attributed to one-body decay and is fit to an exponential decay curve. The $1/e$ lifetime of the molecules is 16.3 ± 1.5 s and 14 ± 4 s, at, respectively, $d = 0$ D and $d = 0.17$ D. The authors explained these long lifetimes by the strong localization of the polar molecules in the 3D lattice preventing bimolecular chemical reaction to occur. The molecular lifetime is independent of the applied electric field due to this strong isolation of the molecules.

Chotia et al. also performed a systematic study to understand what limits the lifetime of the molecules. They measured the lifetime of the molecules for different lattice depths in the z direction, similar to what has been done in the experiment of Syassen et al.²⁰⁸ for Feshbach Rb₂ molecules, as discussed previously in section 3.1.2. This is shown in Figure 83. The lifetime corresponding to the situation of Figure 82 is at a total depth of $186E_R$ in Figure 83. The first point corresponds to a situation where the molecules start in a 2D optical lattice, formed by tubes as sketched in the figure. The lifetime is quite short, ~ 1 s. The authors attributed this lifetime due to loss from two-body chemical reactions. To make sure this is the case, the authors added an electric field along the tubes corresponding to an induced dipole moment of 0.17 D. The lifetime dropped from 1 to 0.1 s, consistent with previous studies in free space.⁴ A small optical lattice is then added in the third z direction, and the depth of this corrugated lattice is increased. The first trend is a strong increase of the lifetime of the molecules. As the third dimension is added, the molecules become more and more isolated, preventing chemical reactions from occurring. The molecules can reach a lifetime as high as 25 ± 5 s for a lattice depth of $34E_R$ in the z direction (the x and y depths are $56E_R$), corresponding to a total depth of $146E_R$. The second trend in Figure 83 is a lifetime decrease when the depth in z is further increased. The authors interpreted this

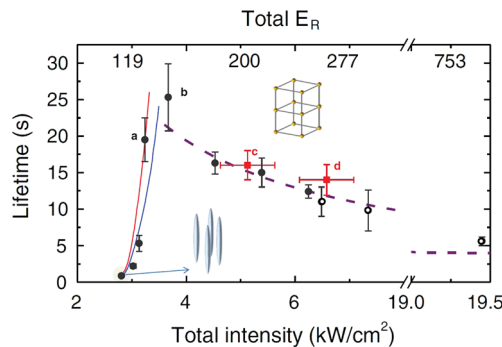


Figure 83. Lifetime of KRb ground-state molecules in an optical lattice. Black circles: x and y lattice beams are fixed at $56E_R$ per beam, while z is varied from 0 to $136E_R$ ($1E_R$ corresponds to a lattice intensity $I = 0.025$ kW/cm²). The lifetime reaches a maximum of 25 ± 5 s when the z lattice depth is $34E_R$ (point b). For higher lattice intensities, the lifetime decreases, which is consistent with loss due to off-resonant light scattering (dashed line). Reprinted with permission from ref 309. Copyright 2012 American Physical Society.

result due to off-resonant photon scattering, a single-body mechanism, becoming the main source of molecular loss. Each off-resonant photon scattering event has a high probability to cause molecular loss due to the rich internal-state structure of the molecules. To verify this, Chotia et al. added a traveling-wave beam to increase the photon-scattering rate without increasing the lattice depth. Points c and d correspond to points a and b. Points c and d have the same lattice depth as points a and b, but with an increased photon-scattering rate. The authors observed a significant reduction of the lifetime due to the additional light, thus confirming the off-resonant photon scattering as the main limiting process for the molecular lifetime. The authors extracted the polarizability of the KRb molecules by fitting the lifetime as a function of the light intensity and found an experimental value of $\alpha_{\text{exp}} = (2.052 \pm 0.009) \times 10^{-12}$ MHz/(W/cm²), consistent with a theoretical calculation by Kotochigova et al.³¹⁰ Finally, Chotia et al. found that the 3D optical lattice can also increase the lifetime of the Feshbach molecules to be >20 s, which is 100 times longer than the lifetime found in previous studies with trapped gases of fermionic KRb. Just as for ground-state molecules, the lifetime of the Feshbach molecules is limited by off-resonant photon scattering, the rate of which is related to the size of the Feshbach molecule. The authors observed that Feshbach molecules can also be dissociated to individual atoms, then back to Feshbach molecules with nearly 100% efficiency.

The studies of Danzl et al.² and Chotia et al.³⁰⁹ showed that molecules can be stable and long-lived in an 3D optical lattice. This is crucial to undertake further studies of many-body physics of polar molecules in optical lattices, as developed in the review article of Baranov et al.²⁸⁰ in this issue.

4.11. Three-Body Collisions of Polar Molecules

In the case of ground-state polar molecules for which two-body chemical reaction is energetically forbidden, three-body collisions will become the limiting process for the formation and lifetime of an ultracold molecular gas, because three-body chemical reactions are still energetically allowed.^{266–268} Furthermore, the Efimov effect^{83,88,90} (previously discussed in section 1.4) could also be observed with dipolar molecules in electric fields, opening a new universal regime for few-body dipoles. Finally, the study of three-body dipolar dynamics is a first step to explore the more complicated many-body physics.

Therefore, it is of great importance to investigate the role of these collisions.

In 2010 Ticknor and Rittenhouse³¹¹ studied the three-body recombination of ultracold bosonic dipoles into weakly bound dimers. They used a Fermi's golden rule for the expression of the differential rate dR of three distinguishable dipoles converted into weakly bound dimers per unit of time,

$$dR = \frac{2\pi}{\hbar} |\langle \Psi_{2+1} | V | \Psi_{1+1+1} \rangle|^2 \delta(E_i - E_f) \quad (68)$$

using a Born approximation where the initial state Ψ_{1+1+1} is the wave function of three free dipoles and the final state Ψ_{2+1} is the wave function of a free weakly bound dipole dimer and a free dipole.

In the above expression, V is the dipole–dipole interaction plus a contact potential proportional to a scattering length a to account for s -wave scattering at short-range,²⁹⁵

$$V(\vec{r}) = \frac{d^2[1 - 3(\hat{r} \cdot \hat{z})^2]}{r^3} + \frac{2\pi\hbar^2 a}{\mu_{2b}} \delta(\vec{r}) \quad (69)$$

where d is the electric dipole moment induced by the electric field and μ_{2b} is the reduced mass of a two-body system. Summing over all final-state energies and dividing by the total incident flux of particles, the authors determined the expression of the differential cross section for distinguishable dipoles

$$\frac{d\sigma}{dk'_2} = \frac{\mu_{3b}^2 k'_2}{4\pi^2 \hbar^4 k} \times \left| \int d^3\rho_1 d^3\rho_2 \Psi^*_d(\rho_1) e^{-i\vec{k}'_2 \cdot \vec{\rho}_2} \times V(\vec{r}_{13}) \times e^{i(\vec{k}_1 \cdot \vec{\rho}_1 + \vec{k}_2 \cdot \vec{\rho}_2)} \right|^2 \quad (70)$$

where $\vec{\rho}_1, \vec{\rho}_2$ are mass-scaled Jacobi vectors associated with the ongoing wavevectors \vec{k}_1 and \vec{k}_2 , \vec{k}'_2 is the outgoing wavevector associated with the motion of the dimer dipole and the free dipole, and $\mu_{3b} = (m_1 m_2 m_3 / (m_1 + m_2 + m_3))^{1/2}$ is the three-body reduced mass. Equation 70 used a Born approximation, where the state-to-state transition is proportional to the square of the overlap integral of a weakly bound dimer state $\psi_d(\vec{\rho}_1)$ and the plane wave associated with a free dipole $e^{i\vec{k}'_2 \cdot \vec{\rho}_2}$, with the interaction potential V and the plane waves associated with three free dipoles $e^{i(\vec{k}_1 \cdot \vec{\rho}_1 + \vec{k}_2 \cdot \vec{\rho}_2)}$. In the study,³¹¹ the authors used a single two-body interaction for the potential in eq 70, assuming the simplest matrix element that connects the outgoing ψ_{2+1} state to the incoming plane wave ψ_{1+1+1} state. In the case of a weakly bound dipole dimer $\psi_d(\vec{\rho}_1) \rightarrow e^{-r/a} / (r(2\pi a)^{1/2})$, when $a \gg D$, where $D = \mu_{2b} d^2 / \hbar^2$ is the dipole length, the authors evaluated eq 70 analytically and found for the three-body recombination rate coefficient of identical bosonic particles into weakly bound dimers

$$K_3^{\text{ident}} \rightarrow 3! \frac{32\sqrt{3}\pi^2 \hbar a^2}{m} [a^2 + \beta D^2] \quad (71)$$

with

$$\beta = \frac{64}{15} (2\sqrt{3} - \pi)^2 = 0.44 \quad (72)$$

The first term is in agreement with what had been found for s -wave three-body recombination of identical bosons^{84,312} for short-range interactions. The second term comes from the dipolar interaction and corresponds to an outgoing d -wave differential cross section. In the other limit, when $a \ll D$, the

bosonic three-body rate is entirely controlled by the dipolar interaction and

$$K_3^{\text{ident}} \rightarrow 495\hbar D^4 / \mu_{2b} \quad (73)$$

The two regimes $a \gg D$ and $a \ll D$ are clearly seen in Figure 84. The solid black curve corresponds to the total three-body

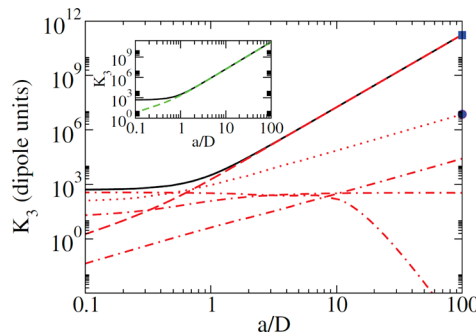


Figure 84. Three-body recombination rate of three identical bosonic dipoles is shown in dipole units (one dipole unit is given by $\hbar D^4 / \mu_{2b}$) as a function of the scattering length. The total recombination rate (solid curves) is universal and independent of the resonance used. The sS (dashed red), dS (dotted red), and higher-order (dot-dashed red curves) partial-wave contributions are shown as well. The a^4 (blue square) and $D^2 a^2$ (blue circle) terms from the asymptotic results of eq 71 are shown as well. Inset: The total recombination rate is shown compared to the result of eq 71 for the large a limit (green dashed curve). Reprinted with permission from ref 311. Copyright 2010 American Physical Society.

recombination rate as a function of the ratio a/D from a numerical calculation (the nonsolid red curves correspond to different partial-wave contributions). The curve from the numerical calculation smoothly connects the two limiting regimes, where when $a \gg D$ the rate behaves as a^4 and when $a \ll D$ the rate behaves as $D^4 \propto a^8$. The three-body rate coefficient has, therefore, a very strong dependence with the induced dipole moment, and this will result in high molecular losses in ground-state polar-molecule experiments. Even with molecules of category II, for which two-body collisions are not reactive and do not yield two-body molecular losses, three-body loss collisions have a strong dependence with the induced dipole moment and the electric field. The inset shows the comparison of the numerical result (black solid line) with the analytical expression in eq 71 for $a \gg D$ (green dashed line), showing the a^4 trend of the rate.

In 2011 Wang et al.³¹³ explored, by exact numerical studies, the dynamics of three bosonic dipoles in the Efimov regime, that is, when the collision energy of two dipoles is near a scattering resonance, making the dipole–dipole scattering length $|a_s| \rightarrow \infty$. In this study, the authors found that the Efimov effect remains for dipolar particles in electric fields and that the Efimov resonances and the scattering properties universally depend on the two-body dipole physics alone. This is illustrated in Figure 85. The figure presents the adiabatic hyperspherical potentials $U_\nu(R)$ for three dipolar bosons where R is the hyperspherical radius characterizing the global size of the triangle made by the three particles and ν describes a specific hyperspherical channel. The curves above zero energy at large R represent the channels of three dissociated dipoles whereas the curves below zero energy represent the channels of a dipolar dimer and a free dipole. In the inset of the figure, the authors found the (diabatized) potential behaves as $U_\nu(R) \approx$

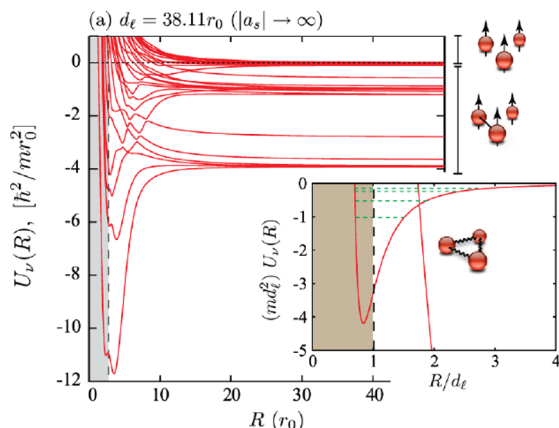


Figure 85. (a) Typical set of adiabatic hyperspherical potentials $U_\nu(R)$ for three dipoles that exhibit the Efimov hyperradial potential curve ($d_\ell/r_0 = 38.11$ and $|a_s| \rightarrow \infty$). Inset: Rescaled adiabatic potentials showing the Efimov potential (the dashed lines are illustrations of the Efimov states in that potential, not to scale). Reprinted with permission from ref 313. Copyright 2011 American Physical Society.

$-(s_0 + 1/4)/(2\mu R^2)$, which supports the infinite number of three-body Efimov states (illustrated as dashed lines in the inset). In the limit of strong dipoles $d_\ell \gg r_0$, where $d_\ell = md_m^2/2$ is the dipole length in atomic units (d_m is the induced dipole moment and m is the mass of the dipolar molecule) and r_0 is the characteristic length of the short-range potential between three dipoles, this rescaled potential is universal because it is independent of the values d_ℓ , r_0 , and the strength of the short-range interaction. Figure 86 shows the three-body spectrum

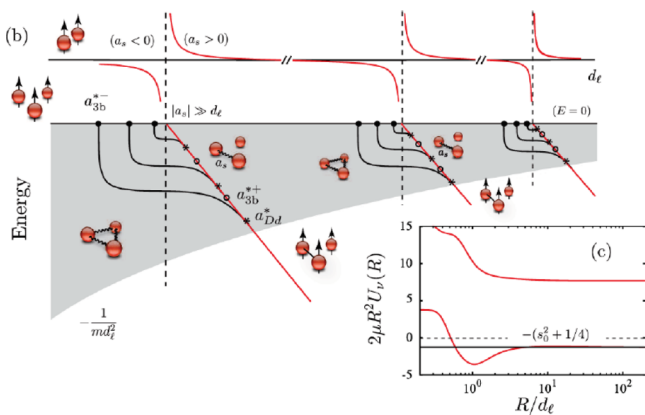


Figure 86. (b) Schematic representation for the d_ℓ dependence of a_s (upper part) and the Efimov spectrum (lower part) for dipolar systems (see the text). (c) The Efimov potential signature at the first pole of a_s ($d_\ell/r_0 = 4.86$). The horizontal solid line shows the Efimov behavior given by $U_\nu(R) \approx -(s_0 + 1/4)/(2\mu R^2)$. Reprinted with permission from ref 313. Copyright 2011 American Physical Society.

versus d_ℓ . The binding energies of the lowest Efimov states scale as $1/(md_\ell^2)$. There is a striking difference between the dipolar Efimov effect and the usual one.^{88,90} For values $R < d_b$, the Efimov potential U_ν is repulsive, so that the trimer Efimov states are well-separated from the short-range region $R \approx r_0$. Therefore, the trimer states will be fully universal in the sense that they only depend on the scattering length a_s and the dipole length d_ℓ . In contrast with Efimov physics of nondipolar particles, the three-body parameter^{90,214} is universal and one can derive the Efimov states or resonances for both $a_s > 0$ and

$a_s < 0$ with $|a_s| > d_b$. In addition, the repulsive behavior of the potential makes the Efimov states long-lived, and this lifetime increases with d_ℓ . This is an ideal condition to create and manipulate Efimov states of dipolar particles.

Wang et al. also deduced the three-body recombination rate from the universal theory⁹⁰ at resonance when $|a_s| \gg d_b$ given by

$$K_3^{(a_s > 0)} \approx \frac{67.1}{e^{2\eta}} \left\{ \sin^2 \left[s_0 \ln \left(\frac{a_s}{d_b} \right) + 2.5 \right] + \sinh^2 \eta \right\} \frac{a_s^4}{m} \quad (74)$$

$$K_3^{(a_s < 0)} \approx \frac{4590 \sinh 2\eta}{\sin^2 \left[s_0 \ln \left(\frac{|a_s|}{d_b} \right) + 0.92 \right] + \sinh^2 \eta} \frac{a_s^4}{m} \quad (75)$$

corresponding, respectively, to three-body recombination into weakly ($a_s > 0$) and deeply ($a_s < 0$) dipole–dimer bound states. The relaxation rate from a weakly bound dipolar dimer D_2^* with $a_s > 0$ to a deeply bound dipolar dimer D_2 with $a_s < 0$ for the inelastic process $D_2^* + D \rightarrow D_2 + D$ was also provided by

$$V_{\text{rel}}^{(a_s > 0)} \approx \frac{20.3 \sinh(2\eta)}{\sin^2 \left[s_0 \ln \left(\frac{|a_s|}{d_b} \right) + 0.86 \right] + \sinh^2 \eta} \frac{a_s}{m} \quad (76)$$

When $|a_s| < d_b$, they found the same strong dipole dependence as the study of Ticknor and Rittenhouse³¹¹ where $K_3 \propto d_\ell^2 \propto d_m^8$, confirming that turning on an electric field increases the three-body molecular losses.

The authors finally found that there is a repulsive barrier between a dipole and a dipolar dimer when the dipolar dimer is deeply bound (also discussed in ref 314). This barrier depends on the dipole length and then can be controlled by an electric field. The repulsive potentials can be seen in Figure 85 for the dipole–dimer and free dipole channels. This is a remarkable property that the authors found, since dipole–dimers and free dipoles can be protected against collisions in the presence of electric fields. This can lead to the creation of stable mixtures of dipoles and two-dipole molecules. In addition, the electric field can be used to control the strength of the interaction between the dipoles and the two-dipole molecules, providing a new playground for future investigations of few-body and many-body physics.

Wang et al. continued their work by studying dipolar fermions.³¹⁵ In the presence of electric fields, the authors found that the dynamics of three dipolar fermions is universal, in contrast with the nondipolar case. No Efimov states exist for three identical fermions because there is no attractive $1/R^2$ potential for the three-body states. However, near a dipole–dipole resonance when a dimer dipole is weakly bound ($E_{2d} \rightarrow 0$), the authors computed the hyperspherical adiabatic curves shown in Figure 87 and found a potential that can carry a universal, long-lived, trimer-dipole state, represented as a dashed line in the inset of Figure 87. This potential is the same for different values of d_ℓ and short-range potential, indicating a strong universal behavior. They have also shown that the size and lifetime of the three-body state grow with increasing electric dipole interaction.

This trimer-dipole state occurs for a unique symmetry of the three-body complex, the $M^\Pi = 0^+$ symmetry, where M is the quantum number associated with the projection of the total angular momentum J onto the quantization space-fixed axis and

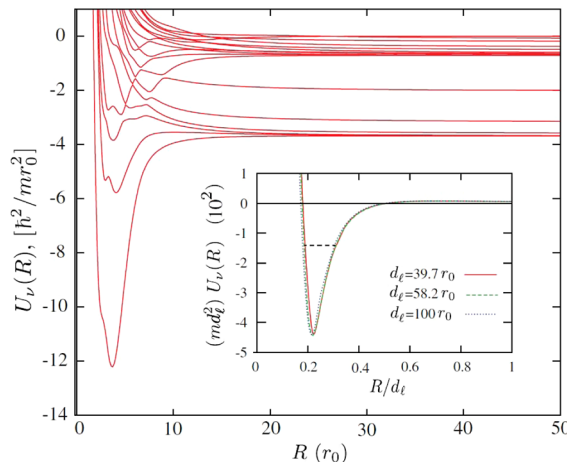


Figure 87. Typical set of adiabatic hyperspherical potentials $U_\nu(R)$ for three fermionic dipoles with $d_l/r_0 = 58.2$ and $E_{2d} \rightarrow 0$. The inset shows rescaled, diabatized potentials exhibiting universal behavior for a few values of d_l at a dipole–dipole resonance. The horizontal dashed line in the diabatic potential wells indicates the position of the universal three-dipole states. Reprinted with permission from ref 315. Copyright 2011 American Physical Society.

Π is the parity of the three-body wave function. The $M^\Pi = 0^+$ corresponds to the least-repulsive interaction for three-body fermions, creating the smallest incident barrier for the incoming three-body collision. This weak barrier can be seen in the inset of Figure 87, just above the zero energy line. The trimer-dipole state was not found for other symmetries such as $M^\Pi = 0^-, 1^+, 1^-$, corresponding to more repulsive effective interaction and higher incident barrier. The probability density $\rho(\vec{r})$ to find a dipole at \vec{r} is shown as isosurfaces in the upper part of Figure 88. The isosurfaces can be interpreted as the revolution of the blue triangle, as shown in the lower part of the figure, along the field axis. Then, the three-dipole state has a strong preferential

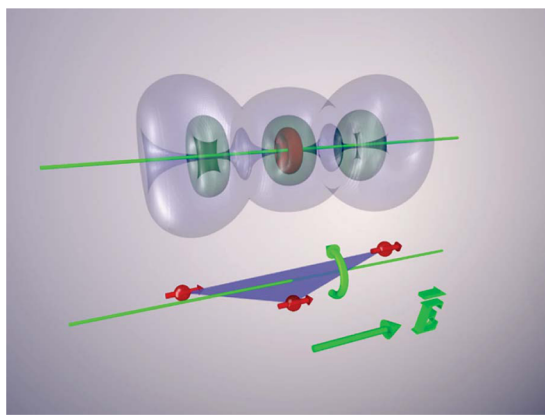


Figure 88. Upper part: the isosurfaces of the one-dipole probability density $\rho(\vec{r})$ for the universal three-dipole states, centered in the space-fixed center-of-mass frame. By normalizing the peak density to be unity, the density of the following surfaces—the innermost one (red), the three middle ones (green), and the outermost one (light blue)—are 0.8, 0.3, and 0.015, respectively. This crankshaft-resembling structure is a figure of rotation about the field axis. The lower part: the most probable orientation and geometry of the triangle formed by three dipoles. The axes (green) show the direction of the external electric field. Reprinted with permission from ref 315. Copyright 2011 American Physical Society.

spatial configuration that tends to align with the electric field. It is universal; only its size grows linearly with d_l .

The three-dipole fermionic recombination rate should scale as

$$K_3 = \hbar \frac{C_3 k^4}{\mu} \quad (77)$$

from a Wigner threshold analysis²⁰² for the $M^\Pi = 0^+$ symmetry, where $k = (2\mu E)^{1/2}$. On a dipole–dipole resonance, Wang et al. found that the C_3 coefficient should be $C_3 \approx 2 \times 10^9 V^{17/2} d_l^{-35/2}$, where V is the scattering volume on resonance. Away from a dipole–dipole resonance, the scattering volume should scale as $d_l^3 \propto d_m^6$ (refs 4, 157, and 162), so that the C_3 coefficient should scale as $d_l^8 \propto d_m^{16}$. The three-body recombination rate for three fermionic dipoles has a strong induced dipole moment dependence (stronger than for bosonic dipoles) and will lead to dramatic molecular losses in ultracold experiments of polar molecules.

Finally, as discussed above for the case of three-body physics with bosonic dipoles,³¹³ fermionic dipoles also offer the remarkable property of collision protection between bound dipole dimers and free dipoles, as seen in Figure 87. As for bosonic dipoles, this is a useful property to form stable mixtures of these dipolar molecular species and provide a way to tune the interactions between them.

5. PERSPECTIVES FOR ULTRACOLD CHEMISTRY

This review has covered the essential background about the cooling and trapping of ultracold atoms and molecules. It has described the existing experimental and theoretical work on understanding and controlling the collisions and reactions of ultracold molecules. We have given special emphasis to recent work with KRB fermionic molecules in the few hundred nK range. This species provides a paradigm for much that one might expect with other species in the future: the precise single quantum state control of all degrees of freedom of an ultracold molecule, namely, electronic, vibration, rotation, electron and nuclear spin, spatial orientation, and even external translational motion by introducing an optical lattice.

While KRB fermions and Cs₂ bosons have been made in their ground state of electronic, vibrational, and rotational motion, many more species are expected to become available in the future. Currently, ultracold molecules can only be made by assembling them from already ultracold atoms. There are a number of atomic species with bosonic isotopes for which Bose–Einstein condensation has been realized, including H, Li, Na, K, Rb, Cs, Ca, Sr, Yb, Cr, Dy, and Er. Ultracold fermionic isotopes are also available for the species Li, K, Sr, Yb, and Dy. Therefore, a variety of molecules are potentially accessible using combinations of these species; see section 1.5.1 for a list of species under active study. We might hope that other direct cooling methods, such as discussed in this review issue on Ultracold Molecules, might eventually produce other molecules in the ultracold regime.

Although KRB is an example of a highly reactive species in the quantum threshold regime, there are other mixed alkali-metal species that are known to be nonreactive in their electronic, vibrational, and rotational ground state, e.g., NaK, NaRb, NaCs, KCs, and RbCs. However, these can quench through inelastic collisions or even have chemical reactions, depending on their degree of vibrational excitation. The species LiNa, LiK, LiRb, and LiCs have exoergic reactions and are

expected to be highly reactive like KRB. The species NaCs and LiCs have dipole moments an order of magnitude larger than KRB, making them good candidates for electric-field control of strong dipolar interactions. The Raman techniques used to make the ground-state molecules could be used to make other vibrational or rotational states as well. Therefore, there are a large number of ultracold molecular species in different vibrational states that are potentially accessible using proven current techniques. When one adds electric, magnetic, or electromagnetic field control to the techniques available, or uses various dimensional optical lattice control, there are large unexplored domains of ultracold molecular collisions and reactions available for future research.

The chemical reaction of two KRB molecules turns out to be especially easy to understand theoretically. We described several approaches, all based on understanding the role of the long-range potential in governing the quantum dynamical approach of the two colliding molecules. Although the standard Langevin model cannot be used because the de Broglie wavelength of the ultracold molecules is much larger than the range of the potential, the new theories incorporate the Bethe–Wigner quantum threshold laws into various generalized quantum threshold Langevin models. This can be done approximately using the known form of the threshold laws, analytically in the case of the van der Waals potential, or numerically in the case of the anisotropic potential of two dipoles. Although these models give good approximations to the total rate coefficient, they give no information about real chemical dynamics or product distributions. For example, why does the collision complex of two KRB molecules not return any scattering flux to the ultracold reactant channel? Or what is the state distribution of the “hot” K_2 and Rb_2 reaction products? No current experiment is seeking to measure product distributions, so this awaits future development. In any case, any theoretical attempt to calculate state-to-state cross sections would need to connect some method for treating conventional chemical dynamics to the unique preparation and long-range control features of the ultracold reactants.

In general, one should expect that the scattering resonances of the collision complex of the two colliding species will be critically important to understand, at least qualitatively, and, if possible, quantitatively as well. Although the short-range reaction “black hole” of the KRB Langevin model suppresses any threshold resonances, there will certainly be many less reactive species with resonance structure. Do a few key resonances control threshold processes, as is known to be the case with the well-characterized Fano-Feshbach resonances of ultracold atomic collisions? Or would many resonances need to be considered, given the much larger density of states in a collision complex of molecular species, especially given the high spin degeneracy that has an important role in the ultracold domain? Any adequate theory would need to understand the spectrum and dynamics of the collision complex prepared from the controlled launching pad of the ultracold reactants. How might these resonances or the dynamics of the complex be controlled using either static external fields or time-dependent pulsed electromagnetic fields? In principle, any Franck–Condon-accessible region of the collision complex is a candidate for one- or multicolor electromagnetic population switching and probing.

We discussed how threshold collision properties are very sensitive to a quantum phase, measured by the *s*-wave scattering length, which is determined by the whole potential.

Consequently, a difficulty with applying conventional chemical dynamics methods in the ultracold domain is that the system Hamiltonian is normally never known with sufficient precision to make confident predictions of quantitative threshold properties. On the other hand, what can be established by theory is which aspects of the threshold scattering is *robust* with respect to variations in the potential. For example, one might predict the density or widths of resonance states but not the location of a particular resonance. There are special cases like KRB reactions where getting a robust model turns out to be remarkably easy, because the unit probability of the short-range reaction and the relatively simple quantum dynamics of the long-range potential turn out to be sufficient. Such reaction rates are robust, independent of any detailed consideration of short-range physics. Will there be robust features of reactions with resonance structure? For example, can reactions be understood statistically, as in the exploratory work by Mayle et al.²⁹⁴ Can multichannel quantum defect methods build in the effects of resonance structure? Such formulations offer the prospects for parametrized semianalytic models or even for numerical models,¹⁷⁵ where a few “quantum defect” parameters capture the relevant resonance structure. The field dependence of collision rates presumably follows without the need to introduce additional parameters.

The collision complex of two ultracold reactants is like the highly excited molecular states that are well-studied in chemistry³¹⁶ under paradigms such as internal relaxation,^{317,318} unimolecular decomposition,^{319–321} transition state theory,³²² or semiclassical or chaotic dynamics.^{323,324} Although the low-energy entrance channel is undoubtedly highly quantum mechanical in its long-range collision dynamics, once it is coupled to the high-energy scale of the collision complex the conventional chemical dynamics from these familiar fields takes over. The kinds of theories that are needed for understanding the dynamics and control inherent in ultracold chemistry are theories that take due account of both the low-energy approach of the reactants and the high-energy dynamics of the complex. One challenge for future theory is to build the bridge between these two quite distinct aspects of the dynamics, while elucidating the role of the resonances of the complex in bridging between the two domains. This means getting theories that can account, either in detail or statistically, for the electronic, vibrational, rotational, and full spin structure of the complex.

If one only desires to use the molecules to study some kind of many-body features of a quantum gas or lattice, it is crucial to ensure that the ensemble of molecules be stable for as long as is needed to probe such features experimentally. Because the time scales are long (ms to s) because of the very low energy scales of the many-body system, the reaction rate coefficients need to be sufficiently small at the molecular densities and temperatures needed. We have shown in sections 4.9 and 4.10 how fast chemical reactions can be suppressed by placing the molecules in reduced dimensional lattice structures. Experimentalists will hopefully learn to control the molecular density, temperature, and entropy sufficiently to realize some of the exotic many-body phenomena with lattices of cold dipoles that are reviewed in this issue on Ultracold Molecules.

One important question to be answered concerns the spin-relaxation properties of the cold molecules. Even the $\nu = 0$ rotationless ground state of a ${}^1\Sigma$ molecule like Cs₂ or RbCs has internal nuclear spin structure with splittings that are large compared to $k_B T$. It will be important to establish whether the

very weakly coupled nuclear spins will relax during a collision. This is not likely if the collision just corresponds to the two species banging together and coming apart. But if there are resonances of the collision complex so that the complex has a long enough dwell time during the collision, there may be time for such weak interactions to depolarize the spins. Such spin-relaxation processes need to be studied experimentally to determine whether they are fast or slow.

The study of true ultracold chemistry awaits further development of the needed theoretical and experimental tools. By ultracold chemistry, we mean taking advantage of the unique preparation and control of the reactants or of resonance states of the collision complex to probe the chemical dynamics of the collision complex or to affect the products of a reaction. The one thing that is clear is that the experimental realization of gases or lattices of fully state controlled ultracold molecules is a reality that is demonstrated and making rapid progress.

AUTHOR INFORMATION

Corresponding Author

*E-mail: goulven.quemener@colorado.edu; psj@umd.edu.

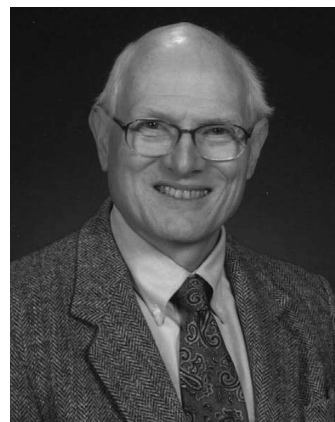
Notes

The authors declare no competing financial interest.

Biographies



Goulven Quéméner (born 1980, in France) received his B.Sc. and M.Sc. in Physics in 2001 and 2003 from the Université de Bretagne Occidentale in Brest and received his Ph.D. in 2006 from the Université de Rennes, under the direction of Pascal Honvaut and Jean-Michel Launay. His thesis focused on the theoretical study of atom–molecule collisions at ultralow energy with a particular emphasis on alkali species. From 2006 to 2008 he started his postdoctoral training as a Research Associate at the University of Nevada Las Vegas (U.S.A.) under the supervision of Naduvalath Balakrishnan, where he pursued his investigations on atom–molecule chemical reactions and molecule–molecule collisions relevant to astrophysics and atmospherical physics. From 2008 to 2012 he joined JILA at the University of Colorado in Boulder (U.S.A.) as a Research Associate and then as a Senior Research Associate, under the supervision of John Bohn. He timely arrived when the formation of ultracold ground-state polar molecules of KRb was achieved in the experimental group of Jun Ye and Deborah Jin, therefore focusing his research on collision and control of polar molecules in electric and magnetic fields, as well as optical lattices. In 2012 he obtained a CNRS position as Chargé de Recherche at the Laboratoire Aimé Cotton in Orsay, France.



Paul Julienne received a B.S. in Chemistry from Wofford College, Spartanburg, SC, U.S.A., in 1965 and a Ph.D. in Chemical Physics from the University of North Carolina at Chapel Hill in 1969. After serving as a National Research Council Postdoctoral associate with Frederick H. Mies at the National Bureau of Standards (NBS), he worked in the Plasma Physics Division at the Naval Research Laboratory. He returned to NBS in 1974, now the National Institute of Standards and Technology (NIST), and has been there ever since. He was formerly the Group Leader of the Quantum Processes Group in the NIST Physics Laboratory and now is a NIST Fellow in the Physical Measurement Laboratory. He also is a Fellow of the Joint Quantum Institute of NIST and the University of Maryland Physics Department. Since the mid-1980s he has primarily been engaged in theoretical research involving cold and ultracold atoms and molecules, especially their interactions and collisions, and has written several review articles on this subject.

ACKNOWLEDGMENTS

This material is based upon work supported by the Air Force Office of Scientific Research under the Multidisciplinary University Research Initiative Grant No. FA9550-09-1-0588 and No. FA9550-09-1-0617.

REFERENCES

- (1) Ni, K.-K.; Ospelkaus, S.; de Miranda, M. H. G.; Pe'er, A.; Neyenhuis, B.; Zirbel, J. J.; Kotochigova, S.; Julienne, P. S.; Jin, D. S.; Ye, J. *Science* **2008**, *322*, 231.
- (2) Danzl, J. G.; Mark, M. J.; Haller, E.; Gustavsson, M.; Hart, R.; Aldegunde, J.; Hutson, J. M.; Nägerl, H.-C. *Nature Physics* **2010**, *6*, 265.
- (3) Ospelkaus, S.; Ni, K.-K.; Wang, D.; de Miranda, M. H. G.; Neyenhuis, B.; Quéméner, G.; Julienne, P. S.; Bohn, J. L.; Jin, D. S.; Ye, J. *Science* **2010**, *327*, 853.
- (4) Ni, K.-K.; Ospelkaus, S.; Wang, D.; Quéméner, G.; Neyenhuis, B.; de Miranda, M. H. G.; Bohn, J. L.; Jin, D. S.; Ye, J. *Nature* **2010**, *464*, 1324.
- (5) Carr, L. D.; DeMille, D.; Krems, R. V.; Ye, J. *New J. Phys.* **2009**, *11*, 055049.
- (6) Herschbach, D. *Faraday Discuss.* **2009**, *142*, 9.
- (7) Krems, R., Friedrich, B., Stwalley, W. C., Eds. *Cold Molecules: Theory, Experiment, Applications*; CRC Press: Boca Raton, FL, 2009.
- (8) Dulieu, O.; Gabbanini, C. *Rep. Prog. Phys.* **2009**, *72*, 086401.
- (9) Schnell, M.; Meijer, G. *Angew. Chem., Int. Ed.* **2009**, *48*, 6010.
- (10) Bell, M. T.; Softley, T. *Mol. Phys.* **2009**, *107*, 99.
- (11) Dulieu, O.; Krems, R.; Weidemuller, M.; Willitsch, S. *Phys. Chem. Chem. Phys.* **2011**, *13*, 18703.
- (12) For simplicity of notation, we only show l , but the additional projection quantum number m_l of the angular momentum l on a space axis is implied, where m_l can take on any of the $2l + 1$ values between $-l$ and $+l$.

- (13) We refer to identical molecules as molecules of the same chemical composition (same mass, same atomic isotopes), whereas we refer to indistinguishable/distinguishable molecules as identical molecules in same/different quantum states.
- (14) Metcalf, H. J.; van der Straten, P. *Laser Cooling and Trapping*; Springer: New York, 1999.
- (15) Chu, S. *Rev. Mod. Phys.* **1998**, *70*, 685.
- (16) Phillips, W. D. *Rev. Mod. Phys.* **1998**, *70*, 721.
- (17) Cohen-Tannoudji, C. N. *Rev. Mod. Phys.* **1998**, *70*, 707.
- (18) Ketterle, W.; van Druten, N. J. *Adv. At. Mol. Opt. Phys.* **1997**, *96*, 181.
- (19) Anderson, M. H.; Ensher, J. R.; Matthews, M. R.; Wieman, C. E.; Cornell, E. A. *Science* **1995**, *269*, 198.
- (20) Bradley, C. C.; Sackett, C. A.; Tollett, J. J.; Hulet, R. G. *Phys. Rev. Lett.* **1995**, *75*, 1687.
- (21) Davis, K. B.; Mewes, M. O.; Andrews, M. R.; van Druten, N. J.; Durfee, D. S.; Kurn, D. M.; Ketterle, W. *Phys. Rev. Lett.* **1995**, *75*, 3969.
- (22) Dalforno, F.; Giorgini, S.; Pitaevskii, L. P.; Stringari, S. *Rev. Mod. Phys.* **1999**, *71*, 463.
- (23) Cornell, E. A.; Wieman, C. E. *Rev. Mod. Phys.* **2002**, *74*, 875.
- (24) Ketterle, W. *Rev. Mod. Phys.* **2002**, *74*, 1131.
- (25) DeMarco, B.; Bohn, J. L.; Burke, J. P., Jr.; Holland, M.; Jin, D. S. *Phys. Rev. Lett.* **1999**, *82*, 4208.
- (26) Schreck, F.; Khaykovich, L.; Corwin, K. L.; Ferrari, G.; Bourdel, T.; Cubizolles, J.; Salomon, C. *Phys. Rev. Lett.* **2001**, *87*, 080403.
- (27) Truscott, A. G.; Strecker, K. E.; McAlexander, W. I.; Partridge, G. B.; Hulet, R. G. *Science* **2001**, *291*, 2570.
- (28) Giorgini, S.; Pitaevskii, L. P.; Stringari, S. *Rev. Mod. Phys.* **2008**, *80*, 1215.
- (29) Grimm, R.; Weidemüller, M.; Ovchinnikov, Y. B. *Adv. At. Mol. Opt. Phys.* **2000**, *42*, 95.
- (30) Kagan, Y.; Svistunov, B. V.; Shlyapnikov, G. V. *Pis'ma Zh. Eksp. Teor. Fiz.* **1985**, *42*, 169; *JETP Lett.* **1985**, *42*, 209.
- (31) Burt, E. A.; Ghrist, R. W.; Myatt, C. J.; Holland, M. J.; Cornell, E. A.; Wieman, C. E. *Phys. Rev. Lett.* **1997**, *79*, 337.
- (32) Bloch, I. *Nat. Phys.* **2005**, *1*, 23.
- (33) Greiner, M.; Fölling, S. *Nature* **2008**, *453*, 736.
- (34) Petrov, D. S.; Shlyapnikov, G. V. *Phys. Rev. A* **2001**, *64*, 012706.
- (35) Olshanii, M. *Phys. Rev. Lett.* **1998**, *81*, 938.
- (36) Greiner, M.; Mandel, O.; Esslinger, T.; Hänsch, T. W.; Bloch, I. *Nature* **2002**, *415*, 39.
- (37) Stoof, H. T. C. *Nature* **2002**, *415*, 25.
- (38) Gao, B. *Phys. Rev. A* **2008**, *78*, 012702.
- (39) Gribakin, G. F.; Flambaum, V. V. *Phys. Rev. A* **1993**, *48*, 546.
- (40) Chin, C.; Grimm, R.; Julienne, P.; Tiesinga, E. *Rev. Mod. Phys.* **2010**, *82*, 1225.
- (41) Bethe, H. A. *Phys. Rev.* **1935**, *47*, 747.
- (42) Wigner, E. P. *Phys. Rev.* **1948**, *73*, 1002.
- (43) Landau, L. D.; Lifshitz, I. M. *Quantum Mechanics (Non-Relativistic Theory)*; Pergamon Press: Elmsford, NY, 1984.
- (44) Mott, N. F.; Massey, H. S. W. *Theory of atomic collisions*, 3rd ed.; Oxford University Press: London, 1965.
- (45) Taylor, J. R. *Scattering theory*; John Wiley and Sons, Inc.: New York, 1972.
- (46) Sadeghpour, H. R.; Bohn, J. L.; Cavagnaro, M. J.; Esry, B. D.; Fabrikant, I. I.; Macek, J. H.; Rau, A. R. P. *J. Phys. B: At. Mol. Opt. Phys.* **2000**, *33*, 93.
- (47) This loss probability follows from the unitarity property of the s -matrix.
- (48) Here we assume that the $2l + 1$ components of the l -wave have the same S-matrix element; it is trivial to generalize to unequal components if this occurs for an anisotropic potential.
- (49) Balakrishnan, N.; Kharchenko, V.; Forrey, R.; Dalgarno, A. *Chem. Phys. Lett.* **1997**, *280*, 5.
- (50) Hutson, J. M. *New J. Phys.* **2007**, *9*, 152.
- (51) Idziaszek, Z.; Julienne, P. S. *Phys. Rev. Lett.* **2010**, *104*, 113202.
- (52) Kitagawa, M.; Enomoto, K.; Kasa, K.; Takahashi, Y.; Ciurylo, R.; Naidon, P.; Julienne, P. S. *Phys. Rev. A* **2008**, *77*, 012719.
- (53) Friedrich, H.; Trost, J. *Phys. Rep.* **2004**, *397*, 359.
- (54) Friedrich, H.; Trost, J. *Phys. Rep.* **2007**, *451*, 234.
- (55) Boisseau, C.; Audouard, E.; Vigué, J. *Europhys. Lett.* **1998**, *41* (4), 349.
- (56) Julienne, P. S. In *Cold Molecules: Theory, Experiments, Applications*; Krems, R. B., Friedrich, B., Stwalley, W. C., Eds.; CRC Press: Boca Raton, FL, 2009; Chapter 6, p 221.
- (57) Köhler, T.; Góral, K.; Julienne, P. S. *Rev. Mod. Phys.* **2006**, *78*, 1311.
- (58) One sometimes speaks of the binding energy of the bound state, which is defined to be positive and equal to $-E_b$.
- (59) For the relation between Δ and the width of the resonance in energy, see ref 40 in eqs 17 and 22.
- (60) Zirbel, J. J.; Ni, K. K.; Ospelkaus, S.; Nicholson, T. L.; Olsen, M. L.; Julienne, P. S.; Wieman, C. E.; Ye, J.; Jin, D. S. *Phys. Rev. A* **2008**, *78*, 013416.
- (61) Julienne, P. S. *Faraday Discuss.* **2009**, *142*, 361.
- (62) LeRoy, R. J.; Bernstein, R. B. *J. Chem. Phys.* **1970**, *52*, 3869.
- (63) Boisseau, C.; Audouard, E.; Vigué, J.; Flambaum, V. *Eur. Phys. J. D* **2000**, *12*, 199.
- (64) Mueller, T.-O.; Kaiser, A.; Friedrich, H. *Phys. Rev. A* **2011**, *84*, 032701.
- (65) Gao, B. *Phys. Rev. A* **1998**, *58*, 1728.
- (66) Mueller, T.-O.; Friedrich, H. *Phys. Rev. A* **2011**, *83*, 022701.
- (67) Jacoby, G.; Friedrich, H. *J. Phys. B: At. Mol. Opt. Phys.* **2002**, *35*, 4839.
- (68) Raab, P.; Friedrich, H. *Phys. Rev. A* **2009**, *80*, 052705.
- (69) Gao, B. *Phys. Rev. Lett.* **2010**, *104*, 213201.
- (70) Idziaszek, Z.; Simoni, A.; Calarco, T.; Julienne, P. S. *New J. Phys.* **2011**, *13*, 083005.
- (71) Gao, B. *Phys. Rev. A* **2000**, *62*, 050702.
- (72) Eltschka, C.; Moritz, M.; Friedrich, H. *J. Phys. B: At. Mol. Opt. Phys.* **2000**, *33*, 4033.
- (73) Eltschka, C.; Friedrich, H.; Moritz, M. *Phys. Rev. Lett.* **2001**, *86*, 2693.
- (74) Boisseau, C.; Audouard, E.; Vigué, J. *Phys. Rev. Lett.* **2001**, *86*, 2694.
- (75) Julienne, P. S.; Hanna, T. M.; Idziaszek, Z. *Phys. Chem. Chem. Phys.* **2011**, *13*, 19114.
- (76) Kotobigova, S. *New J. Phys.* **2010**, *12*, 073041.
- (77) Petrov, D. S.; Salomon, C.; Shlyapnikov, G. V. *Phys. Rev. Lett.* **2004**, *93*, 090404.
- (78) Jochim, S.; Bartenstein, M.; Altmeyer, A.; Hendl, G.; Riedl, S.; Chin, C.; Hecker Denschlag, J.; Grimm, R. *Science* **2003**, *302*, 2101.
- (79) Zwierlein, M. W.; Stan, C. A.; Schunck, C. H.; Raupach, S. M. F.; Gupta, S.; Hadzibabic, Z.; Ketterle, W. *Phys. Rev. Lett.* **2003**, *91*, 250401.
- (80) Bourdel, T.; Khaykovich, L.; Cubizolles, J.; Zhang, J.; Chevy, F.; Teichmann, M.; Tarruell, L.; Kokkelmans, S. J. J. M. F.; Salomon, C. *Phys. Rev. Lett.* **2004**, *93*, 050401.
- (81) Greiner, M.; Regal, C. A.; Jin, D. S. *Nature* **2003**, *426*, 537.
- (82) Inouye, S.; Andrews, M. R.; Stenger, J.; Miesner, H.-J.; Stamper-Kurn, D. M.; Ketterle, W. *Nature* **1998**, *392*, 151.
- (83) Kraemer, T.; Mark, M.; Waldburger, P.; G, D. J.; Chin, C.; Engeser, B.; Lange, A. D.; Pilch, K.; Jaakkola, A.; Nägerl, H.-C.; Grimm, R. *Nature* **2006**, *440*, 315.
- (84) Esry, B. D.; Greene, C. H.; Burke, J. P. *Phys. Rev. Lett.* **1999**, *83*, 1751.
- (85) Nielsen, E.; Macek, J. H. *Phys. Rev. Lett.* **1999**, *83*, 1751.
- (86) Bedaque, P. F.; Braaten, E.; Hammer, H.-W. *Phys. Rev. Lett.* **2000**, *85*, 908.
- (87) Weber, T.; Herbig, J.; Mark, M.; Nägerl, H.-C.; Grimm, R. *Phys. Rev. Lett.* **2003**, *91*, 123201.
- (88) Efimov, V. *Phys. Lett.* **1970**, *33B*, 563.
- (89) Efimov, V. *Sov. J. Nucl. Phys.* **1971**, *12*, 589.
- (90) Braaten, E.; Hammer, H.-W. *Phys. Rep.* **2006**, *428*, 259.
- (91) Shuman, E. S.; Barry, J. F.; DeMille, D. *Nature* **2010**, *467*, 820.
- (92) Van De Meerakker, S. Y. T.; Bethlem, H. L.; Meijer, G. *Nat. Phys.* **2008**, *4*, 595.

- (93) Bethlem, H. L.; Tarbutt, M. R.; Küpper, J.; Carty, D.; Wohlfart, K.; Hinds, E. A.; Meijer, G. *J. Phys. B: At. Mol. Opt. Phys.* **2006**, *39*, R263.
- (94) van de Meerakker, S. Y. T.; Bethlem, H. L.; Vanhaecke, N.; Meijer, G. *Chem. Rev.* **2012**, *112*, DOI: 10.1021/cr200349r.
- (95) Hutzler, N. R.; Lu, H.-I.; Doyle, J. M. *Chem. Rev.* **2012**, *112*, DOI: 10.1021/cr200362u.
- (96) Koch, C. P.; Shapiro, M. *Chem. Rev.* **2012**, *112*, 10.1021/cr200388z.
- (97) Jones, K. M.; Tiesinga, E.; Lett, P. D.; Julienne, P. S. *Rev. Mod. Phys.* **2006**, *78*, 483.
- (98) Thorsheim, H. R.; Weiner, J.; Julienne, P. S. *Phys. Rev. Lett.* **1987**, *58*, 2420.
- (99) Viteau, M.; Chotia, A.; Allegrini, M.; Bouloufa, N.; Dulieu, O.; Comparat, D.; Pillet, P. *Science* **2008**, *321*, 232.
- (100) Viteau, M.; Chotia, A.; Allegrini, M.; Bouloufa, N.; Dulieu, O.; Comparat, D.; Pillet, P. *Phys. Rev. A* **2009**, *79*, 021402.
- (101) Deiglmayr, J.; Grochola, A.; Repp, M.; Mörtlbaumer, K.; Glück, C.; Lange, J.; Dulieu, O.; Wester, R.; Weidmüller, M. *Phys. Rev. Lett.* **2008**, *101*, 133004.
- (102) Hodby, E.; Thompson, S. T.; Regal, C. A.; Greiner, M.; Wilson, A. C.; Jin, D. S.; Cornell, E. A.; Wieman, C. E. *Phys. Rev. Lett.* **2005**, *94*, 120402.
- (103) Jaksch, D.; Venturi, V.; Cirac, J. I.; Williams, C. J.; Zoller, P. *Phys. Rev. Lett.* **2002**, *89*, 040402.
- (104) Damski, B.; Santos, L.; Tiemann, E.; Lewenstein, M.; Kotochigova, S.; Julienne, P.; Zoller, P. *Phys. Rev. Lett.* **2003**, *90*, 110401.
- (105) Bergeman, T.; Kerman, A.; Sage, J.; Sainis, S.; DeMille, D. *Eur. Phys. J. D* **2004**, *31*, 179.
- (106) Stwalley, W. C. *Eur. Phys. J. D* **2004**, *31*, 221.
- (107) Sage, J. M.; Sainis, S.; Bergeman, T.; DeMille, D. *Phys. Rev. Lett.* **2005**, *94*, 203001.
- (108) Thalhammer, G.; Winkler, K.; Lang, F.; Schmid, S.; Grimm, R.; Hecker Denschlag, J. *Phys. Rev. Lett.* **2006**, *96*, 050402.
- (109) Lang, F.; Straten, P. V. D.; Brandstaetter, B.; Thalhammer, G.; Winkler, K.; Julienne, P. S.; Grimm, R.; Denschlag, J. H. *Nat. Phys.* **2008**, *4*, 223.
- (110) Winkler, K.; Lang, F.; Thalhammer, G.; Straten, P. v. d.; Grimm, R.; Denschlag, J. H. *Phys. Rev. Lett.* **2007**, *98*, 043201.
- (111) Lang, F.; Winkler, K.; Strauss, C.; Grimm, R.; Denschlag, J. H. *Phys. Rev. Lett.* **2008**, *101*, 133005.
- (112) Zirbel, J. J.; Ni, K.-K.; Ospelkaus, S.; D’Incao, J. P.; Wieman, C. E.; Ye, J.; Jin, D. S. *Phys. Rev. Lett.* **2008**, *100*, 143201.
- (113) Aldegunde, J.; Ran, H.; Hutson, J. M. *Phys. Rev. A* **2009**, *80*, 043410.
- (114) Ospelkaus, S.; Ni, K.-K.; Quéméner, G.; Neyenhuis, B.; Wang, D.; de Miranda, M. H. G.; Bohn, J. L.; Ye, J.; Jin, D. S. *Phys. Rev. Lett.* **2010**, *104*, 030402.
- (115) Debatin, M.; Takekoshi, T.; Rameshan, R.; Reichsöllner, L.; Ferlaino, F.; Grimm, R.; Vexiau, R.; Bouloufa, N.; Dulieu, O.; Nägerl, H.-C. *Phys. Chem. Chem. Phys.* **2011**, *13*, 18926.
- (116) Lercher, A.; Takekoshi, T.; Debatin, M.; Schuster, B.; Rameshan, R.; Ferlaino, F.; Grimm, R.; Nägerl, H. *Eur. Phys. J. D* **2011**, *65*, 3.
- (117) Takekoshi, T.; Debatin, M.; Rameshan, R.; Ferlaino, F.; Grimm, R.; Nägerl, H.-C.; Le Sueur, C. R.; Hutson, J. M.; Julienne, P. S.; Kotochigova, S.; Tiemann, E. *Phys. Rev. A* **2012**, *85*, 032506.
- (118) Ospelkaus, S.; Pe’er, A.; Ni, K.; Zirbel, J. J.; Neyenhuis, B.; Kotochigova, S.; Julienne, P. S.; Ye, J.; Jin, D. S. *Nat. Phys.* **2008**, *4*, 622.
- (119) Ospelkaus, S.; Ni, K.-K.; de Miranda, M. H. G.; Neyenhuis, B.; Wang, D.; Kotochigova, S.; Julienne, P. S.; Jin, D. S.; Ye, J. *Faraday Discuss.* **2009**, *142*, 351.
- (120) Aikawa, K.; Akamatsu, D.; Hayashi, M.; Oasa, K.; Kobayashi, J.; Naidon, P.; Kishimoto, T.; Ueda, M.; Inouye, S. *Phys. Rev. Lett.* **2010**, *105*, 203001.
- (121) Shuman, E. S.; Barry, J. F.; Glenn, D. R.; DeMille, D. *Phys. Rev. Lett.* **2009**, *103*, 223001.
- (122) Kerman, A. J.; Sage, J. M.; Sainis, S.; Bergeman, T.; DeMille, D. *Phys. Rev. Lett.* **2004**, *92*, 033004.
- (123) Mancini, M. W.; Telles, G. D.; Caires, A. R. L.; Bagnato, V. S.; Marcassa, L. G. *Phys. Rev. Lett.* **2004**, *92*, 133203.
- (124) Haimberger, C.; Kleinert, J.; Bhattacharya, M.; Bigelow, N. P. *Phys. Rev. A* **2004**, *70*, 021402.
- (125) Haimberger, C.; Kleinert, J.; Zabawa, P.; Wakim, A.; Bigelow, N. P. *New J. Phys.* **2009**, *11*, 055042.
- (126) Zabawa, P.; Wakim, A.; Neukirch, A.; Haimberger, C.; Bigelow, N. P.; Stolyarov, A. V.; Pazyuk, E. A.; Tamanis, M.; Ferber, R. *Phys. Rev. A* **2010**, *82*, 040501.
- (127) Wang, D.; Qi, J.; Stone, M. F.; Nikolayeva, O.; Wang, H.; Hattaway, B.; Gensemer, S. D.; Gould, P. L.; Eyler, E. E.; Stwalley, W. C. *Phys. Rev. Lett.* **2004**, *93*, 243005.
- (128) Nemitz, N.; Baumer, F.; Münchow, F.; Tassy, S.; Görlitz, A. *Phys. Rev. A* **2009**, *79*, 061403.
- (129) Gabbanini, C.; Dulieu, O. *Phys. Chem. Chem. Phys.* **2011**, *13*, 18905.
- (130) Ridinger, A.; Chaudhuri, S.; Salez, T.; Fernandes, D. R.; Bouloufa, N.; Dulieu, O.; Salomon, C.; Chevy, F. *Europhys. Lett.* **2011**, *96*, 33001.
- (131) Ji, Z.; Zhang, H.; Wu, J.; Yuan, J.; Yang, Y.; Zhao, Y.; Ma, J.; Wang, L.; Xiao, L.; Jia, S. *Phys. Rev. A* **2012**, *85*, 013401.
- (132) Cho, H.; McCarron, D.; Jenkin, D.; Köppinger, M.; Cornish, S. *Eur. Phys. J. D* **2011**, *65*, 125.
- (133) McCarron, D. J.; Cho, H. W.; Jenkin, D. L.; Köppinger, M. P.; Cornish, S. L. *Phys. Rev. A* **2011**, *84*, 011603.
- (134) Park, J. W.; Wu, C.-H.; Santiago, I.; Tiecke, T. G.; Ahmadi, P.; Zwicknagl, M. W. *ArXiv.org, e-prints* **2011**, *1110*, 4552.
- (135) Deh, B.; Gunton, W.; Klappauf, B. G.; Li, Z.; Semczuk, M.; Van Dongen, J.; Madison, K. W. *Phys. Rev. A* **2010**, *82*, 020701.
- (136) Hara, H.; Takasu, Y.; Yamaoka, Y.; Doyle, J. M.; Takahashi, Y. *Phys. Rev. Lett.* **2011**, *106*, 205304.
- (137) Ivanov, V. V.; Khramov, A.; Hansen, A. H.; Dowd, W. H.; Münchow, F.; Jamison, A. O.; Gupta, S. *Phys. Rev. Lett.* **2011**, *106*, 153201.
- (138) Hansen, A. H.; Khramov, A.; Dowd, W. H.; Jamison, A. O.; Ivanov, V. V.; Gupta, S. *Phys. Rev. A* **2011**, *84*, 011606.
- (139) Munchow, F.; Bruni, C.; Madalinski, M.; Gorlitz, A. *Phys. Chem. Chem. Phys.* **2011**, *13*, 18734.
- (140) Heo, M.-S.; Wang, T. T.; Christensen, C. A.; Rvachov, T. M.; Cotta, D. A.; Choi, J.-H.; Lee, Y.-R.; Ketterle, W. *Phys. Rev. A* **2012**, *86*, 021602.
- (141) While \bar{a} refers to the van der Waals potential, here we have the scale length in mind for any power law potential.
- (142) Aymar, M.; Dulieu, O. *J. Chem. Phys.* **2005**, *122*, 204302.
- (143) Naidon, P.; Julienne, P. S. *Phys. Rev. A* **2006**, *74*, 062713.
- (144) Li, Z.; Alyabyshov, S. V.; Krems, R. V. *Phys. Rev. Lett.* **2008**, *100*, 073202.
- (145) Li, Z.; Krems, R. V. *Phys. Rev. A* **2009**, *79*, 050701.
- (146) Micheli, A.; Idziaszek, Z.; Pupillo, G.; Baranov, M. A.; Zoller, P.; Julienne, P. S. *Phys. Rev. Lett.* **2010**, *105*, 073202.
- (147) Syassen, N.; Bauer, D. M.; Lettner, M.; Volz, T.; Dietze, D.; García-Ripoll, J. J.; Cirac, J. I.; Rempe, G.; Dürr, S. *Science* **2008**, *320*, 1329.
- (148) Dürr, S.; García-Ripoll, J. J.; Syassen, N.; Bauer, D. M.; Lettner, M.; Cirac, J. I.; Rempe, G. *Phys. Rev. A* **2009**, *79*, 023614.
- (149) Büchler, H. P.; Demler, E.; Lukin, M.; Micheli, A.; Prokof’ev, N.; Pupillo, G.; Zoller, P. *Phys. Rev. Lett.* **2007**, *98*, 060404.
- (150) Micheli, A.; Pupillo, G.; Büchler, H. P.; Zoller, P. *Phys. Rev. A* **2007**, *76*, 043604.
- (151) Gorshkov, A. V.; Rabl, P.; Pupillo, G.; Micheli, A.; Zoller, P.; Lukin, M. D.; Büchler, H. P. *Phys. Rev. Lett.* **2008**, *101*, 073201.
- (152) Ticknor, C. *Phys. Rev. A* **2010**, *81*, 042708.
- (153) Quéméner, G.; Bohn, J. L. *Phys. Rev. A* **2010**, *81*, 060701.
- (154) Quéméner, G.; Bohn, J. L. *Phys. Rev. A* **2011**, *83*, 012705.
- (155) de Miranda, M. H. G.; Chotia, A.; Neyenhuis, B.; Wang, D.; Quéméner, G.; Ospelkaus, S.; Bohn, J.; Ye, J. L.; Jin, D. S. *Nat. Phys.* **2011**, *7*, 502.

- (156) Pashov, A.; Docenko, O.; Tamanis, M.; Ferber, R.; Knöckel, H.; Tiemann, E. *Phys. Rev. A* **2007**, *76*, 022511.
- (157) Quéméner, G.; Bohn, J. L. *Phys. Rev. A* **2010**, *81*, 022702.
- (158) Gao, B. *Phys. Rev. Lett.* **2010**, *105*, 263203.
- (159) Gao, B. *Phys. Rev. A* **2011**, *83*, 062712.
- (160) Hudson, E. R.; Gilfoyl, N. B.; Kotochigova, S.; Sage, J. M.; DeMille, D. *Phys. Rev. Lett.* **2008**, *100*, 203201.
- (161) Idziaszek, Z.; Quéméner, G.; Bohn, J. L.; Julienne, P. S. *Phys. Rev. A* **2010**, *82*, 020703.
- (162) Quéméner, G.; Bohn, J. L.; Petrov, A.; Kotochigova, S. *Phys. Rev. A* **2011**, *84*, 062703.
- (163) Greene, C.; Fano, U.; Strinati, G. *Phys. Rev. A* **1979**, *19*, 1485.
- (164) Greene, C. H.; Rau, A. R. P.; Fano, U. *Phys. Rev. A* **1982**, *26*, 2441.
- (165) Mies, F. H. *J. Chem. Phys.* **1984**, *80*, 2514.
- (166) Mies, F. H.; Julienne, P. S. *J. Chem. Phys.* **1984**, *80*, 2526.
- (167) Julienne, P. S.; Mies, F. H. *J. Opt. Soc. Am. B* **1989**, *6*, 2257.
- (168) Burke, J. P.; Greene, C. H.; Bohn, J. L. *Phys. Rev. A* **1998**, *81*, 3355.
- (169) Gao, B. *Phys. Rev. A* **1998**, *58*, 4222.
- (170) Mies, F. H.; Raoult, M. *Phys. Rev. A* **2000**, *62*, 012708.
- (171) Gao, B. *Phys. Rev. A* **2001**, *64*, 010701.
- (172) Gao, B.; Tiesinga, E.; Williams, C. J.; Julienne, P. S. *Phys. Rev. A* **2005**, *72*, 042719.
- (173) Julienne, P. S.; Gao, B. *AIP Conf. Proc.* **2006**, *869*, 261.
- (174) Hanna, T. M.; Tiesinga, E.; Julienne, P. S. *Phys. Rev. A* **2009**, *79*, 040701.
- (175) Croft, J. F. E.; Wallis, A. O. G.; Hutson, J. M.; Julienne, P. S. *Phys. Rev. A* **2011**, *84*, 042703.
- (176) Mies, F. H. *J. Chem. Phys.* **1969**, *51*, 787.
- (177) Mies, F. H. *J. Chem. Phys.* **1969**, *51*, 798.
- (178) Wynar, R.; Freeland, R. S.; Han, D. J.; Ryu, C.; Heinzen, D. J. *Science* **2000**, *287*, 1016.
- (179) Staanum, P.; Kraft, S. D.; Lange, J.; Wester, R.; Weidemüller, M. *Phys. Rev. Lett.* **2006**, *96*, 023201.
- (180) Zahizam, N.; Vogt, T.; Mudrich, M.; Comparat, D.; Pillet, P. *Phys. Rev. Lett.* **2006**, *96*, 023202.
- (181) Fioretti, A.; Comparat, D.; Crubellier, A.; Dulieu, O.; Masnou-Seeuws, F.; Pillet, P. *Phys. Rev. Lett.* **1998**, *80*, 4402.
- (182) Kraft, S.; Mikosch, J.; Staanum, P.; Deiglmayr, J.; Lange, J.; Fioretti, A.; Wester, R.; Weidemüller, M. *Appl. Phys. B: Laser Opt.* **2007**, *89*, 453.
- (183) Smith, I. W. M. *Angew. Chem., Int. Ed.* **2006**, *45*, 2842.
- (184) Langevin, P. *Ann. Chim. Phys.* **1905**, *5*, 245.
- (185) Levine, R. D. *Molecular Reaction Dynamics*; Cambridge University Press: Cambridge, U.K., 2009.
- (186) Clary, D. *Mol. Phys.* **1984**, *53*, 3.
- (187) Quéméner, G.; Balakrishnan, N.; Dalgarno, A. In *Cold Molecules: Theory, Experiments, Applications*; Krems, R., Friedrich, B., Stwalley, W. C., Eds.; CRC Press: Boca Raton, FL, 2009; Chapter 3, p 69.
- (188) Deiglmayr, J.; Repp, M.; Wester, R.; Dulieu, O.; Weidemüller, M. *Phys. Chem. Chem. Phys.* **2011**, *13*, 19101.
- (189) Deiglmayr, J.; Repp, M.; Grochola, A.; Dulieu, O.; Wester, R.; Weidemüller, M. *J. Phys.: Conf. Ser.* **2011**, *264*, 012014.
- (190) Deiglmayr, J.; Repp, M.; Dulieu, O.; Wester, R.; Weidemüller, M. *Eur. Phys. J. D* **2011**, *65*, 99.
- (191) Deiglmayr, J.; Repp, M.; Grochola, A.; Mortlbauer, K.; Gluck, C.; Dulieu, O.; Lange, J.; Wester, R.; Weidemüller, M. *Faraday Discuss.* **2009**, *142*, 335.
- (192) Mukaiyama, T.; Abo-Shaeer, J. R.; Xu, K.; Chin, J. K.; Ketterle, W. *Phys. Rev. Lett.* **2004**, *92*, 180402.
- (193) Xu, K.; Mukaiyama, T.; Abo-Shaeer, J. R.; Chin, J. K.; Miller, D. E.; Ketterle, W. *Phys. Rev. Lett.* **2003**, *91*, 210402.
- (194) Dürr, S.; Volz, T.; Marte, A.; Rempe, G. *Phys. Rev. Lett.* **2004**, *92*, 020406.
- (195) Regal, C. A.; Ticknor, C.; Bohn, J. L.; Jin, D. S. *Nature* **2003**, *424*, 47.
- (196) Herbig, J.; Kraemer, T.; Mark, M.; Weber, T.; Chin, C.; Nägerl, H.-C.; Grimm, R. *Science* **2003**, *301*, 1510.
- (197) Strecker, K. E.; Partridge, G. B.; Hulet, R. G. *Phys. Rev. Lett.* **2003**, *91*, 080406.
- (198) Cubizolles, J.; Bourdel, T.; Kokkelmans, S. J. J. M. F.; Shlyapnikov, G. V.; Salomon, C. *Phys. Rev. Lett.* **2003**, *91*, 240401.
- (199) Jochim, S.; Bartenstein, M.; Altmeyer, A.; Hendl, G.; Chin, C.; Denschlag, J. H.; Grimm, R. *Phys. Rev. Lett.* **2003**, *91*, 240402.
- (200) Zwierlein, M. W.; Stan, C. A.; Schunck, C. H.; Raupach, S. M. F.; Kerman, A. J.; Ketterle, W. *Phys. Rev. Lett.* **2004**, *92*, 120403.
- (201) Petrov, D. S.; Salomon, C.; Shlyapnikov, G. V. *Phys. Rev. A* **2005**, *71*, 012708.
- (202) Esry, B. D.; Greene, C. H.; Suno, H. *Phys. Rev. A* **2001**, *65*, 010705.
- (203) Petrov, D. S. *Phys. Rev. A* **2003**, *67*, 010703.
- (204) Suno, H.; Esry, B. D.; Greene, C. H. *Phys. Rev. Lett.* **2003**, *90*, 053202.
- (205) Chin, C.; Kraemer, T.; Mark, M.; Herbig, J.; Waldburger, P.; Nägerl, H.-C.; Grimm, R. *Phys. Rev. Lett.* **2005**, *94*, 123201.
- (206) The non-SI unit G is widely used in this field and we use it when original authors do; 1 G = 0.1 mT.
- (207) Knoop, S.; Ferlaino, F.; Berninger, M.; Mark, M.; Nägerl, H.-C.; Grimm, R.; D'Incao, J. P.; Esry, B. D. *Phys. Rev. Lett.* **2010**, *104*, 053201.
- (208) Syassen, N.; Volz, T.; Teichmann, S.; Dürr, S.; Rempe, G. *Phys. Rev. A* **2006**, *74*, 062706.
- (209) Lieb, E. H.; Liniger, W. *Phys. Rev.* **1963**, *130*, 1605.
- (210) Gangardt, D. M.; Shlyapnikov, G. V. *Phys. Rev. Lett.* **2003**, *90*, 010401.
- (211) Jaksch, D.; Bruder, C.; Cirac, J. I.; Gardiner, C. W.; Zoller, P. *Phys. Rev. Lett.* **1998**, *81*, 3108.
- (212) Misra, B.; Sudarshan, E. C. G. *J. Math. Phys.* **1977**, *18*, 756.
- (213) D'Incao, J. P.; Esry, B. D. *Phys. Rev. Lett.* **2008**, *100*, 163201.
- (214) D'Incao, J. P.; Esry, B. D. *Phys. Rev. Lett.* **2005**, *94*, 213201.
- (215) D'Incao, J. P.; Esry, B. D. *Phys. Rev. A* **2006**, *73*, 030702.
- (216) Krems, R. V. *Int. Rev. Phys. Chem.* **2005**, *24*, 99.
- (217) Hutson, J. M.; Soldán, P. *Int. Rev. Phys. Chem.* **2006**, *25*, 497.
- (218) Hutson, J. M.; Soldán, P. *Int. Rev. Phys. Chem.* **2007**, *26*, 1.
- (219) Weck, P. F.; Balakrishnan, N. *Int. Rev. Phys. Chem.* **2006**, *25*, 283.
- (220) Bodo, E.; Gianturco, F. A. *Int. Rev. Phys. Chem.* **2006**, *25*, 313.
- (221) Hu, W.; Schatz, G. C. *J. Chem. Phys.* **2006**, *125*, 132301.
- (222) Krems, R. V. *Phys. Chem. Chem. Phys.* **2008**, *10*, 4079.
- (223) Hutson, J. M. In *Cold Molecules: Theory, Experiments, Applications*; Krems, R., Friedrich, B., Stwalley, W. C., Eds.; CRC Press: Boca Raton, FL, 2009; Chapter 1, p 3.
- (224) Bohn, J. L. In *Cold Molecules: Theory, Experiments, Applications*; Krems, R., Friedrich, B., Stwalley, W. C., Eds.; CRC Press: Boca Raton, FL, 2009; Chapter 2, p 39.
- (225) Tscherbul, T. V.; Krems, R. V. In *Cold Molecules: Theory, Experiments, Applications*; Krems, R., Friedrich, B., Stwalley, W. C., Eds.; CRC Press: Boca Raton, FL, 2009; Chapter 4, p 125.
- (226) Balakrishnan, N.; Forrey, R.; Dalgarno, A. *Chem. Phys. Lett.* **1997**, *280*, 1.
- (227) Boothroyd, A. I.; Keogh, W. J.; Martin, P. G.; Peterson, M. R. *J. Chem. Phys.* **1996**, *104*, 7139.
- (228) Hutson, J. M.; Green, S. MOLSCAT computer code, version 14, distributed by Collaborative Computational Project No. 6; Engineering and Physical Sciences Research Council: U.K., 1994.
- (229) Bodo, E.; Gianturco, F. A.; Yurtsever, E. *Phys. Rev. A* **2006**, *73*, 052715.
- (230) Soldán, P.; Cvitaš, M. T.; Hutson, J. M.; Honvárt, P.; Launay, J.-M. *Phys. Rev. Lett.* **2002**, *89*, 153201.
- (231) Launay, J. M.; Le Dourneuf, M. *Chem. Phys. Lett.* **1989**, *163*, 178.
- (232) Soldán, P.; Cvitaš, M. T.; Hutson, J. M. *Phys. Rev. A* **2003**, *67*, 054702.
- (233) Higgins, J.; Hollebeek, T.; Reho, J.; Ho, T.-S.; Lehmann, K. K.; Rabitz, H.; Scoles, G.; Gutowski, M. J. *Chem. Phys.* **2000**, *112*, 5751.

- (234) Stone, A. J. *The theory of intermolecular forces*; Oxford University Press: New York, 1996.
- (235) Kaplan, I. G. *Intermolecular interactions*; John Wiley and Sons, Ltd.: Chichester, U.K., 2006.
- (236) Colavecchia, F. D.; Burke, J. P.; Stevens, W. J.; Salazar, M. R.; Parker, G. A.; Pack, R. T. *J. Chem. Phys.* **2003**, *118*, 5484.
- (237) Kaplan, I. G.; Roszak, S.; Leszczynski, J. *J. Chem. Phys.* **2000**, *113*, 6245.
- (238) Røeggen, I.; Almlöf, J. *J. Chem. Phys.* **1995**, *102*, 7095.
- (239) Lotrich, V. F.; Szalewicz, K. *J. Chem. Phys.* **1997**, *106*, 9688.
- (240) Quéméner, G.; Honvaul, P.; Launay, J.-M. *Eur. Phys. J. D* **2004**, *30*, 201.
- (241) Quéméner, G. Quantum mechanical study of molecular collisions at ultralow energy: Applications to alkali and alkaline-earth systems. Ph.D. thesis, University of Rennes, Rennes (France), 2006.
- (242) Simoni, A.; Launay, J. *Laser Phys.* **2006**, *16*, 707.
- (243) Simoni, A.; Launay, J.-M.; Soldán, P. *Phys. Rev. A* **2009**, *79*, 032701.
- (244) Quéméner, G.; Honvaul, P.; Launay, J.-M.; Soldán, P.; Potter, D. E.; Hutson, J. M. *Phys. Rev. A* **2005**, *71*, 032722.
- (245) Lysebo, M.; Veseth, L. *Phys. Rev. A* **2008**, *77*, 032721.
- (246) Soldán, P. *J. Chem. Phys.* **2010**, *132*, 234308.
- (247) Guérout, R.; Soldán, P.; Aymar, M.; Deiglmayr, J.; Dulieu, O. *Int. J. Quantum Chem.* **2009**, *109*, 3387.
- (248) Cvitaš, M. T.; Soldán, P.; Hutson, J. M.; Honvaul, P.; Launay, J.-M. *Phys. Rev. Lett.* **2005**, *94*, 033201.
- (249) Cvitaš, M. T.; Soldán, P.; Hutson, J. M.; Honvaul, P.; Launay, J.-M. *Phys. Rev. Lett.* **2005**, *94*, 200402.
- (250) Cvitaš, M. T.; Soldán, P.; Hutson, J. M.; Honvaul, P.; Launay, J.-M. *J. Chem. Phys.* **2007**, *127*, 074302.
- (251) Quéméner, G.; Launay, J.-M.; Honvaul, P. *Phys. Rev. A* **2007**, *75*, 050701.
- (252) Stwalley, W. C. *Can. J. Chem.* **2004**, *82*, 709.
- (253) James, H. M.; Coolidge, A. S. *J. Chem. Phys.* **1933**, *1*, 825.
- (254) Quéméner, G.; Balakrishnan, N.; Krems, R. V. *Phys. Rev. A* **2008**, *77*, 030704.
- (255) Quéméner, G.; Balakrishnan, N. *J. Chem. Phys.* **2009**, *130*, 114303.
- (256) Balakrishnan, N.; Quéméner, G.; Forrey, R. C.; Hinde, R. J.; Stancil, P. C. *J. Chem. Phys.* **2011**, *134*, 014301.
- (257) Fonseca dos Santos, S.; Balakrishnan, N.; Lepp, S.; Quéméner, G.; Forrey, R. C.; Hinde, R. J.; Stancil, P. C. *J. Chem. Phys.* **2011**, *134*, 214303.
- (258) Deiglmayr, J.; Aymar, M.; Wester, R.; Weidemüller, M.; Dulieu, O. *J. Chem. Phys.* **2008**, *129*, 064309.
- (259) González-Férez, R.; Mayle, M.; Sánchez-Moreno, P.; Schmelcher, P. *Europhys. Lett.* **2008**, *83*, 43001.
- (260) Aldegunde, J.; Rivington, B. A.; Żuchowski, P. S.; Hutson, J. M. *Phys. Rev. A* **2008**, *78*, 033434.
- (261) Ran, H.; Aldegunde, J.; Hutson, J. M. *New J. Phys.* **2010**, *12*, 043015.
- (262) Aldegunde, J.; Hutson, J. M. *Phys. Rev. A* **2009**, *79*, 013401.
- (263) Barnett, R.; Petrov, D.; Lukin, M.; Demler, E. *Phys. Rev. Lett.* **2006**, *96*, 190401.
- (264) Zemke, W. T.; Byrd, J. N.; Michels, H. H.; Montgomery, J. J. A.; Stwalley, W. C. *J. Chem. Phys.* **2010**, *132*, 244305.
- (265) Tscherbul, T. V.; Barinovs, G.; Kłos, J.; Krems, R. V. *Phys. Rev. A* **2008**, *78*, 022705.
- (266) Żuchowski, P. S.; Hutson, J. M. *Phys. Rev. A* **2010**, *81*, 060703.
- (267) Byrd, J. N.; Montgomery, J. A.; Côté, R. *Phys. Rev. A* **2010**, *82*, 010502.
- (268) Meyer, E. R.; Bohn, J. L. *Phys. Rev. A* **2010**, *82*, 042707.
- (269) Soldán, P. *Phys. Rev. A* **2008**, *77*, 054501.
- (270) Soldán, P. *Phys. Rev. A* **2010**, *82*, 034701.
- (271) Meyer, E. R.; Bohn, J. L. *Phys. Rev. A* **2011**, *83*, 032714.
- (272) Van De Meerakker, S. Y. T.; Bethlehem, H. L.; Meijer, G. In *Cold Molecules: Theory, Experiments, Applications*; Krems, R., Friedrich, B., Stwalley, W. C., Eds.; CRC Press: 2009; Chapter 14, p 509.
- (273) Żuchowski, P. S.; Aldegunde, J.; Hutson, J. M. *Phys. Rev. Lett.* **2010**, *105*, 153201.
- (274) Guérout, R.; Aymar, M.; Dulieu, O. *Phys. Rev. A* **2010**, *82*, 042508.
- (275) Kajita, M.; Gopakumar, G.; Abe, M.; Hada, M. *Phys. Rev. A* **2011**, *84*, 022507.
- (276) Kotochigova, S.; Petrov, A.; Linnik, M.; Kłos, J.; Julianne, P. S. *J. Chem. Phys.* **2011**, *135*, 164108.
- (277) Gopakumar, G.; Abe, M.; Hada, M.; Kajita, M. *Phys. Rev. A* **2011**, *84*, 045401.
- (278) Gopakumar, G.; Abe, M.; Kajita, M.; Hada, M. *Phys. Rev. A* **2011**, *84*, 062514.
- (279) Brown, J. M.; Carrington, A. *Rotational spectroscopy of diatomic molecules*; Cambridge University Press: 2003.
- (280) Baranov, M. A.; Dalmonte, M.; Pupillo, G.; Zoller, P. *Chem. Rev.* **2012**, *112*, DOI: 10.1021/cr2003568.
- (281) Wall, M. L.; Carr, L. D. *Phys. Rev. A* **2010**, *82*, 013611.
- (282) Gorshkov, A. V.; Manmana, S. R.; Chen, G.; Ye, J.; Demler, E.; Lukin, M. D.; Rey, A. M. *Phys. Rev. Lett.* **2011**, *107*, 115301.
- (283) Gorshkov, A. V.; Manmana, S. R.; Chen, G.; Demler, E.; Lukin, M. D.; Rey, A. M. *Phys. Rev. A* **2011**, *84*, 033619.
- (284) Pellegrini, P.; Desouter-Lecomte, M. *Eur. Phys. J. D* **2011**, *64*, 163.
- (285) Pellegrini, P.; Vranckx, S.; Desouter-Lecomte, M. *Phys. Chem. Chem. Phys.* **2011**, *13*, 18864.
- (286) DeMille, D. *Phys. Rev. Lett.* **2002**, *88*, 067901.
- (287) Yelin, S. F.; Kirby, K.; Côté, R. *Phys. Rev. A* **2006**, *74*, 050301.
- (288) Rabl, P.; DeMille, D.; Doyle, J. M.; Lukin, M. D.; Schoelkopf, R. J.; Zoller, P. *Phys. Rev. Lett.* **2006**, *97*, 033003.
- (289) Kuznetsova, E.; Côté, R.; Kirby, K.; Yelin, S. F. *Phys. Rev. A* **2008**, *78*, 012313.
- (290) Yelin, S. F.; DeMille, D.; Côté, R. In *Cold Molecules: Theory, Experiments, Applications*; Krems, R., Friedrich, B., Stwalley, W. C., Eds.; CRC Press: 2009; Chapter 17, p 629.
- (291) We follow the common usage of experimentalists to call a loss-rate coefficient β instead of K .
- (292) Gorin, E. *Acta Physicochim. U.R.S.S.* **1938**, *9*, 681.
- (293) Fernández-Ramos, A.; Miller, J. A.; Klippenstein, S. J.; Truhlar, D. G. *Chem. Rev.* **2006**, *106*, 4518.
- (294) Mayle, M.; Ruzic, B. P.; Bohn, J. L. *Phys. Rev. A* **2012**, *85*, 062712.
- (295) Bohn, J. L.; Cavagnero, M.; Ticknor, C. *New J. Phys.* **2009**, *11*, 055309.
- (296) Wang and Greene³¹⁴ extended the equation in Figure 62 by including in these phase shifts a higher term in k^2 from the contribution of the dipole–dipole long-range potential.
- (297) Gao, B. *J. Phys. B: At. Mol. Opt. Phys.* **2004**, *37*, 4273.
- (298) Wang, D.; Neyenhuis, B.; de Miranda, M. H. G.; Ni, K.-K.; Ospelkaus, S.; Jin, D. S.; Ye, J. *Phys. Rev. A* **2010**, *81*, 061404.
- (299) The Fermi temperature T_F determines where Fermi statistics become important as temperature is lowered.
- (300) Avdeenkov, A. V.; Bohn, J. L. *Phys. Rev. Lett.* **2003**, *90*, 043006.
- (301) Ticknor, C. *Phys. Rev. A* **2009**, *80*, 052702.
- (302) This is equivalent to a_3 in eq 4 with $C_3 = d^2$.
- (303) Kastberg, A.; Phillips, W. D.; Rolston, S. L.; Spreeuw, R. J. C.; Jessen, P. S. *Phys. Rev. Lett.* **1995**, *74*, 1542.
- (304) Greiner, M.; Bloch, I.; Mandel, O.; Hänsch, T. W.; Esslinger, T. *Phys. Rev. Lett.* **2001**, *87*, 160405.
- (305) D’Incao, J. P.; Greene, C. H. *Phys. Rev. A* **2011**, *83*, 030702.
- (306) Hanna, T. M.; Tiesinga, E.; Mitchell, W. F.; Julianne, P. S. *Phys. Rev. A* **2012**, *85*, 022703.
- (307) Ye, J.; Kimble, H. J.; Katori, H. *Science* **2008**, *320*, 1734.
- (308) Kotochigova, S.; DeMille, D. *Phys. Rev. A* **2010**, *82*, 063421.
- (309) Chotia, A.; Neyenhuis, B.; Moses, S. A.; Yan, B.; Covey, J. P.; Foss-Feig, M.; Rey, A. M.; Jin, D. S.; Ye, J. *Phys. Rev. Lett.* **2012**, *108*, 080405.
- (310) Kotochigova, S.; Tiesinga, E.; Julianne, P. S. *New J. Phys.* **2009**, *11*, 055043.

- (311) Ticknor, C.; Rittenhouse, S. T. *Phys. Rev. Lett.* **2010**, *105*, 013201.
- (312) Mehta, N. P.; Rittenhouse, S. T.; D'Incao, J. P.; von Stecher, J.; Greene, C. H. *Phys. Rev. Lett.* **2009**, *103*, 153201.
- (313) Wang, Y.; D'Incao, J. P.; Greene, C. H. *Phys. Rev. Lett.* **2011**, *106*, 233201.
- (314) Wang, Y.; Greene, C. H. *Phys. Rev. A* **2012**, *85*, 022704.
- (315) Wang, Y.; D'Incao, J. P.; Greene, C. H. *Phys. Rev. Lett.* **2011**, *107*, 233201.
- (316) The references cited are a few examples and by no means exhaustive.
- (317) Lehmann, K. K.; Scoles, G.; Pate, B. H. *Annu. Rev. Phys. Chem.* **1994**, *45*, 241.
- (318) Bittinger, K. L.; Virgo, W. L.; Field, R. W. *J. Phys. Chem. A* **2011**, *115*, 11921.
- (319) Ionov, S. I.; Brucker, G. A.; Jaques, C.; Chen, Y.; Wittig, C. J. *Chem. Phys.* **1993**, *99*, 3420.
- (320) Reid, S. A.; Reisler, H. *J. Phys. Chem.* **1996**, *100*, 474.
- (321) Bowman, J. M.; Suits, A. G. *Phys. Today* **2011**, *64*, 33.
- (322) Truhlar, D. G.; Garrett, B. C.; Klippenstein, S. J. *J. Phys. Chem.* **1996**, *100*, 12771.
- (323) Jacobson, M. P.; Jung, C.; Taylor, H. S.; Field, R. W. *J. Chem. Phys.* **1999**, *111*, 600.
- (324) Jacobson, M. P.; Field, R. W. *J. Phys. Chem. A* **2000**, *104*, 3073.